UNIVERSITY OF THE WITWATERSRAND

DOCTORAL THESIS

Digital toolbox for the generation and detection of vectorial structured light

Author:
Keshaan SINGH

Supervisors:
Dr Angela DUDLEY
Prof. Andrew FORBES



A thesis submitted in fulfillment of the requirements
for the degree of Doctor of Philosophy

in the

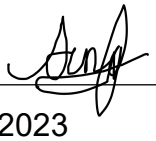
Structured Light Laboratory
School of Physics

June 19, 2023

Declaration of Authorship

I, Keshaan SINGH, declare that this thesis titled, "Digital toolbox for the generation and detection of vectorial structured light" and the work presented in it are my own. I confirm that:

- This work was done wholly or mainly while in candidature for a research degree at this University.
- Where any part of this thesis has previously been submitted for a degree or any other qualification at this University or any other institution, this has been clearly stated.
- Where I have consulted the published work of others, this is always clearly attributed.
- Where I have quoted from the work of others, the source is always given. With the exception of such quotations, this thesis is entirely my own work.
- I have acknowledged all main sources of help.
- Where the thesis is based on work done by myself jointly with others, I have made clear exactly what was done by others and what I have contributed myself.

Signed: 

Date: 19/06/2023

"I shall either find a way or make one."

Hannibal Barca

UNIVERSITY OF THE WITWATERSRAND

Abstract

Doctor of Philosophy

Digital toolbox for the generation and detection of vectorial structured light

by Keshaan SINGH

Light has been an invaluable tool in the development of the modern world, with the myriad of applications increasing along with our degree of control over it. From the development of coherent light sources, to the shaping of amplitude and phase, this development has not ceased for the past half century. The field of structured light, borne out of the necessity and desire for control over light, has been growing steadily in recent years. In the spatial domain, the control over light's polarization (i.e., the local planes in which the electric and magnetic fields oscillate) has been the most recent avenue of improvement, providing enhancements to a variety of applications ranging form microscopy and communication to materials processing and metrology. This class of light, commonly referred to as vectorial light, often requires specialized equipment in order for its its creation before its numerous benefits can be exploited. These tools often incur high costs and suffer from limitations relating to the diversity of vectorial light they can create, wavelength dependence and slow refresh rates.

This thesis follows the development of a series of digital tools for the versatile generation and analysis of vectorial light using low-cost core technologies which can operate at high rates over a broad wavelength range. We follow the development of the generation tool in the context of its application in generating novel accelerating polarization structures, emulating vectorially apertured optics, generating probes to measure birefringence and chirality and creating synthetic spin dynamics. The development of the analysis tool is explored by investigating its application in performing automated digital Stokes polarimetry measurements, completely characterizing the internal degrees of freedom of arbitrary vectorial light and acting as a polarization and wavelength independent wavefront sensor. We then demonstrate how these tools can be used, in conjunction, to investigate the fundamental invariance of vectorial light to perturbing channels and how this invariance can be exploited in a highly robust novel communication scheme. In addition to demonstrating the applicability and versatility of these vectorial light tools, the applications offered a means to highlight areas for the optimization for the design. This culminated in the ongoing prototyping of versatile, fast, broadband devices which operate stably and have a small physical footprint.

Contents

Declaration of Authorship **iii**

Abstract **vii**

1 Introduction **1**
1.1 Applications for vectorial structured light 2
1.2 Current tools for generating and analysing vectorial structured light . 4

2 Preliminary Theory **7**
2.1 The paraxial Helmholtz equation 7
2.2 Scalar spatial modes 9
2.2.1 Laguerre-Gaussian modes 9
2.2.2 Hermite-Gaussian modes 10
2.2.3 Bessel-Gaussian modes 11
2.3 Stokes and Jones polarization formalisms 11
2.3.1 Stokes vectors, the Poincaré sphere and Mueller matrices 11
2.3.2 Jones vectors and Jones matrices 13
2.4 Vector spatial modes, vectorness and the higher-order Poincaré sphere 15
2.4.1 Vector modes 15
2.4.2 Vectorness 15
2.4.3 Higher/Hybrid-order Poincaré spheres 16
2.5 Complex amplitude modulation schemes 17
2.5.1 Liquid crystal spatial light modulators (SLMs) 17
2.5.2 Digital micro-mirror devices (DMDs) 19

3 A versatile vectorial light generator **21**
3.1 SLM based generator used to produce accelerating polarization structures 22
3.1.1 Introduction 22
3.1.2 Concept and Theory 23
3.1.3 Experiment 27
3.1.4 Results 28
3.1.5 Discussion and Conclusion 30
3.2 DMD based generator used to emulate a vectorially apertured axicon . 31
3.2.1 Introduction 31
3.2.2 Concept 34
3.2.3 Experimental Setup 35
3.2.4 Results 36
3.2.5 Discussion and Conclusion 38
3.3 DMD-based birefringence probe 40
3.3.1 Introduction 40
3.3.2 Theoretical description 41
3.3.3 Experiment 43

3.3.4 Discussion and conclusion . . . 49
3.4 DMD based generator used to emulate spin systems . . . 50
3.4.1 Introduction . . . 51
3.4.2 Theory . . . 52
3.4.3 Experiment . . . 56
3.4.4 Results and Discussion . . . 57
3.4.5 Conclusions . . . 59
3.5 Comments on the iterations of vectorial light generators . . . 60

4 A versatile vectorial light analyser 62
4.1 Digital Stokes polarimetry using SLMs and DMDs . . . 62
4.1.1 Introduction . . . 62
4.1.2 Digital Stokes Polarimetry . . . 64
4.1.3 Experimental Realisations and Results . . . 67
4.2 Completely characterizing vector fields using a DMD based analyser . 72
4.2.1 Introduction . . . 72
4.2.2 Concept . . . 73
4.2.3 Experimental procedure . . . 75
4.2.4 Results . . . 78
4.2.5 Conclusion . . . 81
4.3 Versatile wavefront sensing with a DMD . . . 81
4.3.1 Introduction . . . 81
4.3.2 Theory . . . 84
4.3.3 Experiment . . . 86
4.3.4 Results and Discussion . . . 88
4.3.5 Conclusion . . . 89
4.4 Comments on the iterations and variations of vectorial light analysers 90

5 Unitary invariance of vectorial light and how it can be exploited for robust communication 92
5.1 Using our digital tools to investigate the invariance of vectorial light through unitary channels . . . 92
5.1.1 Introduction . . . 92
5.1.2 Concept . . . 93
5.1.3 Experiment . . . 97
5.1.4 Results . . . 99
5.1.5 Discussion and Conclusion . . . 106
5.2 Using our digital tools to achieve robust communication through turbulent free-space . . . 107
5.2.1 Introduction . . . 107
5.2.2 Concept . . . 108
5.2.3 Experiment . . . 110
5.2.4 Results . . . 112
5.2.5 Discussion and conclusion . . . 116

6 Conclusion and prospectives 119

Bibliography 124

List of Figures

2.1 Plots of the normalized intensity (to the maximum in each mode) and phase of various a) Laguerre-Gaussian, b) Hermite-Gaussian and c) Bessel-Gaussian modes. 9
2.2 Diagram showing the relationship between the Cartesian co-ordinates of the Poincaré Sphere and the ellipticity and orientation angles of the polarization ellipse. 13
2.3 Intensity and polarization distributions of some vector spatial modes. 16
2.4 HOPSs for a variety of vectorial superpositions. 17
2.5 a) Grayscale image of an SLM hologram used to produce an LG_0^1 mode. b) Diffraction orders produced by the SLM hologram (the desired information is contained in the +1 diffraction order). c) Cross section (taken from the dashed red line in (a) of the phase modulation produced by the SLM hologram). It is worth noting the function $f(A)$ which modulates the depth of the phase grating. 18
2.6 a) Binary image of a DMD hologram used to produce an LG_0^1 mode. b) Diffraction orders produced by the DMD hologram (the desired information is contained in the +1 diffraction order). c) Cross section (taken from the dashed red line in (a) of the amplitude modulation produced by the DMD hologram. 19

3.1 Diagrams illustrating: (a) the intensity of scalar components used to generate an angularly accelerating/decelerating polarization structure (phases included as insets) and (b) the angularly accelerating/decelerating trajectory with propagation of the right (red) and left (blue) circularly polarized components of the resulting vector mode. The values used in these simulations are $l = 1$ and $\theta = \frac{\pi}{3}$. 23
3.2 Diagram showing the change in total azimuthal angle of the beam profile with right-circular polarization ($S_3 > 0$) changing with propagation. 25
3.3 Simulations of the Poynting vector (top) and total intensity (bottom) of a H-V superposition of weighted petal beams, the total intensity S_0 remains invariant with propagation. 26
3.4 Diagram showing the experimental set-up used to generate and characterize petal beams with azimuthally accelerating polarization structures. HeNe - Helium-Neon laser, EL - expansion lens, CL - collimation lens, SLM - spatial light modulator, M - mirrors, MD - D-shaped mirror, FL - Fourier lens, HWP - half-wave plate, BS - 50:50 beamsplitter, QWP - quarter-wave plate, LP - linear polarizer and CCD - charge-coupled device. 27
3.5 Diagram showing the equivalence of focusing and positive propagation of a beam generated in the focal plane of lens FL. 28

3.6 Experimental results showing the evolution of the SOP (top) and individual right-circular (R), left-circular (L), diagonal (D) and anti-diagonal (A) polarized component intensities (bottom) with propagation distance. 28
3.7 Plots showing: (a) the contribution of radial functions $R_{petal/ring}$ to the total intensity and (b) the normalized power of the ring and petal structures of four propagation dependent polarization components. . . 29
3.8 Diagrams showing the trajectory of the average 'petal' Stokes vector along the Poincaré sphere (left) as well as views along the input axis (right) for generation in the H-V (top) and R-L (bottom) bases, simulated comparisons are included as insets. 30
3.9 a) Half annular slit binary amplitude. b) Diffracted transverse intensity pattern in the far field of the half annular slit and c) Diffracted transverse intensity pattern in the far field of the half annular slit with an azimuthal phase $\exp(i3\varphi)$. 33
3.10 Diagram showing how the separation of orthogonal polarization states by a PBS followed by their recombination using a DMD can be used to replicate a vectorial axicon. Inset on the top left shows a representative example of the encoded multiplexed binary hologram and insets on the bottom right show exemplar CCD images captured at different propagation distances. 35
3.11 Plots showing the theoretical and measured 'splitting' and 'anti-splitting' intensity cross sections of non-diffracting beams generated by a vectorial axicon for a) $l = 0$ and b) $l = 3$ at $z = 250$ mm (complete measured transverse intensity profiles are included as insets). 37
3.12 CCD images showing the formation of non-diffracting polarization components produced by a vectorial axicon for a) $l = 0$ and b) $l = 3$ (simulated comparisons are included as insets). 38
3.13 SOP and Stokes intensities measured at $z = 0.5z_{max}$ for a) $l = 0$ and b) $l = 3$ (red[blue] ellipses represent RCP[LCP]). 39
3.14 The arrangement which allows polarization modulation to be effected by a DMD in order to probe a sample while maintaining stabilility using a reference arm (element details in main text). Insets on the bottom left are representative examples of binary holograms encoded onto the DMD (colored according to their encoded phases), while insets on the top right are CCD images captured in order to acquire a spatially resolved circular birefringence measurement from a liquid crystal q-plate, marked as the sample S. 43
3.15 Plot displaying the precision and accuracy of holographic phase shifting birefringence measurements applied to a half wave- (top) and quarter wave-plate (middle) as well as calibration for the zero point (bottom). Error bands corresponding to the measured standard deviations are included for the measured results. 45
3.16 a) Images showing the measured birefringence for a phase map encoded on an LCoS-SLM, encoded phases are included as insets. b) Plot showing the measured birefringence for a positive (+) and negative (-) phase ramp encoded on an LCoS-SLM, the encoded phase ramps are included for comparison. 46

3.17 a) The measured circular birefringence of a $q = 0.5$ liquid crystal q-plate with the azimuthal section plotted for comparison to its design below. b) The measured linear birefringence of a metasurface with the azimuthal section plotted for comparison to its design below. 47
3.18 a) The circular birefringence measured in L-Alanine crystals (microscope image included as inset). b) Molecular structure of L-Alanine. c) The circular birefringence measured in an *N*-Acetyl-L-cystein crystal (microscope image included as inset). d) Molecular structure of *N*-Acetyl-L-cystein. 48
3.19 Plot showing the measured optical rotation produced by Glucose and Fructose at different concentrations in water. 49
3.20 a) Left: Overlayed theoretical intensity plot of constituent orthogonally polarized Bessel modes as shown by the dashed rings. Right: Skyrme field with Skyrme number $\mathcal{N}$ associated to the concentric annular regions placed as insets. b) Theoretical plots of the relative intensity of the constituent BG_l components ($l_R = 0$, $l_L = 1$) for valid ($k_r^L = 1.2k_r^R$) and invalid ($k_r^L = 1.6k_r^R$) choice of radial wavevectors, where $|\alpha(r)|^2 = |J_{l_L}(k_r^L r)|^{2q}|J_{l_R}(k_r^R r)|^{-2q}$ with q defined in the text. c) Conceptual illustration of local Stokes vector precession about the S_3 axis due to the effective inhomogeneity $\vec{G}$ caused by the Gouy-phase difference between orthogonally polarized constituents. d) Experimentally measured vector plots of BG_l optical skyrmions beating between continuously deformable Bloch- and Néel-types, as well as a section indicating the radial variation of S_3. 52
3.21 Diagram showing the experimental arrangement used to generate and analyse BG_l based optical skyrmions [WP - Wollaston prism, EL - expansion lens, CL - collimation lens, HWP - half-wave plate, QWP - quater-wave plate, DMD - digital micro-mirror device, FL - Fourier lens, LP - linear polarizer]. The top right inset shows an example of binary amplitude holograms featuring individual rings for each of the two multiplexed holograms $H_{A(B)}$ (far-field). The bottom right inset shows examples of Stokes intensities measured by the CCD (near-field). 57
3.22 a) Plot showing the experimentally measured Skyrme number of various BG_l optical (anti-)skyrmions propagated over a well defined distance. b) Experimentally measured Stokes vector fields of the corresponding BG_l skyrmions in a). c) Plots showing the experimentally measured precession of a local Stokes vectors (from the corresponding beams of a) about the S_3 axis with propagation for various $\mathcal{N}$. . . . 58
3.23 a) Plot showing the path traced during propagation of a numerically simulated central ($r = 0$) Stokes vector generated using optical 'frozen-waves', insets show the views from each of the poles. b) Plots showing the ideal (theoretical) and simulated (via the angular spectrum method) relative phase $\Delta k_z z$ and amplitude S_3 of the constituent components of the vector field used to produce the Stokes vector rotation in (a). 60

4.1 Conceptual schematics of (a) the conventional Stokes polarimetry measurements, together with the digital adaptations, implementing (b) a SLM and (c) a DMD. QWP, quarter-wave plate; LP, linear polarizer; SLM, liquid crystal on silicon spatial light modulator; PG, polarization grating; DMD, digital micromirror device; BS, 50:50 beam-splitter. 64

4.2 Experimental diagrams illustrating the arrangement of the optical components used to acquire Stokes parameters for (a) conventional Stokes polarimetry and the digital approaches, implementing (b) a SLM and (c) a DMD. The representative holograms encoded onto the SLM and DMD screens are provided as inserts. HeNe, Helium Neon laser; QP, q-plate; M, mirror. 68
4.3 Conventional Stokes polarimetry. Left: the generated field of interest, on which the Stokes polarimetry is performed [in this case described by Eq. (4.7)]. Middle: measured intensity profiles of the Stokes projections. Right: the corresponding calculated Stokes parameters (min=0 and max=1 for S_0, S_3, while min=-1 and max=1 for S_1, S_2). Theoretical simulations are given as inserts. 68
4.4 Digital SLM Stokes polarimetry. Left: the generated field of interest, on which the Stokes polarimetry is performed [in this case described by a superposition of the two equations in Eq. (4.8)]. Middle: measured intensity profiles of the Stokes projections. Right: the corresponding calculated Stokes parameters (min=0 and max=1 for S_0, S_1, while min=-1 and max=1 for S_2, S_3). Theoretical simulations are given as inserts. 69
4.5 Diagram depicting the alignment of orthogonally polarized components through a 50:50 BS. As the misalignment in the beam paths improves (left to right), so the number of fringes decreases. 70
4.6 Diagram showing the independent phase modulation of orthogonal polarization components (top two rows for DMD holograms, H_A and H_B) and simulated interference of the components through a 50:50 BS (bottom row). 70
4.7 Digital DMD Stokes polarimetry. Left: the generated field of interest, on which the Stokes polarimetry is performed [in this case described by Eq. (4.7)]. Middle: measured intensity profiles of the Stokes projections. Right: the corresponding calculated Stokes parameters (min=0 and max=1 for S_0, S_3, while min=-1 and max=1 for S_1, S_2). Theoretical simulations are given as inserts. 71
4.8 Digital DMD Stokes polarimetry with curvature. Left: the generated field of interest, on which the Stokes polarimetry is performed [in this case described by Eq. (4.7)]. Middle: measured intensity profiles of the Stokes projections. Right: the corresponding calculated Stokes parameters (min=0 and max=1 for S_0, S_3, while min=-1 and max=1 for S_1, S_2). Theoretical simulations are given as inserts. Note the spiral lobes in I_D, I_H, S_1 and S_2. One can also note that the central vortex is slightly off-centered due to slight misalignment of the q-plate vortex with the input beam's center. 72
4.9 A) HOPS with $|\psi_{1(2)}\rangle = LG_{1(3)}^{5(-1)}$, the SOP of two example states on the sphere are included as insets - as well as the intensity and phase of the polar spatial modes and their associated circular polarization handedness. B) Schematic showing the separation of orthogonally polarized components from a vector state $|\Psi\rangle$, by a Wollaston prism, followed by a complex amplitude hologram and their projection into the same diagonal plane using a linear polarizer. 74

4.10 (Left) Diagram showing the arrangement used to generate arbitrary vector beams using a Wollaston prism to separate orthogonal circular polarizations and a DMD to recombine these - post modulation. (Right) Diagram showing the arrangement used to characterize arbitrary vector fields making use of a Wollaston prism to separate and a DMD to recombine orthogonal polarization components, with a linear polarizer to allow for interference of orthogonally polarized components. Abbreviations: HeNe - helium neon laser, EL - expansion lens, CL - collimation lens, HWP - half-wave plate, WP - Wollaston prism, BS - beam splitter, LP - linear polarizer, DMD - digital micro-mirror device, FL - Fourier lens, IFL - inverse Fourier lens, CCD - charge coupled device. 76
4.11 Crosstalk matrices (left), HOPS spheres with associated state vectors (top right) and SOP (bottom right) - measured for beams generated with A) $\alpha = \beta = 0$, $|\psi_{1(2)}\rangle = LG_{0(0)}^{1(-1)}$ B) $\alpha = 0$, $\beta = -\pi/2$, $|\psi_{1(2)}\rangle = LG_{0(0)}^{1(-1)}$ C) $\alpha = -0.1$, $\beta = -\pi/2$, $|\psi_{1(2)}\rangle = LG_{0(0)}^{1(-1)}$ and D) $\alpha = \beta = 0$, $|\psi_{1(2)}\rangle = LG_{1(3)}^{-5(1)}$. The ideal values for α, β and VQF are included in brackets to the right of the measured values. 79
4.12 OAM spectra for individual components $|\psi_{1(2)}\rangle = e^{\pm i5.5\varphi}$ (red - $|\psi_1\rangle$, blue - $|\psi_2\rangle$; experimental results in solid bars and theoretical prediction in dashed lines). The vector on the HOPS sphere and SOP for the vector beam generated by the orthogonal fractional OAM components are included as insets. 80
4.13 Crosstalk matrices and state vector lying on the HOPS sphere for $|\psi_{1(2)}\rangle = LG_{0(0)}^{40(-40)}$ (top left). HOPS sphere for $l \pm 40$ with the state vector (top right). Cropped regions displaying the SOP. 80
4.14 a) Experimental arrangements used to demonstrate how the DMD-TIE based wavefront sensor can recover digital (top) and physical (bottom) aberrations (note the sensor is comprised of $L_{1,2}$, DMD_2 and CCD while the BS and CCD_F were only used to asses the effectiveness of adaptive compensation). b) Diagram showing how the aberrated/probe beams generated by DMD_1 are used to create digital/physical wavefront distortions, how DMD_2 is used to digitally propagate the field at three distances and how phase recovered using the TIE is conjugated to perform adaptive (pre-)correction using DMD_1. 83
4.15 a) Measured astigmatic (top) and trefoil (bottom) aberrations at various strengths, insets show the encoded aberrations. b) Measured (left) and recorded (right) wavefronts of turbulence phase aberrations with Fried parameters of $r_0 = 1.3$ mm (top) and $r_0 = 0.5$ mm (bottom) - insets show the aberrated and adaptively corrected far field intensities. 84
4.16 Recovered wavefront aberrations (left) produced by a turbulence phase plate translated in the x direction, along with the aberrated (middle) and corrected (right) far-field intensities. 87
4.17 a) Recovered transverse phase profiles of a $f = 50$ mm focal length, N-BK7 spherical lens using TIE sensing implemented with a DMD at wavelengths of 457 nm and 488 nm. b) Radial cross sections of the phase profiles at 457 nm and 488 nm along the dashed lines. Dotted square indicates a cylindrically assymetric aberration in the 488 nm measurement. 89

4.18 a) Phase profiles recovered from a turbulence phase plate using Gaussian probe beams with vertical (left) and horizontal (right) polarization. b) CCD images containing the intensity profiles (captured in a single shot at each of the three propagation distances) for each polarized beam through vertical (top) and horizontal (bottom) linear polarizers. 90

5.1 Complex light in complex channels. A vectorial light field propagates through a perturbing medium. Examples of such perturbing media could be turbid, underwater, optical fiber or turbulent air. Here and elsewhere the beam profiles illustrate intensities (green gradients) overlaid with polarization ellipses indicating right-handed (red), left-handed (blue) and linear (orange) polarizations. 94

5.2 Vectorial light through a tilted lens. (a) The experiment has four stages: a generation stage to create the vectorial fields, a perturbation stage to pass it through a perturbing medium, and two detection stages to perform Stokes projections and modal decomposition. The insets show the initial $\ell = \pm 1$ (left panel) and $\ell = \pm 4$ (right panel) beams at plane Z_0. (b) Illustration of the propagation through a tilted lens, with exemplary measurement planes indicated as Z_1 through to Z_3. (c) The output $\ell = \pm 1$ and $\ell = \pm 4$ beams at these distances, confirm that the spatial structure alters with distance but that the vectorness (the inset number to each beam frame) does not, remaining above 93%. The optical elements comprise a HWP: half-wave plate, PBS: polarising beam splitter, Pol: polarizer, BS: beam splitter, QWP: quarter-wave plate, and CAM: camera, with the laser at wavelength $\lambda = 633$ nm. All beam profiles are shown as false colour intensity and polarization maps. 94

5.3 Impact of scattering across multiple subspaces. (a) The initial vector beam is geometrically represented by an equatorial state vector of unit length on a single $\ell = \pm 4$ HOPS, indicative of a maximally non-separable pure state. The experimental basis states are shown on the poles (as intensities with their respective polarization state on the right) and the vectorial sum (amplitude and polarization structure) is shown on the equator. The tilted lens deforms the initial mode into (b), and this new state can be mapped to multiple HOPSs, each spanned by a different OAM and radial mode (c). Each of these potentially describes a mixed state of some degree of non-separability (non-unit and/or non-equatorial state vectors). The (d) scattering probabilities and (e) phases over the OAM (ℓ) and radial (p) modes for the right (left) ($R(L)$) circular polarization components after the $\ell = \pm 4$ vectorial field traverses the tilted lens channel. The right and left components have equivalent scattering probabilities. There are $N = 5$ states, (ℓ, p), with non-zero probabilities and $N(N-1)/2 = 10$ pairs of multiple subspaces that can be formed. (f) The pairs of states constituting the subspace and corresponding VQF for the vector field in that particular subspace can be represented with a graph having a set of vertices (as the contributing states) connected by weighted edges, respectively. The weights of the edges correspond to the VQF. 96

5.4 The unitary channel mapping and its inversion. The unitary channel (tilted lens) $\mathbb{1}_A \otimes T_B$ maps the initial $\ell \pm 4$ vector field from the equator of its corresponding subspace onto a new HOPS spanned by an adjusted basis (shown as experimental images on the poles) where the vectorial structure is also a maximally non-separable pure state. (a) shows the $\ell = \pm 4$ example and (b) the $\ell = \pm 1$ example. Because the unitary channel is a change of basis, the inverse $(\mathbb{1}_A \otimes T_B)^\dagger$ can be applied to map the field back to the original sphere. In (c) the state $(\mathbb{1}_A \otimes T_B)^\dagger |\Psi_{\text{in}}\rangle$ is inserted as a pre-channel correction, resulting in the initial field $|\Psi_{\text{in}}\rangle$ as the output, shown here for $\ell = \pm 4$. In (d) post-channel correction is achieved on the output, shown for $\ell = \pm 1$, where the operation is simply a quarter waveplate, since $\mathbb{1}_A \otimes T_B = T_A \otimes \mathbb{1}_B$ for this subspace. 100

5.5 The choice of measurement basis. (a) Measurement of the vectorness in the original (Ori.) and adjusted (Adj.) basis $\ell = \pm 1$ (left) and $\ell = \pm 4$ (right) in the far-field of the tilted lens. (b) Measurement of the vectorness of an initial $\ell = \pm 1$ mode through experimentally simulated atmospheric turbulence as a function of the turbulence strength (D/r_0). A basis-dependent (BD) measurement in the original basis ($\ell = \pm 1$) shows a decay in vectorness, while the basis-independent (BI) approach reveals an invariance. Experimental data (points) show excellent agreement with theory (dashed curves). The insets show the left (red) and right (blue) polarization projections on the $\ell = \pm 1$ modal sphere for three example turbulence strengths (low, medium and strong). Each point on the spheres represents one instance from the experimental turbulence ensemble. Error bars are plotted as standard deviations from 50 instances of simulated turbulence. 102

5.6 Unravelling turbulence. Cross-talk matrices for preparation and measurement in the original basis for (a) no turbulence and (b) medium turbulence ($D/r_0 = 1.6$). (c) Measuring or (d) preparing in the adjusted basis removes the cross-talk. (e) The unitary action of the channel distorts the polarization structure of the initial beam but not its vectorial homogeneity, with the vectorness given in the insets. Below the polarization structure are the spatial modes composing the original basis ($u_{1,2}$) and perturbed basis ($v_{1,2}$) along with their polarization states $|R\rangle$ and $|L\rangle$. (f) The unravelling of the turbulence by a lossless unitary applied pre-channel, restoring the initial beam after the turbulence. The adjusted basis modes ($v^*_{1,2}$) and the corrected basis modes ($u_{1,2}$) are shown below the polarization structures with their respective polarization states. In (g), an image (left) encoded in the original basis is distorted after transmission through moderately weak (middle) and medium (right) turbulence characterized by $D/r_0 = 1$ and $D/r_0 = 1.6$, respectively. The same image is transmitted through the channel but decoded in the adjusted basis, for distortion-free communication, shown in the insets. 103

5.7 Real-world channels. (a) Measured VQF as a function of time for an $\ell = \pm 10$ beam over a temperature controlled hot plate ($\approx$ 200 mm path), with the inset showing a zoomed time window. The right panel shows the averaged VQF for particular temperature settings for $\ell = \pm 1$ and $\ell = \pm 5$ beams, showing the invariance of the vectorness for a basis independent (BI) measurement, and a decay when measured in a basis dependent (BD) fashion. (b) Particle movement (measured in x and y co-ordinates) in an optical trapping and tweezing system shows a trap stiffness decrease by $10\times$ when aberrated, recovering by $6\times$ when a pre-channel unitary is applied. (c) Delivery of vectorial light through a 1 m length of few-mode optical fiber shows a low Fidelity of 39% due to cross-talk when measured in the original basis, but increasing to 90% when measured in the adjusted basis. (d) After a 50 mm passage through a liquid medium, the vectorness remains intact (for input VQF of 0.5 and 1) even for chiral media such as D-Limonene. The graph shows VQF measurements for $\ell = \pm 2$ and $\ell = \pm 5$ through various liquids. The insets in the right panel show $\ell = \pm 20$ and $\ell = \pm 50$ output beams after the D-Limonene sample, both with a VQF above 0.99 (measured in a basis independent manner). 105

5.8 Modal vectorness for multi-bit encoding. Conceptual visualization of a sequence of vector beams with tuneable vectorness (denoted as C). Each C value is binned into the user-defined basis allowing for the received C to map to a bit-string of length determined by the basis choice. After propagating through an aberrating channel (e.g. atmospheric turbulence, underwater, single-mode fiber or even transparent cellular material) the intensity and polarization profiles of the beams are distorted, however the C is left unaffected. 107

5.9 Experimental demonstration. a) Diagram showing the setup used to generate vector fields with tune-able concurrence (EMITTER) and measure the concurrence (RECEIVER) after propagating through heated air (CHANNEL) - [L_i - lens, HWP_i - half-wave plate, WP - Wollaston prism, DMD_i - digital micro-mirror device, LP - linear polarizer, CCD - charge-coupled device]. b) Exemplar multiplexed binary amplitude holograms used to holographically control the concurrence of generated beams via weighting parameter a - associated bit strings are displayed. c) Exemplar Stokes intensities which are integrated over the dashed circles in order to calculate the concurrence [P_H - horizontal, P_V - horizontal, P_D - diagonal and P_R - right-circular polarization integrated powers]. 109

5.10 Discretized bases, crosstalk and multi-bit information transfer. a) Received concurrence of an input value varied in 16 discreet steps (insets show partial results for 8 and 32 steps) through still (solid line) and turbulent (dashed line) air. b) Crosstalk matrices (with associated fidelity) for the emitted and received concurrence through still (top) and turbulent (bottom) air for bases with $N = 8, 16$ and 32 (left to right). c) 3 Bit (8 level) image transmitted through still (top) and turbulent (bottom) air - red pixels highlight errors (inset shows the ground truth image) while the values report the image fidelity. 113

5.11 Noise, statistical variation and bit-errors. a) Mean received concurrence (over 50 points) per element in the $N = 16$ basis in both still (circles) and turbulent (triangles) air, error bars are visible in the inset. b) Distribution of received C values about their target for two example basis elements both without (top) and with (bottom) turbulence - values report the mean deviations across the $N = 16$ basis. c) Measured standard deviation for each element in the $N = 16$ basis through still and turbulent air, where the large overlap illustrates the turbulence invariance. d) Theoretically predicted BER as a function of the statistical spread δC and basis choice N, the white solid line represents the points where $N\delta C = 1$ and white dashed lines represent the deviations of our receiver under different channel conditions - δC_{still} and $\delta\tilde{C}_{\text{turb}}$. 114

5.12 Channel invariance comparison to OAM encoding. Crosstalk matrices through a) ideal and b) aberrated channels using both OAM (with $N = 11$) and vectorness (with $N = 11$ and $N = 50$) encoding schemes. The turbulence phase screen used to aberrate the beams is shown in the left panel of b). A truncated 32 mode subset of the $N = 50$ basis is highlighted showing improved fidelity. 115

6.1 Elements for a versatile, compact and stable vectorial light generator. . 122

List of Tables

2.1 Stokes vectors for various sates of polarization 12
2.2 Mueller matrices for various optical elements (θ is the angle of the transmission/fast axis from the $x-$axis). 14
2.3 Jones vectors for various sates of polarization. Note the chosen the phase convention expressing right-circular polarization with a $-\pi/2$ phase delay between the vertical and horizontal components. 14
2.4 Jones matrices of various optical elements (θ is the angle of the transmission/fast axis from the $x-$axis). 15

4.1 Table showing the Jones matrix parameters imparted by the DMD in order to acquire Stokes intensity measurements. 67
4.2 Table showing the transmission functions $T_{A(B)}$ used to acquire measurements to specify: orthogonal circularly polarized components of a vector field (top), the relative amplitudes and phases of the orthogonal components (middle) and the Stokes intensity measurements (bottom). 77

List of Publications

1. **Singh, K.**, Buono, W.T., Forbes, A. and Dudley, A., 2021. Accelerating polarization structures in vectorial fields. Optics Express, 29(2), pp.2727-2737.

2. **Singh, K.**, Buono, W.T., Chavez-Cerda, S. and Forbes, A., 2021. Demonstrating Arago–Fresnel laws with Bessel beams from vectorial axicons. JOSA A, 38(9), pp.1248-1254.

3. **Singh, K.**, Buono, W.T., Fernandes, M.A., Dudley, A. and Forbes, A., 2021. Spatially resolved birefringence measurements with a digital micro-mirror device. Optics Express, 29(21), pp.34616-34628.

4. **Singh, K.**, Tabebordbar, N., Forbes, A. and Dudley, A., 2020. Digital Stokes polarimetry and its application to structured light: tutorial. JOSA A, 37(11), pp.C33-C44.

5. **Singh, K.**. and Dudley, A., 2022. Digital toolbox for vector field characterization. Nanophotonics, 11(4), pp.753-761.

6. Nape, I., **Singh, K.**, Klug, A., Buono, W., Rosales-Guzman, C., McWilliam, A., Franke-Arnold, S., Kritzinger, A., Forbes, P., Dudley, A. and Forbes, A., 2022. Revealing the invariance of vectorial structured light in complex media. Nature Photonics, 16(7), pp.538-546.

7. **Singh, K.**, Nape, I., Buono, W.T., Dudley, A. and Forbes, A., 2023. A Robust basis for multi-bit optical communication with vectorial light. Laser & Photonics Reviews, p.2200844.

8. **Singh, K.**, Dudley, A. and Forbes, A., 2023. Versatile all-digital transport-of-intensity based wavefront sensor and adaptive optics using a DMD. Optics Express, 31(5), pp.8987-8997.

9. **Singh, K.**, Ornelas, P., Dudley, A. and Forbes, A., 2023. Synthetic spin dynamics with Bessel-Gaussian optical skyrmions. Optics Express, 31(10), pp.15289-15300.

Publication	1	2	3	4	5	6	7	8	9
Initial development of concept	25	25	25	25	50	12.5	50	100	60
Construction of experiment	50	85	100	66	100	66	100	100	100
Data acquisition	75	75	100	66	100	66	100	100	100
Data analysis and interpretation	100	100	100	66	100	50	100	100	100
Theoretical model	100	75	100	33	100	20	100	100	75
Complete first manuscript draft	25	25	20	25	50	12.5	25	33	25
Referee replies and revisions	25	25	20	25	50	12.5	25	33	25

Table showing the percentage contributions by the author to each listed publication.

Chapter 1

Introduction

Light has played an invaluable role in our development throughout recorded history and likely before. One can imagine our primitive ancestors having a sense of security as their dwellings were illuminated by the first man-made fires. In more conventional forms, it is believed that ancient Middle-Eastern societies used observations of refraction in quartz to produce lenses 3000 years ago [1]. For millennia this level of control over incoherent and unpolarized light afforded us many tools to communicate and observe the universe as well as our place in it [2]. A momentous leap in control came in 1960, when Theodor Maiman constructed the first laser giving us power over spatially and temporally coherent light [3]. This highly controlled source helped sculpt the modern world as we know it, from barcode scanners, printers and thermometers to the global undersea fiber optic network, industrial manufacturing and precision medical procedures [4–10]. These advances were enabled by the simple planar wavefront and Gaussian amplitude profile characteristic of the fundamental mode of conventional laser cavities. Within the last four decades a resurgence in our desire to improve our control over light has emerged and has, as expected, led to an avalanche of new applications, provided monumental improvements to existing ones and opened new avenues to probe the fundamental nature of the indispensable resource that is light. These latest advancements have focused on the manipulation of light's various degrees-of-freedom (DoFs) birthing a field referred to as structured light [11]. The DoFs can be further categorized into the temporal and the spatial domains, while this thesis will focus on the latter (as will be discussed throughout the remainder of this chapter) it can be noted that temporal light shaping enabled by tools such as ultra-fast pulsed lasers have spurred incredible advances [12].

This thesis follows the development of a set of self-contained, low-cost digital tools which allow for the versatile generation and detection of vectorial structured light: that is, light where the amplitude, phase and polarization are controlled. The remainder of Chapter 1 outlines applications and provides an overview of existing tools and techniques used to create and measure structured light, making note of existing limitations. Chapter 2 contains pre-requisite theory describing: scalar and vector spatial modes, Jones and Stokes-Mueller polarization formalisms as well as complex amplitude modulation schemes using phase and amplitude modulators. Theory relevant to specific subsequent chapters is presented within them. Chapter 3 describes the development of a versatile tool for the generation of vectorial structured light, demonstrating the effectiveness of the iterations through the generation of novel vectorial fields as well as providing a source to probe arbitrary birefringent materials. Chapter 4 follows the development of a versatile tool for the analysis of vectorial structured light, while demonstrating the effectiveness through digital Stokes polarimetry measurements, complete vectorial field characterization and a

broadband implementation of a stable, high-resolution wavefront sensor. Chapter 5 contains an investigation into the robust nature of vectorial light (using the developed tools) and a description of a novel robust information encoding scheme enabled by its findings. Chapter 6 will summarize the conclusions of the work and consider prospectives for the future of these digital tools.

1.1 Applications for vectorial structured light

The field of modern communication using light has historically relied on the fundamental Gaussian mode in both optical fiber and free-space, where the most conventional form of encoding referred to as on-off keying (OOK) assigns a bit value of 0(1) to the absence(presence) of light at the receiver [13]. The introduction of structured light, in the form of higher-order spatial modes significantly increased the data transmission rate. The orthogonality of spatial modes in a given basis allow multiple OOK signals to be superimposed into a single beam and separated at the receiver, multiplying the amount of data transferred by the number of modes used through this process known as mode-division-multiplexing (MDM) [14]. A significant problem with the MDM protocol is the potential for the transmission channel to induce modal mixing/crosstalk, this occurs both in atmospheric turbulence and optical fiber, and results in errors in the received signal [15]. Initially only scalar (homogenously polarized) spatial modes were used in MDM, however vector (inhomogeneously polarized) modes can also form orthogonal bases and some investigations demonstrated that they present less power scintillation through turbulence [16, 17]. This lower scintillation did not, however, translate into resilience to crosstalk as was later shown [18]. In Chapter 5 we present a novel encoding scheme, demonstrated using our digital tools, which exploits a property of vector beams which is truly invariant to atmospheric turbulence and shows promise in mitigating modal dispersion in fiber.

Metrology, being the science of measurement, has long benefited from the fundamental Gaussian mode as its planar phase has provided a bedrock for interferometric profilometry and wavefront sensing. For instance, conventional determination of the thickness of thin-films (on the order of nm) involves inspecting the interference of Gaussian X-ray beams reflected off of the films at different angles requiring complex, dangerous and expensive diffractometers [19]. Structured light offers a more elegant solution in the form of first-order Hermite-Gaussian modes (see Chapter 2). These modes feature a half-wave phase discontinuity along their center, the depth of which is altered proportional to the film thickness when reflecting from a film-substrate interface. This altering of the discontinuity effectively mixes the first-order mode with the fundamental and when the relative weightings are measured the thickness of the film can be determined from only two power measurements [20]. Another example of structured light addressing metrology needs is in the form of optical wavefront sensing. Common wavefront sensors include high resolution (but vibration sensitive) inteferometric sensors which interfere the beam of interest with a fundamental reference to extract the wavefront, and stable low resolution Shack-Hartmann lenslet arrays which focus individual segments of the beam of interest in order to determine local wavefront gradients [21]. Wavefront sensing using structured light involves exploiting the orthonormality and completeness of spatial

mode bases. This allows any optical field propagating in free space to be decomposed into a given spatial mode basis. With the measured complex weightings of the basis elements, the entire field (including the wavefront) can be reconstructed at high resolution [22]. An additional benefit provided by the structured light approach is the ability to determine the field's propagation dynamics using its constituent modes. This modal propagation scheme avoids the numerical artefacts prevalent in many numerical propagation approaches [23]. Chapter 4 follows the development and demonstration of a tool that is able to perform arbitrary modal projections even on vectorial light as well as the demonstration of a tool used to digitally propagate a field in order to perform high sensitivity wavefront sensing using another approach which utilizes the transport-of-intensity equation [24]. Another form of metrology widespread in industry is the measurement of birefringence (or optical chirality when relating to circular polarizations), where it is used to determine the handedness of chiral molecules in pharmaceuticals, the stresses in polymers/glasses and the concentrations of sugars in food/beverages. Conventionally this is done using a fundamental probe beam which has its polarization modulated by peizo-optic modulators (or rotating waveplates) before and after the sample and the resulting intensity projected using a linear polarizer [25, 26]. A curious aspect of this practice is that the piezo-optic materials/wave plates are birefringent themselves; Chapter 3 describes how our tools used to generate vectorial light can also be implemented to measure birefringence in a spatially resolved manner by exploiting holographic interference as opposed to birefringence itself.

In the field of microscopy, the traditional resolution limit is determined by the Abbe criterion which occurs around half of the illuminating light's wavelength [27]. Structured light assisted in the development of a field of superesolution microscopy which surpasses this limit. This is achieved through the selective deactivation of flourophores using beams containing a phase vortex where the intensity null at the vortex leaves active flourophores in regions allowing for resolutions in the order of 10 nm [28, 29]. The limitation of this technique is, however, still associated with how tightly the structure can be focused. Considerations of the time reversal of spherical waves emitted by atomic sources reveal that the focusing limit can surpass the Abbe criterion if the longitudinal polarization component of the optical field is significant [30]. To this end, radially polarized vectorial light fields which exhibit larger longitudinal polarization components than their scalar counterparts (when tightly focused) have enabled resolutions exceeding the subwavelength level [31]. Another considerable field of microscopy is that of light-sheet microscopy, where a cylindrical lens is used to focus a laser beam along a single axis into a thin sheet before entering a sample. The light scattered perpendicular to the direction of the sheet is imaged and the sheet translated axially to provide a 3-dimensional reconstruction of the sample. Fundamental modes naturally diffract upon propagation leading to a loss of power along the sample in the propagation direction. The utilization of structured Bessel-Gaussian modes (see Chapter 2) mitigates this effect due to their approximate non-diffracting nature [32]. Chapter 3 outlines the generation of vectorial Bessel-Gaussian beam superpositions which exhibit azimuthally accelerating and decelerating propagation dynamics, generated using an early iteration of the digital tool for vectiorial light generation.

The implementation of high powered lasers in materials processing has allowed for accurate automated cutting and drilling procedures to be implemented using focused fundamental Gaussian modes. The rectangularly structured cross-sections of

flap-top beams have naturally improved the accuracy of such procedures [33]. The previously discussed tight focusing superiority of radially polarized vector beams provides higher power densities for these processes [34]. The propagation invariance of Bessel-Gaussian beams has also lent itself to superior performance in deep hole drilling [33]. Chapter 3 includes an outline for a digital tool with the capability of generating all these structures at low power, which can be subsequently amplified for the above applications utilizing procedures such as those described in [35].

Optical manipulation involves using the minute forces which focused light can exert in order to trap and generally control microscopic objects. Naturally fundamental beams provided the initial steps in developing the technology, however noting that the axial and transverse forces are dependent on the intensity and transverse intensity gradient respectively makes it clear that structuring the beams will enhance operation [36]. Beams with optical vortices (e.g. Laguerre-Gaussian beams, see Chapter 2) have been used to create so-called optical spanners which can allow particles to circulate within their profiles [37]. The introduction of vectorial light, has led to propagation invariant flat-top beams which can be used to more reliably trap particles for in-situ fluorescence measurements [38]. In Chapter 5 we show how unitary aberrations which reduce the performance of an optical trap can be compensated for through appropriate characterization and pre-correction.

It should be noted that these are but a small subset of an incredibly large range of applications which exploit structured vectorial light, that have arisen in just the last few decades. Interested readers are advised to consult review papers which outline many more of the applications enabled by scalar and vectorial structured light [11, 39, 40].

1.2 Current tools for generating and analysing vectorial structured light

It should be clear that the development of the aforementioned applications, which are clearly relevant in many aspects of modern society, have benefited substantially from the introduction of structured light in the form of tailored intensity and phase profiles. Even greater advances are achieved when introducing the structured polarization of vectorial light. Consequently, the development of tools for both the generation and analysis of vectorial structured light is of great importance in taking these (and future) advances from proof-of-concept lab demonstrations to commercially available and viable options for widespread industrial implementation. We will first discuss static elements which by design are able to produce a single (or set of) structured light mode(s) by exploiting various physical processes, we will then discuss dynamic approaches involving the implementation of liquid crystal spatial-light-modulators (SLMs) and digital micro-mirror devices (DMDs).

One common method of generating vectorial light is using a device called a q-plate, a static device which is comprised of liquid crystals on a film sandwiched between glass plates [41, 42]. The crystals themselves are birefringent, meaning that light polarized along the crystals fast-axis experiences a different refractive index than light polarized along the orthogonal slow-axis. The thickness of the crystals

are designed to induce a half-wave phase difference between the fast- and slow-polarization axes. This causes circularly polarized light passing through the device to acquire a geometric-phase dependent on the orientation of the crystals [43]. Conventionally the crystals are given an azimuthally varying orientation resulting in right-/left-circularly polarized light being imparted with equal but oppositely charged (denoted by $\pm 2q$) helical phase profiles. Consequently, passing linearly polarized light through a q-plate leads to the generation of vector vortex modes (see Chapter 2). The specific type of vector vortex mode (of a given charge) can be controlled by the orientation of the input linear polarization and electronically addressable variations of q-plates allow for control over the desired charge. It is notable that the symmetry in geometric phase prevents the generation of asymmetrically charged components required, for instance, in creating vectorial flat-top beams. A notable deficiency of a q-plate is that it is a pure-phase element. This means that additional radial mode orders are introduced proportional to the charge [44]. This lack of amplitude control can lead to problems when coupling vector modes into optical fiber for communication applications. Q-plates are also designed for a single or small band of wavelengths (due to the refractive index being wavelength dependent). This significantly reduces their versatility. In Chapter 3 the geometric phase profiles of a liquid crystal q-plate is measured using one of our digital tools.

Another type of vectorial light generating device which has seen much development of late is the metasurface, a static device that can exploit both propagation-/dynamic-phase and geometric-phase in order to structure amplitude and phase in orthogonally polarized components independently, thus overcoming many of the obstacles faced by liquid crystal q-plates [45, 46]. This improved degree of control is afforded by the subwavelength nature of the device, composed of nanostructured posts each with customised height, width, length and angular orientation allowing for locally tunable dynamic-phase, birefringence and geometric-phase respectively. These devices have been implemented in Stokes polarization cameras, a tool with the ability to measure the spatially varying polarization structures of vectorial light [47]. While metasurfaces provide a high degree of control over vectorial light, their static nature limits their versatility since multiple specially fabricated optics will be required for different vector beams/applications, while their phase based modulation limits their ability to produce the amplitude envelopes of true spatial modes similar to q-plates. The birefringence of a dielectric metasurface is measured using our digital tool in Chapter 3.

The static nature of the devices/optics discussed so far have all been limited to a large degree in the variety of scalar/vector spatial modes they are able to create. Naturally the use of dynamically addressable devices for the generation of vectorial light has sought to remedy this. Two such classes of devices have found a place in recent years: SLMs and DMDs (the operational principles of each are covered in detail within Chapter 2). SLMs are comprised of pixels filled with birefringent liquid crystals between a glass substrate and mirror (while transmission based SLMs exist the reflective arrangement is more commonly employed and our discussions will be restricted to these). A transparent electrode on the glass surface is used to apply a potential difference across individual pixels which induces a rotation in the crystals proportional to the applied voltage, this changes the path length of incident light through the pixels and consequently the relative phase induced by the birefringence [48]. This allows for the phase of light polarized along the crystal slow-axis to be controlled in a dynamic manner, furthermore a diffraction grating can be encoded

allowing for the amplitude of light in the first diffraction order to be controlled by locally adjusting the depth of the grating [49] (Chapter 2 contains an overview of this encoding technique). For the purposes of creating vectorially structured light this scalar modulation can be integrated into interferrometric arrangements which facilitate the independent control and combination of arbitrary orthogonally polarized spatial modes. In Chapter 3 we utilize an SLM based vectorial light generator to create vector fields with accelerating and decelerating propagation dynamics. These schemes allow for the generation of an extremely large subset of the infinite possible vectorial light fields on demand, however the necessity for multi-element interferometers leads to instability in the intra-modal phase between the orthogonally polarized components which results in fluctuations between types of vector modes (e.g. the fluctuation between radially and azimuthally polarized vector modes will lead to a drastic variation in tight focusing enhancement). SLMs are available which operate in different wavelength regimes (e.g. visible from 400 nm to 650 nm, near-infrared from 650 nm to 1100 nm and telecommunication from 1.4 μm to 1.7 μm). To operate effectively at a well defined wavelength (e.g. 633 nm) the device will need to be calibrated appropriately (due to the wavelength dependence of the refractive index) which limits their versatility when rapid generation at multiple wavelengths is desired.

DMDs are devices which were initially designed for, and are still employed in, projector technology. They are comprised of an array of individually addressable mirrors generally <10 μm in size, the mirrors can be made to actuate about their hypotenuse by angles of $\pm 12^{\circ}$ corresponding to the binary pixel values of 0 or 1 [50]. Based on this reflective operation, the devices can function as binary amplitude elements and a grating can be introduced where local shifts in the grating enable phase control based on path length differences [51]. A more detailed explanation of this procedure is given in Chapter 2. DMDs provide some inherent advantages over SLMs: their refresh rates reach >9 kHz which far surpasses the 60 Hz rates of SLMs [52, 53], they are polarization insensitive allowing them to modulate and combine orthogonal components directly (this concept is explored throughout Chapters 3 to 5), they operate calibration-free over a broad wavelength range (400 nm to 900 nm by design, however some work has displayed operation in the telecomunications regime >1 μm [54]). Perhaps most notably DMDs are low cost with evaluation models available for 3000 USD in stark contrast to SLMs which start around 15000 USD (these are approximate average prices at the time of writing this thesis). Consequently the majority of tools developed in the work contained in this thesis utilized DMDs to facilitate versatile, high-speed, broadband and low cost vectorial light control.

We have considered a few of the most commonly employed light shaping techniques. There are however other schemes such as inter-cavity generation [55] and nanostructured silica based modal-plates [56]. Interested readers are directed to a good review for more information about the aforementioned and additional light shaping techniques [57].

Chapter 2

Preliminary Theory

Parts of this chapter are based on the paper:

Singh, K., Tabebordbar, N., Forbes, A., & Dudley, A. Digital Stokes polarimetry and its application to structured light: tutorial. JOSA A, 37(11), C33-C44. (2020).

This chapter will cover the preliminary theory relating to scalar and vector spatial modes, the Stokes-Mueller and Jones polarization formalisms as well as complex amplitude modulation using both SLMs and DMDs. Any additional theory requisite for the following chapters will be introduced as it becomes relevant.

2.1 The paraxial Helmholtz equation

To begin, let us consider Maxwell's equations [58]:

$$\vec{\nabla} \cdot \vec{D} = \rho \,, \tag{2.1}$$

$$\vec{\nabla} \cdot \vec{B} = 0 \,, \tag{2.2}$$

$$\vec{\nabla} \times \vec{E} = -\frac{\partial \vec{B}}{\partial t} \,, \tag{2.3}$$

$$\vec{\nabla} \times \vec{H} = \vec{J} + \frac{\partial \vec{D}}{\partial t} \,, \tag{2.4}$$

where $\vec{E}$ and $\vec{B}$ are the electric and magnetic fields respectively, ρ is the charge density distribution, $\vec{J}$ is the current density field. $\vec{D}$ and $\vec{H}$ are the electric and magnetic flux densities determined as

$$\vec{D} = \epsilon_0 \vec{E} + \vec{P} \,, \tag{2.5}$$

$$\vec{H} = \frac{1}{\mu_0} \vec{B} - \vec{M} \,, \tag{2.6}$$

where $\vec{P}$ and $\vec{M}$ are the respective polarization and magnetization fields due to bound charges and currents, ϵ_0 and μ_0 are the vacuum permittivity and permeability respectively. For our purposes we can assume the absence of charge and current

densities (i.e., $\rho = \vec{J} = 0$), additionally for a discussion of propagation through free-space we have no polarization and magnetization (i.e. $\vec{P} = \vec{M} = 0$) resulting in the simplified set of equations

$$\vec{\nabla} \cdot \vec{E} = 0\,, \tag{2.7}$$

$$\vec{\nabla} \cdot \vec{B} = 0\,, \tag{2.8}$$

$$\vec{\nabla} \times \vec{E} = \frac{\partial \vec{B}}{\partial t}\,, \tag{2.9}$$

$$\vec{\nabla} \times \vec{B} = \mu_0 \epsilon_0 \frac{\partial \vec{E}}{\partial t}\,. \tag{2.10}$$

We can now derive a wave equation for the electric field by taking the curl of Eqn. 2.9, exploiting the vector identitiy $\vec{\nabla} \times (\vec{\nabla} \times \vec{A}) = \vec{\nabla}(\vec{\nabla} \cdot \vec{A}) - \vec{\nabla}^2 \vec{A}$ and substituting in Eqns. 2.7 and 2.10

$$\vec{\nabla}^2 \vec{E} - \frac{1}{c^2} \frac{\partial^2 \vec{E}}{\partial t^2} = 0\,, \tag{2.11}$$

where $c = (\epsilon_0 \mu_0)^{-1/2}$ is the vacuum phase velocity of light. It should be noted that an identical equation (and subsequent solutions) can be acquired for $\vec{B}$ using Eqns. 2.10, 2.8 and 2.9. This equation has a solution for light of angular frequency ω of the form

$$\vec{E} = \vec{E_0} e^{i(\vec{k} \cdot \vec{r} \pm \omega t)}\,, \tag{2.12}$$

where $\vec{E_0}$ is the electric field value at $\vec{r} = 0$ with $\vec{r}$ being the three dimensional position vector, $\vec{k}$ is the wavevector indicating the direction of wave propagation with magnitude/wavenumber given by $k = |\vec{k}| = \frac{2\pi}{\lambda}$ which is related to the angular frequency according to $c = \frac{\omega}{k}$. Substituting this solution into Eqns. 2.7 and 2.8 allows us to see that the electric(magnetic) field vectors oscillate normal to the propagation direction since $\vec{k} \cdot \vec{E_0} = 0$. Substituting Eqn. 2.12 into Eqn. 2.11 simplifies into the Helmholtz equation

$$\vec{\nabla}^2 \vec{E} + k^2 \vec{E} = 0\,, \tag{2.13}$$

if we now consider points close to the beam axis with wavevector angles deviating from the propagation axis at small angles we can apply the small angle approximation, which can be expressed by restricting the Cartesian components of the wavevector according to

$$k_z \approx k - \frac{k_x^2 + k_y^2}{2k}\,, \tag{2.14}$$

this allows us to rewrite our solutions as

$$\vec{E}(\vec{r}) = \vec{U}(\vec{r}) e^{ikz}\,, \tag{2.15}$$

where $\vec{U}(\vec{r})$ is the vectorial complex amplitude envelope which describes the shape of the field in any two orthogonal polarizations, under the paraxial approximation the variation of $\vec{U}$ in z is small enough to ignore the $\frac{\partial^2 \vec{U}}{\partial z^2}$ term which appears when substituting the paraxial solutions in Eqn. 2.15 into Eqn. 2.13 which simplifies into the paraxial Helmholtz equation

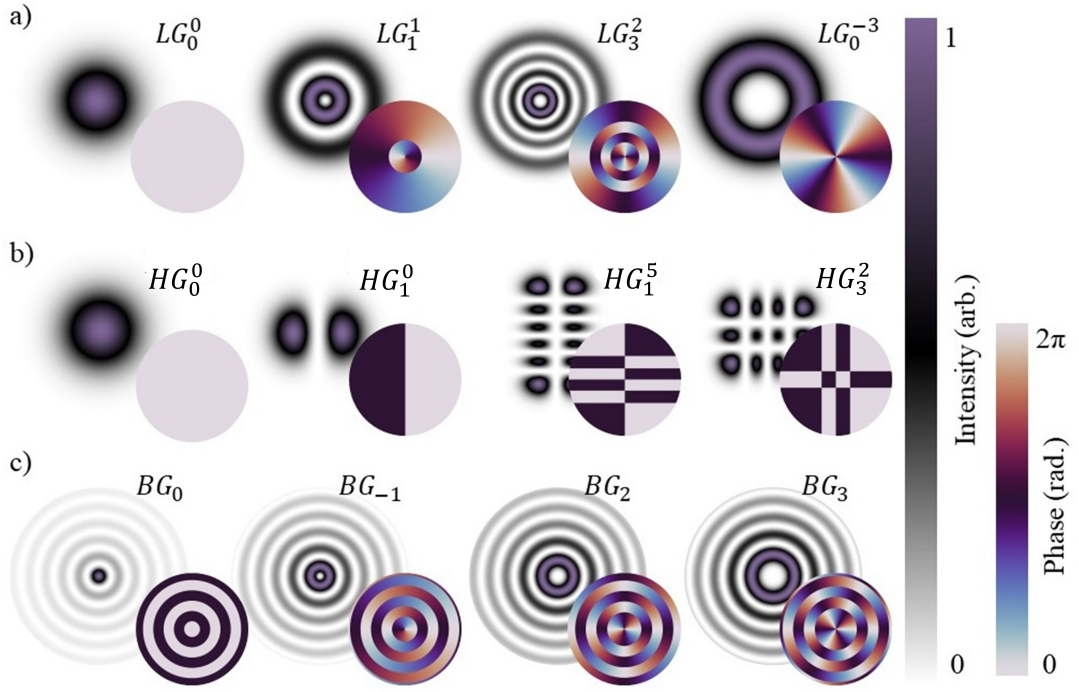


FIGURE 2.1: Plots of the normalized intensity (to the maximum in each mode) and phase of various a) Laguerre-Gaussian, b) Hermite-Gaussian and c) Bessel-Gaussian modes.

$$\vec{\nabla}_T \vec{U} + 2ik\frac{\partial \vec{U}}{\partial z} = 0\,, \tag{2.16}$$

where $\vec{\nabla}_T$ is the Laplacian in the plane transverse to the propagation direction. Solutions to this equation determine the states of light which can propagate through free-space in a paraxial manner. The vectorial nature of $\vec{U}$, which relates to the polarization of the fields, can be greatly simplified by exploiting the linear nature of the equation where solutions to the scalar form of the paraxial Helmholtz equation

$$\vec{\nabla}_T U + 2ik\frac{\partial U}{\partial z} = 0\,, \tag{2.17}$$

can be superimposed in any two orthogonal polaizations to reveal solutions to the vectorial paraxial Helmholtz equation (Eqn. 2.16).

2.2 Scalar spatial modes

2.2.1 Laguerre-Gaussian modes

We can find solutions to the scalar paraxial Helmholtz equation (Eqn. 2.17) in various coordinate systems using the separation of variables. To begin we can consider cylindrical coordinates which gives the following

$$\left(\frac{1}{r}\frac{\partial}{\partial r} + \frac{\partial^2}{\partial r^2} + \frac{1}{r^2}\frac{\partial^2}{\partial \phi^2} + 2ik\frac{\partial}{\partial z}\right) U = 0\,. \tag{2.18}$$

Solutions U to the above equation are referred to as the Laguerre-Gaussian (LG_p^l) modes and are denoted using radial p and azimuthal l indices. These modes have

intensity profiles characterized by cylindrically symmetric ring patterns and are defined by the following expression [59]

$$LG_p^l = \underbrace{\sqrt{\frac{2p!}{w^2(z)\pi(p+|l|)!}}}_{\text{I}} \underbrace{\left(\frac{r\sqrt{2}}{w(z)}\right)^{|l|}}_{\text{II}} \underbrace{L_p^{|l|}\left(\frac{2r^2}{w^2(z)}\right)}_{\text{III}} \underbrace{e^{-\frac{r^2}{w^2(z)}}}_{IV} \underbrace{e^{ik\frac{r^2}{2R(z)}}}_{\text{V}} \underbrace{e^{il\phi}}_{\text{VI}} \underbrace{e^{i(2p+|l|+1)\xi(z)}}_{\text{VII}}, \tag{2.19}$$

where factor I represents the mode normalization. Factor II represents the intensity null at the center of beams with nonzero $|l|$. Factor III contains the Laguerre function ($L_p^{|l|}$) amplitude envelope. Factor IV is the Gaussian amplitude envelope. Factor V describes the wavefront curvature of radius $R(z) = z(1 + \frac{z_R^2}{z^2})$ where the Rayleigh length $z_R = \frac{\pi w^2(0)}{\lambda}$ is the distance over which the beam waist $w(z)$ doubles. Factor VI shows the azimuthally varying phase defined by the integer topological charge l corresponding to $l\hbar$ units of orbital angular momentum (OAM) per photon in the quantum regime [60]. Factor VII defines the Gouy-phase $\xi = \arctan\left(\frac{z}{z_R}\right)$ which is scaled by the mode order $M = (2p + |l| + 1)$. This phase originates from the uncertainty in the wavevector directions for spatially confined modes [61]. Plots of the intensity and phase of a variety of LG_p^l modes are given in Fig. 2.1.a.

2.2.2 Hermite-Gaussian modes

We could also solve Eqn. 2.17 in Cartesian coordinates which takes the form

$$\left(\frac{\partial^2}{\partial x^2} + \frac{\partial^2}{\partial y^2} + 2ik\frac{\partial}{\partial z}\right) U = 0\,, \tag{2.20}$$

solutions U to the above equation are referred to as Hermite-Gaussian (HG_n^m) modes and are denoted using the horizontal n and vertical m indices. These modes have characteristic rectangular grid like intensity patterns and are defined by the following equation [62]

$$HG_n^m = \underbrace{\sqrt{\frac{2^{1-n-m}}{w^2(z)\pi n!m!}}}_{\text{I}} \underbrace{H_n\left(\frac{\sqrt{x}}{w(z)}\right) H_m\left(\frac{\sqrt{y}}{w(z)}\right)}_{\text{II}} \underbrace{e^{-\frac{r^2}{w^2(z)}}}_{\text{III}} \underbrace{e^{ik\frac{r^2}{2R(z)}}}_{\text{IV}} \underbrace{e^{i(m+n+1)\xi(z)}}_{\text{V}}, \tag{2.21}$$

where factor I is the mode normalization. Factor II is the Hermite function ($H_{n(m)}$) dependent amplitude envelope in the x and y directions. Factors III and IV represent the same behaviour as in the LG_p^l modes. Factor IV is still determined by the Gouy phase scaled by the HG_n^m mode order $M = (m + n + 1)$. The intensity and phase distributions of a variety of HG_n^m modes are given in Fig. 2.1.b. One interesting and useful property of both the LG_p^l and HG_n^m modes is that they form complete orthonormal bases of modes. This orthonormality allows all diffracting, monochromatic, paraxial fields which could propagate in free-space to be expressed as a linear superposition of these basis elements.

2.2.3 Bessel-Gaussian modes

Another set of modes which are of relevance to the work presented in this thesis are the Bessel-Gaussian (BG_l) modes denoted by an azimuthal index l similar to that of LG_p^l modes. Bessel-Gaussian modes are a physically realizable form of Bessel modes which are propagation invariant (i.e., non-diffracting) optical fields that satisfy the scalar form of Eqn. 2.13 in cylindrical coordinates. Bessel modes have infinite transverse spatial extent, while the BG_l modes have a Gaussian envelop, and are defined as [63]

$$BG_l = \underbrace{J_{|l|}(k_r r)}_{\text{I}} \underbrace{e^{-\frac{r^2}{w_0^2}}}_{\text{II}} \underbrace{e^{ik_z z}}_{\text{III}}, \tag{2.22}$$

where factor I contains the amplitude envelope dependent on the Bessel function of the first kind (order l) $J_{|l|}$ scaled according to the radial wavevector component k_r. Factor II represents the Gaussian envelope with fixed waist w_0. Factor III represents the Gouy-phase which has a linear dependence on the axial wavevector component $k_z = \sqrt{k^2 - k_r^2}$. These modes are approximately non-diffracting within the range $z_{max} = \frac{kw_0}{k_r}$, meaning their intensity profiles remain almost unchanged over this distance, the intensity and phase profiles of various BG_l beams are shown in Fig. 2.1.c.

2.3 Stokes and Jones polarization formalisms

As previously mentioned, the linear nature of Eqns. 2.16 and 2.13 allow the solutions to their scalar counterparts to be superimposed with orthogonal polarizations in order to express the vector solutions. Before we can discuss these vectorial solutions we need to understand light's polarization. There are two treatments which will be used throughout this thesis: the Stokes-Mueller formalism and the Jones formalism, which become interchangeable under certain conditions (namely where the degree-of-polarization, to be discussed later in this chapter, is equal to unity.) Due to this both formalisms remain valid throughout this thesis.

2.3.1 Stokes vectors, the Poincaré sphere and Mueller matrices

We begin by considering two monochromatic plane waves polarized (i.e., oscillating) in the orthogonal x and y directions [64]

$$E_{x(y)} = E_{0x(y)} \cos\Big(\omega t + \delta_{x(y)}\Big). \tag{2.23}$$

Here $E_{0x(y)}$ are the amplitudes, and $\delta_{x(y)}$ are phases. Using trigonometric identities yields the following ellipse equation

$$\frac{E_x^2}{E_{0x}^2} + \frac{E_y^2}{E_{0y}^2} - \frac{2E_xE_y}{E_{0x}E_{0y}} \cos(\delta) = \sin^2(\delta), \tag{2.24}$$

where $\delta = \delta_y - \delta_x$ is the phase difference between the waves. We can then substitute Eqn. 2.23 into Eqn. 2.24 and exploit the following time averages (since physical observables are generally of time averages of optical wave oscillations)

$$\lim_{T\to\infty}\frac{1}{T}\int_0^T \cos^2(\omega t-\delta_{x(y)})dt=\frac{1}{2}\,, \tag{2.25}$$

$$\lim_{T\to\infty}\frac{1}{T}\int_0^T \cos(\omega t-\delta_x)\cos\big(\omega t-\delta_y\big)dt=\frac{1}{2}\cos(\delta)\,, \tag{2.26}$$

to obtain the following expression

$$\underbrace{(E_{0x}^2+E_{0y}^2)^2}_{S_0^2}-\underbrace{(E_{0x}^2-E_{0y}^2)^2}_{S_1^2}-\underbrace{(2E_{0x}E_{0y}\cos(\delta))^2}_{S_2^2}=\underbrace{(2E_{0x}E_{0y}\sin(\delta))^2}_{S_3^2}\,, \tag{2.27}$$

where, as indicated by the underbraces, each term represents the square of what are referred to as the Stokes parameters S_i which can in general spatially vary in the transverse plane. The parameters (when normalized) can be understood as follows: $S_0 \in [0,1]$ represents the total field intensity, $S_1 \in [-1,1] = I_H - I_V$ represents the difference between the horizontally and vertically polarized components, $S_2 \in [-1,1] = I_D - I_A$ represents the difference between the diagonally and anti-diagonally polarized components and $S_3 \in [-1,1] = I_R - I_L$ represents the difference between the right- and left-circularly polarized components. Here I_i represents the intensity projection of a certain polarization component. The Stokes parameters contain complete information about light's polarization which is conveniently described and visualized using an ellipse with an orientation angle ψ and ellipticity angle χ which can be calculated as

$$\psi=\arctan\left(\frac{S_2}{S_1}\right)\in[-\frac{\pi}{4},\frac{\pi}{4}]\,, \tag{2.28}$$

$$\chi=\arctan\left(\frac{S_3}{S_0}\right)\in[0,\pi]\,. \tag{2.29}$$

The ellipse represents the path traced out by the electric field vector upon propagating one wavelength. An example ellipse is shown on the right of Fig. 2.2. The Stokes parameters are commonly collected into a Stokes vector $\vec{S}=[S_0,S_1,S_2,S_3]^T$. The Stokes vectors for various states of polarization are given in Tab. 2.1

Polarization	Stokes vector
Horizontal	$\begin{pmatrix}1 & 1 & 0 & 0\end{pmatrix}^T$
Vertical	$\begin{pmatrix}1 & -1 & 0 & 0\end{pmatrix}^T$
Diagonal	$\begin{pmatrix}1 & 0 & 1 & 0\end{pmatrix}^T$
Anti-diagonal	$\begin{pmatrix}1 & 0 & -1 & 0\end{pmatrix}^T$
Right-circular	$\begin{pmatrix}1 & 0 & 0 & 1\end{pmatrix}^T$
Left-circular	$\begin{pmatrix}1 & 0 & 0 & -1\end{pmatrix}^T$

TABLE 2.1: Stokes vectors for various sates of polarization

The Stokes parameters are also used to determine the degree-of-polarization (DOP) according to

$$\mathrm{DOP} = \frac{S_1^2 + S_2^2 + S_3^2}{S_0^2} \in [0, 1]\,, \tag{2.30}$$

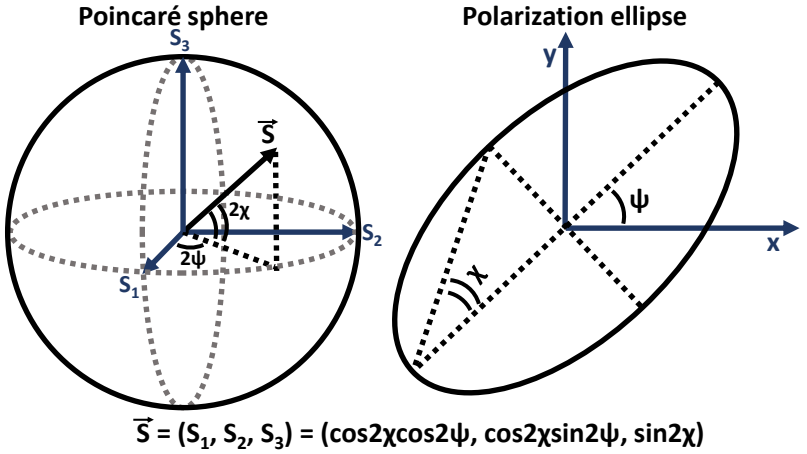


FIGURE 2.2: Diagram showing the relationship between the Cartesian co-ordinates of the Poincaré Sphere and the ellipticity and orientation angles of the polarization ellipse.

where values from 0 to 1 respectively represent unpolarized (i.e randomly oscillating) to completely polarized (i.e., oscillating according to a well defined ellipse orientation) light. In this thesis no consideration of unpolarized or partially polarized light is necessary and all discussions which follow will assume DOP $= 1$. The Stokes parameters also serve as the Cartesian coordinates of a parameter space in which an abstract graphical a tool referred to as the Poincaré sphere is constructed. This unit sphere, illustrated in the left of Fig. 2.2, is constructed with right- and left-circular polarizations on the North and South poles respectively and linearly polarized states spanning the equator. The DOP dictates the magnitude of the reduced Stokes vector $[S_1, S_2, S_3]^T$ and the azimuthal 2ψ and polar 2χ angles of the vector are respectively related to the ellipse orientation and ellipticity angles. Various optical elements can be used to control light's polarization. The effect of these elements can be represented using Mueller matrices $\hat{M}$ which are used to operate on an input Stokes vector $\vec{S}_{in}$ resulting in an output Stokes vector $\vec{S}_{out}$ according to

$$\vec{S}_{out} = \hat{M}\vec{S}_{in}\,, \tag{2.31}$$

the Mueller matrices for certain optical elements are shown in Tab. 2.2.

2.3.2 Jones vectors and Jones matrices

While the Stokes parameters and Mueller matrices allow for a complete description of polarized and partially/unpolarized light, the large matrices are uneccessary when dealing with purely polarized states. A reduced representation in the form of 2×1 Jones vectors $\vec{J}$ and 2×2 Jones matrices $\hat{J}$ which operate on them, offers a convenient alternative. The first(second) row of the Jones vector contains the horizontally(vertically) polarized component of the field. The Jones vectors of example polarization states are given in Tab. 2.3, where we also introduce the quantum mechanics inspired ket notation which is commonly used when discussing vectorial structured light and will be adopted throughout this thesis.

Component	Abbreviation	Mueller matrix
Linear polarizer	LP	$\frac{1}{2}\begin{pmatrix} 1 & \cos(2\theta) & \sin(2\theta) & 0 \\ \cos(2\theta) & \cos^2(2\theta) & \cos(2\theta)\sin(2\theta) & 0 \\ \sin(2\theta) & \cos(2\theta)\sin(2\theta) & \sin^2(2\theta) & 0 \\ 1 & 0 & 0 & 0 \end{pmatrix}$
Half-wave plate	HWP	$\begin{pmatrix} 1 & 0 & 0 & 0 \\ 0 & \cos(4\theta) & \sin(4\theta) & 0 \\ 0 & \sin(4\theta) & -\cos(2\theta) & 0 \\ 0 & 0 & 0 & -1 \end{pmatrix}$
Quater-wave plate	QWP	$\begin{pmatrix} 1 & 0 & 0 & 0 \\ 0 & \cos^2(2\theta) & \sin(2\theta)\cos(2\theta) & -\sin(2\theta) \\ 0 & \sin^2(2\theta) & -\sin(2\theta)\cos(2\theta) & \cos(2\theta) \\ 0 & \sin(2\theta) & -\cos(2\theta) & 0 \end{pmatrix}$

TABLE 2.2: Mueller matrices for various optical elements (θ is the angle of the transmission/fast axis from the $x-$axis).

Polarization	Ket notation	Jones vector
Horizontal	$\lvert H\rangle$	$\begin{pmatrix} 1 \\ 0 \end{pmatrix}$
Vertical	$\lvert V\rangle$	$\begin{pmatrix} 0 \\ 1 \end{pmatrix}$
Diagonal	$\lvert D\rangle$	$\frac{1}{\sqrt{2}}\begin{pmatrix} 1 \\ 1 \end{pmatrix}$
Anti-diagonal	$\lvert A\rangle$	$\frac{1}{\sqrt{2}}\begin{pmatrix} 1 \\ -1 \end{pmatrix}$
Right-circular	$\lvert R\rangle$	$\frac{1}{\sqrt{2}}\begin{pmatrix} 1 \\ -i \end{pmatrix}$
Left-circular	$\lvert L\rangle$	$\frac{1}{\sqrt{2}}\begin{pmatrix} 1 \\ i \end{pmatrix}$

TABLE 2.3: Jones vectors for various sates of polarization. Note the chosen the phase convention expressing right-circular polarization with a $-\pi/2$ phase delay between the vertical and horizontal components.

Jones vectors can be converted into the latter three Stokes parameters according to a Hopf map where

$$S_1 = |J_1|^2 - |J_2|^2\,, \tag{2.32}$$
$$S_2 = 2\,\mathrm{Re}\{J_1 J_2^*\}\,, \tag{2.33}$$
$$S_3 = 2\,\mathrm{Im}\{J_1 J_2^*\}\,. \tag{2.34}$$

The Hopf map defines a many-to-one relationship between a 4-dimensional hypersphere to a 3-dimensional sphere, in the above case the real and imaginary parts of the two Jones vector components lie on the hypersphere and are mapped to the three real Stokes vector components which lie on the Poincaré sphere [65]. The Jones matrices for various optical elements are given in Tab. 2.4, these can be converted into Mueller matrices according to

$$\hat{M} = \hat{A}(\hat{J} \otimes \hat{J}^*)\hat{A}^{-1}\,, \tag{2.35}$$

$$\hat{A} = \begin{pmatrix} 1 & 0 & 0 & 1 \\ 1 & 0 & 0 & -1 \\ 0 & 1 & 1 & 0 \\ 0 & i & -i & 0 \end{pmatrix}\,, \tag{2.36}$$

where $\otimes$ represents the Kronecker product (i.e., element-wise multiplication).

Component	Jones matrix
LP	$\begin{pmatrix} \cos^2(\theta) & \sin(\theta)\cos(\theta) \\ \sin(\theta)\cos(\theta) & \sin^2(\theta) \end{pmatrix}$
HWP	$\begin{pmatrix} \cos(2\theta) & \sin(2\theta) \\ \sin(2\theta) & -\cos(2\theta) \end{pmatrix}$
QWP	$\frac{1}{\sqrt{2}}\begin{pmatrix} 1+i\cos(2\theta) & i\sin(2\theta) \\ i\sin(2\theta) & 1-i\cos(2\theta) \end{pmatrix}$

TABLE 2.4: Jones matrices of various optical elements (θ is the angle of the transmission/fast axis from the $x-$axis).

2.4 Vector spatial modes, vectorness and the higher-order Poincaré sphere

2.4.1 Vector modes

Now that we have established the necessary polarization formalism we can express solutions to Eqn. 2.16 as a superposition of scalar spatial modes with orthogonal polarizations

$$|\Psi\rangle = |U_1\rangle|P_+\rangle + |U_2\rangle|P_-\rangle\,, \tag{2.37}$$

where we have adopted ket notation with $|U_{1(2)}\rangle$ representing the spatial DoF, when we project into the position basis these are revealed to be spatial modes such as the LG_p^l, HG_n^m or BG_l modes as well as their superpositions (i.e., $\langle\vec{r}|U_{1(2)}\rangle = U_{1(2)}(\vec{r})$). $|P_\pm\rangle$ are orthonormal Jones vectors representing the polarization DoF (i.e., $\langle P_+|P_-\rangle = \delta_{ij}$ where δ_{ij} is the Kronecker-delta). The result of this superposition is an optical field which can have spatially varying polarizations. Figure 2.3 shows examples of the intensity and polarization distributions of some example vector spatial modes.

2.4.2 Vectorness

The example vector modes shown in Fig. 2.3 contain orthonormal spatial components (i.e., $\langle U_1|U_2\rangle = \delta_{12}$). In general the spatial modes are not orthonormal, for instance if $|U_1\rangle = |U_2\rangle$ the mode is simply a scalar mode solution. The impact of the orthonormality of the constituent spatial modes is the degree of inhomogeneity of the polarization distribution which is commonly referred to as the vectorness [66]. The vectorness can be quantified as followed: first we can form an orthonormal pair of spatial modes ,$|U_\pm\rangle$, using our arbitrary modes by applying the the Gram-Schmidt orthonormalization procedure [67]

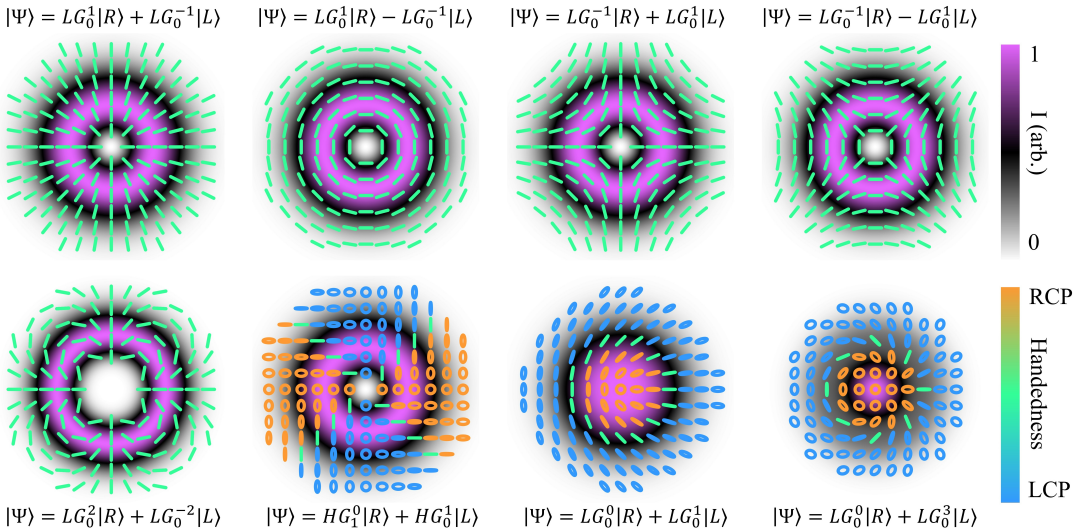


FIGURE 2.3: Intensity and polarization distributions of some vector spatial modes.

$$|U_\pm\rangle = (2(1 \pm \langle\tilde{U}_1|\tilde{U}_2\rangle))^{\frac{1}{2}}(|\tilde{U}_1\rangle \pm |\tilde{U}_2)\,, \tag{2.38}$$

$$|\tilde{U}_{1(2)}\rangle = \frac{U_{1(2)}}{\langle U_{1(2)}|U_{1(2)}\rangle}\,. \tag{2.39}$$

We can then express our vector mode in this orthonormal spatial and polarization basis as

$$|\Psi\rangle = a|U_+\rangle|P_+\rangle + b|U_+\rangle|P_-\rangle + c|U_-\rangle|P_+\rangle + d|U_-\rangle|P_-\rangle\,. \tag{2.40}$$

Inspecting Eqn. 2.40 reveals how our vector mode takes the exact form of qubit state where instead of two particles being entangled we have two DoFs being non-separable, this is one of the motivations behind adopting the ket notation. The following convenient expression exists for the entanglement entropy of a 2-dimensional qubit state referred to as the concurrence [68]

$$C = 2|ad - bc|\,, \tag{2.41}$$

$$C = \sqrt{\langle U_1|U_1\rangle\langle U_2|U_2\rangle - |\langle U_1|U_2\rangle|^2}\,, \tag{2.42}$$

where Eqn. 2.42 follows from substituting Eqns. 2.38, 2.39 and 2.40 into 2.41. The same way $C \in [0, 1]$ provides a measure of the degree of entanglement in qubit systems it provides a measure of non-separability between the spatial and polarization DoFs (i.e., vectorness) of our vector beams, where $C = 0$ corresponds to a homogeneously polarized scalar mode and $C = 1$ indicates an inhomogeneously polarized vectorial field.

2.4.3 Higher/Hybrid-order Poincaré spheres

The same way the Poincaré sphere provides a useful graphical aid to understand light's polarization, we can construct an analogue to visualize how the vectorness changes for a specific vector field of the form

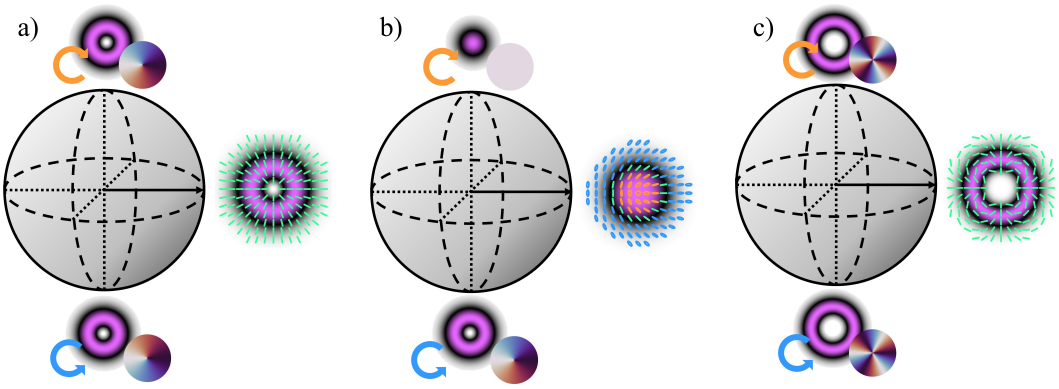


FIGURE 2.4: HOPSs for a variety of vectorial superpositions.

$$|\Psi\rangle = \sqrt{\alpha}|U_+\rangle|R\rangle + e^{i\beta}\sqrt{1-\alpha}|U_-\rangle|L\rangle\,, \tag{2.43}$$

where we have considered orthonormal spatial and right-/left-circular polarization bases, where $\alpha \in [0,1]$ and $\beta \in [0,2\pi]$ describe the respective relative amplitudes and phases. A higher order Poincaré sphere (HOPS) can be constructed, which contains all possible vector modes (for a fixed pair $|U_\pm\rangle$) with the constituent orthogonally polarized scalar modes on the poles and purely vector modes on the equator, where $\alpha(\beta)$ dictates the polar(azimuthal) angle. It is notable that sometimes a distinction is made between spheres constructed with modes having similar(different) order M as higher-(hybrid-)order [69], for simplicity we will adopt the same acronym for both. An example of some HOPSs are given in Fig. 2.4.

2.5 Complex amplitude modulation schemes

Now that we have an understanding of scalar and vector spatial modes, it is clear that the manipulation of both light's amplitude and phase is essential in their creation and analysis. This combined control is often referred to as complex amplitude modulation (CAM), since the absolute value and argument of a complex number relate to the amplitude and phase respectively. We will now cover some widely employed schemes for CAM using two digital devices.

2.5.1 Liquid crystal spatial light modulators (SLMs)

As mentioned in Chapter 1, SLMs function by applying controllable voltages across individual liquid crystal filled pixels. This causes rotation of the crystals changing the path length of light through the cells allowing for the birefringence of the crystals to impart a desired phase on the interval $[0,2\pi]$. We want to impart a complex modulation $U(x,y)$ described by

$$U(x,y) = A(x,y)e^{i\varphi(x,y)} \tag{2.44}$$

where (x,y) are the 2-dimensional pixel coordinates, $A(x,y)$ is the desired amplitude and $\varphi(x,y)$ the desired phase at each pixel. We need to do this by employing a phase transmission function $T(x,y)$ dependent on A and φ, i.e.,

$$T(x,y) = e^{i\Phi(A,\varphi)}\,, \tag{2.45}$$

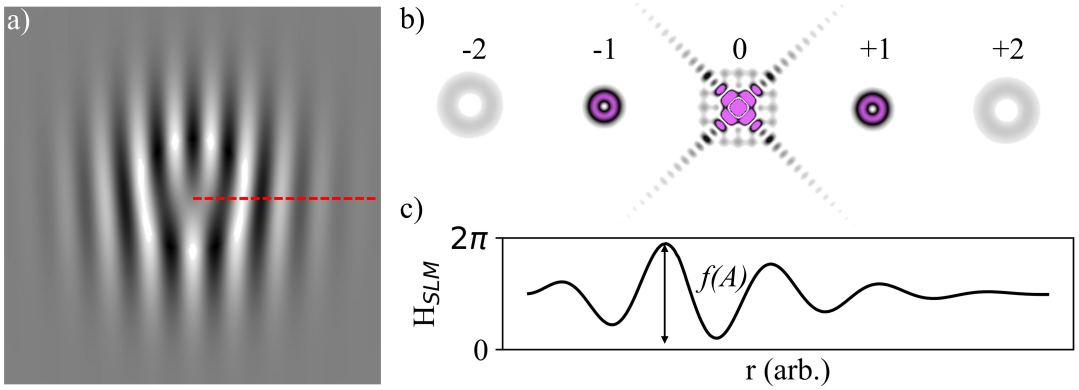


FIGURE 2.5: a) Grayscale image of an SLM hologram used to produce an LG_0^1 mode. b) Diffraction orders produced by the SLM hologram (the desired information is contained in the +1 diffraction order). c) Cross section (taken from the dashed red line in (a) of the phase modulation produced by the SLM hologram). It is worth noting the function $f(A)$ which modulates the depth of the phase grating.

to this end let us consider a Fourier series expansion of $T(x,y)$ in the φ domain [49]

$$T(x,y) = \sum_{q=-\infty}^{\infty} \underbrace{(2\pi)^{-1} \int_{-\pi}^{\pi} e^{i\Phi(A,\varphi)} e^{-iq\varphi} d\varphi}_{c_q^A} e^{iq\varphi} \tag{2.46}$$

where c_q^A are the expansion coefficients of order q dependent on the amplitude $A(x,y)$. We can ensure that the desired field $U(x,y)$ is captured in the $q = 1$ order by requiring $c_1^A = \alpha A$ where α is a positive constant. This enforces the following conditions

$$\int_{-\pi}^{\pi} \sin(\Phi(A,\varphi) - \varphi) d\varphi = 0\,, \tag{2.47}$$

$$\int_{-\pi}^{\pi} \cos(\Phi(A,\varphi) - \varphi) d\varphi = 2\pi\alpha A\,. \tag{2.48}$$

While various functions $\Phi(A,\varphi)$ satisfy the above conditions we will restrict our discussion to the following

$$\Phi(A,\varphi) = f(A)\sin(\varphi)\,, \tag{2.49}$$

where for now $f(A)$ is an unknown function. Substituting this into Eqn. 2.45 allows us to apply the Jacobi-Anger expansion giving

$$T(x,y) = e^{if(A)\sin(\varphi)} = \sum_{q=-\infty}^{\infty} J_q(f(A)) e^{iq\varphi}\,, \tag{2.50}$$

comparing this to Eqn. 2.46 reveals that $c_q^A = J_q(f(A))$. Considering the previous condition for $q = 1$ results in the following form of $f(A)$ which can be evaluated

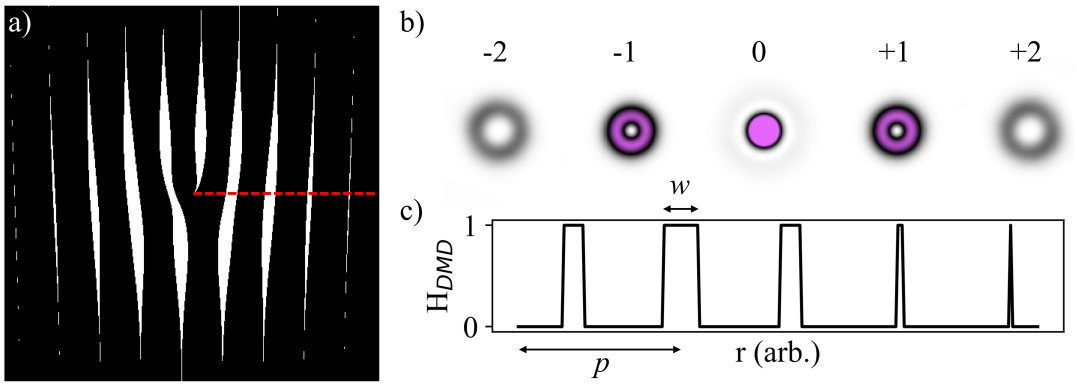


FIGURE 2.6: a) Binary image of a DMD hologram used to produce an LG_0^1 mode. b) Diffraction orders produced by the DMD hologram (the desired information is contained in the +1 diffraction order). c) Cross section (taken from the dashed red line in (a) of the amplitude modulation produced by the DMD hologram.

numerically

$$f(A) = J_1^{-1}(\alpha A) \tag{2.51}$$

where $J_1^{-1}()$ indicates an inverted first order Bessel function of the first kind. This gives us the result for the pure phase hologram $H_{SLM}(x,y)$ to be displayed on an SLM which will result in the encoding of the desired complex field $U(x,y)$ in the first diffraction order which can be isolated by introducing a phase grating with spatial carrier frequencies $g_{x,y}$

$$H_{SLM}(x,y) = J_1^{-1}(\alpha A(x,y)) \sin\big(2\pi(g_x x + g_y y)\big)\,, \tag{2.52}$$

where α is chosen based on the desired grating depth. An intuitive understanding of the resulting pure phase hologram is as a grating designed to maximize diffraction of power into the first diffraction order where reducing the grating depth in a spatially varying manner (according to $J_1^{-1}()$) allows for amplitude control (i.e., a depth of 0 will result in no diffraction into the first order). Figure 2.5 contains a schematic of SLM holograms displaying how they facilitate complex amplitude control. As mentioned, to operate at a given wavelength the SLM will need to be calibrated in order to facilitate the correct phase modulation described in Eqn. 2.52.

2.5.2 Digital micro-mirror devices (DMDs)

As discussed in Chapter 1 DMDs function by tilting mirrors by $\pm 12^\circ$ angles in order to act as binary amplitude gratings. We, again, want to modulate the complex amplitude $U(x,y)$ given by

$$U(x,y) = A(x,y)e^{i\varphi(x,y)}\,. \tag{2.53}$$

We can define a 1-dimensional binary amplitude grating produced by the DMD as

$$T(x) = \sum_{m=-\infty}^{\infty} \text{rect}\left(\frac{x-(m+p)x_0}{wx_0}\right)\,, \tag{2.54}$$

where m represents each *opening* in the grating at the position p of width w, forming series of spatial 'pulses'. We can expand $T(x)$ into a Fourier series according to [70]

$$T(x) = \sum_{m=-\infty}^{\infty} \underbrace{\frac{\sin(\pi m w)}{\pi m} e^{i2\pi m p}}_{c_m} e^{i2\pi m \frac{x}{x_0}}, \tag{2.55}$$

we can see that the coefficients c_m dictate the amplitude and phase diffracted into the m^{th} order. In order to control amplitude and phase into a given order we can make the pulse width $w(x,y)$ and position $p(x,y)$ spatially varying respectively according to

$$w(x,y) = \frac{1}{\pi} \arcsin(A(x,y)), \tag{2.56}$$

$$p(x,y) = \frac{1}{2\pi} \varphi(x,y), \tag{2.57}$$

where we are now treating a 2-dimensional pulse train to shape the 2-dimensional complex amplitude $U(x,y)$. To produce the desired amplitude hologram H_{DMD} these can be substituted into the following expression

$$H_{DMD}(x,y) = \frac{1}{2} + \frac{1}{2}\text{sign}[\cos\big(2\pi(g_x x + g_y y) + 2\pi p(x,y)\big) - \cos(\pi w(x,y))], \tag{2.58}$$

where $g_x(y)$ are spatial carrier frequencies used to separate the first diffraction order into which the desired field is encoded. The encoding can be understood as larger pulse widths in the grating leading to larger amplitudes being diffracted into the first order while local shifts in the pulse position allow for propagation phase control through small path length differences. Figure 2.6 show examples of DMD holograms and how they function.

Chapter 3

A versatile vectorial light generator

This chapter is based on the papers:

Singh, K., Buono, W. T., Forbes, A., & Dudley, A. Accelerating polarization structures in vectorial fields. Optics Express, 29(2), 2727-2737. (2021).

Singh, K., Buono, W. T., Chavez-Cerda, S., & Forbes, A. Demonstrating Arago–Fresnel laws with Bessel beams from vectorial axicons. JOSA A, 38(9), 1248-1254. (2021).

Singh, K., Buono, W. T., Fernandes, M. A., Dudley, A., & Forbes, A. Spatially resolved birefringence measurements with a digital micro-mirror device. Optics Express, 29(21), 34616-34628. (2021).

Singh, K., Ornelas, P., Dudley, A., & Forbes, A. Synthetic spin dynamics with Bessel-Gaussian optical skyrmions. Optics Express, 31(10), 15289-15300. (2023).

We will now discuss the development of a tool capable of generating arbitrary vectorial fields. We will explore the development in the context of demonstrations of the various approaches using both SLMs and DMDs which lead to novel observations and applications. Firstly, we will explore the use of an SLM and Mach-Zehnder interferometer to generate vectorial Bessel mode superpositions which exhibit accelerating and decelerating propagation dynamics. Secondly, we investigate how a DMD can be simultaneously used as a complex amplitude modulating device and interferometer drastically reducing the number of elements needed to generate vectorial fields, the first demonstration of this approach is for the emulation of an axicon lens with vectorial spatial dependence and the second demonstration is using the DMD to generate a series of probes used to digitally measure spatially resolved birefringence. Finally, we consider an alternative DMD arrangement which further reduced the size of the setup required and demonstrate its effectiveness in generating vector beams which can be made to emulate magnetic spin dynamics. The chapter will conclude with key observations and comparisons observed through the testing of the various iterations.

3.1 SLM based generator used to produce accelerating polarization structures

3.1.1 Introduction

Light travels on a straight line at a constant velocity regardless of the speed of the observer. Despite this universal law, light can be tailored to produce exotic effects by interference, for example, transversely accelerating [71], radially accelerating [72] and angularly accelerating [73, 74] forms of structured light have been demonstrated, and even examples in curved space [75]. These effects have been extended to other waves too, including matter [76, 77]. Such accelerating waves have found a myriad of applications, including optical sorting, plasma control, particle acceleration and many others (see Refs. [78, 79] for good reviews).

The aforementioned work considered the intensity structure of the light (or its equivalent in other waves), whereas it is now topical to control other DoFs including polarization [39, 80, 81]. There have been significant advances in the latter, tailoring polarization not only in the transverse plane (2D) but also along the propagation direction for 3D polarization structures [82]. These include singularity lines [83], polarization knots [84, 85], high-order Poincaré structures [86, 87], longitudinally varying polarization structures [88–90] and rotating polarization structures in free-space [91–93]. Of particular relevance to our work is the advances in producing accelerating polarization states, thus so far achieved in free-space by varying the Gouy phase of scalar beams [90] and in non-linear media [94–96]. The interest in such beams is diverse, including selection rules in parametric processes [97, 98], eletromagnetic induced transparency [99], and the chiral interactions of light with matter [100, 101].

In this work, we demonstrate the first accelerating state-of-polarization (SOP) with vectorial light propagating in free-space, where a non-homogeneous polarization structure can be made to periodically accelerate and decelerate, independently from the spatial profile. We derive the analytical expressions for the acceleration of the Stokes vector and intensity patterns for each polarization basis, which we interpret as a simulation of accelerated Optical Activity (OA) during free-space propagation. In addition to achieving accelerated OA, we demonstrate how the accelerated intensity transport associated with each polarization component, results in an accelerated trajectory in the Poincaré sphere, as well as the transfer of optical current between various local positions within the optical field.

3.1.2 Concept and Theory

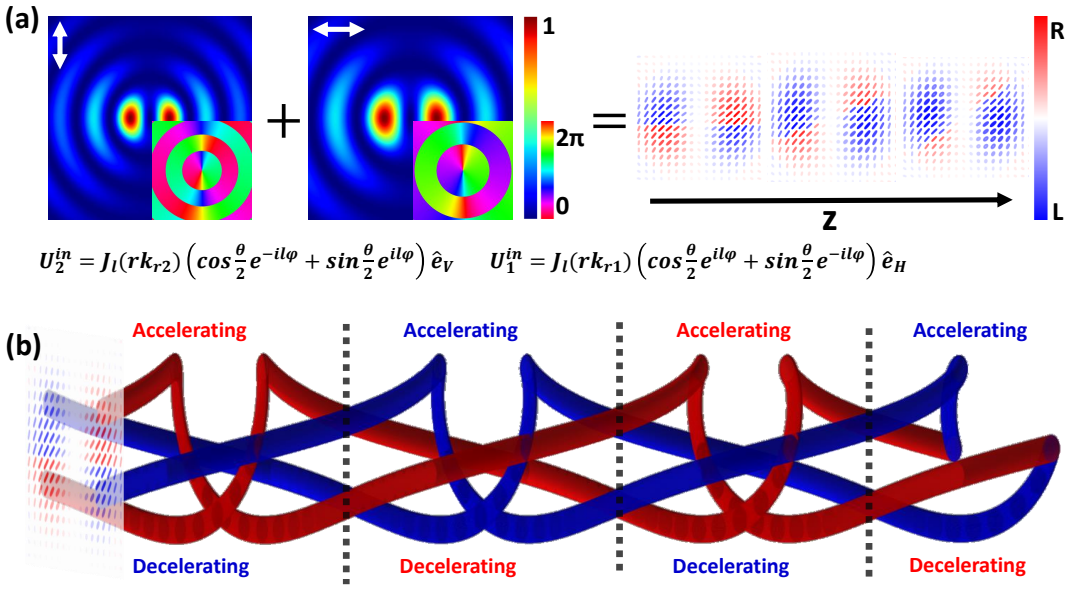


FIGURE 3.1: Diagrams illustrating: (a) the intensity of scalar components used to generate an angularly accelerating/decelerating polarization structure (phases included as insets) and (b) the angularly accelerating/decelerating trajectory with propagation of the right (red) and left (blue) circularly polarized components of the resulting vector mode. The values used in these simulations are $l = 1$ and $\theta = \frac{\pi}{3}$.

Consider the following two scalar fields, which represent weighted superpositions of oppositely charged Bessel beams (i.e., weighted petal beams)

$$U_1 = J_l(rk_{r1})\left[\cos\left(\frac{\theta}{2}\right)e^{il\varphi} + \sin\left(\frac{\theta}{2}\right)e^{-il\varphi}\right]e^{ik_{z1}z}, \tag{3.1}$$

$$U_2 = J_l(rk_{r2})\left[\cos\left(\frac{\theta}{2}\right)e^{-il\varphi} + \sin\left(\frac{\theta}{2}\right)e^{il\varphi}\right]e^{ik_{z2}z}, \tag{3.2}$$

where r and φ are the radial and azimuthal cylindrical coordinates, $J_l()$ are the Bessel polynomials of order l, while θ is a morphology (weighting) parameter and z is the propagation distance. The differences between the two fields are the topological charges $\pm l$ and the transverse and axial wavevector components k_r, k_z. It should be noted that these beams are naturally attenuated by a Gaussian envelope $e^{-(r^2/w_0^2)}$ (i.e., they are superpositions of BG_l beams where w_0 is the Gaussian beam waist), this factor is omitted for brevity as it does not significantly impact subsequent arguments. The intensity and phase of the respective scalar components are shown in Fig. 3.1.a. These fields can be path interfered through a Beam Splitter (BS) according to the Jones matrix operation (where $U_{1/2}^{in} = U_{1/2}$)

$$\begin{pmatrix} U_1^{out} \\ U_2^{out} \end{pmatrix} = \frac{1}{2}\begin{pmatrix} 1 & 1 \\ 1 & -1 \end{pmatrix}\begin{pmatrix} U_1^{in} \\ U_2^{in} \end{pmatrix} = \frac{1}{2}\begin{pmatrix} U_1^{in} + U_2^{in} \\ U_1^{in} - U_2^{in} \end{pmatrix}. \tag{3.3}$$

If these fields are in orthogonal polarization basis states, there are two other bases which will satisfy the following relationships, post path interference, $U_{3/4} \propto U_1 \pm U_2$ and $U_{5/6} \propto U_1 \pm iU_2$ (e.g. $1,2,3,4,5,6 = H,V,D,A,R,L = D,A,H,V,L,R = R,L,H,V,A,D$ - for purely linear and circular basis states). Therefore the Stokes

intensity distributions, which can be used to fully describe the polarization structure of the resulting vector beam, can be determined by taking each field and multiplying by its complex conjugate (i.e., $I_i = U_i^* U_i$). These intensity distributions are given by

$$I_1 = J_l^2(rk_{r1})(1 + \sin\theta\cos 2l\varphi)\,, \tag{3.4a}$$
$$I_2 = J_l^2(rk_{r2})(1 + \sin\theta\cos 2l\varphi)\,, \tag{3.4b}$$
$$I_3 = \frac{1}{2}\left(R_{petal}^2\Phi_+^\alpha + R_{ring}^2\Phi_-^\alpha\right)\,, \tag{3.4c}$$
$$I_4 = \frac{1}{2}\left(R_{petal}^2\Phi_-^\alpha + R_{ring}^2\Phi_+^\alpha\right)\,, \tag{3.4d}$$
$$I_5 = \frac{1}{2}\left(R_{petal}^2\Phi_+^\beta + R_{ring}^2\Phi_-^\beta\right)\,, \tag{3.4e}$$
$$I_6 = \frac{1}{2}\left(R_{petal}^2\Phi_-^\beta + R_{ring}^2\Phi_+^\beta\right)\,, \tag{3.4f}$$

where:

$$R_{petal}(r, k_{r1}, k_{r2}, l) = J_l(rk_{r1}) + J_l(rk_{r2})\,, \tag{3.5a}$$
$$R_{ring}(r, k_{r1}, k_{r2}, l) = J_l(rk_{r1}) - J_l(rk_{r2})\,; \tag{3.5b}$$

and

$$\Phi_\pm^\alpha(\varphi, \theta, \Delta, z, l) = (1 \pm \sin\theta\cos\Delta z)\left(1 + \cos\left(2l\varphi \mp \arctan\left[\frac{\sin\theta\cos\Delta z}{\sin\theta \pm \cos\Delta z}\right]\right)\right)\,, \tag{3.6a}$$
$$\Phi_\pm^\beta(\varphi, \theta, \Delta, z, l) = (1 \pm \sin\theta\sin\Delta z)\left(1 + \cos\left(2l\varphi \pm \arctan\left[\frac{\cos\theta\cos\Delta z}{\sin\theta \pm \sin\Delta z}\right]\right)\right)\,; \tag{3.6b}$$
$$\Delta = k_{z2} - k_{z1}\,. \tag{3.6c}$$

Here the 'petal' and 'ring' factors, which contain the radial dependence, define central and outer regions of the transverse intensity profiles - while the $\Phi_\pm^{\alpha/\beta}$ factors which contain the azimuthal and propagation dependence describe the angular rotation and intensity transport behaviour. It is clear from these expressions that the input component intensities $I_{1/2}$ are propagation invariant and, consequently, the total intensity profile. Other orthogonally polarized pairs of components exhibit a π phase difference in their behavior during propagation, while these pairs exhibit a $\pi/2$ phase difference between each other. The propagation dependent behaviour of the polarization structure of the resulting vector mode is shown in Fig. 3.1.a.

The behavior of the spatial structure in the polarization indicates that upon propagation there is an angularly accelerating trajectory of Stokes vectors (for both the central and outer regions) on the surface of the Poincaré sphere. This is clear when one considers the Stokes parameters (where generation in the H-V basis will be used throughout the rest of our discussion, i.e., $U_{1/2} = U_{H/V}$)

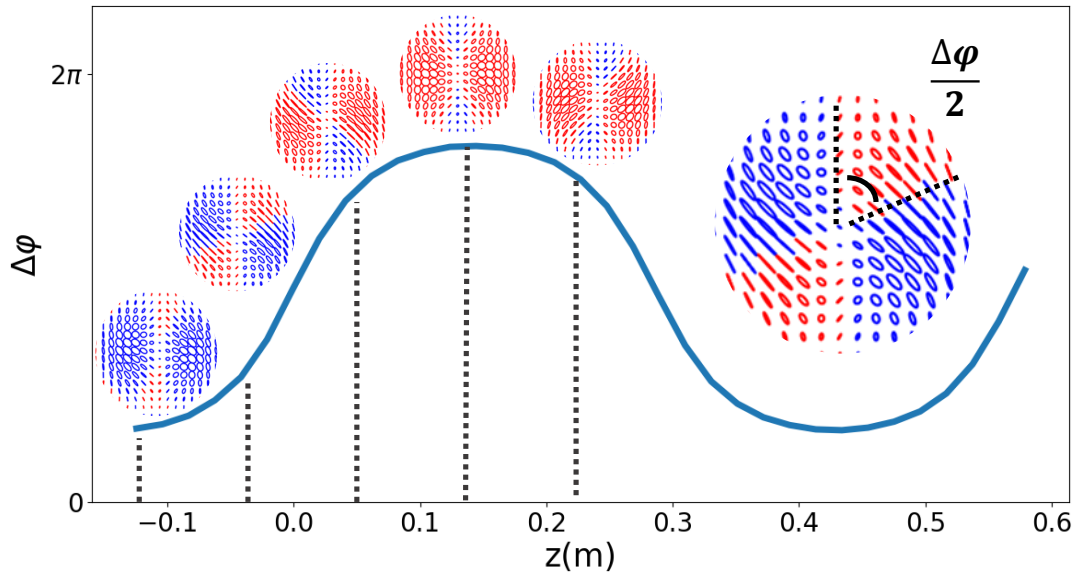


FIGURE 3.2: Diagram showing the change in total azimuthal angle of the beam profile with right-circular polarization ($S_3 > 0$) changing with propagation.

$$\partial_z^2 S_0 = \partial_z^2 S_1 = 0\,, \tag{3.7}$$

$$\partial_z^2 S_2 = 2\Delta^2(R_{petal}^2 - R_{ring}^2)(-\sin\Delta z \sin 2l\varphi - \cos\Delta z(\cos 2l\varphi + \sin\theta))\,, \tag{3.8}$$

$$\partial_z^2 S_3 = 2\Delta^2(R_{petal}^2 - R_{ring}^2)(\cos\Delta z \sin 2l\varphi - \sin\Delta z(\cos 2l\varphi + \sin\theta))\,. \tag{3.9}$$

According to these expressions it is clear that beams generated as orthogonally polarized superpositions of weighted petal beams will experience accelerated OA about the generation axis. The negative sign between the central and outer components indicate that this accelerated rotation will occur with a phase difference of π between the two regions (i.e., an angle of π between the ring and petal Stokes vectors at any given propagation distance). During propagation, the trajectory taken by the positive (red) and negative (blue) S_3 components (i.e., the right and left circularly polarized components respectively) in the central region can be seen in Fig. 3.1.b. An interesting observation of the resulting polarization structure is that the total angle $\Delta\varphi$ (in the transverse plane) covered by $\pm S_{2/3}$ changes in a non-linear manner with z, this behaviour is highlighted for S_3 in Fig. 3.2. We can note that it would be difficult to observe this experimentally since the regions around $\varphi = -\pi, \pi$ are low intensity regions for $\theta \neq 0$. Thus, for the remainder of this article the value $\theta = \frac{\pi}{3}$ will be used as this corresponds to the most prominent accelerating/decelerating behaviour [73]. An important observation is that, as seen in Figs. 3.1.a and 3.2, the polarization structure is not uniform, but Eqns. 3.7, 3.8 and 3.9 show that every point in the spatial distribution of the polarization follows a path on the Poincaré sphere during propagation that is identical, except for the starting point. We can note that $\Delta\varphi$ would remain constant for a case of constant rotation (i.e. when $\theta = 0$).

The intensity transport, for the case of a coherent vector beam is best described by the Poynting vector. This vector current contains both a term associated with the phase structure (orbital component) as well as a term associated with the polarization structure (spin component) according to [102–105]

$$\vec{P} = \frac{c^2}{2\omega}\epsilon_0[\underbrace{Im\{\vec{E}^* \cdot \vec{\nabla}\vec{E}\}}_{\text{Orbital component}} + \frac{1}{2}\underbrace{\vec{\nabla} \times Im\{\vec{E}^* \times \vec{E}\}}_{\text{Spin component}}], \tag{3.10}$$

where c is the phase velocity of light, ω is the frequency, ϵ_0 is electric permittivity of free-space, $\vec{\nabla} = (\partial_x, \partial_y, \partial_z)$ and $\vec{E} = (E_x, E_y, E_z)$. For our case we can assume $E_z = 0$, therefore

$$\vec{P} = \frac{c^2}{2\omega}\epsilon_0[(E_i^*\partial_i + E_j^*\partial_j)E_i + \frac{1}{2}\partial_j Im\{E_i^* E_j - E_j^* E_i\}]\hat{e}_i\,, \tag{3.11}$$

where $i, j = x, y$. The x and y electric field components are the respective horizontal and vertical polarization components $E_x, E_y = U_H, U_V$. Simulations of the Poynting current (see Fig. 3.3) reveals no net intensity transport into and out of the central region (i.e., $\int \vec{P} d\vec{r} = 0$, in the bounds indicated by the dashed line in Fig. 3.3), which corresponds to the intensity profile of the vector mode remaining the same throughout propagation. This observation was validated through experimental observations, as well as the theoretical expressions Eqns. 3.4a - 3.4f.

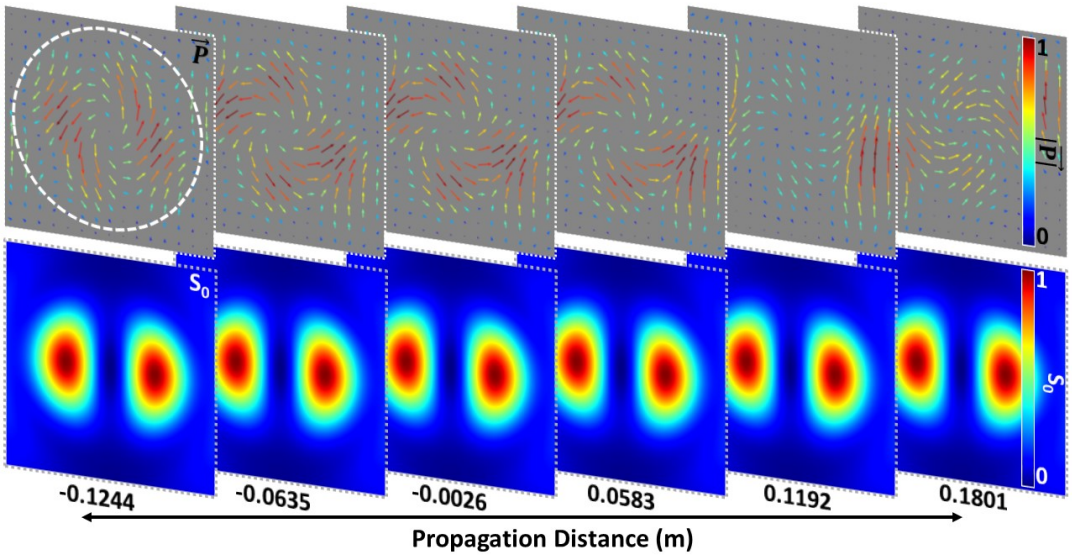


FIGURE 3.3: Simulations of the Poynting vector (top) and total intensity (bottom) of a H-V superposition of weighted petal beams, the total intensity S_0 remains invariant with propagation.

3.1.3 Experiment

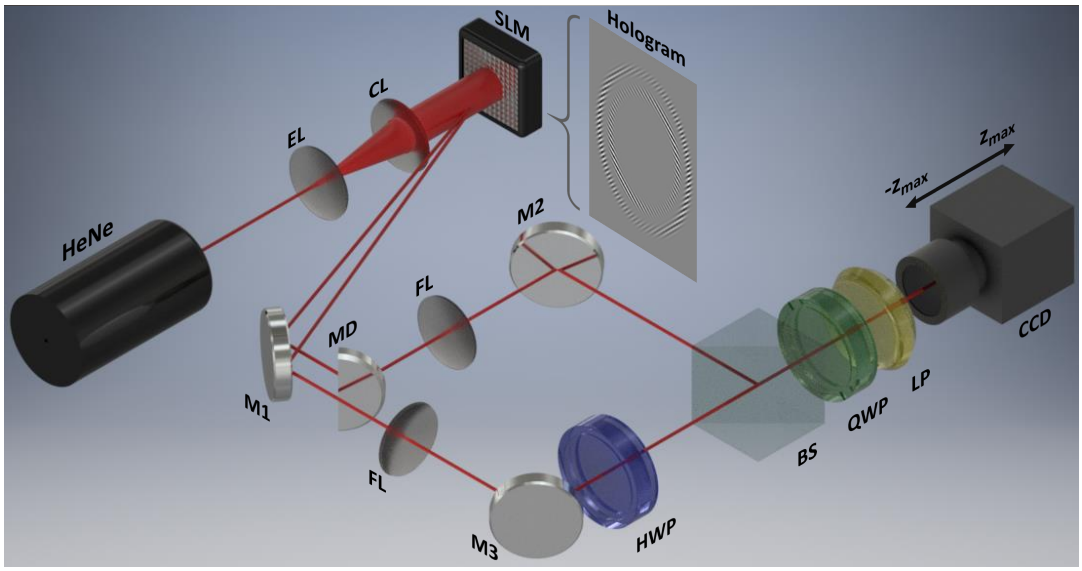


FIGURE 3.4: Diagram showing the experimental set-up used to generate and characterize petal beams with azimuthally accelerating polarization structures. HeNe - Helium-Neon laser, EL - expansion lens, CL - collimation lens, SLM - spatial light modulator, M - mirrors, MD - D-shaped mirror, FL - Fourier lens, HWP - half-wave plate, BS - 50:50 beam-splitter, QWP - quarter-wave plate, LP - linear polarizer and CCD - charge-coupled device.

In this work, vector petal beams with radially self-accelerating polarization structures were generated experimentally using the set-up shown in Fig. 3.4. A HeNe laser (wavelength 633 nm) was used to produce a horizontally polarized Gaussian beam, which was expanded and collimated using lenses EL and CL, respectively. The beam was then used to illuminate a PLUTO-2-NIR-015 SLM. It is notable that this SLM model is designed to operate in the 650 nm to 1100 nm range, however compensating calibration was applied for effective operation at 633 nm. The SLM was addressed with phase holograms encoded via the complex amplitude modulation scheme described in Chapter 2. The desired modulation $H(x,y)$ was determined by computing the pixel-wise inverse Fourier transform of the weighted petal beams using the discrete inverse Fourier transform matrix $\mathcal{F}^{-1}$, according to:

$$H_{1/2}(x,y) = (\mathcal{F}^{-1}(x,y))^T(U_{1/2}(x,y))\mathcal{F}^{-1}(x,y). \tag{3.12}$$

The two petal beams were given: $l = -1$, $k_{r2} = 0.75k_{r1} = 0.75(0.0025k)$ (where k is the total wavevector magnitude) and $w_0 = 2.25 \times 10^{-3}$ m; while the x-component of the holographic grating frequency for the two beams were given opposite directions. The spatially separated first order diffraction components associated with the two petal beams were then directed into a 50:50 beam-splitter (BS) through a series of mirrors (M1 - M3), D-shaped mirror (MD) and Fourier lenses (FL - with focal lengths $f = 750 \times 10^{-3}$ m forming a $2f$ system between the SLM screen and the coinciding focal planes of these lenses). Prior to entering the BS a half-wave plate (HWP) was used to convert the polarization of one of the beams to vertical. The intensity of the six polarization components of the resulting vector beam was then imaged using a FLIR Grasshopper3 CCD camera, after passing through a conventional Stokes polarimetry arrangement (quarter-wave plate (QWP) and linear polarizer (LP) [106]).

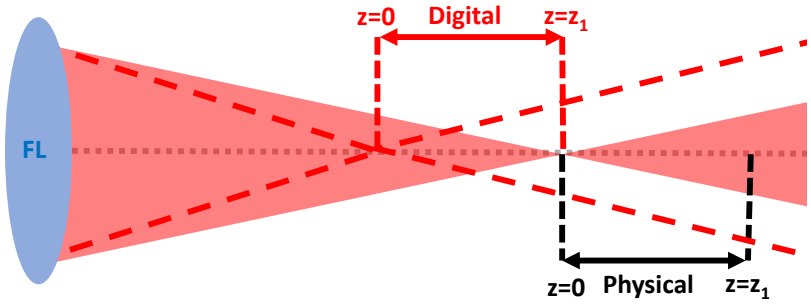


FIGURE 3.5: Diagram showing the equivalence of focusing and positive propagation of a beam generated in the focal plane of lens FL.

The Stokes intensity measurements were taken within $z \in [-z_{max}, z_{max}]$, where $z = 0$ corresponds to the focal plane of the Fourier lenses (as the beam paths were made equal) and $z_{max} = \frac{2\pi w_0}{\lambda k_r}$ is the maximum distance in which the BG beams are valid. The measurements over this range were acquired by encoding a lens phase ($e^{i(k-kr^2/f)z}$) into the holograms to digitally move the position of the Fourier plane as shown in Fig. 3.5. From the expression for z_{max} it is also clear that beams with differing k_r will maintain their structure over different ranges. The results presented in the following sections ensure that $z \leq (z_{max} \approx 0.9\text{ m})$ of U_1 which has a shorter valid range.

3.1.4 Results

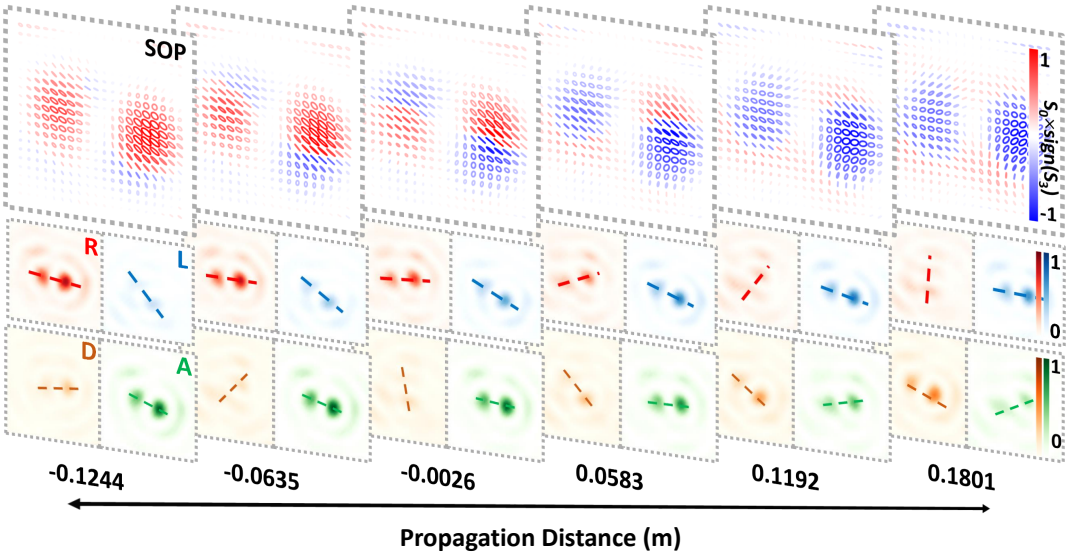


FIGURE 3.6: Experimental results showing the evolution of the SOP (top) and individual right-circular (R), left-circular (L), diagonal (D) and anti-diagonal (A) polarized component intensities (bottom) with propagation distance.

In Fig. 3.6 we can see the SOP of a beam generated in the manner described above, at equally spaced values for z. From visual inspection, it is clear that the structured SOPs in the petals change in a non-linear manner, i.e., a transition from right-circular

[R] to anti-diagonal [A] to left circular [L] is visible in the range shown. This is further highlighted by inspecting the orientation of the polarization components, the R component begins to accelerate (in the azimuthal direction of the transverse plane) while the L component begins to decelerate at the same time the D component is accelerating and the A component is decelerating - the energy flow away from (in to) accelerating (decelerating) components observed in previous work is also verified here [73]. The local SOP progression of a point in the beam with propagation is representative of propagation through a birefringent material (i.e., QWP) which is experiencing periodically accelerating/decelerating rotation of its fast axis. It is notable that this behaviour originates from the non-linear azimuthal phase profiles of the constituent BG_l beam superpositions, coupled with the linear Gouy phase inherent to BG_l beams.

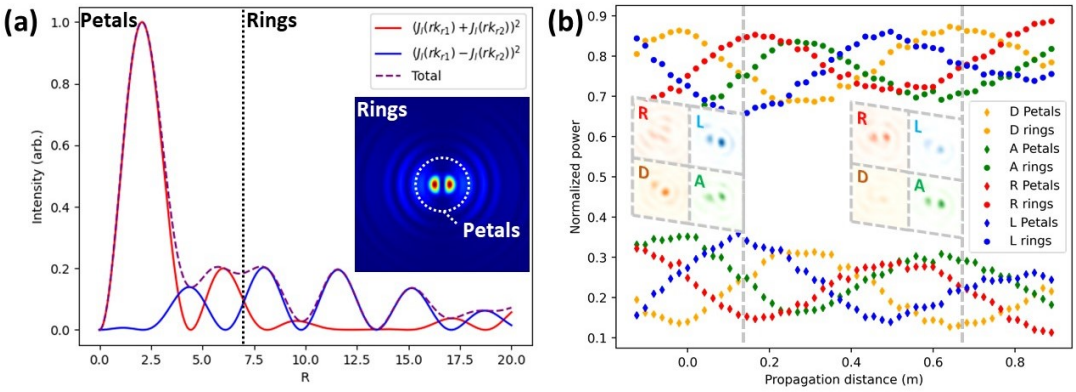


FIGURE 3.7: Plots showing: (a) the contribution of radial functions $R_{petal/ring}$ to the total intensity and (b) the normalized power of the ring and petal structures of four propagation dependent polarization components.

Figure 3.7.a shows how radial functions $R_{petal/ring}$ characterize the inner and outer regions as well as a transverse profile showing the circular cropping region which was used to approximate measurements of these components experimentally. It should be noted that although the ring components appear to contain a greater overall fraction of the total power, that this power distributed over a large area and the ring region therefore has a general low intensity - for this reason it is more convenient to consider the petal region when making experimental observations. Figure 3.7.b shows the normalized power of the petal and ring components of the four propagation dependent polarization components. These agree with previous observations of energy exchange in scalar superposed petal beams with different radial and axial wavevector components [73]. The phase difference of the exchange behaviour between the polarized components also agrees with the intensity expressions in Eqns. 3.4a - 3.4f.

Considering only the petal region and observing the non-linear changes to the Stokes parameters (Cartesian coordinates of the Stokes vector on the Poincaré sphere) within this region, one can observe the accelerating polarization behaviour in a more general manner. In Fig. 3.8 we can see the spatially averaged SOP of the inner region at different points along the propagation distance plotted on the Poincaré sphere. From the density of points, it is clear that the Stokes vector is experiencing periodic angular acceleration/deceleration, while executing rotation about the input axis (i.e., accelerated OA). Theoretical predictions using the intensity expressions reveal

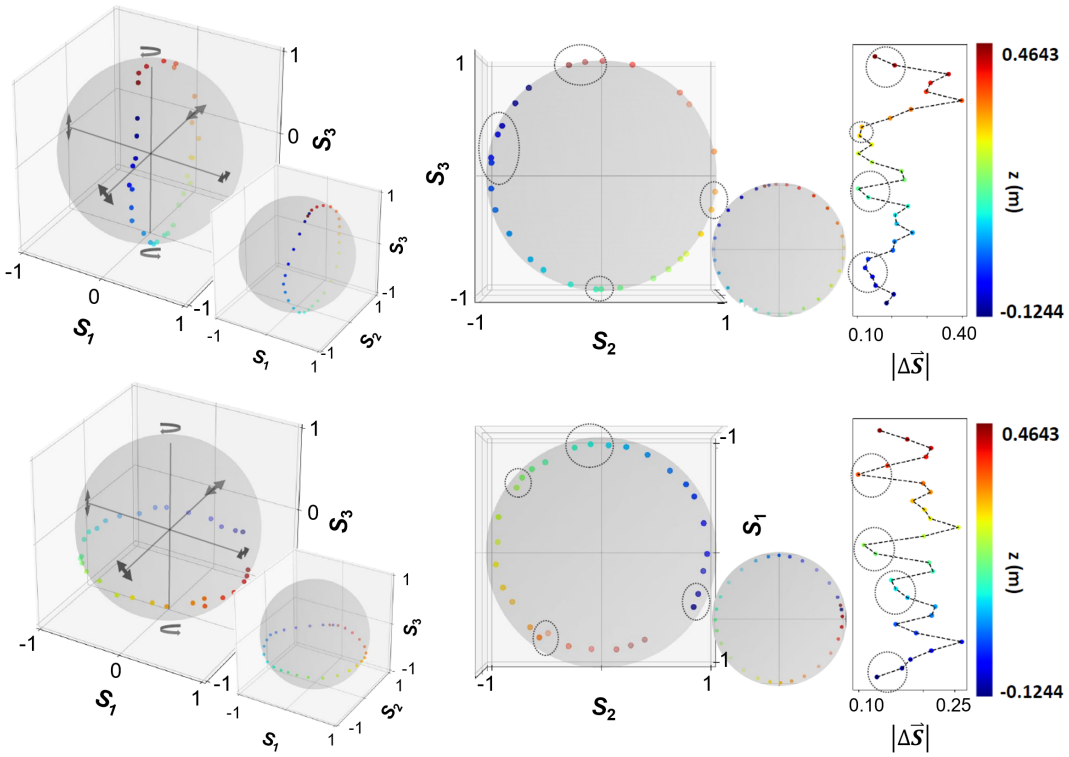


FIGURE 3.8: Diagrams showing the trajectory of the average 'petal' Stokes vector along the Poincaré sphere (left) as well as views along the input axis (right) for generation in the H-V (top) and R-L (bottom) bases, simulated comparisons are included as insets.

that deceleration occurs at the equator and poles (meridians) for H-V (R-L) generation. This observation is reasonably verified in the experimental plot (highlighted by the dashed ovals), furthermore the measured magnitude of the Stokes vector change with propagation $|\Delta\vec{S}|$ is included alongside, displaying periodic acceleration/deceleration.

3.1.5 Discussion and Conclusion

Optical Activity is the effect of the rotation of the SOP of linearly polarized light, first observed more than 200 years ago, and is associated with the transmission of light through a birefringent medium [107]. Unlike normal birefringence, where the refractive indices differ for the x and y axes, in order to demonstrate OA, the medium needs to emulate circular (or chiral) birefrigence. Optical Activity has been obserevd in liquid crystals [108], Raman scattering [109, 110] and non-chiral metasurfaces [111, 112]. Recently OA has been simulated by inducing the Gouy phase in free-space, resulting in a longitudinally changing local polarization vector [90], e.g., from radial to azimuthal. Here we have shown how to employ non-diffracting vectorial fields to produce long-range, periodic acceleration in the rotation of the *global* polarization structure, i.e., the entire polarization structure experiences angular acceleration, while maintaining a constant intensity profile. By judicious choice of superposition states it will be possible to accelerate arbitrary polarization structures by this approach. This is analogous to OA with periodical acceleration and deceleration of the Stokes vector during propagation, an effect not observed previously in free-space. During propagation, the SOP of the petal structure rotates around a given axis in the Poincaré sphere, which can be rotated by changing the generating basis. When

the rotation occurs along the equator of the Poincaré sphere, the behaviour exhibited is known traditionally as OA. The structure of angular sectors of right and left handedness is maintained at any given plane, rotating with periodic acceleration and deceleration. Even though this kind of evolution is typical of propagation in birefringent media, either linear or chiral, we have shown that it is achievable in free-space. The acceleration and deceleration can be associated with propagation in a non-uniform birefrigent medium. Adding this to the degrees of control presented in the structure, can make a powerful tool to characterize materials regarding their interactions with polarized light and chiral structures. This can motivate new studies of light with changing features in free-space propagation, as well as interaction of vectorial light with different types of media. Further work could involve the use of Airy beams to acquire non-periodic accelerating structures [78].

3.2 DMD based generator used to emulate a vectorially apertured axicon

3.2.1 Introduction

Bessel beams are so-called non-diffracting [63, 113] and self-healing [114–117] forms of structured light [11], solutions to the paraxial wave equation in cylindrical symmetry, and have found use in optical trapping [118, 119], communication [120–124], imaging microscopy [125], laser machining [33], quantum studies [126–132] and have even been produced as matter waves [77, 133, 134]. It is common to produce Bessel beams by the interference of plane waves travelling on a cone: conical waves [135]. The first creation of such beams used amplitude masks in the form of annular rings, exploiting the far field pattern of the desired Bessel beam, which is created after a Fourier lens. Proposals exist to generalize this approach to tailored sources on a ring [136]. Scalar 2D Bessel beams have since been created using holographic annular rings [137], refractive [138] and holographic [139] axicons, interferometers [140] and inside laser resonators [141–146]. One dimensional (1D) scalar Bessel beams have also been created by using a $4f$-Fourier-transformer setup and their propagation characteristics investigated. Even though they are not non-diffracting, they exhibit discrete diffraction similar to that of leaky modes in fiber arrays [147–149]. Vectorial 2D Bessel beams have been created by geometric phase-based liquid crystals [150, 151], by spin-orbit interactions [152] and metasurfaces [153], while using space-time control has seen the creation of 1D non-diffracting Bessel beams [154, 155]. Here and in the general literature one speaks of Bessel beams, the laboratory generation is always some approximation, often in the form of BG_l beams [156].

Young's double slit experiment, as first conceived and performed, applies for scalar wavefields resulting in an interference pattern of bright and dark fringes. Arago and Fresnel considered the vector characteristics of the field by studying the effect of polarization. They introduced identical polarizers with the same plane of polarization in front of each of the slits and observed the fringes described by Young. Then, in one of the slits, they rotated the polarizer until it reached the perpendicular plane of polarization with respect to the other slit and reported that, at this position, the interference pattern disappeared. From their observations they stated four laws known as Arago-Fresnel laws [157]: (1) Two waves, linearly polarized in the same plane, can interfere; (2) Two waves, linearly polarized with perpendicular polarizations, cannot interfere; (3) Two waves, linearly polarized with perpendicular polarizations, if derived from perpendicular components of unpolarized light and

subsequently brought into the same plane, cannot interfere; and (4) Two waves, linearly polarized with perpendicular polarizations, if derived from the same linearly polarized wave and subsequently brought into the same plane, can interfere.

The interference fringes referred to in these laws are in the intensity of the observed light, yet light has many DoFs that can be controlled, for what is now referred to as structured light [11]. Amplitude/intensity is the most well known DoF of light, with interference fringes observed and understood at least since the time of Thomas Young [158]. Here two waves with a relative phase (θ) difference, $\Delta\theta = \theta_2 - \theta_1$ add to produce a modulation in intensity: $I = |A\exp(i\omega t - ikz)[\exp(-i\theta_1) + \exp(-i\theta_2)]|^2 = 4A^2\cos^2(\Delta\theta/2)$ - where ω, t, k, z and A are respectively the temporal frequency, time, spatial frequency, propagation distance and amplitude. Originally $\Delta\theta$ was the path length difference described by Thomas Young, but can be a general phase delay in any co-ordinate for linear, radial or azimuthal fringes [159]. In the context of interference one may legitimately ask: fringes in what? Interference of differing frequencies give rise to the familiar beating (fringes in time) observed in electronic and optical signals, angular slits produce fringes in OAM [160], while fringes in polarization have been known and understood since at least 100 years, following seminal work by Robert Wood [161]. One can understand the polarization fringes by again considering the superposition of two waves, this time of orthogonal (e.g. $\hat{\mathbf{x}}$ and $\hat{\mathbf{y}}$) polarizations: $\exp(i\omega t - ikz)[A_{0x}\exp(-i\theta_1)\hat{\mathbf{x}} + A_{0y}\exp(-i\theta_2)\hat{\mathbf{y}}]$. One can show that the components of the final field (E_x and E_y) may be written as [64]

$$\frac{E_x^2}{A_{0x}^2} + \frac{E_y^2}{A_{0y}^2} - 2\frac{E_x E_y}{A_{0x}A_{0y}}\cos\Delta\theta = \sin^2\Delta\theta, \tag{3.13}$$

which is the well-known equation for the polarization ellipse and represents a general polarization state. Once again, $\Delta\theta$ is the phase difference which can be spatially varying, so that by changing the relative phases of the waves, one can construct a polarization varying map: fringes in polarization. This topic has a rich history and the reader is referred to further reading on the topic (see for example Ref. [157, 162, 163] for a more general theoretical treatment and Ref. [159] for a modern experimental treatment).

If instead of slits the experiment is done with two pinholes illuminated with light with the same polarization (scalar case), and a lens is placed at its focal distance, the result is the same: an intensity interference cosine pattern is created just after the lens that transforms the spherical incoming wavefronts into two coherent tilted plane waves, say $\exp[i(k_t x + k_z z)]$ and $\exp[i(-k_t x + k_z z)]$, respectively, that interfere to produce a field with intensity proportional to $|\cos(k_t x)|^2$. If the pinholes are rotated with respect to their midpoint in such a way that they produce an annular slit, the resulting wavefield is proportional to the integral

$$E(r)_A \propto e^{ik_z z}\int_0^{\pi}\cos(k_t r\cos\varphi)d\varphi\,, \tag{3.14}$$

where the magnitude of the respective wavevectors of the plane waves is $k^2 = k_t^2 + k_z^2$ and $r^2 = x^2 + y^2$. The integral on the right is proportional to the integral representation of the Bessel function of the first kind $J_0(k_t r)$. In other words, the resulting wavefield is a Bessel beam. Now, one wonders, what would be the result if the pinholes are illuminated with orthogonal polarizations? The resulting annular slit is composed with two semi-circumferences with orthogonal polarization. Analyzing the field of only one half of the annular slit with one of the polarizations

(scalar case), the wavefield will now be of the form

$$E_{\frac{1}{2}A}(x,y) \propto e^{ik_z z} \int_0^{\pi} e^{ik_t(x\cos\varphi + y\sin\varphi)} d\varphi\,, \tag{3.15}$$

which is not a Bessel pattern, as can be seen in Fig. 3.9. Notice that the far field

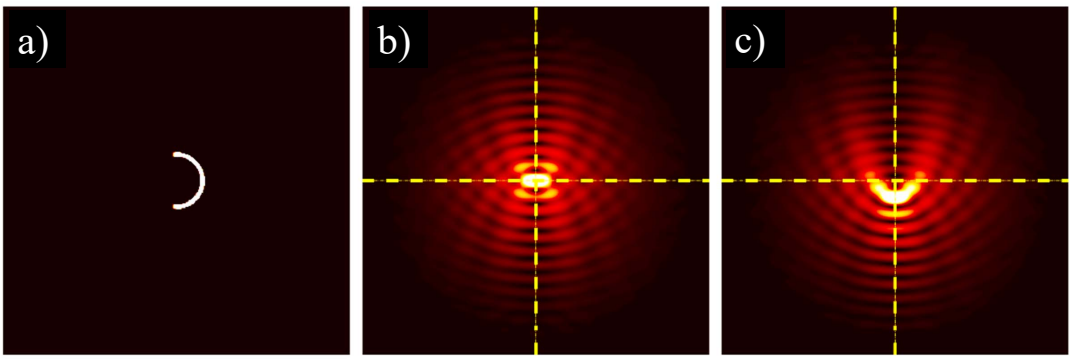


FIGURE 3.9: a) Half annular slit binary amplitude. b) Diffracted transverse intensity pattern in the far field of the half annular slit and c) Diffracted transverse intensity pattern in the far field of the half annular slit with an azimuthal phase $\exp(i3\varphi)$.

intensity pattern is very similar to that of parabolic non-diffracting beams [164]. The reason for this is that the latter have their spectrum in a semi-circumference for the stationary case and split into two semi-circumferences for the non-stationary case. Strictly speaking, the small difference is due to the phase of the spectrum of the parabolic beams near each extreme of the arc. Also, even if the initial field is not symmetrical, Fig. 3.9.a, its diffracted far field has symmetry along the transverse $x-$ and $y-$axes, Fig. 3.9.b. If a linear azimuthal phase is included in the input field, the symmetry only remains along the $x-$axis, Fig. 3.9.c. As will be seen below, along the vertical axis the 1D profile is still determined by the Bessel function.

Here we use the Arago-Fresnel laws to understand the interference of conical waves created by a segmented vectorial axicon, that is, when one half of the axicon produces a conical wave that is orthogonal (in polarization) to that produced by the other half of the axicon. In the context of conical interference, we may imagine that the orthogonally polarized contributions will not produce fringes in intensity, but will produce fringes in polarization structure. Further, the situation is conceptually equivalent to a conventional axicon but with a vectorial aperture, allowing only half the field of each polarization component through (e.g., the left portion of the axicon passes the left-handed polarization but blocks the right-handed component, and vice versa), resembling a vectorial version of a scalar parabolic field. We show that the resulting vectorial structure has embedded in it a scalar Bessel beam in 1D, along the plane of intersection of the two conical waves, while polarization projections reveal the 2D scalar Bessel fields of each polarization component of the field. We find that fields resulting from vectorial axicons endowed with OAM are represented by perturbed Bessel functions along the plane of intersection while the orthogonal plane exhibits dependence on the Struve functions. This work contributes to the topical field of structured light, probing the optical processes at play between the boundary of scalar and vectorial light, where scalar interference patterns reveal the intricate structured polarizations characteristic of vectorial light fields.

3.2.2 Concept

It is known that the interference of light waves diffracting from a ring produces, in the far field, an electric field which varies radially according to the Bessel function of the first kind [113]. The oscillatory behaviour in the radial direction manifests as a result of the path length induced phase difference of rays traveling along a cone after a Fourier lens. Conversely, this type of field can be produced directly (after some well defined distance from the near field) through the use of a conical lens known as an axicon. The axicon also allows for azimuthally varying phase profiles associated with OAM to be simultaneously introduced along with the radial variation. Let us consider an axicon which acts with spatially inhomogeneous polarization dependence, for instance acts only on right-circularly polarlized (RCP) light for $y > 0$ (top half) and left-circularly polarized (LCP) light for $y \leq 0$ (bottom half) which can be characterized by the transmission function

$$t(\rho, \varphi) = \begin{cases} e^{-i(\alpha(n-1)k\rho + l\varphi)} \langle R| & 0 \leq \varphi < \pi\,, \\ e^{-i(\alpha(n-1)k\rho + l\varphi)} \langle L| & \pi \leq \varphi < 2\pi\,, \end{cases} \tag{3.16}$$

where ρ and φ are the radial and azimuthal transverse coordinates, while α is the axicon angle, n is the refractive index, $k = 2\pi/\lambda$ is the wavevector and l is the topological charge. $\langle R, L|$ represent the transpose of the RCP and LCP Jones matrices which indicate that each half of the axicon projects only RCP or LCP. Considering diffraction from each half, the intensity can be shown to be proportional to [139]

$$I_{R(L)}(x, y, z) \propto z \left| \int_{0(\pi)}^{\pi(2\pi)} e^{ik_t(x\cos\varphi + y\sin\varphi) + l\varphi} d\varphi \right|^2 , \tag{3.17}$$

where $k_t = \alpha(n-1)k$ is the transverse wavevector component introduced by the axicon. Now if we consider only looking along the splitting line (i.e., $y = 0$) and the perpendicular "anti-splitting" line (i.e., $x = 0$) the intensity proportionality (for the $l = 0$ case) reduces to

$$I_{R(L)}(x, 0, z) \propto z\pi^2 J_0^2(k_t x)\,, \tag{3.18}$$

$$I_{R(L)}(0, y, z) \propto z\pi^2 \left| J_0(k_t y) \pm i\mathbf{H}_0(k_t y)) \right|^2 , \tag{3.19}$$

where $J_n()$ is the n^{th} order Bessel function of the first kind and $\mathbf{H}_n()$ is the n^{th} order Struve function. Here we can see a resulting 1-dimensional Bessel intensity profile along the splitting line of the axicon, due to the light diffracted across the split being able to conically interfere with itself. While along the anti-splitting line, intensity is modulated by the Struve function. For the $l = 3$ case we get

$$\begin{aligned} I_{R(L)}(x, 0, z) \propto & \left| -i\pi J_3(k_t x) \mp 16((k_t x)^{-2}\cos(k_t x) + (k_t x)^{-3}) \right. \\ & \left. - 6(k_t x)^{-1}\sin((k_t x)) \right|^2 , \end{aligned} \tag{3.20}$$

$$\begin{aligned} I_{R(L)}(0, y, z) \propto & \left| \pm 8i/3 - \pi J_3(k_t y) - \mp i\pi(\mathbf{H}_{-1}(k_t y) \right. \\ & \left. + 4(k_t y)^{-1}\mathbf{H}_2(k_t y)) \right|^2 , \end{aligned} \tag{3.21}$$

here we note that the function along the splitting line is asymmetric along y due to the rotating diffraction of light associated with OAM, while the anti-parallel case once again shows dependence on Struve functions. Finding a description of the

diffractive behaviour for general l may prove difficult due to the cylindrically assymetric nature of the Cartesian symmetry breaking.

3.2.3 Experimental Setup

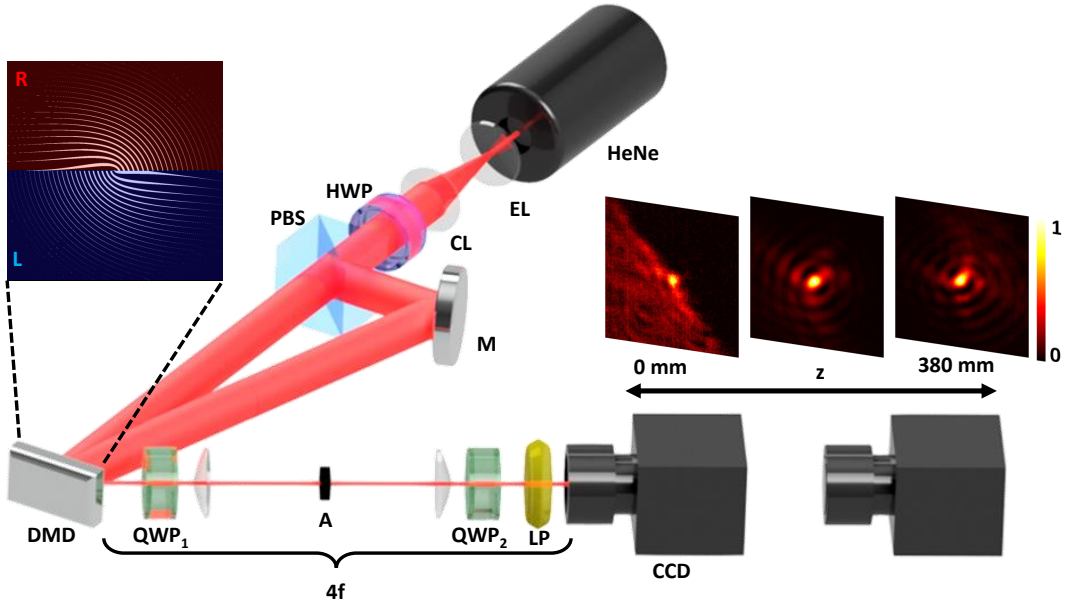


FIGURE 3.10: Diagram showing how the separation of orthogonal polarization states by a PBS followed by their recombination using a DMD can be used to replicate a vectorial axicon. Inset on the top left shows a representative example of the encoded multiplexed binary hologram and insets on the bottom right show exemplar CCD images captured at different propagation distances.

In order to generate vectorial fields from polarization dependent axicons we used the experimental set-up shown in Fig. 3.10. A horizontally polarized Gaussian beam was produced by a HeNe laser (wavelength 633 nm), then expanded and collimated using lenses EL (f=2 mm) and CL (f=250 mm) respectively. A HWP was used to rotate the polarization state to diagonal before the expanded beam passed through a polarizing beam splitter (PBS). The horizontally polarized component of the expanded beam was used to illuminate the screen of a DMD (Texas Instruments DLP6500). The vertically polarized component, exiting the reflected port of the PBS, was directed by a mirror (M) to overlap the horizontal component at the DMD screen - with an angle of $\approx 1.5^\circ$ between the two expanded beams. The $125\times$ magnification, present in the expansion and collimation system, served to project plane waves of approximately constant amplitude (in each polarization component) onto the DMD screen. The DMD was simultaneously addressed (multiplexed) with two amplitude holograms H_H and H_V of the form discussed in Chapter 2:

$$H_{H/V}(x,y) = \frac{1}{2} + \frac{1}{2}\left(\cos(2\pi G_{H/V}(x,y) + 2\pi\Phi_{H/V}(x,y)) - \cos(A_{H/V}(x,y))\right), \tag{3.22}$$

$$G_{H/V}(x,y) = x g^{x}_{H/V} + y g^{y}_{H/V}, \tag{3.23}$$

$$\Phi_{H/V}(x,y) = \frac{\arg(U_{H/V}(x,y))}{2\pi}, \tag{3.24}$$

$$A_{H/V}(x,y) = \frac{\arcsin(|U_{H/V}(x,y)|)}{\pi}, \tag{3.25}$$

where $U(x,y)$ is a desired complex field which is encoded into the +1 diffraction order of the grating defined by spatial carrier frequencies $g^{x}_{H/V}$ and $g^{y}_{H/V}$. The multiplexing is achieved by adding the two holograms $H_{H/V}$ together while giving them unequal carrier frequencies. Since the 0^{th} diffraction orders of the H and V (horizontally and vertically polarized) components leave the DMD at the same $\approx 1.5^{\circ}$ incidence angle, the grating frequencies $g^{x/y}_{H/V}$ can be chosen such that the +1 diffraction orders of holograms H_H and H_V from the horizontal and vertical diffraction components spatially overlap [165]. Conventionally the field before an axicon has a Gaussian profile the width of which will affect the propagation dynamics of the formed Bessel beam, since we are illuminating the DMD with a plane wave we chose to encode the Gaussian profile into the axicon (i.e., $|U(x,y)| = e^{-(x^2+y^2)/w_0^2}$ where w_0 is the beam waist). The axicon was encoded into the phase profile according to $\arg(U(x,y)) = k_t\sqrt{x^2+y^2} + l\arctan(y/x)$. Directly after the DMD a QWP_1 was used to convert the generating polarizations according to $H \rightarrow LCP$ and $V \rightarrow RCP$. The plane at the DMD was imaged through a $4f$ imaging system including an iris (A) used to filter out the desired combined diffraction order. Additionally a second QWP_2 and a LP were placed in the imaging system to project four Stokes intensities (right, left, horizontal and diagonally polarized) on to a CCD (FLIR Grasshopper3). The CCD was then translated along the beam axis, using a rail, from the image plane of the DMD ($z = 0$ mm) to $z = 360$ mm to investigate the formation and propagation of the resulting fields.

3.2.4 Results

The conventional plane of interest when generating non-diffracting beams from an axicon is $z = 0.5z_{max} = 0.5kw_0/k_t$, where z_{max} is the valid range of the generated field. In our case we chose $\alpha = 0.02$ rad (allowing for paraxial treatment), $n = 1.1$ and $w_0 = 1$ mm; which results in our plane of interest at $z = 250$ mm. In Figs. 3.11.a. and 3.11.b. we display the appropriately sectioned intensity profiles at the $z = 0.5z_{max}$ plane for the cases of beams generated from vectorial axicons with $l = 0$ and $l = 3$ respectively. It should be noted that, for practical reasons, the DMD is orientated at 45° - the consequence of this is the proportional rotation of the coordinate system of Sec. 3.2.2 in the experimental results. In both cases we can see good agreement between the theory described in Sec. 3.2.2 and the measured results along the spliting line, while along the anti splitting line general qualitative agreement is clear. Note that the total measured intensity corresponds to the sum of the intensities of the diffracted orthogonally polarized field components described by Eqns. 3.18 - 3.21.

In order to verify the physical origin of the observed functional behaviour seen in the sectioned profiles, we measured the intensity of the RCP and LCP projections of

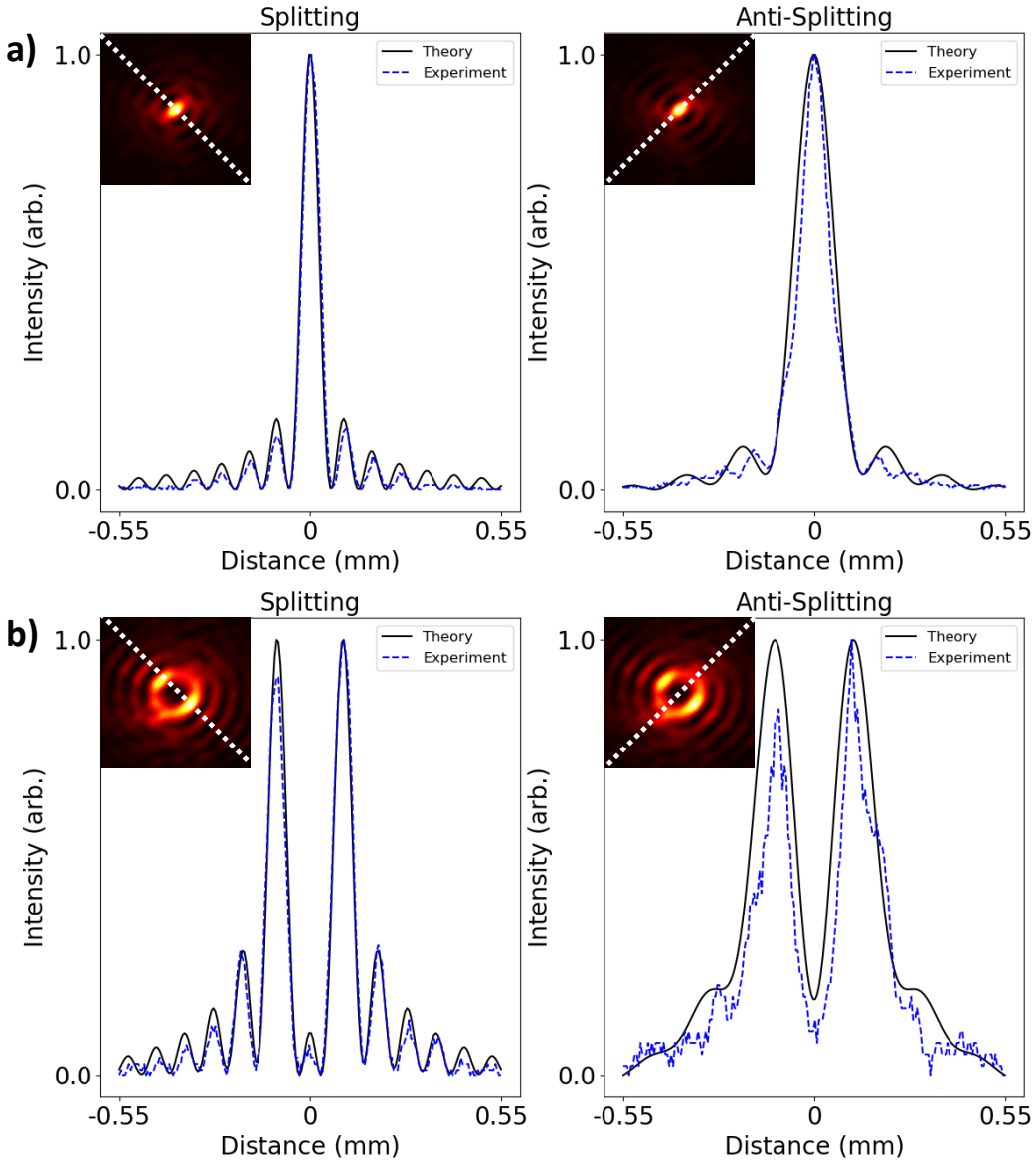


FIGURE 3.11: Plots showing the theoretical and measured 'splitting' and 'anti-splitting' intensity cross sections of non-diffracting beams generated by a vectorial axicon for a) $l = 0$ and b) $l = 3$ at $z = 250$ mm (complete measured transverse intensity profiles are included as insets).

the generated beam from the axicon plane (i.e., $z = 0$ mm) to $z = 320$ mm (the maximum z was a function of the rail system used to translate the CCD). Additionally numerical simulations were generated for comparison using the technique outlined in [166]. The results are shown in Fig. 3.12.

For the $l = 0$ case we can see how the diffraction across the splitting line occurs immediately with propagation from the axicon plane, thus allowing the interference of conical (now triangular in one dimension) rays along the splitting line. This interference leads to the formation of identical Bessel structures along the splitting line for each of the orthogonal components resulting in a scalar one dimensional Bessel beam. When OAM ($l = 3$) is introduced the diffraction across the splitting line is accompanied by the rotational energy/intensity flow imparted by the azimuthal phase factor. The resulting asymmetric structures are non-diffracting over the valid range and occupy opposing ends of the splitting line resulting in a one dimensional

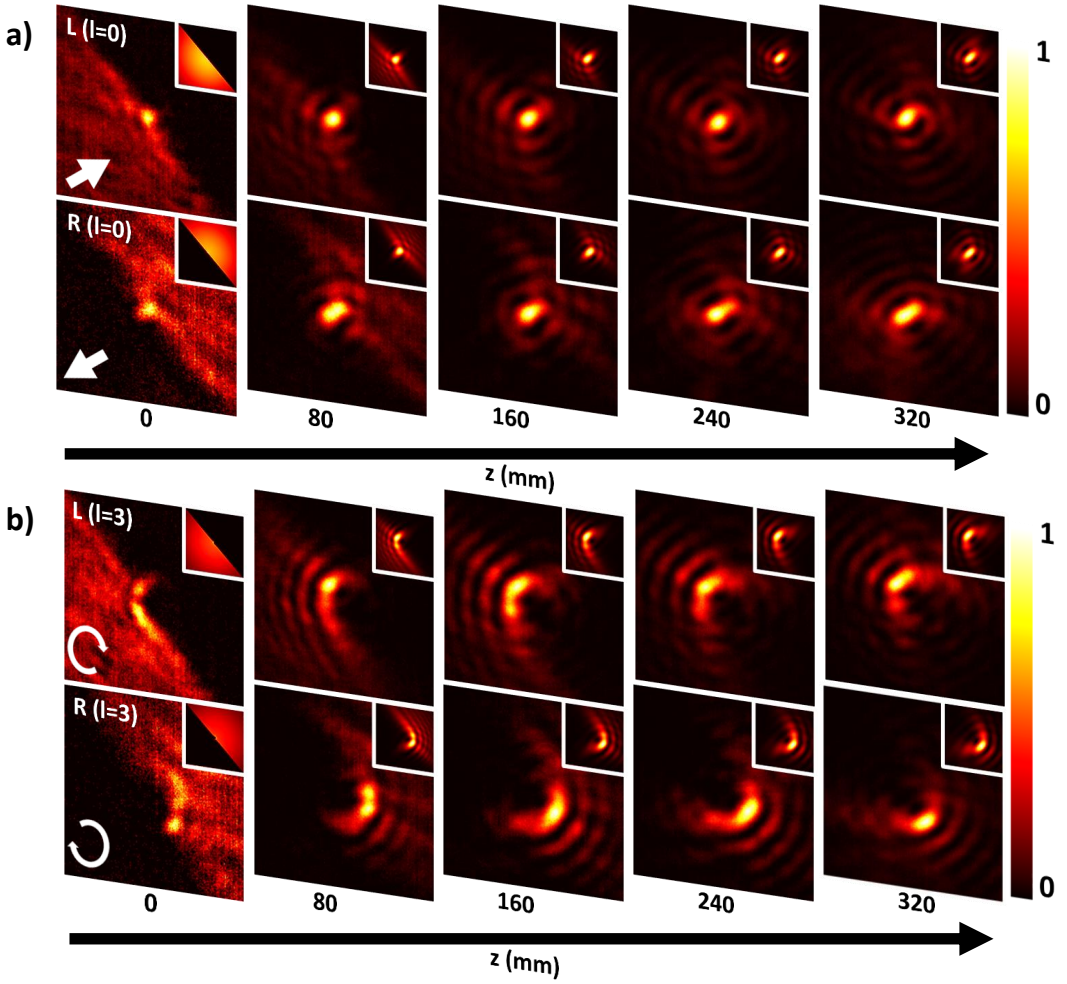


FIGURE 3.12: CCD images showing the formation of non-diffracting polarization components produced by a vectorial axicon for a) $l = 0$ and b) $l = 3$ (simulated comparisons are included as insets).

vectorial structure resembling a perturbed Bessel function along the splitting line. It was also observed that the rotation direction is changed when $l = -3$. To investigate the structure of the complete two dimensional vectorial field we acquired sets of reduced Stokes intensity measurements [106], at the $z = 0.5z_{max}$ plane and reconstructed the SOP.

From the results presented in Fig. 3.13 we can see that the transverse profiles of the optical fields generated by diffraction through a vectorial axicon are indeed structured in polarization. Naturally the diagonal polarization projections represent conventional scalar Bessel beams for both cases due to this projection 'seeing' a complete axicon, while the horizontal projection contains a discontinuity for $l = 0$ as it sees an axicon with a constant 0.5π phase difference between the halves, in the $l = 3$ case this distorts the projection.

3.2.5 Discussion and Conclusion

This work can be framed in the context of classical entanglement [167–174], where the non-separability of vectorial structured light resembles that of its quantum entangled analogue. Here the initial beam is fully vectorial but spatially separated

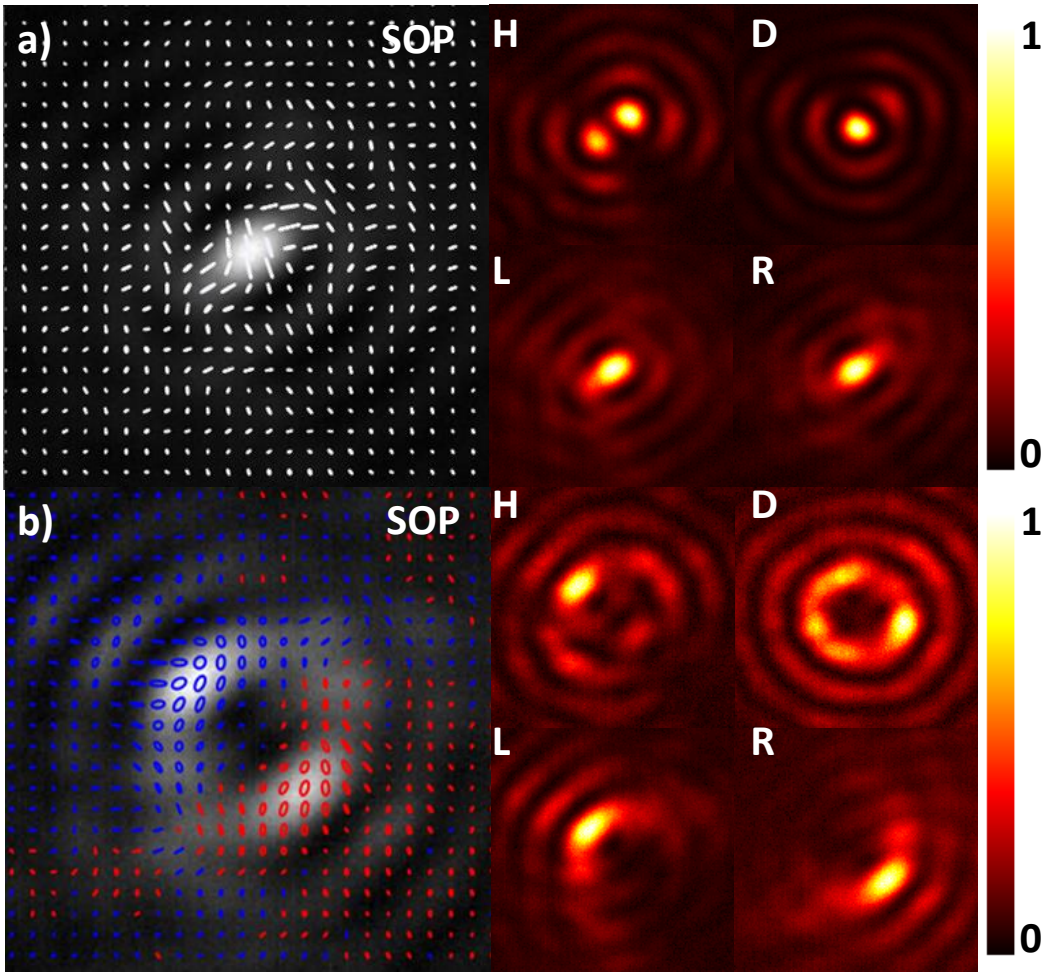


FIGURE 3.13: SOP and Stokes intensities measured at $z = 0.5z_{max}$ for a) $l = 0$ and b) $l = 3$ (red[blue] ellipses represent RCP[LCP]).

into two distinct parts, simulating a prior reported situation that revealed counter-intuitive non-separability dynamics [175], where the local non-separability changed dramatically even though the global non-separability remained the same. In our case the situation can be thought of as analogous to Young's double slit experiment, but with a vectorial twist courtesy of the Arago-Fresnel laws. Each half of the axicon is a "slit", passing through a polarization state orthogonal to the other. Orthogonal polarization states do interfere, but the fringes are seen in the polarization structure itself and not the intensity. At the interface of the two waves we observe the Bessel beam, orthogonal to this plane we do not. We imagine that this simple arrangement may be useful to unravel the vectorial dynamics at play in interference when viewed from a visibility and distinguishability perspective [176]. This would involve utilizing the orthogonality of polarization states transmitted by adjacent apertures (similar to the axicons investigated here) to control the visibility of polarization fringes and the power transmitted through each aperture to model the distinguishability.

The beams we present simultaneously demonstrate the first, second and fourth Arago-Fresnel laws. The first (second) law is verified by the presence (lack) of intensity fringes along (across) the interface - due to the identical (orthogonal) planes of polarization of overlapping waves. The fourth law manifests in the polarization

fringes across the interface, which occur due to initially orthogonal planes of polarization being projected into an identical plane during Stokes intensity measurements.

In conclusion we have observed how the diffraction dynamics introduced by a vectorial axicon lead to 1-dimensional scalar and vector Bessel structures embedded into non-diffracting vector fields, due to self interference from polarization similar conical waves. We have also observed how OAM embedded into the vectorial axicons interact with the Cartesian symmetry breaking resulting in spatially periodic perturbations to the generated 1-dimensional structures. We have framed the work in the context of the well-known Arago-Fresnel laws, testing the interplay between scalar and vectorial processing in the creation of structured light fields.

3.3 DMD-based birefringence probe

3.3.1 Introduction

The study of birefringence, the change of refractive index of a material depending on the polarization and direction of light, can be traced back at least 200 years [177, 178]. This effect has been historically known to be caused by mechanical stress [179], thermal excitation[180], Kerr medium excitation [181] and the Faraday effect [182, 183]. In material analysis, circular birefringence is associated with chirality in media such as crystals [184], fibers [185] and thin films [186]. One effect it causes in light is the change of the SOP. When the birefringence is circular (between right- and left-handed circular polarization components of light) the observed effect is often called optical activity and/or optical rotation. The measurement of this effect is, therefore, important to understanding a medium's interaction with vectorial light, a recent topic of interest [100]. Measuring and observing birefringence has shown to be important in many fields of study, including meteorology [187, 188], biology [189, 190], crystallography[191], stressed materials [192], liquid crystal analysis [193–195] and object recognition [196].

The progression of birefringence measurement techniques has led to modern, automated solutions making use of phase-shifting polarimetry [197–202], which rely on photoelasticity [203–210] or liquid crystal birefringence [194, 211] to rotate the incident polarization state. The phase shifting technique, used in the aforementioned references, allows for the reconstruction of the full-field magnitude and orientation of the birefringence. However, many approaches make use of interferometric techniques, making them sensitive to instability and alignment [198], as well as requiring additional compensation optics to suppress the transmitted phase-retardation effect of the beam splitter [199]. The approach can also be applied to local sampling, leading to precise and accurate measurements of the retardation and azimuthal angle of the fast axis of optical components, although these measurements are relative [197]. The implementation of polariscopes has advanced algorithmic and computational techniques to improve image acquisition and noise reduction [202], of which some approaches require additional liquid crystal compensators [201]. In order to decrease acquisition time and reduce the number of moving components, this has been addressed by increasing the number of photoelastic modulators [205, 206, 208, 209], which can be a costly exercise. Although liquid-crystal displays offer high spatial resolutions when sampling across optical fields, as well as automated and dynamic implementation [194, 211], they too carry a higher cost.

An important point to highlight is that in all the aforementioned examples, birefringence is used to measure birefringence. For example, the rotation of the SOP

is achieved by means of a birefringent material, whether passively occurring from the structure of the material or induced by electro-optical or mechano-optical effects. Here we break this paradigm and present an all-digital holographic approach to polarimetry for spatially resolved measurements of both the circular and linear birefringence. We write computer generated holograms to a DMD to rotate the SOP of the light impinging on it, and go on to demonstrate the technique on a variety of topical birefringent structures, from nano-fabricated metasurfaces to chiral crystals. Our approach is cheap, wavelength independent and calibration free, allowing fast hologram switching and triggering, with high precision and excellent reproducibility, all in a compact setup with no mechanical moving parts.

3.3.2 Theoretical description

An electric field E composed of an arbitrary complex pattern $U(\vec{r})$ in a general elliptical polarization state can be expressed as

$$E = U(\vec{r}) \left(\cos\left(\frac{\alpha}{2}\right) e^{i\phi} |R\rangle + \sin\left(\frac{\alpha}{2}\right) e^{-i\phi} |L\rangle \right) , \tag{3.26}$$

with its temporal part omitted for simplicity and Stokes vector Ψ described by

$$\Psi = U(\vec{r}) \begin{pmatrix} 1 \\ \cos 2\alpha \cos 2\phi \\ \cos 2\alpha \sin 2\phi \\ \sin 2\alpha \end{pmatrix} . \tag{3.27}$$

Here $|R, L\rangle$ represent the right- and left-circular polarization Jones matrices, α represents the amplitude weighting of these components and 2ϕ is the phase difference between the components [39]. By varying only α (fixing $\phi = \pi/4$) we can access states along the meridian of the Poincaré sphere, while varying ϕ (fixing $\alpha = \pi/2$) makes the equatorial states available. Now, consider passing this state through a linear polarizer with its transmission axis at 45° to the horizontal (i.e., diagonally transmitting). We can use the Mueller matrix of the polarizer M_{pol} to operate on the state and obtain a prediction of the resulting field's Stokes vector

$$\Psi' = M_{pol}\Psi = U(\vec{r}) \begin{pmatrix} 1 & 0 & 1 & 0 \\ 0 & 0 & 0 & 0 \\ 1 & 0 & 1 & 0 \\ 0 & 0 & 0 & 1 \end{pmatrix} \begin{pmatrix} 1 \\ \cos 2\alpha \cos 2\phi \\ \cos 2\alpha \sin 2\phi \\ \sin 2\alpha \end{pmatrix} = U(\vec{r}) \begin{pmatrix} 1 + \cos 2\alpha \sin 2\phi \\ 0 \\ 1 + \cos 2\alpha \sin 2\phi \\ \sin 2\alpha \end{pmatrix} . \tag{3.28}$$

Concerning ourselves with only the total intensity (i.e., $\Psi'_{11} = S_0$), we can see that a case of equal weightings ($\alpha = \frac{\pi}{2}$) results in intensity patterns that will produce a cosine curve dependent on ϕ. Alternatively the case of constant phase difference between polarization components ($\phi = \frac{\pi}{4}$) will produce a similar curve dependent on α:

$$\Psi'_{11}\left(\alpha = \frac{\pi}{2}\right) = U(\vec{r}) \left(1 - \cos\left(\frac{\pi}{2} - 2\phi\right)\right) , \tag{3.29}$$

$$\Psi'_{11}\left(\phi = \frac{\pi}{4}\right) = U(\vec{r})(1 + \cos 2\alpha) . \tag{3.30}$$

Now let us consider placing a sample, represented by a general elliptical retarder, before the polarizer. Let the variables η and θ be the respective linear retardance (phase difference between horizontal and vertical polarization components) and optical rotation (rotation of linear polarization due to the phase difference, 2θ, between right and left circular polarization components)[212]. The Mueller matrix of the sample M_{sam} is then

$$M_{sam} = \begin{pmatrix} 1 & 0 & 0 & 0 \\ 0 & \cos 2\theta \sin^2\frac{\eta}{2} + \cos^2\frac{\eta}{2} & \sin 2\theta \sin^2\frac{\eta}{2} & -\sin\theta\sin\eta \\ 0 & \sin 2\theta \sin^2\frac{\eta}{2} & -\cos 2\theta \sin^2\frac{\eta}{2} + \cos^2\frac{\eta}{2} & \cos\theta\sin\eta \\ 0 & \sin\theta\sin\eta & -\cos\theta\sin\eta & \cos\eta \end{pmatrix}, \tag{3.31}$$

and the resulting Stokes vector, Ψ°, of the entire system becomes

$$\begin{aligned} \Psi^\circ &= M_{pol} M_{sam} \Psi \\ &= \begin{pmatrix} 1 + \cos 2\alpha \sin 2\phi (\cos^2\frac{\eta}{2} + \cos 2\theta \sin^2\frac{\eta}{2}) - \sin 2\alpha \sin\eta \cos\theta + \cos 2\alpha \sin^2\frac{\eta}{2} \sin 2\theta \cos 2\phi \\ 0 \\ 1 + \cos 2\alpha \sin 2\phi (\cos^2\frac{\eta}{2} + \cos 2\theta \sin^2\frac{\eta}{2}) - \sin 2\alpha \sin\eta \cos\theta + \cos 2\alpha \sin^2\frac{\eta}{2} \sin 2\theta \cos 2\phi \\ \cos\eta \sin 2\alpha + \cos 2\alpha \cos 2\phi \sin\eta \sin\theta - \cos 2\alpha \cos\theta \sin\eta \sin 2\phi \,. \end{pmatrix}. \end{aligned} \tag{3.32}$$

To consider a circularly birefringent sample, let us fix $\eta = \pi$ - akin to a half wave plate - where double the rotation of the axes 2θ then represents circular birefringence generated through geometric phase. Applying this together with the previous $\alpha = \frac{\pi}{2}$ we get

$$\Psi^\circ_{11}\left(\alpha = \frac{\pi}{2}, \eta = \pi\right) = U(\vec{r})\left(1 - \cos\left(\frac{\pi}{2} - (2\phi + 2\theta)\right)\right). \tag{3.33}$$

Alternatively if we consider fixing $\theta = 0$ we can measure birefringence between the horizontal and vertical axes, then together with $\phi = \frac{\pi}{4}$ we get

$$\Psi^\circ_{11}(\phi = 0, \theta = 0) = U(\vec{r})(1 + \cos(2\alpha - \eta)). \tag{3.34}$$

The situations considered above describe the following behaviour. In the case of fixing $\alpha = \frac{\pi}{2}$ we are considering a linearly polarized scalar field whose polarization state is tracing a circle around the equator of the Poincaré sphere with ϕ (Eqn. 3.29). Then, when we place a circularly birefringent material before the polarizer, the path traced is delayed proportionally to the circular birefringence. When considering $\phi = \frac{\pi}{4}$ as fixed, the polarization state of the scalar beam rotates around the meridian of the Poincaré sphere with changing α (i.e., accessing the circularly and $\pm 45^\circ$ linearly polarized states, as well as all the intermediate elliptical states - Eqn. 3.30). When a sample exhibiting linear birefringence is introduced, the rotation is delayed proportional to the linear birefringence. Thus by varying either α or ϕ and measuring the intensity of the 45° projection after travelling through a respectively linearly or circularly birefringent sample, the linear retardation η or circular retardation 2θ can be determined through fitting the measured intensities to Eqns. 3.34 and 3.33 . While we have focused on the cases of linear and circular birefringence measurements, it should be clear from the Poincaré sphere representation that this technique can measure sample induced phase differences between any two orthogonal polarizations (i.e., elliptical birefringence). To do this only the rotation axis of the input

states on the sphere and the orientation of the analyzer will need to change - which can be achieved through the placement of static wave plates in the system.

3.3.3 Experiment

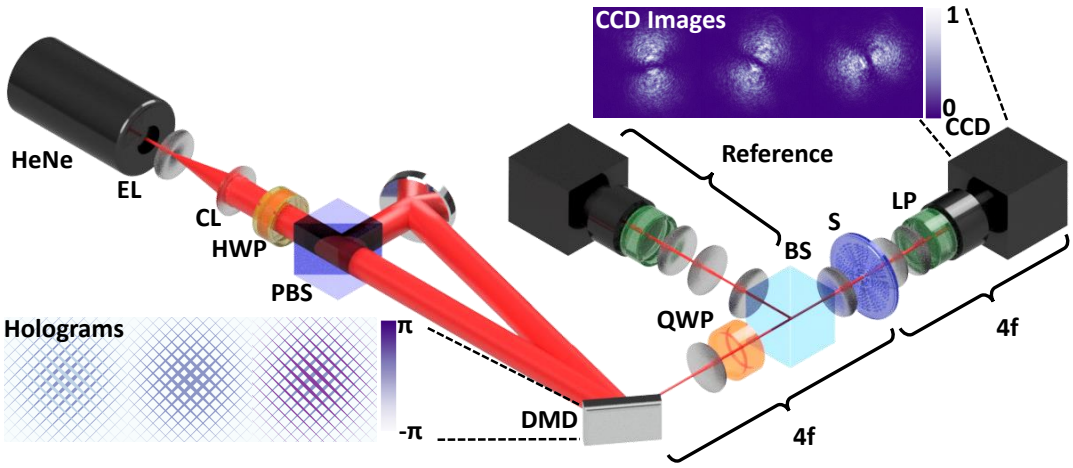


FIGURE 3.14: The arrangement which allows polarization modulation to be effected by a DMD in order to probe a sample while maintaining stabilility using a reference arm (element details in main text). Insets on the bottom left are representative examples of binary holograms encoded onto the DMD (colored according to their encoded phases), while insets on the top right are CCD images captured in order to acquire a spatially resolved circular birefringence measurement from a liquid crystal q-plate, marked as the sample S.

A core novelty of this work is to implement the aforementioned mathematics in an all-digital approach using DMDs. To demonstrate how holography, implemented with a DMD, can be used to digitally acquire spatially resolved phase shift measurements - we employed the experimental setup shown in Fig. 3.14. A horizontally polarized Gaussian beam (with plane phase) was produced using a HeNe laser (wavelength 633 nm), and subsequently expanded and collimated using lenses EL ($f = 2$ mm) and CL ($f = 200$ mm) respectively. The expanded beam was then passed through a HWP to control the plane of polarization before entering a PBS (Thorlabs PBS201, extinction ratio 1000:1). The horizontally and vertically polarized beams leaving the PBS were then aligned such that their central regions (of approximately constant amplitude) illuminated the screen of a DMD (DLP6500, 1080p, pixel size 7.6 μm) with the angle between two beams $\approx 1.5°$. The DMD was addressed with two multiplexed binary amplitude holograms (A and B) as discussed in Chapter 2

$$H_{A/B} = \frac{1}{2}\left\{ 1+\cos\left[2\pi\left(g_x^{A/B}x + g_y^{A/B}y\right) + 2\pi\varphi^{A/B}\right] - \cos\left[\arcsin\left(e^{-\frac{x^2+y^2}{w_0^2}}\right)\right]\right\}, \tag{3.35}$$

where a Gaussian amplitude profile was chosen to avoid interference present when using a flat profile. $\varphi^{A/B}2\pi$ is an induced phased difference. The spatial carrier frequencies ($g_{x/y}^{A/B}$) of the gratings were adjusted so that the +1 diffraction orders of H_A from the horizontal component and H_B from the vertical component

spatially overlap upon leaving the DMD. This overlapped diffraction order was spatially filtered at the focal plane of a $4f$ imaging system which directed the beam onto the sample (S). A *removable* QWP was used to convert the horizontal and vertical polarization components to right and left circular respectively to allow for circular birefringence measurements. After traveling through the sample, the beam was imaged onto a CCD (FLIR Grasshopper3) using a second $4f$ system including a diagonally orientated LP. A BS was used to image a copy of the beam onto another CCD (FLIR Chameleon) for use as a reference in measuring spatially homogeneous samples with improved stability. Example holograms with enlarged gratings as well as exemplar sample CCD images are shown on the bottom left and top right of Fig. 3.14 respectively. The beams generated using this setup (with and without the QWP) before passing through S or LP can be described as

$$\Psi(wo/QWP) = e^{-\frac{x^2+y^2}{w0^2}}\left(|H\rangle + e^{i\varphi}|V\rangle\right) \tag{3.36}$$

$$\Psi(w/QWP) = e^{-\frac{x^2+y^2}{w0^2}}\left(|R\rangle + e^{i\varphi}|L\rangle\right), \tag{3.37}$$

where $\varphi = \varphi_B - \varphi_A$. Therefore as φ is varied holographically the intensity measured by the CCDs vary according to Eqns. 3.30 and 3.29 - where $\varphi = 2\alpha$ and $\varphi = 2\phi$ with and without the QWP respectively.

In this way, on the main arm of Fig. 3.14 we take measurements relative to Eqns. 3.33 and 3.34. In addition to this, we used a reference arm to measure data relative to Eqns. 3.29 and 3.30. This reference arm is identical to the main measurement arm except for the presence of the sample. Now, using two of these curves (depending on the analysed basis of birefringence), we use a fitting procedure to obtain the birefringence parameter.

An essential aspect of this technique is the fitting method used to extract η and 2θ from the experimental data. The method needs to be robust enough to obtain accurate reproducible birefringence values from noisy experimental images as well as absorption from samples; while also fast enough to acquire spatially resolved information at high resolution within a reasonable time frame. To this end, a maximum likelihood estimation was chosen as it produced accurate results faster than built in fitting routines we tested - and avoided potential convergence issues. For instance gradient descent approaches would risk converging to local minima if the acquired data is noisy (e.g. due to scattering from samples), while the maximum likelihood approach allowed us to isolate the global minimum with certainty due to the finite domain of our fitting parameter. The estimation involved taking a function $f(x,p)$ of variable x and of fitting parameter p and determining the χ^2 value for possible values of p, when compared to experimental data $g(x)$. The result is χ^2 as a function of p

$$\chi^2(p) = \sum_{x=x_{min}}^{x_{max}} \left(f(x,p) - g(x)\right)^2. \tag{3.38}$$

Then, by simply finding the value of p which minimises χ^2 the desired information is extracted. In our case $f(x,p) = \Psi_{11}^{\circ}(\phi,\theta)$ for circularly birefringent samples and $f(x,p) = \Psi_{11}^{\circ}(\alpha,\eta)$ for linearly birefringent samples (i.e., Eqns. 3.33 and 3.34). We chose $x_{min} = 0$ and $x_{max} = 4\pi$, where 30 evenly spaced values of ϕ and α in this range were used to obtain the experimental images which gave $g(x)$. The resolution of $p = \theta, \eta$ was chosen to be 200 possible values naturally ranging from 0 to 2π. This

procedure is carried out N^2 times in order to acquire a birefringence image of $N \times N$ pixels. A 500×500 pixel image can be acquired in under a minute on mid-range hardware with the estimation encoded using Python or Matlab (both were tested), the use of a low-level language as well as improved hardware is expected to result in shorter acquisition times. In this work, Matlab's image acquisition toolbox was used to facilitate the rapid acquisition of the intensity images as well as perform the estimation routine in a completely automated manner.

In order to validate how accurately and precisely our technique is able to recover birefringence information, a HWP (FOCtek AWP215H) and a QWP (FOCtek AWP212Q) were used as samples, with their fast axes set to 0°. The birefringent material used in these wave plates is a combination of quartz, MgF_2 and Al. A series of 100 linear birefringence measurements (for each plate) were acquired over a period of 1 hour to allow for long term stability to be investigated. The difference between the mean of the measured birefringence and π for the HWP (0.5π for the QWP) shows how accurately our technique was able to measure birefringence of the optic while the standard deviation gives a measure of how precisely our technique can reproduce results. It can be noted that the total standard deviation $\sigma = \sigma_{res} + \sigma_{sys}$ can be thought of as being composed of two components: $\sigma_{res} = 0.005\pi$ being half the sampling resolution of the fitting parameter , and σ_{sys} approximating the error introduced by the system itself. In addition to the wave plates, measurements were taken with no object in either the sample or reference arms in order to determine the zero point $\bar{\eta}_{Zero} = 0.0071$ rad. which fell within the measured deviation $\sigma_{Zero} = \pm 0.0278$ rad..

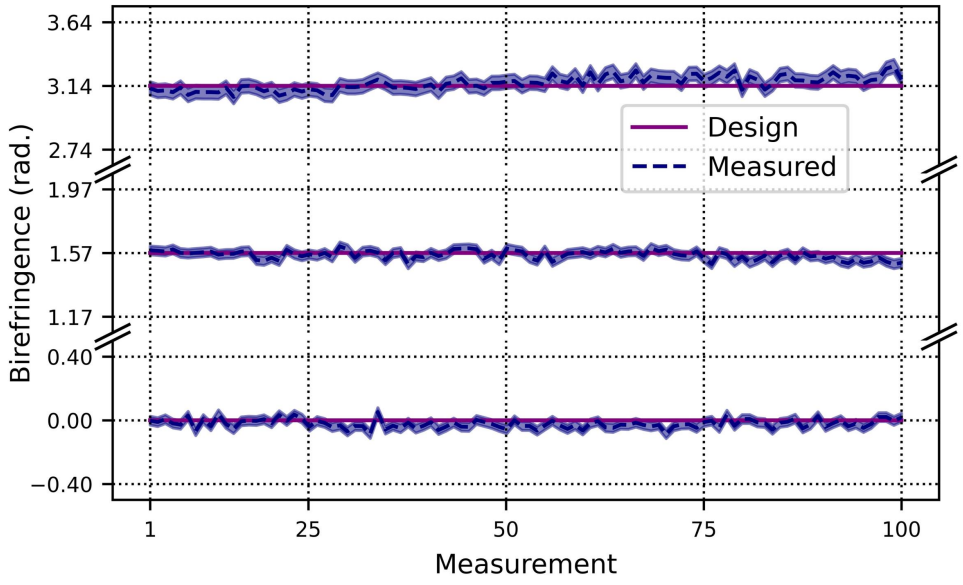


FIGURE 3.15: Plot displaying the precision and accuracy of holographic phase shifting birefringence measurements applied to a half wave- (top) and quarter wave-plate (middle) as well as calibration for the zero point (bottom). Error bands corresponding to the measured standard deviations are included for the measured results.

The mean linear birefringence measured for the QWP was $\bar{\eta}^{QWP} = 0.4960\pi$ rad. with a deviation of $\sigma^{QWP} = \pm 0.0278$ rad., while the measured values for the HWP were $\bar{\eta}^{HWP} = 1.0053\pi$ rad. and $\sigma^{HWP} = \pm 0.0425$ rad. From these results it is clear that DMD based holographic phase shifting birefringence measurements are accurate and precise to a high degree. Additionally, it follows that the precision relating to σ_{res} can be further improved at the expense of fitting time. The average

of $\sigma = \pm 0.0327 rad.$ (across the HWP, QWP and Zero measurements) is used as the error throughout the rest of this work.

To illustrate the capabilities of our approach we first measure complex birefringent structures encoded into a SLM (Holoeye-Pluto2 HED6010-VIS-014-C). In Fig. 3.16.a. we see our university logo encoded as a binary image with $\eta = \{0.5\pi, \pi, 1.5\pi, 2\pi\}$. The SLM was encoded using a gamma file provided by the manufacturer for operating the specific model with 2π modulation at 633 nm after which the digital potentiometer voltages were adjusted until a full 2π modulation could be observed. The observed results indicate good agreement at high resolution between the encoded and measured birefringence, where a small discrepancy in the measured value is observed in the $\eta = 0.5\pi$ measurement.

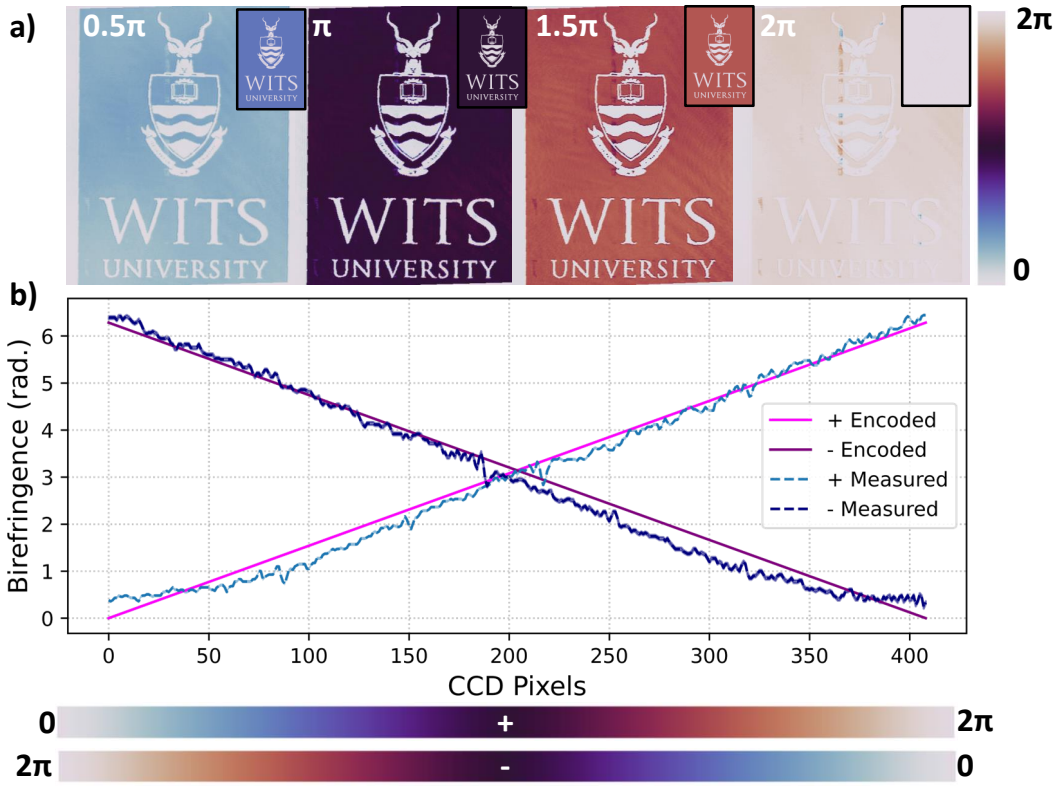


FIGURE 3.16: a) Images showing the measured birefringence for a phase map encoded on an LCoS-SLM, encoded phases are included as insets. b) Plot showing the measured birefringence for a positive (+) and negative (-) phase ramp encoded on an LCoS-SLM, the encoded phase ramps are included for comparison.

To highlight how we can overcome any non-linearity introduced by the gamma curve, Fig. 3.16.b. shows a sectioned plot of linear birefringence measured from positive and negative (+/-) phase ramps encoded on a central region of the SLM. From these results it is clear that the $\eta \in [\pi, 2\pi]$ region correlates better with the encoded phase than the $\eta \in [0, \pi)$ region. From these observations compensating factors can be introduced into encoded phases to produce more accurate results. The less reliable phase control in the low retardance region is due to the lookup table used to calibrate the SLM being inaccurate in this region, this file can be adjusted using the acquired measurements in order to provide more optimal performance of the SLM.

Metasurfaces are versatile optical elements which can be used to arbitrarily manipulate the phase and polarization of light fields [213]. They are comprised of many

sub-wavelength posts of fixed height h, which have independently chosen rectangular dimensions w_x and w_y which can also be independently rotated by an angle θ. The dimensions $w_{x/y}$ determine the linear birefringence η between the x and y linearly polarized components, while the angle θ defines the orientation of the x and y axes. A metasurface with constant $\theta = 0$ displays spatially varying linear birefringence. Contrastingly, liquid crystal q-plates are optical elements composed of an array of liquid crystals exhibiting $\eta = \pi$ birefringence between their primary axis and its orthogonal counterpart. The spatially varying orientation of the crystals in turn imparts opposite azimuthal phases onto the circularly polarized components - proportional to double the q-value of the plate - resulting in a circular birefringence of $2\theta = 4q\psi$ (where ψ is the azimuthal coordinate). Another way in which circular birefringence manifests is in chiral molecular structures such as D- and L-Alanine which exhibit circular birefringence of opposite signs. The physical mechanism resulting in the optical rotation/circular birefringence can be understood through the relationship between the optical activity tensor and the electric-dipole-magnetic-dipole polarizability tensor; which can subsequently be simulated through the implementation of density functional theory. The details of this are beyond the scope of this work (see Refs. [214, 215] for further information on the topic).

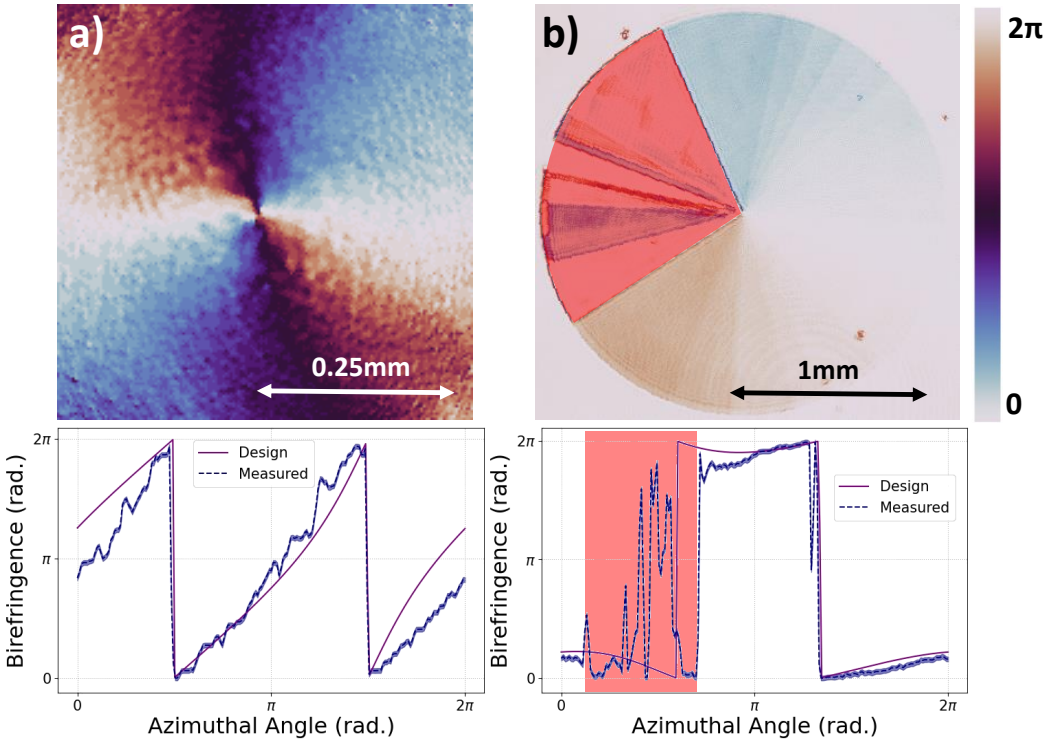


FIGURE 3.17: a) The measured circular birefringence of a $q = 0.5$ liquid crystal q-plate with the azimuthal section plotted for comparison to its design below. b) The measured linear birefringence of a metasurface with the azimuthal section plotted for comparison to its design below.

In Fig. 3.17.a. we can see the spatially resolved circular birefringence of a liquid crystal q-plate [42] with $q = 0.5$ designed for operation at 1064 nm. This q-plate has a conversion efficiency of $\approx$ 70 % for the measured wavelength. The scaled efficiencies were calculated by accounting for the wavelength discrepancy as well as the efficiencies reported in [216]. Therefore the expected circular birefringence when considering this design constraint can be expressed as

$$2\theta = \arg\left(0.7e^{i2\psi} + 0.3e^{i0}\right) . \tag{3.39}$$

Comparing the imprinted phase structure as a function of the azimuthal coordinate (extrapolated using Python) shows good agreement between the design and measured values, displaying the presence of two phase ramps of 2π depth.

Figure 3.17.b. shows the measured linear birefringence of a metasurface designed to exhibit a $\eta = 2\psi$ at a wavelength of 532 nm. At a wavelength of 633 nm the efficiency of the optical element drops to ≈ 20 %, therefore the birefringence can be expressed as

$$\eta = \arg\left(0.2e^{i2\psi} + 0.8e^{i0}\right) , \tag{3.40}$$

again, taking an azimuthal section reveals agreement in the presence of a shallow phase ramp with a single discontinuity, while damage to the optic (highlighted in red) severely impacts the measured azimuthal profile.

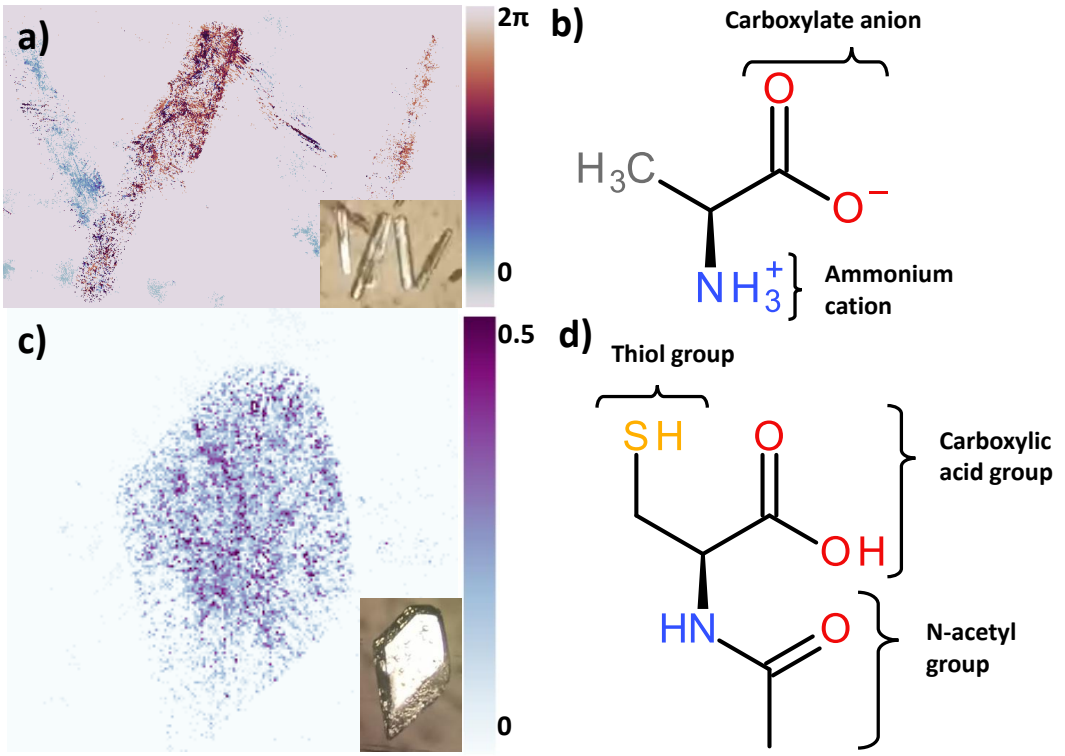


FIGURE 3.18: a) The circular birefringence measured in L-Alanine crystals (microscope image included as inset). b) Molecular structure of L-Alanine. c) The circular birefringence measured in an *N*-Acetyl-L-cystein crystal (microscope image included as inset). d) Molecular structure of *N*-Acetyl-L-cystein.

In Fig. 3.18.a. we can see the measured circular birefringence produced by four L-Alanine ($C_3H_7NO_2$) crystals exhibiting multiple chiral crystalline structures according to the $P2_12_12_1$ space group. The crystals were arranged in a shape of a 'W', it is known that the orientation of the carboxyl and amino groups (see Fig. 3.18.b.) impact both the magnitude and sign of circular birefringence produced by the molecules [215]. The third crystal from the left displays almost no circular birefringence indicating that the molecules in this crystal are orientated in a configuration of the above mentioned groups which results in no net circular birefringence. Figure 3.18.c

shows the measured circular birefringence produced by a single *N*-Acetyl-L-cystein ($C_5H_9NO_3S$) crystal. The *N*-Acetyl-L-cystein sample was confirmed to crystalize in the P1 space group via X-ray diffraction and the beam axis was made to coincide with the *c*-axis of the crystal.

To illustrate our technique's applicability regarding measuring the concentration of solutions, we used solutions of Glucose and Fructose sugars with known concentrations (in water) and placed them in a 200 mm long polarimeter tube while the reference arm had a similar tube filled with water alone. The circular birefringence of the solutions were then measured at 22 °C and used to calculate the optical rotation.

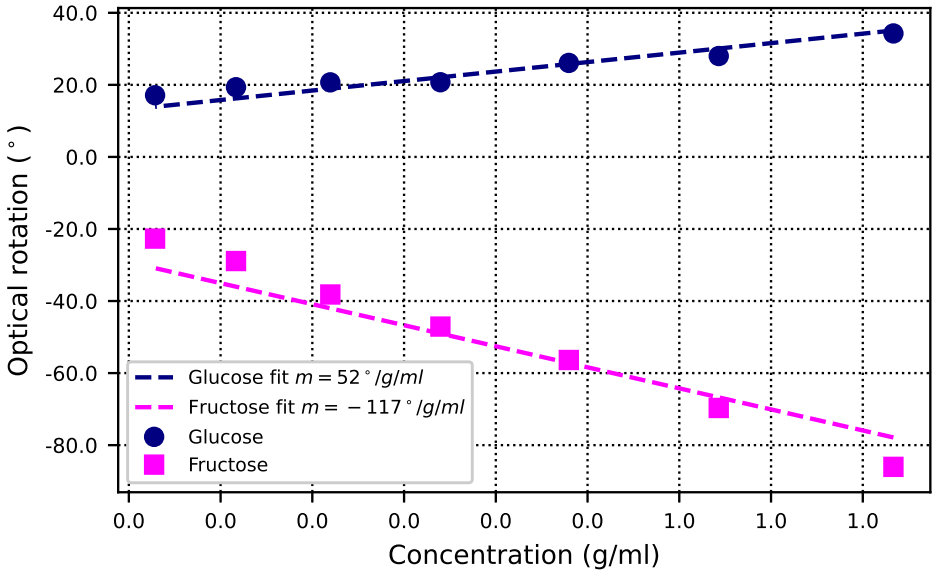


FIGURE 3.19: Plot showing the measured optical rotation produced by Glucose and Fructose at different concentrations in water.

The results shown in Fig. 3.19 show how the optical rotation produced by Glucose and Fructose changes with concentration. The dashed lines represent linear fits to the data illustrating gradients of $m_G = 26.0\ ^\circ\ \mathrm{dm}^{-1}\ \mathrm{cm}^3\ \mathrm{g}^{-1}$ and $m_F = -58.5\ ^\circ\ \mathrm{dm}^{-1}\ \mathrm{cm}^3\ \mathrm{g}^{-1}$ for Glucose and Fructose respectively (using same fitting routine as the measurement). It is notable that error bars are present but are smaller than the plotted points and that the observed behaviour shows qualitative agreement with previous studies conducted at a wavelength of 840 nm [217].

3.3.4 Discussion and conclusion

Strictly speaking, the micromirrors in our DMD are moving parts, but their fast switching that is integral to the device allows the DMD to be treated as a static device to which digital holograms can be displayed, in a similar vein that SLMs may be considered static elements although the liquid crystals themselves rotate.

Regarding the polarization rotation devices, analogous methods such as mechanically rotating waveplates or photoelastic modulators are more robust to enviromental perturbations due to being based on on-axis optical interference. However, our approach can be made more resilient by employing optical elements such as polarization gratings or a Wollaston prism. When comparing our approach to other digitally controlled implementations using SLMs, three aspects should be highlighted:

power efficiency, refresh rates and wavelength dependence. The DMDs are notoriously lossy, with works reporting around 8% efficiency against 42% of a SLM[218] for complex light modulation. This can be easily overcome as more efficient CCD sensors and more compact and powerful laser sources are becoming more accessible everyday. Regarding refresh rates, while SLMs operate around the $60Hz$ range, recent works have already highlighted the speed advantage of DMDs over liquid crystal displays [219–221]. Finally, SLMs need to be recalibrated to operate at fixed wavelengths within their operating range.

It is also important to point out that, even though polarimetry with digital instruments [106] has been demonstrated previously, this referenced technique is not enough to measure birefringence: the input polarization state in the sample is crucial. If the input polarization state happens to be the same as the axis of birefringence (for example: horizontally polarized light impinging on a HWP whose fast axis is orientated horizontally) no birefringence will be measured. By implementing the holographic control of the polarization before the sample, we solve this problem and make our solution orientation independent, while digitally controlled.

In our approach, polarization control is achieved holographically, by controlling the phase programmed to each polarization component, on a pixel for pixel basis. This holographic control allows us to compensate for wavefront aberrations that could be detected in the system, as highlighted in [222]. Because our approach is all-digital, the measurement process can reach extremely fast speeds, in the order of kilohertz rates on the DMD and limited primarily by the detector. The spatial resolution is directly related to the imaging system, enabling this method to be used in a wide range of scales. There is however a tradeoff between the imaging scale and laser power, as bigger measurements means expanding the beam, which in turn means lower signal-to-noise ratio. Complex data analysis techniques could be used to improve the measurements, substituting the maximum likelihood technique with a phase unwrapping algorithm, such as in [223].

To conclude, we have presented a holographic approach to measure birefringence in complex materials with high spatial resolution. By implementing it on a DMD we offer a solution that is robust, simple, cheap and fast, with no precalibration necessary and able to work across a very broad wavelength range. Our device is, in essence, a digitally controlled polariscope, breaking the paradigm of using birefringence to measure birefringence. We believe modern techniques can be employed to extend the capabilities of this approach, such as subwavelength analysis [224], volumetric imaging [225], quantum polarimetry [226], polarization sensitive metasurfaces [227] and measurements with complex vector structures [228], paving a path to new polarimetry applications.

3.4 DMD based generator used to emulate spin systems

As a demonstration of a further optimized version of the vectorial light generator we conducted experiments which involved the generation of complex topological structures in the Stokes vector fields of vector beams. This allowed us to probe some interesting physics related to the analogy between free-space dynamics of vectorial light and the time dynamics of spins in a magnetic field. The complexity of the structures further highlights the efficacy of the optimized design, revealing its viability as a powerful tool for probing the fundamental physics of light.

3.4.1 Introduction

Skyrmions are topologically stable vector-field configurations which were initially proposed to explain strong force phenomena [229–232]. Observations of these structures in magnetic electron-spin systems have received increasing interest due to their superior stability, making them enticing candidates for spintronic information transfer [233–238]. In parallel, optical realizations of skyrmion quasi-particles have garnered much interest in recent years as non-trivial topologically structured light in both classical and quantum regimes [239–243], and have found applications in areas such as optical communication [244, 245] and particle trapping [100, 246, 247], with new advancements being made in tuning topological degrees of freedom[248–251]. Observations of skyrmion-like structures in the optical-spin of evanescent waves [252] and focused propagating waves carrying orbital angular momentum revealed that the structures can exist at sub-wavelength scales [253]. In condensed matter systems skyrmions have been observed in plasmonic lattices and exiton-polaritons [254, 255]. It has been shown that full Poincaré beams [256, 257] contain transverse Stokes vector (i.e., psuedospin) distributions which satisfy the topological conditions for 2-dimensional skyrmions [258–260], a distribution formed by the map from the infinite plane, $\mathbb{R}^2 \cup \{\infty\}$, to the sphere, $\mathbb{S}^2$, and are consequently referred to as optical skyrmions [261, 262]. These optical skyrmions are commonly constructed using orthogonally polarized LG_p^l beams (having asymmetric azimuthal indices l, with unequal absolute values). A mechanism for full parametric tuning between skyrmion types such as Néel, Bloch, and anti, which have respective diverging, spiraling and hyperbolic textures, has also been demonstrated [248]. Tracking the trajectories of individual psuedospin states with propagation also revealed mapping to the 4-dimensional hypersphere, which the full Skyrme field maps to, through a Hopf fibration [65, 263, 264].

Here, we demonstrate how BG_l beams can be used to engineer optical skyrmions. This is achieved by superimposing two orthogonally polarized BG_l beams of different order l, which ensures that all possible relative phases and amplitudes between the beams occur along their transverse profile. The relative phases are imposed along the azimuthal coordinate, φ, by the differing helical phases $e^{il\varphi}$ while the relative amplitudes are achieved in the radial direction by the differing distributions of Bessel functions $J_l()$ having different orders. The resulting distribution of Stokes (i.e., psuedospin) vectors have global topologies which are conveniently confined to a finite on-axis region. We then reveal how the engineered difference between continuously variable radial k_r and axial k_z wavevector components can be used to control the periodic precessional beating of local Stokes vectors. This linear beating with propagation is the result of the Gouy phase difference between the two beams, which is proportional to the difference in k_z. The global effect of the local precession of psuedospins is a change in skyrmion texture with propagation, while preserving the Skyrme number. We then show analytically and by numerical simulation that superpositions of BG_l beams forming optical frozen-waves can be used to engineer psuedospin vectors which, in addition to precession about the polar axis of the Poincaré sphere, also trace a trajectory between the poles. This level of control over propagation dynamic pseudospin trajectory forms a powerful analogy to temporal dynamics of magnetic spin systems in the presence of effective magnetic fields, which can be understood using the Maxwell-Schrödinger formalism. A strong similarity can be drawn to temporal dynamics of psuedospin states in polariton condensates, where the physical mechanism inducing the precession is transverse-electric

and transverse-magnetic mode splitting which is also modelled using effective magnetic fields [265]. Another phenomenon, also found in polariton condensates, which shares similarities with our free-space work is the Rabi trajectories of quantum state vectors on the Bloch-Sphere [266]. This highlights how the analogy can extend beyond spin/polarization states to spatial/Bloch states. This connection between the optical and solid-state regimes allows for the powerful free-space optical toolkit to be applied in understanding dynamics of more complex systems, treating the optical skyrmions as quasi-particles with stability imbued courtesy of their topological soliton nature.

3.4.2 Theory

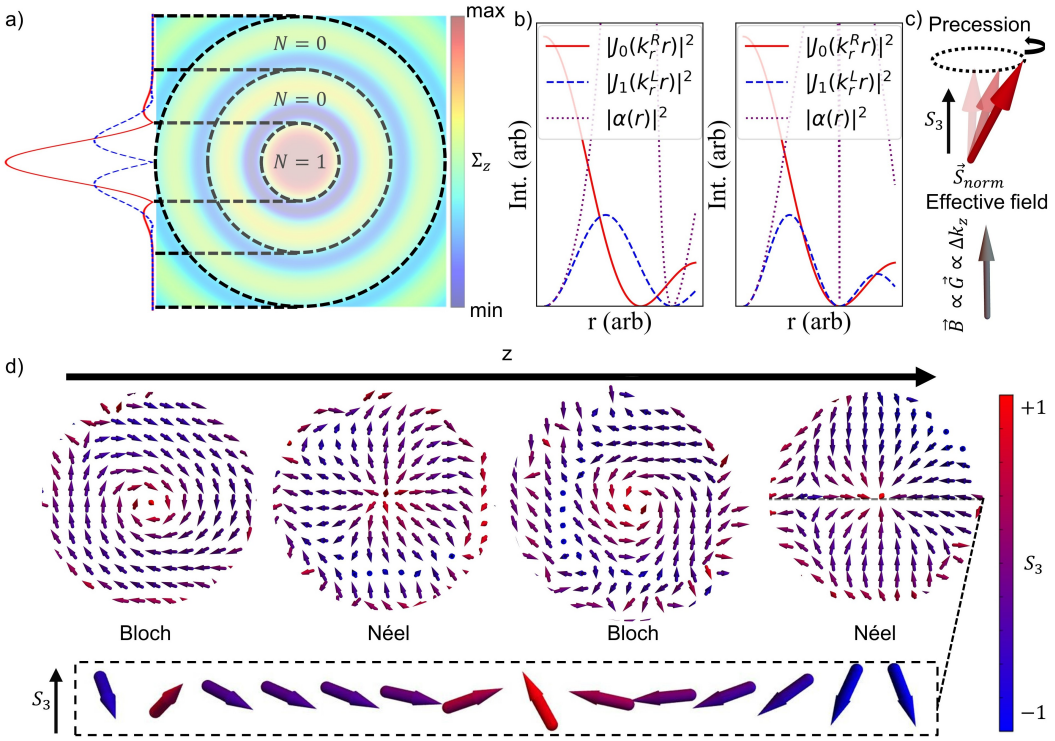


FIGURE 3.20: a) Left: Overlayed theoretical intensity plot of constituent orthogonally polarized Bessel modes as shown by the dashed rings. Right: Skyrme field with Skyrme number $\mathcal{N}$ associated to the concentric annular regions placed as insets. b) Theoretical plots of the relative intensity of the constituent BG_l components ($l_R = 0$, $l_L = 1$) for valid ($k_r^L = 1.2k_r^R$) and invalid ($k_r^L = 1.6k_r^R$) choice of radial wavevectors, where $|\alpha(r)|^2 = |J_{l_L}(k_r^L r)|^{2q}|J_{l_R}(k_r^R r)|^{-2q}$ with q defined in the text. c) Conceptual illustration of local Stokes vector precession about the S_3 axis due to the effective inhomogeneity $\vec{G}$ caused by the Gouy-phase difference between orthogonally polarized constituents. d) Experimentally measured vector plots of BG_l optical skyrmions beating between continuously deformable Bloch- and Néel-types, as well as a section indicating the radial variation of S_3.

Consider the superposition of two BG_l beams in the orthogonal right-circular (left-circular) $R(L)$ polarization basis

$$|\Psi\rangle = BG_{l_R}(r, \varphi, z, k_z^R)|R\rangle + BG_{l_L}(r, \varphi, z, k_z^L)|L\rangle\,, \tag{3.41}$$

$$BG_l(r, \varphi, z, k_z) = e^{-\frac{r^2}{w_0^2}} J_l(rk_r)e^{il\varphi}e^{ik_z z}\,, \tag{3.42}$$

where r, φ and z are the respective radial, azimuthal and axial cylindrical coordinates and $J_l()$ denotes the l^{th} order Bessel function of the first kind. $|R\rangle$ and $|L\rangle$ represent the appropriate polarization Jones vectors, k_z and $k_r = \sqrt{k^2 - k_z^2}$, are the respective axial and radial wavevector components. We use l to label the topological charge and w_0 is the width of the Gaussian amplitude envelope which will be subsequently omitted for brevity. Now let us recall that the Skyrme field components Σ_i are given by [261]

$$\Sigma_i(x,y,z) = \epsilon_{ijk}\epsilon_{pqr}S_p\partial_j S_q \partial_k S_r\,, \tag{3.43}$$

where $(i,j,k) = (x,y,z)$ and $(p,q,r) = (1,2,3)$, $S_p(x,y,z)$ are the (locally normalized) Stokes parameters (where we have omitted the spatial dependence for brevity) and $\epsilon_{ijk(pqr)}$ are the Levi-Cevita permutation operators. If we confine ourselves to a single transverse plane (e.g., $z = 0$), we can calculate the field's Skyrme number, $\mathcal{N}$, as

$$\mathcal{N} = \frac{1}{4\pi}\int_0^\infty\int_0^{2\pi}\Sigma_z(r\cos\varphi, r\sin\varphi)d\varphi dr\,, \tag{3.44}$$

where the Σ_z component of the Skyrme field is given by

$$\begin{aligned}\Sigma_z(r\cos\varphi, r\sin\varphi) = \Sigma_z(x,y) = {} & S_1\partial_x S_2\partial_y S_3 + S_2\partial_x S_3\partial_y S_1 + S_3\partial_x S_1\partial_y S_2 \\ & -(S_1\partial_x S_3\partial_y S_2 + S_2\partial_x S_1\partial_y S_3 + S_3\partial_x S_2\partial_y S_1)\,.\end{aligned} \tag{3.45}$$

Note that we choose to define Σ_z in cartesian coordinates (as this correlates better with experimentally acquired CCD images), while the integral is performed in polar coordinates to exploit the cyrlindrical symmetry of the fields. It can be shown that by exploiting the cylindrical symmetry of the BG_l modes, the above calculation yields the following simplified integral [248, 267]

$$\mathcal{N} = q\Delta\ell\int_0^\infty g(\alpha)dr \tag{3.46}$$

where $g(\alpha) = \frac{\partial\alpha^2}{\partial r}\frac{1}{(1+\alpha^2)^2}$, $\alpha(r) = |J_{l_L}(rk_r)|^q\,|J_{l_R}(rk_r)|^{-q}$, $\Delta\ell = \ell_R - \ell_L$ with $|\ell_R| \neq |\ell_L|$ and $q = \frac{|\ell_L|-|\ell_R|}{||\ell_L|-|\ell_R||}$. It is clear then for the roots of the lower order Bessel function, we have that $\alpha \to \infty$. This then means that α is only continuous in the domains $(0, r_0)\bigcup_{i=0}^{\infty}(r_i, r_{i+1})$, where $r_i \in \mathbb{R}$ are the roots of the lower order Bessel function. As such, to evaluate Eqn. 3.46 such that we obtain an integer Skyrme number, we choose to break up the integral as follows

$$\mathcal{N} = q\Delta\ell\left[\int_0^{r_0} g(\alpha)dr + \sum_{i=0}^{\infty}\int_{r_i}^{r_{i+1}} g(\alpha)dr\right], \tag{3.47}$$

which can then be evaluated to give

$$\mathcal{N} = q\Delta\ell\left[\left(\frac{1}{1+\alpha(0)^2} - \frac{1}{1+\alpha(r_0)^2}\right) + \sum_{i=0}^{\infty}\left(\frac{1}{1+\alpha(r_i)^2} - \frac{1}{1+\alpha(r_{i+1})^2}\right)\right]. \tag{3.48}$$

Clearly the second term in Eqn. 3.48 will always evaluate to zero unless the two Bessel functions share roots. However, this is not the case, as according to Bourgat's Hypothesis [268], Bessel functions of varying positive orders do not have any roots in common. And so we are left with

$$\mathcal{N} = q\Delta\ell \left(\frac{1}{1+\alpha(0)^2} - \frac{1}{1+\alpha(r_0)^2} \right), \tag{3.49}$$

which analytically indicates that the generated state given in Eqn. 3.41 has a skyrmionic topology in the localized region $(0, r_0)$. From the definition given to α, it is clear that the term within the brackets will always evaluate to an integer as $\alpha(r)$ can only tend to either 0 or ∞ at both $r = 0$ and $r = r_0$ which implies that our field is in fact skyrmionic. Furthermore, since the ratio given in the definition of α inverts depending on the sign of q, we have that the first term in the brackets always evaluates to 1 while the second always evaluates to 0, as such the Skyrme number in this central region is easily controlled by modifying q and $\Delta\ell$, which independently control the polarity [248] (affected by which component in Eqn. 3.41 dominates at $r = 0, r_0$.) and the order/vorticity [248] of the Skyrme number. A truncated segment of the Skyrme field, Σ_z, is shown in Fig. 3.20.a, where we can see that the central region's Skyrme number evaluates to 1, whereas the Skyrme number in concentric annulus regions around the origin evaluate to 0. By subdividing each of these outer annulus regions into regions where the function $\zeta = \alpha + \alpha^{-1}$ is continuous, we obtain Skyrme number contributions of $\mathcal{N}$ and $-\mathcal{N}$ which compensate for one another thereby yielding an effective skyrmion contribution of 0. This is evident in Fig.3.20.a where each concentric annulus ring can clearly be divided into two annulus rings which contribute only positive or negative values to the Skyrme field, Σ_z. Physically this phenomenom can be seen as wrapping around the Poincaré sphere and then unwrapping again within the same region. This, along with the approximately non-diffracting nature of BG_l beams, allows for a more practical implementation than the infinite bounds required by LG_p^l skyrmions. We note that the above analysis has been done for $k_z^R = k_z^L$, however as long as for $k_z^R \neq k_z^L$, the first zeroes do not overlap, then Eqn. 3.49 will still evaluate to an integer, thereby forming a skyrmionic topology which wraps the Poincaré sphere $\mathcal{N}$ times. For practical purposes, we do require that the zeroes of the Bessel functions be sufficiently far apart.

In Fig.3.20.b, we show theoretical plots of relative intensities of the orthogonally polarized components for valid and invalid choices of $k_r^{R(L)}$. An invalid choice is characterized by values of $k_r^{R(L)}$ which result in $J_{l_R(l_L)}(k_r^{R(L)} r)$ distributions with first minima (excluding those at $r = 0$) which overlap. An overlap will result in a pseudospin field which does not map to the complete Poincaré sphere, and therefore does not constitute a skyrmion.

The Stokes parameters of our vector beam are calculated using Pauli matrices σ_p - and $\sigma_0 = \mathcal{I}$ as $S_p = \langle \Psi | \sigma_p | \Psi \rangle$, resulting in

$$S_0 = |J_{l_R}(rk_r^R)|^2 + |J_{l_L}(rk_r^L)|^2, \tag{3.50}$$
$$S_1 = 2J_{l_R}(rk_r^R) J_{l_L}(rk_r^L) \cos(\Delta l\varphi + \Delta k_z z), \tag{3.51}$$
$$S_2 = -2J_{l_R}(rk_r^R) J_{l_L}(rk_r^L) \sin(\Delta l\varphi + \Delta k_z z), \tag{3.52}$$
$$S_3 = |J_{l_R}(rk_r^R)|^2 - |J_{l_L}(rk_r^L)|^2, \tag{3.53}$$

where $\Delta l = l_R - l_L$ and $\Delta k_z = k_z^R - k_z^L$. From Eqns. 3.50 to 3.53 we can see

that each local transverse Stokes vector [i.e., fixed $\vec{r}_T = (r, \varphi)$] will experience a periodic precession about the S_3 axis proportional to Δk_z as the vector field propagates. Important cases are where $r = 0$ and $r = r_0$ where we get $S_3 = \pm 1$, which is constant with z. It is also notable that due to the relationship $k_r = \sqrt{k^2 - k_z^2}$, either $\Delta k_r = k_r^R - k_r^L$ or Δk_z could be used to tune the precession rate. The linear Gouy phase of our BG_l beams allow for true periodic beating between (continuously deformable) skyrmion types over a well defined distance, which differs from the asymptotic arctan behaviour of conventional free-space LG_p^l optical skyrmion dynamics. It can be noted that in polariton condensates periodic trajectories of state/pseudospin vectors has been realized through various mechanisms [265, 266]. It should also be noted that Eqns. 12 and 13 experience symmetry under the interchange of z and ϕ which means that complete precession leads to skyrmion textures in planes orthogonal to the propagation direction. This can be seen by taking a plane at a fixed azimuthal angle and projecting it along r and z until the radial bound for the skyrmion and the axial bound of one complete pseudospin precession respectively. This results in a skyrmion texture in rectangular planes orthogonal to the beam axis for all azimuthal angles. To draw a comparison to anisotropic optical systems we can adopt the Maxwell-Schrödinger formalism, which describes pseudospin transformations of light propagating in anisotropic media and reveals the equation of motion [269]

$$\lambda \frac{\partial \vec{S}}{\partial z} = \vec{S} \times \vec{G}\,. \tag{3.54}$$

Here λ is the wavelength, $\vec{S} = S_0^{-1}(S_1, S_2, S_3)^T$ is the locally normalized Stokes vector and $\vec{G} = (2\alpha, 2\beta, 2\gamma)^T$ is the vector describing the anisotropic medium. The parameters α, β and γ specify the axes of linear birefringence, the retardance between this axes and the retardance between pure circular polarizations respectively. In the case we have been examining, we observe a pseudospin evolution in free-space when $\alpha = \beta = 0$ and $\gamma = \frac{1}{2}\lambda \Delta k_z$. A resemblance between Eqn. 3.54 and the temporal equation of motion of a magnetic spin system in a magnetic field is clear, where λ plays the role of Planck's constant and $\vec{G}$ resembles an applied magnetic field [269]. A schematic illustrating the Larmor-like precession of the normalized Stokes vector about the $\vec{G}$ axis is included in Fig. 3.20.c. In order to further highlight the value of the free-space optical analogy (beyond static homogeneous $\vec{G}$ fields), we can utilize so-called optical frozen waves (FWs) which are constructed using superpositions of BG_l beams given by [270, 271]

$$\mathrm{FW}(r, z, f(z), Q) = e^{iQz} \sum_{n=-N}^{N} A_n(f(z)) J_0(k_{r,n} r) e^{i\frac{2\pi}{L_{FW}} nz}\,, \tag{3.55}$$

$$An = \frac{1}{L_{FW}} \int_0^{L_{FW}} f(z) e^{-i\frac{2\pi}{L_{FW}} nz} dz\,. \tag{3.56}$$

Here Q is the 'central' k_z about which the superposition is constructed, $2N + 1$ is the number of BG_l modes in the superposition and $f(z)$ is an arbitrary function which the central intensity of the FW will approximate (i.e., $|\mathrm{FW}(0, z, f(z))|^2 \approx |f(z)|^2$). L_{FW} is the propagation distance over which the FW is defined. We can use these FWs as the constituent components of our vector field

$$|\Psi\rangle = \mathrm{FW}(r,z,f^R(z),Q_R)|R\rangle + \mathrm{FW}(r,z,f^L(z),Q_L)|L\rangle\,. \tag{3.57}$$

By choosing $Q_R \neq Q_L$ with an appropriate choice of $f^{R(L)}(z)$, we can have an on-axis (i.e., $r = 0$) Stokes vector which, in addition to the precession about S_3, can trace paths between the poles of the Poincaré sphere. As an example we can consider $f^R(z) = \sqrt{z/L_{FW}}$ and $f^L(z) = \sqrt{1 - z/L_{FW}}$ resulting in Stokes parameters approximated by

$$S_0 \approx 1\,, \tag{3.58}$$

$$S_1 \approx 2\sqrt{\frac{z}{L_{FW}}}\sqrt{1-\frac{z}{L_{FW}}}\cos(\Delta k_z z)\,, \tag{3.59}$$

$$S_2 \approx -2\sqrt{\frac{z}{L_{FW}}}\sqrt{1-\frac{z}{L_{FW}}}\sin(\Delta k_z z)\,, \tag{3.60}$$

$$S_3 \approx \frac{2z}{L_{FW}} - 1\,. \tag{3.61}$$

We then model axially dependent $\vec{G}$, analagous to a time-varying $\vec{B}$ field , in free-space

$$\vec{G}(z) \approx \begin{pmatrix} \frac{\sin(\Delta k_z z)}{L_{FW}\sqrt{\frac{z}{L_{FW}}}\sqrt{1-\frac{z}{L_{FW}}}} \\ \frac{\cos(\Delta k_z z)}{L_{FW}\sqrt{\frac{z}{L_{FW}}}\sqrt{1-\frac{z}{L_{FW}}}} \\ \frac{(L_{FW}-2\Delta k_z(z-1)z-2z)\cot(\Delta k_z)+L_{FW}-2z}{2z(L_{FW}-z)} \end{pmatrix}. \tag{3.62}$$

The case of FWs is distinct from the case of optical skyrmions as the control is over a single on-axis pseudospin vector as opposed to a transverse distribution of pseudospins, our implementation of FWs serves as a first step toward the use of spatially varying FWs which could exhibit changes of not only skyrmion textures but also Skyrme number during propagation [272, 273]. It should be noted that while FWs have been generated experimentally, the large range of k_z values required to accurately approximate $f(z)$ creates some requirements for large system apertures to acquire this. Due to these restrictions our demonstration of pseudospin control using FWs is based on simulations involving propagating the field using numerical angular spectrum propagation [166].

3.4.3 Experiment

To investigate the predicted behaviour of the vector fields described in Sec.3.4.2, we used the arrangement shown in Fig.3.21. A horizontally polarized Gaussian beam from a HeNe laser (operating at a wavelength of $\lambda = 632.5$ nm) was expanded and collimated using lenses EL ($f = 2$ mm) and CL ($f = 250$ mm) respectively, such that the central transverse region of the beam approximated a plane wave of constant amplitude. The expanded beam then had its polarization axis rotated by 45° with a HWP before it was passed through a Wollaston prism (WP) and QWP which separated the R and L polarized components of the expanded beam by an angle of $\approx 1°$ (in the horizontal $x-z$ plane). A $4f$ system was then used to image the plane at the WP onto the screen of a DMD (TI-DLP6500). To facilitate complex amplitude modulation of the incident light [51], we make use of two binary amplitude holograms of the form

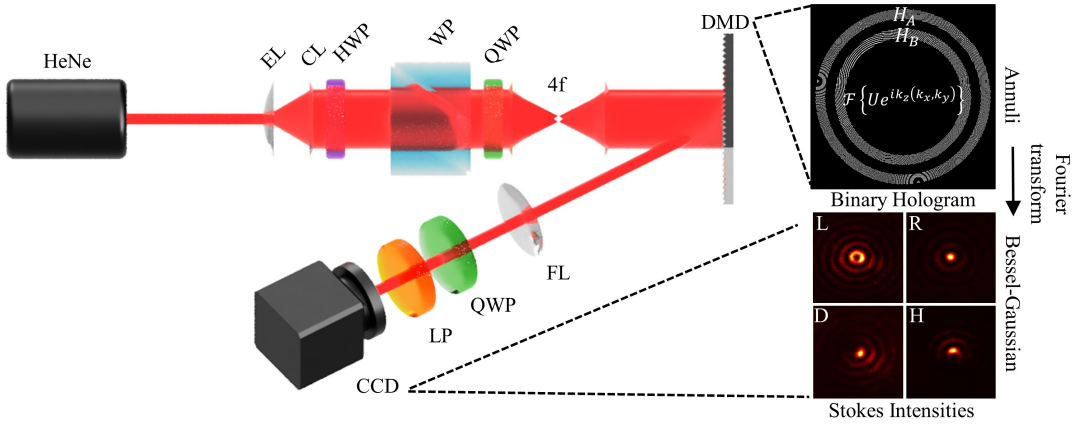


FIGURE 3.21: Diagram showing the experimental arrangement used to generate and analyse BG_l based optical skyrmions [WP - Wollaston prism, EL - expansion lens, CL - collimation lens, HWP - half-wave plate, QWP - quater-wave plate, DMD - digital micro-mirror device, FL - Fourier lens, LP - linear polarizer]. The top right inset shows an example of binary amplitude holograms featuring individual rings for each of the two multiplexed holograms $H_{A(B)}$ (far-field). The bottom right inset shows examples of Stokes intensities measured by the CCD (near-field).

$$H_{A(B)}(\vec{r}) = \frac{1}{2} + \frac{1}{2}\left(\cos\left(2\pi\Phi(\vec{r}) + 2\pi\vec{g}^{A(B)}\cdot\vec{r}\right) - \cos(\pi A(\vec{r}))\right), \tag{3.63}$$

which were multiplexed and displayed by the DMD. We define $\vec{r} = (x, y)$ as the Cartesian pixel coordinates, $\Phi(\vec{r}) = \frac{\arg(T^{A(B)}(\vec{r}))}{2\pi}$ and $A(\vec{r}) = \frac{\arcsin\left(|T^{A(B)}(\vec{r})|\right)}{\pi}$ are the re-normalized phases and amplitudes of the complex transmission functions $T^{A(B)}(\vec{r})$. With the 0^{th} diffraction orders of the $R(L)$ components leaving the DMD screen at the same 1° separation angle, the spatial carrier frequencies $\vec{g}^{A(B)} = (g_x^{A(B)}, g_y^{A(B)})$ were chosen such that the 1^{st} diffraction order containing the complex field distributions $T^A(\vec{r})$ in the R polarization spatially overlapped (co-linearly) with the 1^{st} order of the $T^B(\vec{r})$ distribution in the L polarization [165]. It should be noted that the resulting gratings have spatially constant frequencies (for each hologram $H_{A(B)}$), with local shifts in the fringes associated with the desired phase modulation [70]. Finally a Fourier lens (F: $f = 0.2$ m) was used to project the far-field intensity onto a CCD camera. The transmission functions were set according to $T^{A(B)}(\vec{r}) = \mathcal{F}\{\langle R(L)|\Psi\rangle_{z=0}\}e^{iq_z(q_x,q_y)z}$, where $\mathcal{F}\{\}$ represents the Fourier transform, $q_z(q_x, q_y)$ is the spatially varying transverse angular spectrum used to digitally propagate the field captured at the CCD by the distance z [274]. A QWP and LP were used to project Stokes intensities of the generated fields onto the CCD [106]. It is notable that the digital propagation scheme should result in similar results to those which could be obtained by physically translating the CCD along z. The digital scheme was preferable as it allowed for automated measurements and for the Stokes intensities to be more accurately aligned since there was no risk of the CCD shifting.

3.4.4 Results and Discussion

Using the arrangement in Sec.3.4.3, we generated vector fields of the form in Eqn. 3.41. We set the parameters $l_R = 0$, $l_L = [1, -2, 3]$ and $k_z^{R(L)} = 0.999995(0.999986)k$. Using

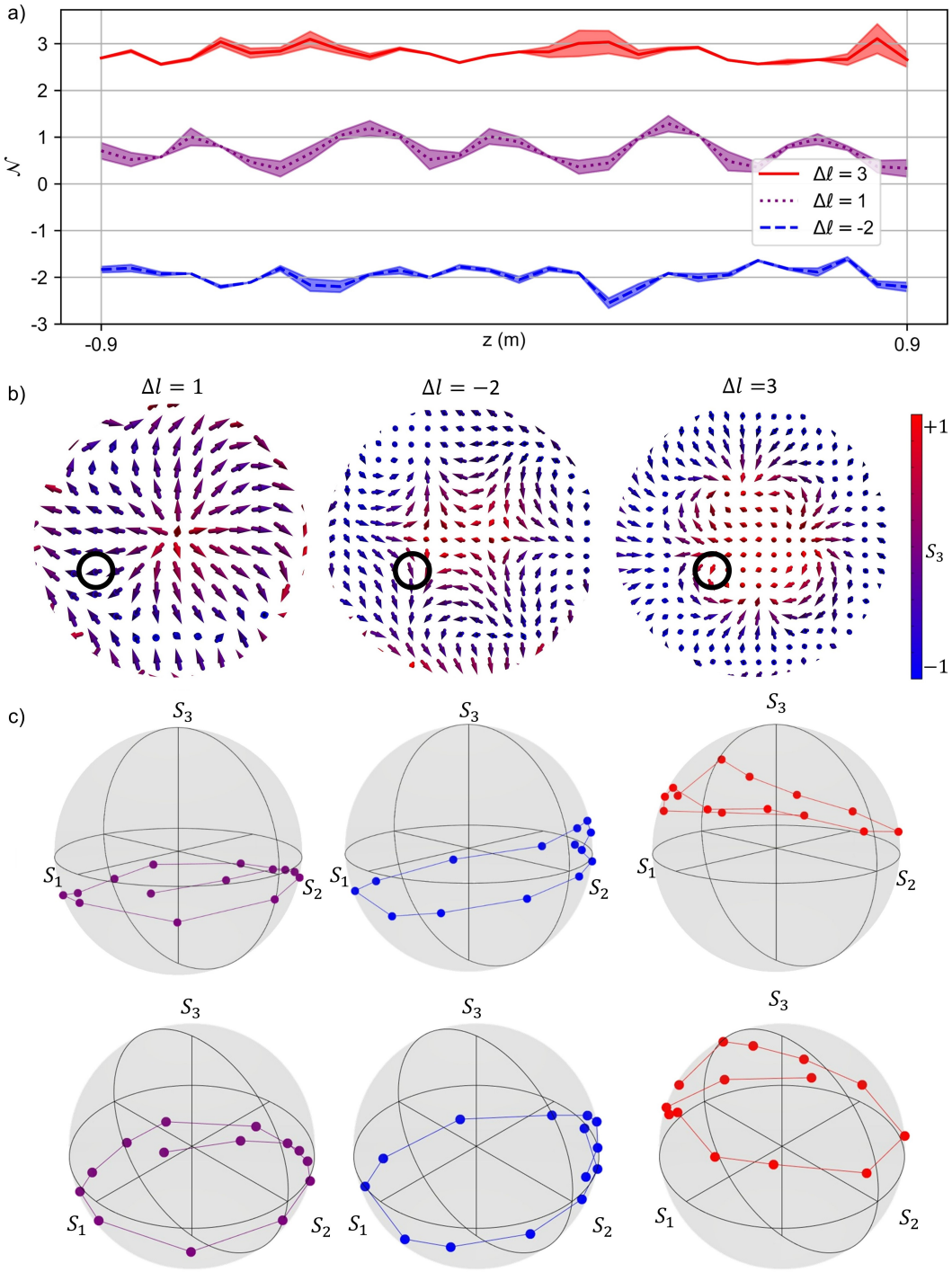


FIGURE 3.22: a) Plot showing the experimentally measured Skyrme number of various BG_l optical (anti-)skyrmions propagated over a well defined distance. b) Experimentally measured Stokes vector fields of the corresponding BG_l skyrmions in a). c) Plots showing the experimentally measured precession of a local Stokes vectors (from the corresponding beams of a) about the S_3 axis with propagation for various $\mathcal{N}$.

Stokes intensity measurements of the *R*, *L*, *D* (diagonal) and *H* (horizontal) polarization projections, we extracted the transverse Stokes vector distribution at 26 evenly spaced planes over the digitally propagated range $z \in [-0.9, 0.9]$ m. In Fig. 3.20.d we show the experimentally measured Stokes vector fields of the case with $l_L = 1$

at various planes where the transition between Bloch- and Néel-type skyrmions, characterized by the respective 'hedgehog' and 'spiral' textures, is clear. Inspection of the local behaviour of individual vectors reveals the precessional dynamics akin to that of anisotropic and magnetic systems. In Fig. 3.22.a we show how the topological index of $\mathcal{N}$ is preserved over the propagation range, here $\mathcal{N}$ was calculated using Eqn. 3.44 where the transverse gradients were determined using a numerical second-order finite difference approximation, while the error-bands were calculated by propagating the observed 2 % shot noise through Eqn. 3.44. Notwithstanding the visible fluctuations in the approximated $\mathcal{N}$, the invariance of the distinct values with propagation is evident. The cause of the excessive fluctuations in the $l_L = 1$ case is due to the effect of rapidly changing relative amplitudes for lower order skyrmions, which induce errors in the computation method used to calculate gradients. The invariance of the Skyrme number highlights the stability of the structures to the effect of the $\vec{G}$ fields in the Maxwell-Schrödinger formalism. Plots of the locally normalized Stokes vector fields (sampled at every 3 pixels of the measured data) for various Δl are shown in Fig. 3.22.b where the azimuthally varying vector orientations give the characteristic textures associated which each Skyrme number. In Fig. 3.22.c we show plots of the paths, on the Poincaré sphere, traced by sample Stokes vectors (at the positions indicated in Fig. 3.22.b). The predicted complete rotation of the local vectors about the S_3 axis over a finite distance is clear, it is notable that to observe a complete rotation utilizing LG_p^l modes one would need to observe the field propagation to infinity. In Fig. 3.23.a we show the numerically simulated spiraling path traced out by the central Stokes vector of a field taking the form in Eqn. 3.57, modeling the dynamics of an electron spin/Stokes vector and a magnetic field/anisotropic material of the form in Eqn. 3.62. The dynamics were simulated over a 200 mm distance with $Q_R(L) = (0.99997)0.99985$. We can note that the path deviates from an ideal spiral at the poles, this is due to the approximate nature of the FW which is highlighted when comparing the simulated relative phase and amplitude to the ideal case shown in Fig. 3.23.b. This system emulates a dynamic applied magnetic field or, equivalently an axially dependent anisotropic material which results in a (pseudo)spin state which accesses a large portion of possible orientations over a well defined propagation length. It is also notable that this propagation dynamic trajectory is similar to that observed in time dynamic Bloch vectors which evolve in polariton condensates [266]. This extension of the Maxwell-Schrödinger formalism, which is generally restricted to anisotropic media, to the realm of free-space optics provides a more accessible form of the analogy [269].

3.4.5 Conclusions

We have generated and analysed a variation of skyrmions in the Stokes field engineered using BG_l beams, with different absolute values in their l indices. We have shown how the global topological invariant can be extracted from a finite region and how unequal axial wavevector components in the constituent beams lead to precessional dynamics of pseudospins which cause a global transformation between Bloch and Néel type skyrmions with different initial angles. We experimentally verify the invariance of the topological index of the generated fields with propagation. We also propose a technique to extend the optical control of psuedospin dynamics by exploiting optical frozen-waves constructed by superpositions of BG_l beams. We show how these propagation dynamics of pseudospin states are analogous to time dynamics of magnetic spin states, where the skyrmion beating is characteristic of behaviour in a static magnetic field and the frozen-wave case allows for dynamic magnetic fields

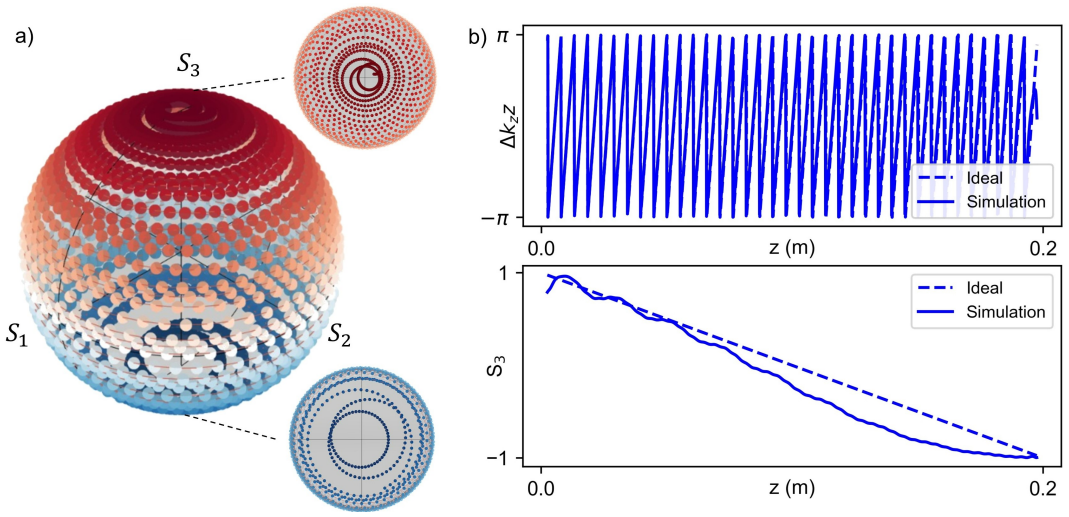


FIGURE 3.23: a) Plot showing the path traced during propagation of a numerically simulated central ($r = 0$) Stokes vector generated using optical 'frozen-waves', insets show the views from each of the poles. b) Plots showing the ideal (theoretical) and simulated (via the angular spectrum method) relative phase $\Delta k_z z$ and amplitude S_3 of the constituent components of the vector field used to produce the Stokes vector rotation in (a).

to be emulated. The analogy can be described using the Maxwell-Schrödinger formalism, which often relates optical propagation through anisotropic media to magnetic systems. Further work exploiting spatially structured frozen-waves, could see Stokes vector fields with Skyrme numbers which change with propagation - analogous to temporal dynamics of spin systems in applied magnetic fields which vary spatially and temporally [272, 273]. Further investigation into the dynamic changes between skyrmion types observed in condensed matter systems may be more easily probed using the optical analogue. Furthermore, the generation of Skyrmions in other optical DOFs, such as the Poynting vector field, may be possible with specialized optics exhibiting tunable dielectric tensors.

3.5 Comments on the iterations of vectorial light generators

This chapter began using a generator based on an SLM and Mach-Zehnder type interferometer to create vectorial states of light. The high cost of the SLM makes this an undesirable option for widespread use. Additionally the Mach-Zehnder setup produced a large amount of instability due to the many optical elements comprising the arrangement, the consequence of this was fluctuations in the relative phase between the orthogonally polarized components which is undesirable. The next iteration utilized a PBS to separate orthogonally polarized components which were simultaneously shaped and interfered using a DMD. The lower cost of the DMD makes this a much more viable option for large scale implementation, along with the single element nature of using the DMD as the interferometer which improved stability drastically. One area of improvement which was highlighted throughout testing was the long distance between the PBS and the DMD which resulted in some residual phase fluctuations and beam wander. The third, and final, iteration replaced the PBS with a WP having a 1° separation angle. This allowed the imaging of the two orthogonally polarized beams onto the DMD screen by a $4f$ imaging system, this resulted in both beams passing through identical elements throughout the entire generation process leading to an extremely stable arrangement which is ideal for

many applications. The works discussed above which involved applications of the vectorial light generator for physical optics, metrology and optical analogy research, revealing how powerful the tool is in a variety of contexts. The independent applications also served as an evaluation procedure for various generator concepts leading to a clear path forward for the development of a commercially viable digital tool for versatile vectorial light generation. A further optimized design for the generator, which reduces the physical footprint of the device is discussed in Chapter 6.

Chapter 4

A versatile vectorial light analyser

This chapter is based on the papers:

Singh, K., Tabebordbar, N., Forbes, A., & Dudley, A. Digital Stokes polarimetry and its application to structured light: tutorial. JOSA A, 37(11), C33-C44. (2020).

Singh, K., & Dudley, A. Digital toolbox for vector field characterization. Nanophotonics, 11(4), 753-761. (2022).

Singh, K., Dudley, A., & Forbes, A. Versatile all-digital transport-of-intensity based wavefront sensor and adaptive optics using a DMD. Optics Express, 31(5), 8987-8997. (2023).

We will now discuss the development of a tool capable of analysing vectorial light fields. Firstly we will explore the ability of SLMs and DMDs to perform digital Stokes polarimetry measurements required to reconstruct the spatially varying polarization distributions characteristic of vectorial light fields. Then we discuss how a DMD based interferometric arrangement can be used to completely characterize arbitrary vectorial light fields, from the modal content of their constituent components to the relative phases and amplitudes of these components and even the degree of non-separability of their polarization and spatial DoFs. Finally we demonstrate how a DMD can be used as a high-resolution, versatile, broadband and polarization insensitive wavefront sensor enabled by the implementation of the transport-of-intensity equation. The chapter will conclude with some observations made about the analysis capabilities of the various arrangements and possible avenues for the development of commercially viable sensors for industry.

4.1 Digital Stokes polarimetry using SLMs and DMDs

4.1.1 Introduction

Understanding the SOP plays an important role in many areas, such as imaging, metrology, fiber-based communication, microscopy, radar and quantum optics [275, 276]. Therefore, its measurement and assessment are extremely important, resulting in a plethora of research dedicated to the topic. The most common theoretical approach to describe the SOP of light is based on the polarization ellipse [277, 278]. Although this approach allows one to describe various SOPs by a single equation, it has some drawbacks [279]. Firstly, it is not possible to physically observe, via any

measurement technique, the polarization ellipse, due to the fact that light's vector traces out an ellipse in an extremely short time period (of the order of 10^{-5} seconds). The second drawback is that this description is only applicable to completely polarized light. Therefore, the polarization ellipse is not an ideal means to describe light's SOP. In 1852, Sir George Gabriel Stokes solved this problem by demonstrating that one can describe the SOP of light with just four parameters, now known as the Stokes parameters as discussed in Chapter 2 [279, 280]. The realisation of these observables removed the need to measure the polarization ellipse and its associated limitations.

Since Stokes' formulation of these four parameters, many measurement techniques have been dedicated to their physical acquisition. The most commonly used techniques are based on measuring all six orthogonal polarized intensity profiles, namely I_H, I_V, I_D, I_A, I_R and I_L. Here, the subscripts for the intensities, I, denote: H - horizontal, V - vertical, D - diagonal, A - anti-diagonal, R - right-circular, and L - left-circular. For a more detailed discussion of these techniques (based on polarizers and phase retarders), the reader is directed to the following textbooks [64, 281–283]. The Stokes parameters have also been described in terms of the density matrix in order to formulate an analogy between photon polarization and elementary particles [284], as well as being applied to investigate light-matter interactions [285]. An easier, more frequently implemented approach consists of only measuring four intensity profiles, rather than the standard, over-complete set of six. This approach also makes use of the two previous mentioned optical components, namely a polarizer and a phase retarder. Here the angle of the polarizer and phase retarder are sequentially altered in order to extract the associated intensity profile [286]. Although these techniques have been around for many years, their simple arrangement and ease in experimental implementation means they are still popular in many optics laboratories.

Adaptations and improvements of these long-standing measurement techniques have included the implementation of wavefront [287] and amplitude division [288, 289], as well as the use of photopolarimeters [290, 291], to negate the need for sequential measurements. Automation approaches incorporating a monochromator and a single photon counting unit [292] have also been developed. Polarimetry techniques utilising liquid crystal polymer or sub-wavelength metasurfaces have also been shown to allow for simultaneous measurements, some of which (namely the division of focal plane polarization cameras) provide full polarimetry-imaging [47, 211, 293–295]. A real-time technique based on three-way polarization-preserving beam splitters has also been proposed [296].

Today there exists a modern, digital toolkit comprising of SLMs [48, 297, 298] and DMDs [50, 299, 300], which has fuelled the creation and detection of structured light [40, 301–304], particularly those with exotic polarization structures [39, 80, 81, 85, 305–313]. Naturally, measuring the polarization structure is just as important as creating it. Can one implement a digital toolkit for polarimetry? Yes, these digital devices have shown to be ideal tools in not only creating unique polarization structures, but also in performing Stokes polarimetry for the detection of structured polarization states. For example, SLMs have been used for an all-digital approach to polarization analysis and used to extract wavefronts [22], vector quality factors [66, 314], infer quantum states [315, 316], determine the motion of objects [317], with the benefit of efficient single shot analysis with no moving parts. More recently DMDs have been used for Stokes analysis [318, 319], concurrence determination [67, 320], wavefront analysis [54, 321], phase imaging [322], ushering in a faster, and cheaper alternative (in the order of a few hundred dollars), but at a lower efficiency [218].

Here, we provide the requirements for measuring the Stokes parameters via two real-time, digital approaches, one of which makes use of a SLM, while the other uses a DMD. These two digital methods are demonstrated on various vector vortex beams, which have shown growing interest in the area of structured light. As discussed in Chapter 2 these measured Stokes parameters can be used to determine various optical properties, such as the SOP visualised by the local polarization ellipses and as will be discussed in Chapter 5 to calculate the non-separability of vectorial fields.

4.1.2 Digital Stokes Polarimetry

To illustrate the concept of digital Stokes polarimetry techniques, we will construct analogies from the standard, conventional method. Here, the essential components of the two digital approaches are amplitude and phase modulating devices. The first of which is a SLM, which uses electrically controlled birefringence for optical phase modulation, while the second approach makes use of a DMD, consisting of an array of individually actuating micromirrors for amplitude modulation [323–326]. The main difference between the DMD and the SLM, which significantly affects their versatility, is the fact that DMDs are polarization invariant, while the majority of SLMs are not. In the case of the DMD, orthogonal polarization components are equally modulated by encoded holograms, diffracting the modulated beam into its associated first diffraction order. Whereas, SLMs exhibit diffraction inefficiency in one of the orthogonal polarization components (resulting in it remaining in the zeroth order) with only the complimentary component being diffracted into the first order [22]. We discuss the concept behind each approach in detail below.

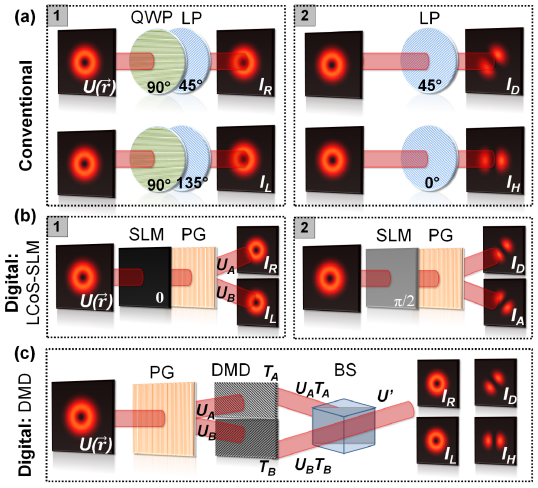


FIGURE 4.1: Conceptual schematics of (a) the conventional Stokes polarimetry measurements, together with the digital adaptations, implementing (b) a SLM and (c) a DMD. QWP, quarter-wave plate; LP, linear polarizer; SLM, liquid crystal on silicon spatial light modulator; PG, polarization grating; DMD, digital micromirror device; BS, 50:50 beam-splitter.

Just as the conventional Stokes polarimetry requires the projection of a beam of interest into the various polarization states, the digital approaches follow the same requirement. It is well-known that an optical field $U(\vec{r})$ can be decomposed into orthogonal polarization bases, such as $|H\rangle$ and $|V\rangle$, with the use of a PBS. However, a lesser-known optic that is capable of mapping the right- and left-circular polarization basis ($|R\rangle$ and $|L\rangle$) to independent optical paths (let's call these paths, A and B), is a polarization dependent diffraction grating (PG) [150, 327–329]. One should

note that when using a PG, the input field may have a spatially inhomogeneous or homogeneous polarization structure (i.e., a vector or scalar beam, respectively) but the components in the polarization basis will always be scalar [39]. We will use a PG for the experimental demonstrations in this thesis but we stress that a PBS (or other polarization sensitive components) for the linear states would work just as well.

First, the incident field is split into two fields $U_A(\vec{r})$ and $U_B(\vec{r})$ representing the orthogonally polarized components, $|R\rangle$ and $|L\rangle$, as illustrated in Fig. 4.1.b-1, and mathematically described as

$$\begin{aligned} U(\vec{r}) = U_A(\vec{r})|R\rangle + U_B(\vec{r})|L\rangle \rightarrow \\ \textbf{PG} \rightarrow |U_A(\vec{r})|e^{i\delta_A}|R\rangle \ \textbf{\&} \ |U_B(\vec{r})|e^{i\delta_B}|L\rangle\,, \end{aligned} \tag{4.1}$$

where each component has its own intrinsic phase $\delta_{A/B}$. It should be noted that these phases could vary in the transverse plane and the spatial dependence (i.e., $\delta_{A/B}(\vec{r})$) has been omitted. From a mere comparison, the action of the PG allows for the replacement of the QWP and the polarizer in the manual, conventional approach [Fig. 4.1.a-1] for the acquisition of both I_R and I_L in one single measurement [Fig. 4.1.b-1].

Next, to measure two additional intensity profiles for this particular digital method, namely I_D and I_A, usually a QWP with its fast-axis set at 45° would need to be introduced before the PG to project I_D and I_A into the two detectable paths: A (I_R) and B (I_L), respectively. However, since we know that a QWP induces a quarter-wavelength phase shift on an incident beam, converting linearly polarized light to circular and visa versa, we can achieve this digitally by merely encoding the SLM with an additional $\pi/2$ phase term, as illustrated in Fig. 4.1.b-2. The advantage with this technique [22] is that the optics (namely, PG and SLM) remain static, while only a phase-change (affecting only the incident vertical component) is encoded on the SLM, to mimic the transformation of the QWP [Fig. 4.1.b-2].

In implementing this technique, we would like to point out to the reader that the intensity profiles that can be extracted, only allow for the reconstruction of three of the four Stokes parameters (namely, S_0, S_2 and S_3). Since the SLM is polarization-sensitive, acquisition of one of the two remaining polarization states necessary for the reconstruction of the Stokes parameter, S_1, (namely, I_H) for this conceptual configuration is not possible. Even though this approach does not offer reconstruction of all four Stokes parameters, it is still possible to investigate interesting optical properties from only two of the Stokes parameters (namely, S_2 and S_3) such as the phase difference between horizontaly and vectically polarized components.

For the second digital approach [319] we make use of the previously discussed PG together with a DMD. Here the intensity profiles, I_R and I_L, are again mapped to independent paths A and B, respectively with the implementation of the PG [Fig. 4.1.c]. Each path is directed to one half of a DMD screen, which can be independently encoded with a binary amplitude and phase modulating hologram (labeled as H_A and H_B) according to the following functions discussed in Chapter 2

$$\begin{aligned} H_A(\vec{r}) = \frac{1}{2} + \frac{1}{2}\text{sign}(\cos\big(2\pi(g_x x + g_y y) + 2\pi\Phi_A(\vec{r})\big) \\ - \cos(\pi A_A(\vec{r}))\,, \end{aligned} \tag{4.2}$$

$$\begin{aligned} H_B(\vec{r}) = \frac{1}{2} + \frac{1}{2}\text{sign}(\cos\big(2\pi(g_x x + g_y y) + 2\pi\Phi_B(\vec{r})\big) \\ - \cos(\pi A_B(\vec{r}))\,. \end{aligned} \tag{4.3}$$

Here g_x and g_y are the directional spatial carrier (grating) frequencies, while $\Phi_{A/B}(\vec{r}) = \frac{\arg(T_{A/B}(\vec{r}))}{2\pi}$ and $A_{A/B}(\vec{r}) = \frac{\sin^{-1}(abs(T_{A/B}(\vec{r})))}{\pi}$ are the respective phase and amplitude modulation terms, with $T_{A/B}(\vec{r})$ being the transmission function intended for the modulation of each path. For simple spatially constant (i.e., $\forall\ \vec{r}$) phase modulation, the transmission functions required can be represented as

$$T_A = e^{ic_A} \quad \text{and} \quad T_B = e^{ic_B}\,, \tag{4.4}$$

where $c_{A/B}$ are merely independent constants. The first diffraction order of each path reflected off of the DMD, due to the encoded diffraction grating, carries the desired modulation given by $U_{A/B}T_{A/B}$. The modulated paths are combined by coupling them into orthogonal ports of a BS, after which the necessary intensity profiles are acquired.

The field, $U'(\vec{r})$, after the BS, now represents a superposition of the independently modulated orthogonally polarized components of the initial field $U(\vec{r})$

$$U'(\vec{r}) = U'_A(\vec{r}) + U'_B(\vec{r}) = U_A(\vec{r})e^{i\varphi_A}T_A + U_B(\vec{r})e^{i\varphi_B}T_B\,, \tag{4.5}$$

where $\varphi_{A/B}$ are the phases which will be incurred by each independent path, propagating through the respective optical components.

With this digital approach, it is easy to see how the I_R and I_L measurements can be obtained naturally from the PG by allowing $T_{A/B} = 0$ (the DMD is in the off-state) and $T_{B/A} = e^{ic_{B/A}}$, where $U' = U_{B/A}e^{i\varphi_{B/A}}e^{ic_{B/A}}$ (i.e., either only the $|L\rangle/|R\rangle$ component with some spatially constant phase). In order to acquire the I_H measurement, one can make use of the following relationship, $|H\rangle = \frac{1}{\sqrt{2}}(|R\rangle + |L\rangle)$, which implies that a phase difference of $\Delta\varphi = \varphi_A - \varphi_B = 0$ is required. Subsequently, from the following relationship, $|D\rangle = |R\rangle + e^{i\frac{\pi}{2}}|L\rangle$, an addition of $\frac{\pi}{2}$ to one of the constants, $c_{A/B}$, will allow for the measurement of I_D. These phase modulation steps can be achieved by simply adjusting the hologram transmission functions $T_{A/B}$, which are substituted into the holograms $H_{A/B}$ through $A_{A/B}$ and $\Phi_{A/B}$.

To summarize, the entire procedure can be compactly described via the Jones matrix representation of the transformations associated with each optical element (under the assumption $\varphi_A = \varphi_B = 0$), given by

$$\begin{aligned}
&\underbrace{\frac{1}{\sqrt{2}}\begin{pmatrix}1 & 1\\ 1 & -1\end{pmatrix}}_{\text{BS Matrix}}\underbrace{\begin{pmatrix}Ae^{ic_A} & 0\\ 0 & Be^{ic_B}\end{pmatrix}}_{\text{DMD Matrix}}\underbrace{\frac{1}{\sqrt{2}}\begin{pmatrix}U_A\\ U_B\end{pmatrix}}_{\text{Input Field}} =\\
&\underbrace{\frac{1}{2}\begin{pmatrix}Ae^{ic_A} & Be^{ic_B}\\ Ae^{ic_A} & -Be^{ic_B}\end{pmatrix}}_{\text{Jones Matrix of System}}\begin{pmatrix}U_A\\ U_B\end{pmatrix} = \underbrace{\begin{pmatrix}\frac{1}{2}(Ae^{ic_A}U_A + Be^{ic_B}U_B)\\ \frac{1}{2}(Ae^{ic_A}U_A - Be^{ic_B}U_B)\end{pmatrix}}_{\text{BS Outputs}}.
\end{aligned} \tag{4.6}$$

Here $A, B \in \{0, 1\}$ and must be set according to Table 4.1 below, which describes the system transformations that the reader will need to use in order to acquire the four intensity measurements. The reader must also take note that only one of the BS outputs needs to be monitored. We recommend monitoring the $BS^{out}_{1,1}$ matrix element, as this corresponds to the $|H\rangle$ component as shown by Eq. (4.5), while $BS^{out}_{2,1}$ corresponds to $i|V\rangle$.

Having described the underlying principles of the two digital measurement techniques, we will now outline their respective experimental setups, highlighting any nuances and issues to be considered when implementing these techniques in the lab.

TABLE 4.1: Table showing the Jones matrix parameters imparted by the DMD in order to acquire Stokes intensity measurements.

Intensity Measurement	A	B	c_A	c_B
I_R	0	1	0	0
I_L	1	0	0	0
I_H	1	1	0	0
I_D	1	1	0	$\frac{\pi}{2}$

4.1.3 Experimental Realisations and Results

For completeness, we will start with and consider the experimental realisation of the standard, conventional Stokes polarimetry method, depicted in Fig. 4.2.a. To demonstrate the approach we apply it to a radially polarized beam, which we must first generate. To do so we used a $\lambda = 633$ nm HeNe laser, producing a horizontally polarized Gaussian beam, and passed it through a half-wave plate (HWP - with its fast axis orientated at 45° to convert the incident polarization to vertical), and a q-plate [41] ($q = 1/2$ - which imparts an azimuthally varying phase of $e^{il\phi}$ via an anisotropic medium, with $\ell = 1$) in order to generate a radially polarized (TE) vector vortex beam, represented by

$$TE(\vec{r}) = LG_0^1(\vec{r})|R\rangle + LG_0^{-1}(\vec{r})|L\rangle\,. \tag{4.7}$$

Here $LG_p^l(\vec{r})$ takes the form discussed in Chapter 2. It is notable that in order to ensure the generation of a TE beam, the input linear polarization should be in the plane of the q-plate's global fast axis. There is an intrinsic $\delta = \delta_A - \delta_B = \{0, \pi\}$ phase difference between the orthogonally polarized components. A QWP and polarizer were orientated at various angles [as outlined in Figs. 4.1.a-1 and a-2] to acquire the four intensity measurements [which were imaged on a Spiricon charged coupled device (CCD)], used to obtain the Stokes parameters.

In reproducing this experiment in the lab, the reader should expect to capture intensity profiles similar to those depicted in Fig. 4.3, together with their corresponding Stokes parameters. Here, simulated predictions of the four intensity profiles with their corresponding Stokes parameters are given as inserts, to help aid the reader with what to expect.

The experimental procedure for digitally extracting Stokes parameters with the use of a SLM is outlined in Fig. 4.2.b. Here, a HeNe laser was expanded and collimated to illuminate the screen of a reflective SLM (Pluto Holoeye, 1920×1080 pixels, 8 μm pixel pitch, $60\% - 80\%$ diffraction efficiency) preceded by a polarizer to generate linear polarization [namely, diagonal (45°)]. For this particular case we chose the screen of the SLM to be encoded with a phase-only azimuthal hologram [insert in Fig. 4.2.b]. The SLM only diffracts the vertically polarized component into the off-axis, diffraction orders which possess the encoded phase profile. While the horizontal component remains unaffected in the on-axis, undiffracted (zero) order. We exploited this polarization-variant property to generate the following structured field, consisting of two orthogonal components

$$\begin{aligned} \mathbf{U}_{\leftrightarrow}(r,\phi) &= \exp\left(-r^2/\omega_0\right) \text{ and} \\ \mathbf{U}_{\updownarrow}(r,\phi) &= \exp\left(-r^2/\omega_0\right)\exp\left(i\delta(r,\phi)\right). \end{aligned} \tag{4.8}$$

Here each component consists of a common Gaussian field, while the vertical component has an additional phase term of $\exp(i\delta(r,\phi))$, which for this particular case

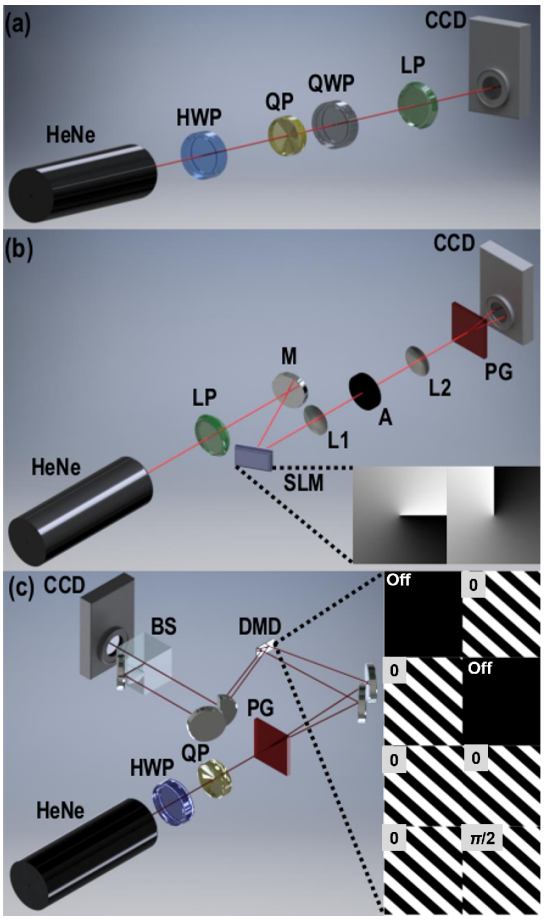


FIGURE 4.2: Experimental diagrams illustrating the arrangement of the optical components used to acquire Stokes parameters for (a) conventional Stokes polarimetry and the digital approaches, implementing (b) a SLM and (c) a DMD. The representative holograms encoded onto the SLM and DMD screens are provided as inserts. HeNe, Helium Neon laser; QP, q-plate; M, mirror.

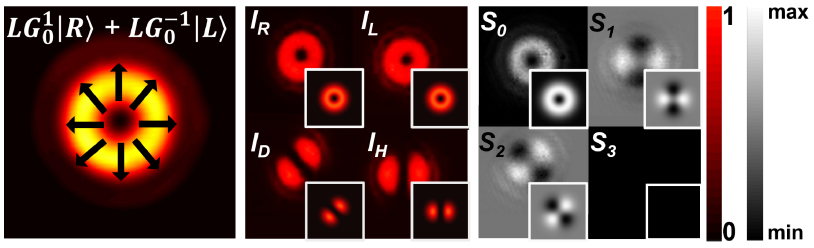


FIGURE 4.3: Conventional Stokes polarimetry. Left: the generated field of interest, on which the Stokes polarimetry is performed [in this case described by Eq. (4.7)]. Middle: measured intensity profiles of the Stokes projections. Right: the corresponding calculated Stokes parameters (min=0 and max=1 for S_0, S_3, while min=-1 and max=1 for S_1, S_2). Theoretical simulations are given as inserts.

is: $\exp(i\ell\phi)$, where $\ell = 1$. The generated field (denoted in the first block of Fig. 4.4) was imaged from the plane of the SLM screen to the CCD camera (preceded by a PG) where the various intensity profiles were recorded. The hologram required to create our beam of interest [first insert in Fig. 4.2.b] was encoded onto the SLM, followed by the same hologram encoded with an additional $\pi/2$ phase term [producing the second insert in Fig. 4.2.b].

For each of the two holograms, the corresponding intensity profiles (I_D, I_A and I_R, I_L) (middle block of Fig. 4.4) were captured, respectively. Their corresponding Stokes parameters (S_0, S_2 and S_3) were determined and are presented in the right-most block of Fig. 4.4. Here, we would like to point out to the reader that since the SLM is polarization dependant, it will not be possible (with the current presented configuration) to perform a phase dependant transformation in order to extract the horizontal and vertical intensity profiles, (I_H and I_V) needed for the calculation of the Stokes parameter, S_1. However, simulated predictions of the four intensity profiles together with their corresponding Stokes parameters are given as inserts, so that the reader can verify their measurements on this particular field [described by a superposition of the two equations in Eq. (4.8)] if they so acquire the Stokes measurements via another method.

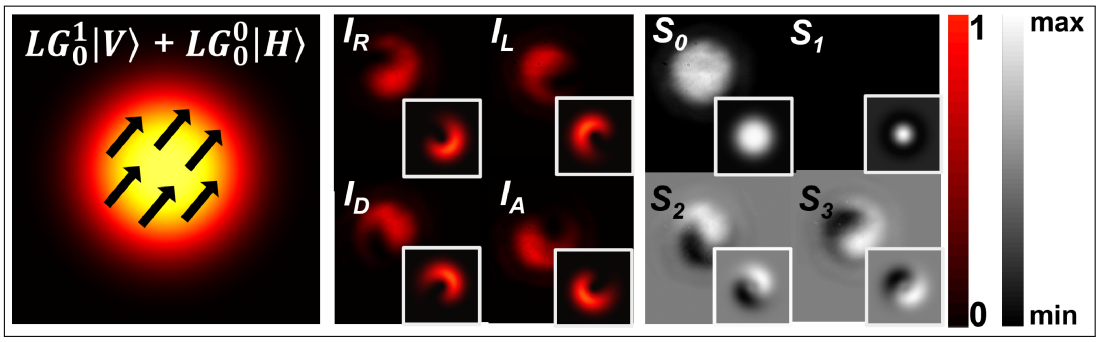


FIGURE 4.4: Digital SLM Stokes polarimetry. Left: the generated field of interest, on which the Stokes polarimetry is performed [in this case described by a superposition of the two equations in Eq. (4.8)]. Middle: measured intensity profiles of the Stokes projections. Right: the corresponding calculated Stokes parameters (min=0 and max=1 for S_0, S_1, while min=-1 and max=1 for S_2, S_3). Theoretical simulations are given as inserts.

The experimental procedure for obtaining the four Stokes intensity measurements, via the digital DMD approach [depicted in Fig. 4.2.c], was conducted on a radially polarized vector vortex beam, as described in Eq. 4.7 and generated in the same manner as that described for the conventional case [Fig. 4.2.a]. The vector beam was propagated through a PG which mapped the $|L\rangle$ and $|R\rangle$ components to two independent paths A and B, respectively. The two paths were then directed to their associated halves of the DMD screen (TI-DLP650NE), which were addressed separately to facilitate the independent modulation of the left- and right-circularly polarized components. Ideally, DMDs have an inherent diffraction efficiency of 60%, additional details regarding their diffraction efficiencies can be found in Ref. [50] At the DMD screen, binary holographic gratings, generated using the technique presented by *Lee* [330] [Eqns. (4.2) and (4.3)], were displayed. An expanded representation of the holograms encoded onto the DMD screen are provided as inserts in Fig. 4.2.c. The gratings used were generated in order to effect a constant (in the transverse plane) phase modulation. By encoding the grating on either DMD half A/B and encoding zeros (off-states) in the other, the right and left components were independently imaged by the CCD [shown by the top two holograms in Fig. 4.2.c].

By encoding gratings onto both halves and adjusting the constant phase modulation of each half independently, relative phases of $\delta = \{0, \frac{\pi}{2}\}$ were induced into the interfering beams, resulting in the imaging of the horizontal and diagonal components by the CCD [as shown by the bottom two holograms in Fig. 4.2.c]. The first diffraction orders (which carry the desired modulation) from each half of the DMD were isolated (from the zeroth and higher diffraction orders) with the use of an aperture and coupled into orthogonal ports of a 50:50 BS, through which the paths were interfered. The resulting beam (from one of the BS output ports) was then imaged by a CCD camera. One important aspect that the reader needs to consider when implementing this in the lab, is that the paths exiting the BS must be completely co-propagating. The resulting interference pattern - as captured by the CCD - for misaligned beam paths will be characterized by fringes (vertical for x-misalignment and horizontal for y-misalignment). The reader will notice that as good alignment is approached, the spatial frequency of the fringes will decrease until the lobes (for the example case presented) are visible. For the benefit of the reader, this procedure is simulated in Fig. 4.5.

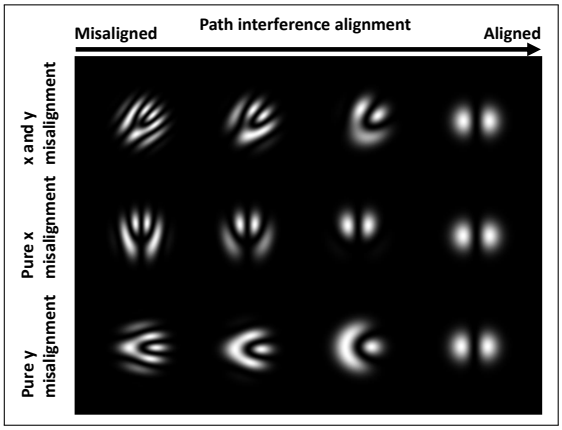


FIGURE 4.5: Diagram depicting the alignment of orthogonally polarized components through a 50:50 BS. As the misalignment in the beam paths improves (left to right), so the number of fringes decreases.

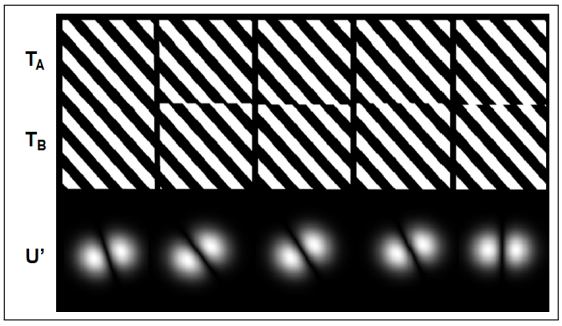


FIGURE 4.6: Diagram showing the independent phase modulation of orthogonal polarization components (top two rows for DMD holograms, H_A and H_B) and simulated interference of the components through a 50:50 BS (bottom row).

Another important aspect to consider is that, practically in constructing this experiment, one cannot guarantee equal path lengths of the orthogonally polarized components to within the wavelength of visible light. The path length discrepancy will manifest as some non-zero phase difference between the orthogonally polarized components $\Delta\varphi \neq 0$. This can be compensated for by encoding the transmission

functions $T_{A/B} = e^{ic_{A/B}}$ onto both of the relevant sides of the DMD, where one of the constants is held fixed (e.g. $c_A = 0$) and the other is varied until the image captured by the CCD correlates well with a theoretically predicted I_H. For the benefit of the reader, a simulated example of this procedure is shown in Fig. 4.6 where orthogonal components $U_A = LG_0^1$ and $U_B = LG_0^{-1}$ are interfered with $\Delta\varphi = \frac{\pi}{2}$; $c_A = 0$ is held fixed while $c_B = \{0, \frac{\pi}{8}, \frac{\pi}{6}, \frac{\pi}{4}, \frac{\pi}{2}\}$ is varied. Expanded images of the holographic gratings as well as the behaviour of the intensity patterns illustrates how the final grating with $c_B = \frac{\pi}{2}$ compensates for the phase difference $\Delta\varphi$ and results in the expected I_H intensity pattern for the given components.

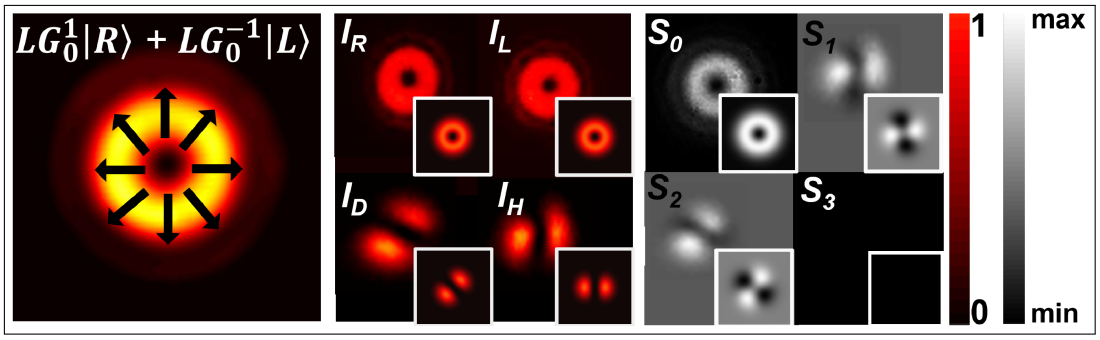


FIGURE 4.7: Digital DMD Stokes polarimetry. Left: the generated field of interest, on which the Stokes polarimetry is performed [in this case described by Eq. (4.7)]. Middle: measured intensity profiles of the Stokes projections. Right: the corresponding calculated Stokes parameters (min=0 and max=1 for S_0, S_3, while min=-1 and max=1 for S_1, S_2). Theoretical simulations are given as inserts.

Reproducing this digital measurement, the reader should obtain intensity profiles I_R, I_L, I_H and I_D, as well as the Stokes parameters, similar to those depicted in Fig. 4.7. Simulated predictions are given as inserts, to help aid the reader with what to expect.

We would like to highlight to the reader that if a vector vortex beam propagates by some non-negligible factor of the Rayliegh length z_R (which is the distance over which the beam remains well collimated), there will be some curvature observed in the intensity lobes of the I_H and I_D components. This curvature (or 'spiralling' of the lobes) will manifest in the Stokes parameters, S_1 and S_2, as illustrated with exemplar results obtained using the digital DMD method in Fig. 4.8. This presents us with a possible improvement on the measurement device in the form of the requirement of a $4f$ imaging system in order to image the desired measurement plane onto the DMD screen directly. Another notable feature is that the S_3 parameter was approximated to zero, discrepancies in this parameter may arise from the modulated components reaching the BS with different spot sizes, indicating another possible improvement in the form of an appropriate imaging system between the DMD and the BS. The latter improvement would be of large consequence to calculating the handedness of circular polarization.

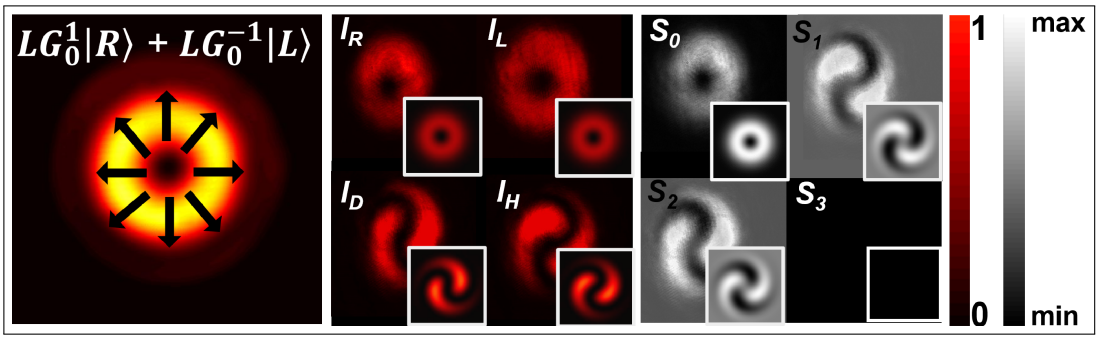


FIGURE 4.8: Digital DMD Stokes polarimetry with curvature. Left: the generated field of interest, on which the Stokes polarimetry is performed [in this case described by Eq. (4.7)]. Middle: measured intensity profiles of the Stokes projections. Right: the corresponding calculated Stokes parameters (min=0 and max=1 for S_0, S_3, while min=-1 and max=1 for S_1, S_2). Theoretical simulations are given as inserts. Note the spiral lobes in I_D, I_H, S_1 and S_2. One can also note that the central vortex is slightly off-centered due to slight misalignment of the q-plate vortex with the input beam's center.

4.2 Completely characterizing vector fields using a DMD based analyser

4.2.1 Introduction

As mentioned in Chapter 1 the field of structured light focuses on the tailoring of light's DoFs to probe fundamental features of nature as well as to extend the industrial optics toolbox [11, 39, 40]. Prior to the last two decades, disproportionate focus has been given to structuring the intensity and phase DoFs. Recent interest in the tailoring of light's polarization has lead to observations of interesting topological [85, 305] and energy transport [151, 331] behaviour - which, in some cases, prove useful for communication [332], metrology [333], microscopy [334] and even laser machining [335]. The increased interest in these structured polarization fields (referred to as vector fields [336]), has unsurprisingly coincided with the development of tools allowing for their convenient generation. These tools take the form of dynamic and geometric phase elements such as nano-structured metasurfaces [337, 338] and liquid crystal q-plates [42]; as well as versatile digital devices such as SLMs [339] and DMDs [165]. Techniques used to characterize these vector fields include Stokes polarimetry measurements capable of recovering the total spatially varying polarization structure. Stokes measurements also have the ability to recover the concurrence based non-separability of the spatial and polarization DoFs, or vector quality factor (VQF) [67]. Of additional importance to characterizing quantum channels using vector fields, is a basis dependent non-separability measurement (VQF') acquired through polarization projections in conjunction with spatial mode projections [66, 340]. Naturally, the efficient characterization of vector fields needs to grow in conjunction with their increasing popularity. The basis dependent characterizations have been carried out using arrangements including PGs, mode sorters and q-plates, which - while effective - only permit the measurements in a limited subset of spatial mode bases [341, 342]. Recently a more versatile and efficient approach to the basis dependent measurement was proposed, where the polarization independence of a DMD was exploited - however, this technique requires a set of parallel polarization optics, making the arrangement complex [320]. Only recently have a few publications been dedicated to full Poincaré polarimetry [343, 344] and the adaptive control

of vectorial fields via polarization and phase correction [345, 346]. Universal polarization mapping has been demonstrated with the use of a GRIN lens [343, 344] to map the polarization analyser states to vectorial fields with very high-precision and single acquisition measurements. However, this requires custom made optics (in the form of a specially designed GRIN lens), restricting the versatility of the measurement device.

We have previously demonstrated digital Stokes measurements, which provides general information about polarization homogeneity/inhomogeneity, but no modal information [106]. In this work we present a system, based on a DMD capable of performing sequential and simultaneous spatial and polarization measurements on arbitrary vector fields, permitting their full characterization in a rapid, compact and completely automated manner. Our scheme exploits the small separation angle afforded by a 1° WP, the polarization independence of DMDs and polarization interference phenomena to achieve its functionality. The ability to simultaneously project into the spatial and polarization DoFs allows us to extract the global relative phase and amplitude between the constituent orthogonally polarized components, while exclusive spatial mode and polarization projections lead to reconstructions of the scalar fields and resulting polarization structure. Previously demonstrated methods which have been used to acquire polarization and phase information have been reliant on interference with reference plane waves leading to cumbersome optical systems [347, 348], while other techniques use light with polarization known *a priori* to probe anisotropic systems [349]. Our system provides a versatile, fast and compact solution to full field characterization without any prior information or reference. We demonstrate the effectiveness of our approach on a variety of vector beams including beams with large OAM, fractional OAM and beams with non-zero radial orders. Our scheme serves as a versatile automated detection solution to complement the growing utilisation of vector fields in research and industrial settings.

4.2.2 Concept

To represent our vector field, we will adopt the convenient quantum mechanical notation [39]

$$|\Psi\rangle = \cos\left(\frac{\alpha}{2}\right) e^{i\beta/2}|\psi_1\rangle|R\rangle + \sin\left(\frac{\alpha}{2}\right) e^{-i\beta/2}|\psi_2\rangle|L\rangle. \tag{4.9}$$

Here $|\psi_i\rangle$ represent arbitrary, un-normalized spatial modes, while $|R, L\rangle$ represent the respective right- and left-circular polarization Jones matrices (these can be any two orthogonal Jones matrices - $|R, L\rangle$ are chosen without loss of generality). The parameters $\alpha \in [0, \pi]$ and $\beta \in [-\pi, \pi]$ represent the relative amplitudes and phases of the orthogonally polarized components. This state can be represented by a vector lying on the surface of the HOPS [69], as discussed in Chapter 2. A HOPS is constructed with the scalar (i.e., $\alpha = 0, \pi$) states on the poles and vector (i.e., $\alpha = \pi/2$) states lying on the equator. The vector of a given field lying on the HOPS is specified by the same parameters α and β which are the respective polar and azimuthal coordinates. An example of a HOPS and two states lying on its surface are shown in Fig. 4.9 A (note that the tensor product operator $\otimes$ has been suppressed in the text for brevity). The ellipses overlaying the "non-scalar" fields represent the local SOP across the transverse plane - where green ellipses are used to represent approximately linear polarization and red(blue) to represent right-(left-) circular handedness. From Eqn 4.9 and Fig. 4.9 A we can see that, in order to completely specify

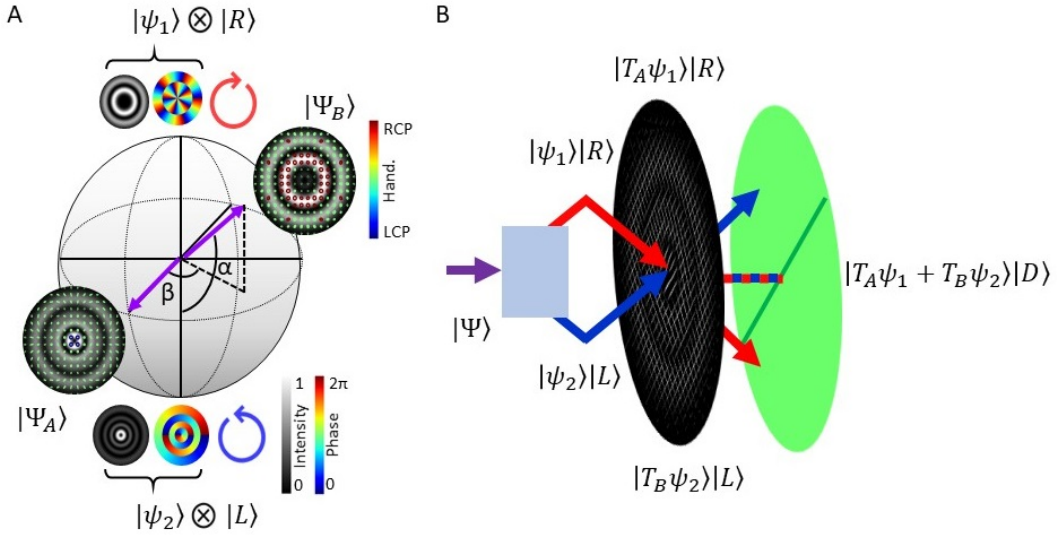


FIGURE 4.9: A) HOPS with $|\psi_{1(2)}\rangle = LG^{5(-1)}_{1(3)}$, the SOP of two example states on the sphere are included as insets - as well as the intensity and phase of the polar spatial modes and their associated circular polarization handedness. B) Schematic showing the separation of orthogonally polarized components from a vector state $|\Psi\rangle$, by a Wollaston prism, followed by a complex amplitude hologram and their projection into the same diagonal plane using a linear polarizer.

the state of a vector field, we need to know the spatial modes $|\psi_{1,2}\rangle$ as well as the parameters α and β. In order to determine $|\psi_{1,2}\rangle$, we can independently compute their inner products with the modes of a complete orthogonal basis (e.g., LG^l_p basis), according to:

$$c^l_p = \langle LG^l_p|\psi_{1,2}\rangle\,. \tag{4.10}$$

If $c^l_p \neq 0$ for more than one LG^l_p mode, then the relative phases ϕ^l_p between these modes and a reference mode $LG^{l_{ref}}_{p_{ref}}$ (with $c^{l_{ref}}_{p_{ref}} \neq 0$) can be acquired by executing their unbiased inner products

$$d^l_p = \langle LG^l_p + LG^{l_{ref}}_{p_{ref}}|\psi_{1,2}\rangle \tag{4.11}$$

$$e^l_p = \langle LG^l_p + iLG^{l_{ref}}_{p_{ref}}|\psi_{1,2}\rangle, \tag{4.12}$$

and then computing

$$\phi^l_p = \arctan\left(\frac{2|e^l_p|^2 - |c^{l_{ref}}_{p_{ref}}|^2 - |c^l_p|^2}{2|d^l_p|^2 - |c^{l_{ref}}_{p_{ref}}|^2 - |c^l_p|^2}\right). \tag{4.13}$$

We can then reconstruct $|\psi_{1,2}\rangle$ according to

$$|\psi_{1,2}\rangle = \sum_{l,p} c^l_p e^{i\phi^l_p} LG^l_p. \tag{4.14}$$

This procedure is known as modal decomposition [350].

With $|\psi_{1(2)}\rangle$ specified, we can now determine α and β. To begin, let us consider taking inner products of $|\Psi\rangle$ with $|\psi_{1(2)}\rangle|D\rangle$ individually (i.e., we project into the

spatial mode and polarization DoF simultaneously) - where we denote the intensities of these projections as $I_{1(2)}$

$$I_1 = |\langle\psi_1|\langle D|\Psi\rangle|^2 = \frac{1}{2}\cos^2\left(\frac{\alpha}{2}\right) \tag{4.15}$$

$$I_2 = |\langle\psi_2|\langle D|\Psi\rangle|^2 = \frac{1}{2}\sin^2\left(\frac{\alpha}{2}\right). \tag{4.16}$$

Next we can consider taking inner products with respect to superpositions of spatial modes $|\psi_{1(2)}\rangle$

$$I_{3(4)} = |\langle\psi_1 \pm \psi_2|\langle D|\Psi\rangle|^2 = \frac{1}{2} \pm \sin(\alpha)\cos(\beta) \tag{4.17}$$

$$I_{5(6)} = |\langle\psi_1 \pm i\psi_2|\langle D|\Psi\rangle|^2 = \frac{1}{2} \pm \sin(\alpha)\sin(\beta). \tag{4.18}$$

Using these six intensity measurements I_i, we can construct the Cartesian coordinates Σ_i of the state vector $|\Psi\rangle$

$$\Sigma_1 = I_3 - I_4 = 2\sin(\alpha)\cos(\beta) \tag{4.19}$$

$$\Sigma_2 = I_5 - I_6 = 2\sin(\alpha)\sin(\beta) \tag{4.20}$$

$$\Sigma_3 = I_1 - I_2 = \cos(\alpha). \tag{4.21}$$

Therefore we can extract α and β as

$$\alpha = \arctan\left(\frac{\Sigma_3}{\sqrt{\Sigma_1^2 + \Sigma_2^2}}\right) \tag{4.22}$$

$$\beta = \arctan\left(\frac{\Sigma_1}{\Sigma_2}\right). \tag{4.23}$$

The projection into the $|D\rangle$ polarization allows for the exploitation of the third Arago-Fresnel law which states "Orthogonally polarized light derived from polarized light, when brought into the same plane of polarization, will interfere" [351]. From Eqns. 4.22 and 4.23 we can see how only six intensity measurements are required to extract global parameters α and β. Additionally by simply replacing the spatial mode projections with identity projections, we recover spatially varying Stokes intensity measurements.

4.2.3 Experimental procedure

In order to test our detection scheme on a variety of vector beams we implemented a generation process which used the arrangement shown in (the left of) Fig. 4.10 [165]. A Gaussian beam from HeNe laser (wavelength 633 nm) was expanded and collimated using lenses EL and CL respectively - such that the central region approximated a constant intensity plane wave. A HWP was used to change the plane of polarization to diagonal. The expanded beam was passed through a WP (splitting the horizontally and vertically polarized components at an angle of $\approx 1^\circ$). A $4f$ imaging system was used to image the plane at the WP on to the screen of a

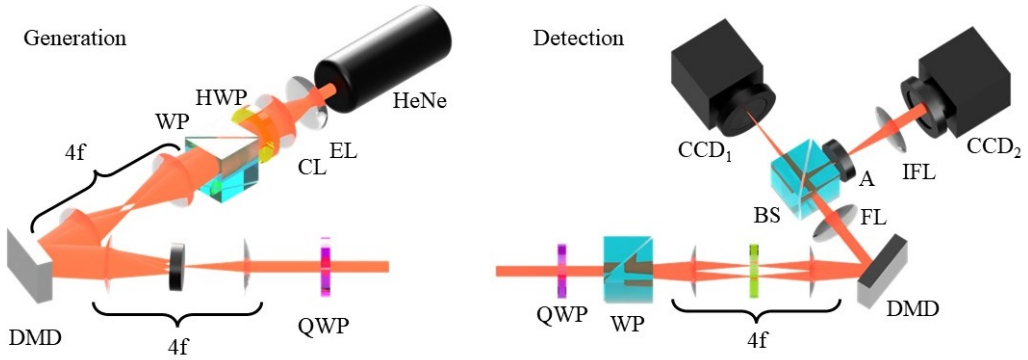


FIGURE 4.10: (Left) Diagram showing the arrangement used to generate arbitrary vector beams using a Wollaston prism to separate orthogonal circular polarizations and a DMD to recombine these - post modulation. (Right) Diagram showing the arrangement used to characterize arbitrary vector fields making use of a Wollaston prism to separate and a DMD to recombine orthogonal polarization components, with a linear polarizer to allow for interference of orthogonally polarized components. Abbreviations: HeNe - helium neon laser, EL - expansion lens, CL - collimation lens, HWP - half-wave plate, WP - Wollaston prism, BS - beam splitter, LP - linear polarizer, DMD - digital micro-mirror device, FL - Fourier lens, IFL - inverse Fourier lens, CCD - charge coupled device.

DMD (TI-DLP6500). The DMD was encoded with multiplexed binary amplitude holograms of the form discussed in Chapter 2

$$H_{A(B)} = \frac{1}{2} + \frac{1}{2}\text{sign}(\cos\Big(2\pi G_{A(B)}(\mathbf{r}) + 2\pi\Phi_{A(B)}(\mathbf{r})\Big) - \cos\Big(\pi A_{A(B)}(\mathbf{r})\Big)), \quad (4.24)$$

here $G_{A(B)}(\mathbf{r}) = g^x_{A(B)}x + g^y_{A(B)}y$ are gratings with spatial carrier frequencies $g^{x,y}_{A(B)}$. The 0^{th} diffraction orders of the two orthogonally polarized beams leaving the DMD do so at the 1° separation angle, therefore it is possible to pick $g^{x,y}_{A(B)}$ such that the 1^{st} diffraction orders of each polarization component modulated by either H_A or H_B perfectly overlap [165]. $\Phi_{A(B)}(\mathbf{r}) = \arg(T_{A(B)}(\mathbf{r}))/2\pi$ and $A_{A(B)}(\mathbf{r}) = \arcsin\Big(|T_{A(B)}(\mathbf{r})|\Big)/\pi$ are normalized phase and amplitude modulations of any desired complex transmission function $T_{A(B)}(\mathbf{r})$. A $4f$ imaging system was used to image the beam produced by the generation DMD into the detection setup (with an aperture at the focal plane to spatially filter the desired combined 1^{st} diffraction order and a QWP to convert horizontal and vertical linear polarization to left- and right-circular respectively). Compensating aberration correction and holographic scaling (following beam shaping best practice [50]) was a applied to this beam prior to passing it through the detection system. This technique allowed for the generation of high quality arbitrary vector fields (e.g. by setting $T_{A(B)} = LG^{5(-1)}_{1(3)}$ we can generate the vector field shown in in Fig. 4.9).

The core device - the detection system (shown on the right of Fig. 4.10), was arranged with a QWP placed before a WP positioned at the plane of interest, which - together - separated the right- and left-circularly polarized components of the input field at an angle of 1°. A $4f$ imaging system was used to image this plane onto the screen of a DMD (TI-DLP4710). A diagonally orientated LP was placed within the $4f$ system in order to acquire projections of orthogonal polarizations in the same plane. The detection DMD was also addressed with multiplexed complex amplitude holograms of the form in Eqn 4.24. The Fourier instensity of the modulated combined

$\mathbf{T_A}$	$\mathbf{T_B}$	CCD	Component	Measurement
$(\mathbf{LG_p^l})^*$	0	1	$\|\psi_1\rangle$	$\mathbf{c_p^l}$
0	$(\mathbf{LG_p^l})^*$	1	$\|\psi_2\rangle$	$\mathbf{c_p^l}$
$(\mathbf{LG_p^l} + \mathbf{LG_{p_{ref}}^{l_{ref}}})^*$	0	1	$\|\psi_1\rangle$	$\mathbf{d_p^l}$
0	$(\mathbf{LG_p^l} + \mathbf{LG_{p_{ref}}^{l_{ref}}})^*$	1	$\|\psi_2\rangle$	$\mathbf{d_p^l}$
$(\mathbf{LG_p^l} + \mathbf{iLG_{p_{ref}}^{l_{ref}}})^*$	0	1	$\|\psi_1\rangle$	$\mathbf{e_p^l}$
0	$(\mathbf{LG_p^l} + \mathbf{iLG_{p_{ref}}^{l_{ref}}})^*$	1	$\|\psi_2\rangle$	$\mathbf{e_p^l}$
$(\|\psi_1\rangle)^*$	0	1	$\|\psi_1\rangle$	$\mathbf{I_1}$
0	$(\|\psi_2\rangle)^*$	1	$\|\psi_2\rangle$	$\mathbf{I_2}$
$(\|\psi_1\rangle)^*$	$(\|\psi_2\rangle)^*$	1	$\|\psi_1\rangle$ & $\|\psi_2\rangle$	$\mathbf{I_3}$
$(\|\psi_1\rangle)^*$	$e^{i\pi}(\|\psi_2\rangle)^*$	1	$\|\psi_1\rangle$ & $\|\psi_2\rangle$	$\mathbf{I_4}$
$(\|\psi_1\rangle)^*$	$e^{i\pi/2}(\|\psi_2\rangle)^*$	1	$\|\psi_1\rangle$ & $\|\psi_2\rangle$	$\mathbf{I_5}$
$(\|\psi_1\rangle)^*$	$e^{i3\pi/2}(\|\psi_2\rangle)^*$	1	$\|\psi_1\rangle$ & $\|\psi_2\rangle$	$\mathbf{I_6}$
1	**0**	2	$\|\psi_1\rangle$	$\mathbf{I_R}$
0	**1**	2	$\|\psi_2\rangle$	$\mathbf{I_L}$
1	**1**	2	$\|\psi_1\rangle$ & $\|\psi_2\rangle$	$\mathbf{I_H}$
1	$\mathbf{e^{iß/2}}$	2	$\|\psi_1\rangle$ & $\|\psi_2\rangle$	$\mathbf{I_D}$

TABLE 4.2: Table showing the transmission functions $T_{A(B)}$ used to acquire measurements to specify: orthogonal circularly polarized components of a vector field (top), the relative amplitudes and phases of the orthogonal components (middle) and the Stokes intensity measurements (bottom).

beam at the DMD was imaged onto a CCD_1 using a Fourier lens (FL), measuring on-axis intensities at this plane together with appropriate $T_{A(B)}$ allowed for determination of inner products [350]. A BS was used to capture the image plane intensity using a second CCD_2 after an aperture (A) and an inverse Fourier lens (IFL). In Table 4.2 we show the transmission functions $T_{A(B)}$ used to acquire c_p^l, d_p^l, e_p^l and I_i measurements in order to completely characterize the vector fields. The top segment of Tab. 4.2 has the DMD encoded with transmission functions to decompose the right-/left- circularly polarized fields into LG_p^l modes, the middle segment contains the transmission functions to extract global parameters α and β, while the bottom segment has transmission functions to extract four Stokes intensity (I_R, I_L, I_H and I_D) measurements used to extract the SOP and VQF [67, 106, 319]. The VQF is extracted according to

$$VQF = \mathcal{R}e\left(\sqrt{1 - \frac{s_1^2 + s_2^2 + s_3^2}{s_0^2}}\right) \tag{4.25}$$

where $s_i = \int S_i(\mathbf{r})d\mathbf{r}$ are the global Stokes parameters, with S_i being the spatially varying Stokes parameters determined as

$$S_0 = I_R + I_L \tag{4.26}$$
$$S_1 = 2I_H - S_0 \tag{4.27}$$
$$S_2 = 2I_D - S_0 \tag{4.28}$$
$$S_3 = I_R - I_L \tag{4.29}$$
$$\tag{4.30}$$

4.2.4 Results

As an initial demonstration of arbitrary vector state measurements, we generated cylindrical vector vortex beams (i.e., $|\psi_{1(2)}\rangle = LG_0^{\pm 1}$), and varied the relative amplitude and phases (i.e., α and β) of the generated beams to determine how accurately these parameters can be extracted from our detection system. Additionally, each measurement was preceded by a decomposition of $|\psi_{1(2)}\rangle$ into (a subset of) the LG_p^l basis in order to ensure the measurements are occurring on the correct HOPS (here we approximated any LG_p^l mode containing $> 90\,\%$ of the total power as $|\psi_{1,2}\rangle$). In Fig. 4.11 we can see the modal cross-talk matrices for $|\psi_{1(2)}\rangle$ and the state vectors represented on the appropriate HOPS sphere with α and β compared to the ideal values in brackets. Also included in Fig. 4.11 are spatially varying SOP and VQF measurements. In Fig. 4.11.D we show the results obtained for $|\psi_{1(2)}\rangle = LG_{1(3)}^{-5(1)}$ to demonstrate our technique's viability for the accurate characterisation of radial orders. We can note some slight vertical stretching of the SOP results, this is due to the DMD diffracting light at 12° to its surface normal (computational re-scaling of the Stokes intensities could alleviate this artefact). The results show good agreement with the ideal values.

In Fig. 4.12 we present results, displaying our technique's performance in characterizing vector beams made up of orthogonally polarized components with fractional OAM. The beams were generated by encoding $T_{A(B)} = e^{\pm i\varphi M}$ on the generation DMD, where φ is the azimuthal coordinate and $M = m + \mu$ is a fractional OAM index, with $m \in \mathbb{Z}$ and $\mu \in (0, 1)$. This generation hologram behaves like a spiral phase plate with a non-integer winding number. It has been shown that beams generated by such systems can be approximated as a finite superposition of beams with integer OAM, weighted by complex coefficients f_l calculated as [216, 352, 353]

$$f_l = \left(\frac{i}{2\pi(M-l)}\right)(1 - e^{i(2\pi\mu)}). \tag{4.31}$$

It should be noted that factors of the above expression relating the orientation of the phase discontinuity to the intra-modal phases have been omitted for brevity. We also adjusted our detection scheme to that of a phase only OAM decomposition, this avoids the need to sample the variety of radial orders which naturally manifest from phase plates (interested readers are directed to Refs [44, 353]). The OAM decomposition involves setting transmission functions equal to $e^{-il\varphi}$, since these are not eigenmodes of free space the physical effect is measuring the total power of LG_p^l modes for all values of p (truncated by the DMD screen size) - therefore the resulting OAM spectrum gives only the weightings of spiral phases (with charge l) in a given field. The OAM spectra of the $|\psi_1\rangle$ (red) and $|\psi_2\rangle$ (blue) components show good correlation with the theoretical predictions (dashed). The HOPS inset demonstrates the relative stability of the system in characterizing vector coordinates, while the SOP inset reveals the detail captured by the Stokes intensity measurements. It is notable that the VQF of this beam is lower than unity, this is due to the modal crosstalk evident in the OAM spectrum.

In Fig. 4.13 we can see results obtained for beams with $l = \pm 40$. This represents the largest mode order our system is able to analyse (with a beam waist of $w_0 = 0.6$ mm). This limitation of the system is determined by the size of the DMD and/or WP which impedes detection of beams with a larger spatial extent, this limit will generally precede the mode fidelity limit of the DMD which has been shown to exceed that of SLMs [218]. The crosstalk matrices presented, represent a portion of the

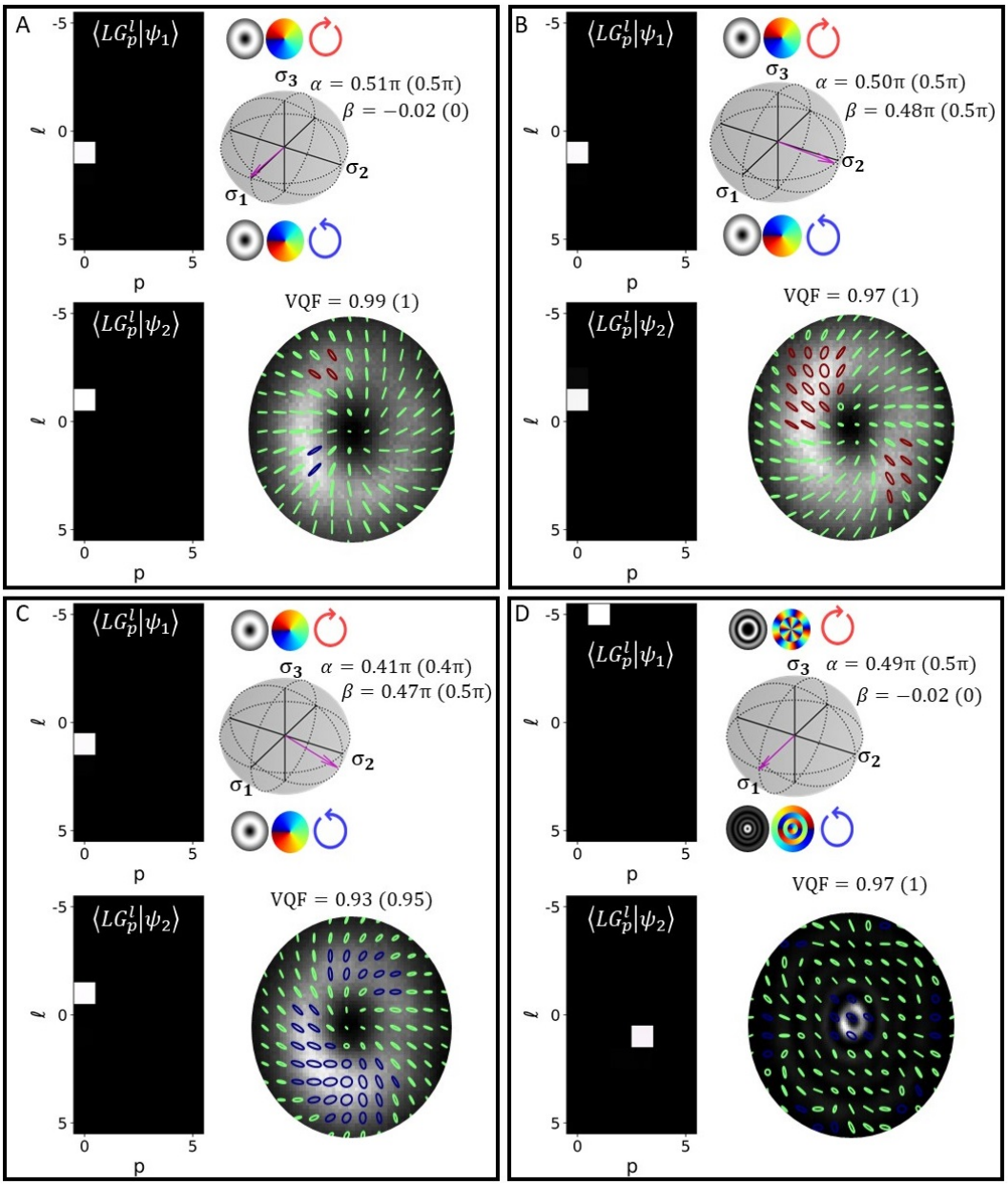


FIGURE 4.11: Crosstalk matrices (left), HOPS spheres with associated state vectors (top right) and SOP (bottom right) - measured for beams generated with A) $\alpha = \beta = 0$, $|\psi_{1(2)}\rangle = LG_{0(0)}^{1(-1)}$ B) $\alpha = 0$, $\beta = -\pi/2$, $|\psi_{1(2)}\rangle = LG_{0(0)}^{1(-1)}$ C) $\alpha = -0.1$, $\beta = -\pi/2$, $|\psi_{1(2)}\rangle = LG_{0(0)}^{1(-1)}$ and D) $\alpha = \beta = 0$, $|\psi_{1(2)}\rangle = LG_{1(3)}^{-5(1)}$. The ideal values for α, β and VQF are included in brackets to the right of the measured values.

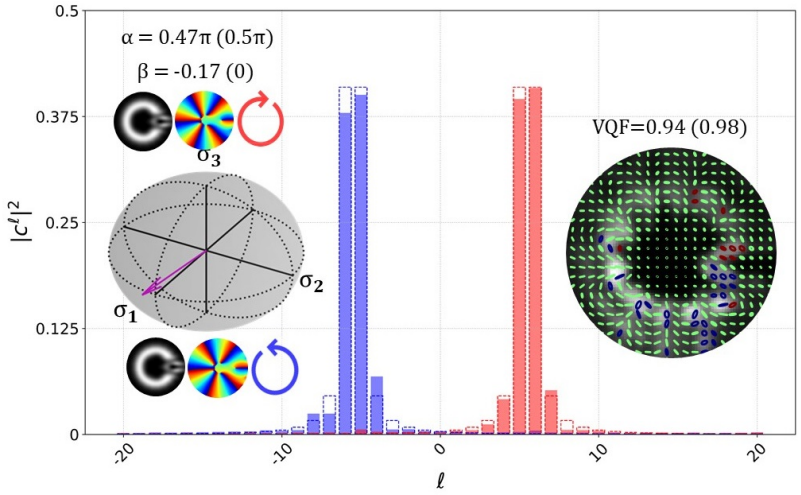


FIGURE 4.12: OAM spectra for individual components $|\psi_{1(2)}\rangle = e^{\pm i5.5\varphi}$ (red - $|\psi_1\rangle$, blue - $|\psi_2\rangle$; experimental results in solid bars and theoretical prediction in dashed lines). The vector on the HOPS sphere and SOP for the vector beam generated by the orthogonal fractional OAM components are included as insets.

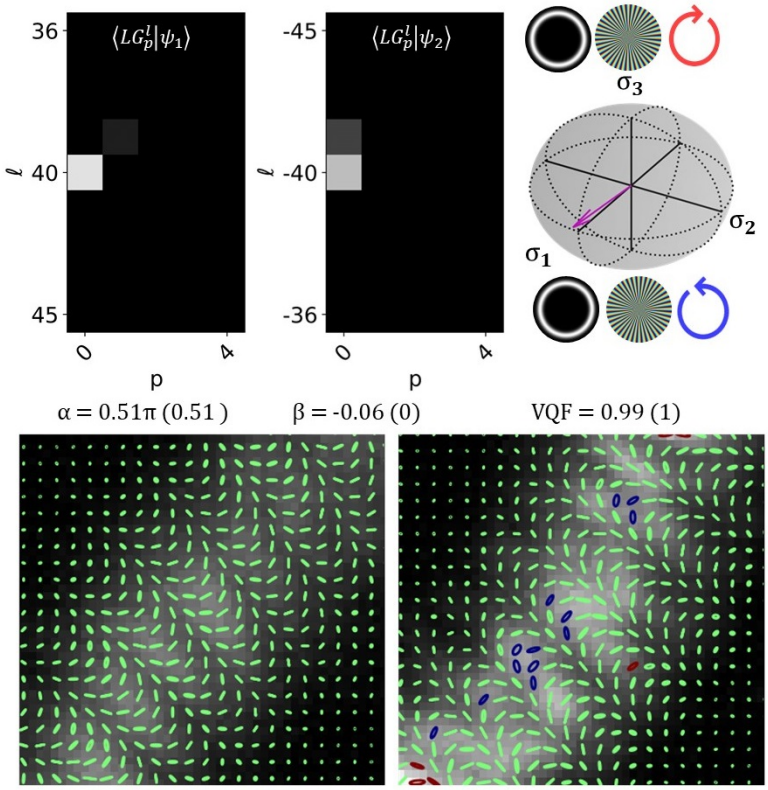


FIGURE 4.13: Crosstalk matrices and state vector lying on the HOPS sphere for $|\psi_{1(2)}\rangle = LG_{0(0)}^{40(-40)}$ (top left). HOPS sphere for $l \pm 40$ with the state vector (top right). Cropped regions displaying the SOP.

entire $l \in [-50, 50]$, $p \in [0, 10]$ subspace which was sampled. The power in the desired $LG_0^{\pm 40}$ for $|\psi_{1(2)}\rangle$ was $0.883(0.739)$. The power dispersion arises due to larger mode orders being more sensitive to phase aberrations as well as on-axis centering at CCD_1, choosing a FL with a longer focal length is expected to improve the performance. This result, however, still implies our device's ability to reliably analyze cylindrically symmetric vector fields with $M = |l| + 2p \leq 40$; as is revealed by the state vector displayed on the $l = \pm 40$ HOPS. Additionally the image plane Stokes intensities allowed for the recovery of the detailed inhomogenous SOP distribution embedded in this beam.

4.2.5 Conclusion

We have presented a device, comprised of a WP to separate orthogonal polarization components, a DMD to modulate and recombine them as well as a static linear polarizer to project the orthogonally polarized components into the same plane and interfere. We have demonstrated the effectiveness of our approach in completely specifying the state of a vector field, as well as in reconstructing the SOP of the field along with the associated VQF. We have shown how we can accurately characterise cylindrical vector vortex beams, vector beams with radial orders and vector beams with orthogonal components containing fractional OAM while also being able to extract digital Stokes intensity measurements. Additionally our system is able to characterize a significantly large subset of mode orders while maintaining a more compact arrangement while avoiding the need for reference fields, therefore addressing some of the problems faced by preceding vectorial characterization techniques. Furthermore the dynamic nature of the arrangement as well as the dual Fourier and image plane sampling leaves room for extensions to the functionality of our scheme. We believe this scheme will be of interest in industry, particularly for the characterization of liquid crystal and metasurface q-plates and j-plates, as well as other areas such as communications, microscopy and laser machining - where vectorial structured light is seeing increasing interest.

4.3 Versatile wavefront sensing with a DMD

4.3.1 Introduction

An optical wavefront is defined as the surface which lies (approximately) normal to the Poynting vector field, thus indicating where the field's energy will flow as it propagates [354]. Determining the effect a system has on the wavefront of an optical field passing through it is therefore important in characterizing, correcting and optimizing the system. In microscopy and astronomy the quality of microscope and telescope images is dictated by the point-spread-function (PSF) of the optical system, with deviations from the ideal PSF (dictated by the diffraction limit) due to wavefront aberrations induced by manufacturing limitations [355–357]. However, if the aberrations are known, computational techniques can be used to improve the quality of the images [358, 359]. In ophthalmology, wavefront aberrations inherent in the human eye which cause vision impairment are surgically compensated for once measured [360, 361]. In free-space optical communication, modal crosstalk due to aberrations caused by atmospheric turbulence result in signal errors, post-/pre-correction of these aberrations can reduce the bit error rate [362–365]. In laser cutting the ability of focusing lenses to concentrate the power of an optical field into a small

region is compromised by wavefront aberrations which distort the focal field distribution [366–368], correction of these aberrations can be performed using robust deformable mirrors. In all the above cases the accurate determination of aberrations caused by a given optical system is essential in effectively compensating for them, either through physical or computational means. Currently employed methods include interferometric sensors which provide high accuracy and sensitivity, but involve large systems with reference beams which are susceptible to environmental perturbations [369–371]. The ophthalmology and astronomy communities often utilise Shack-Hartman lenslet arrays to acquire fast, low resolution wavefront measurements which are then interpolated [372]. Certain specialized applications, such as calibration of large interferometers, use modal techniques to estimate aberrations with extremely high sensitivity [373, 374]. The transport-of-intensity equation (TIE) describes how the phase of light is related to its energy flow under propagation, and was proposed for use in wavefront sensing and adaptive compensation decades ago [375, 376]. Since, the TIE has found applications most notably in quantitative phase imaging (QPI) [377–379] while also being use to measure lens induced curvature [380], as well as atmospheric turbulence [381]. The equation itself can be derived using Poynting's theorem, which highlights the elegance of the technique: that it is based directly on the conservation of energy [24]. Conventionally the intensity images required to extract phase using the TIE are acquired through translation of a camera along the light's path, single shot measurements at fixed propagation lengths can be achieved using beam displacement setups [382] and tune-able propagation lengths can be implemented using liquid crystal SLMs [383, 384]. These methods do, however, suffer from a variety of drawbacks such as bulky arrangements, high costs, alignment instability, wavelength dependent calibration and polarization constraints.

Here we present an all-digital scheme that can accurately extract the global wavefront of an optical field in a fast, cheap and versatile manner. Our approach exploits a DMD. Initially developed for the digital projection industry [385], DMDs offer relatively low-cost, rapid modulation, polarization insensitivity and broadband operation making them an attractive alternative for manipulating structured light. The essential component consists of an array of individually-addressable micro-mirrors situated behind a glass protective film and attached to a driver unit which facilitates control via an external source. Each micro-mirror can pivot about a hinge in either one of two directions, representing the two possible states for operation, namely: on and off. This allows the DMD to mimic a dynamic amplitude-only grating [50]. The DMD is placed at the focal plane of a $4f$ imaging system to perform angular spectrum propagation of the field, the intensity of which is imaged using a CCD. The captured intensities at 3 (or more) planes are used to determine the wavefront of the field using the TIE. Our approach offers a number of advantages over alternative methods: the polarization insensitivity and broadband nature of DMDs removes the need to calibrate for the specific polarization and wavelength required by SLMs, while still retaining the tune-ability and automation provided by a digital propagation scheme [274]. Additionally, the kHz order frame rates offered by DMDs make them a more powerful tool for adaptive optics applications where rapidly changing wavefronts need to be characterized and corrected. We highlight the resolution and sensitivity of our approach by measuring induced Zernike aberrations in static samples, and demonstrate the real-time ability on dynamically changing turbulence phase screens. We then demonstrate broadband operation in a single optical setup probed at multiple wavelengths and with multiple polarizations. We believe this work will be of relevance to fields where wavefront measurements are ubiquitous.

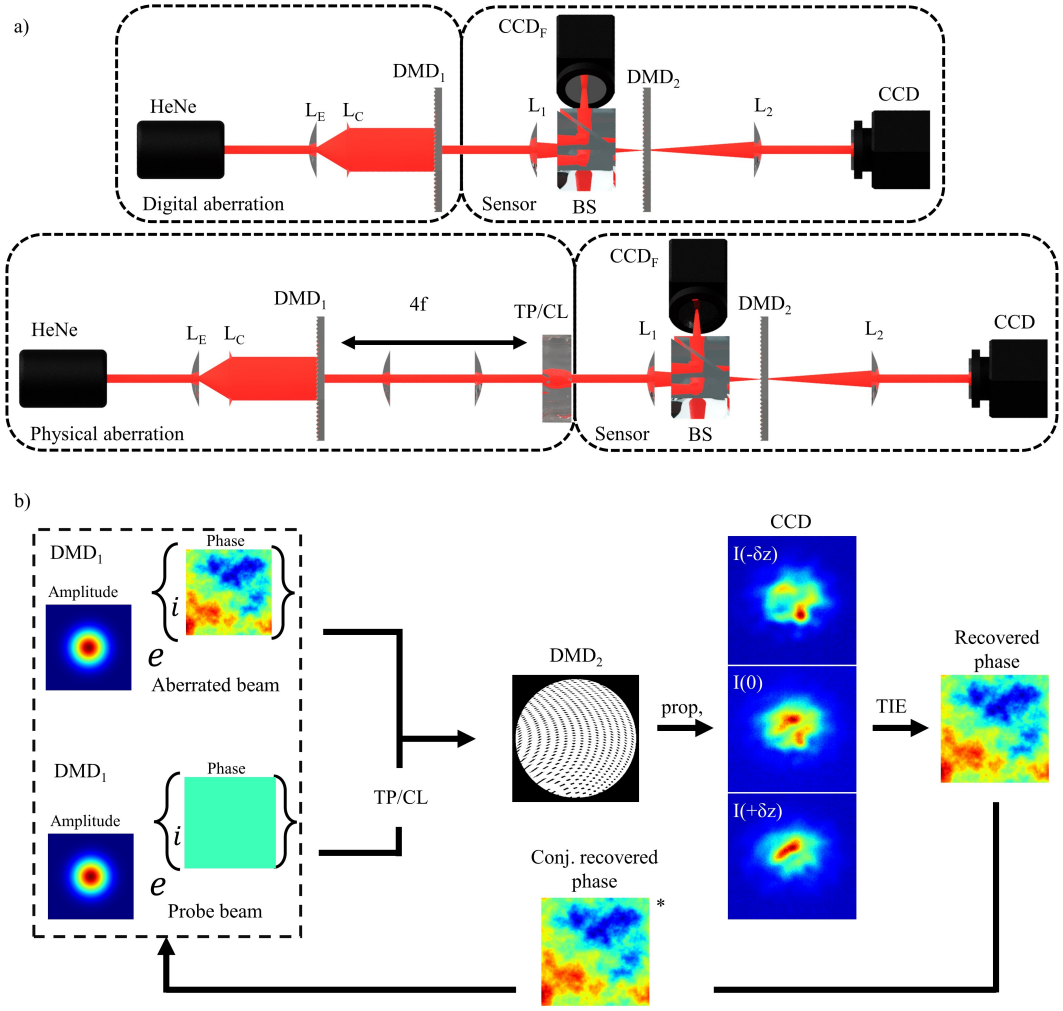


FIGURE 4.14: a) Experimental arrangements used to demonstrate how the DMD-TIE based wavefront sensor can recover digital (top) and physical (bottom) aberrations (note the sensor is comprised of $L_{1,2}$, DMD_2 and CCD while the BS and CCD_F were only used to asses the effectiveness of adaptive compensation). b) Diagram showing how the aberrated/probe beams generated by DMD_1 are used to create digital/physical wavefront distortions, how DMD_2 is used to digitally propagate the field at three distances and how phase recovered using the TIE is conjugated to perform adaptive (pre-)correction using DMD_1.

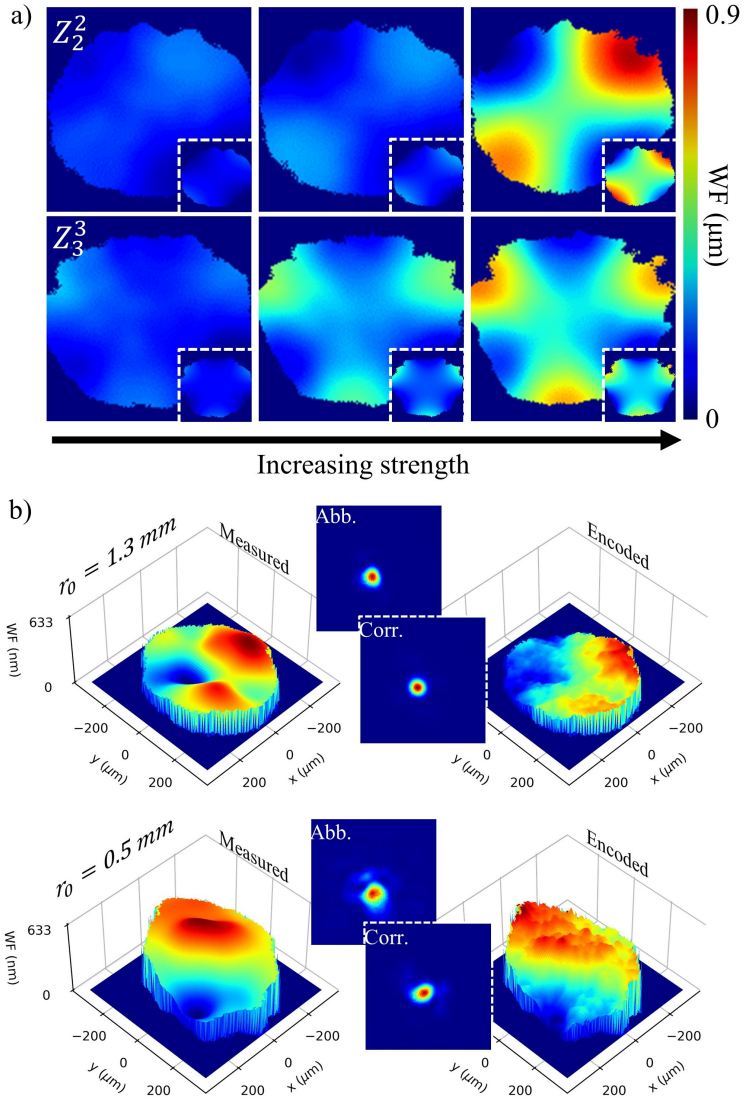


FIGURE 4.15: a) Measured astigmatic (top) and trefoil (bottom) aberrations at various strengths, insets show the encoded aberrations. b) Measured (left) and recorded (right) wavefronts of turbulence phase aberrations with Fried parameters of $r_0 = 1.3$ mm (top) and $r_0 = 0.5$ mm (bottom) - insets show the aberrated and adaptively corrected far field intensities.

4.3.2 Theory

The Poynting vector, $\vec{S} = \vec{S}(\vec{r})$, represents the directional energy flux of an electromagnetic field. Conservation of energy provides us with the condition that the total flux over a closed surface **s** must be zero for a system free of charge and current densities, namely

$$\int_{\mathbf{s}} \vec{S} d\mathbf{s} = \vec{\nabla} \cdot \vec{S} = 0\,, \tag{4.32}$$

where $\vec{\nabla} = (\partial_x, \partial_y, \partial_z)$. For monochromatic light (of frequency ω) we can use a Helmholtz decomposition to separate $\vec{S}$ into a curl-free scalar potential $\varphi = \varphi(\vec{r})$ and divergence-free vector potential $\vec{A} = \vec{A}(\vec{r})$, according to

$$\vec{S} = \frac{\omega}{4\pi}\left(\vec{\nabla}\varphi + \vec{\nabla}\times\vec{A}\right). \tag{4.33}$$

We can now substitute Eqn 4.33 into Eqn 4.32, and use the paraxial approximation (assuming propagation along z) to find

$$-k\partial_z I = \vec{\nabla}_T\cdot\left(I\vec{\nabla}_T\varphi\right) + \vec{\nabla}_T I\cdot\left(\vec{\nabla}\times\vec{A}\right)_T, \tag{4.34}$$

where I is the field intensity at some plane of interest, say $z = 0$, and the subscript T indicates quantities in the plane transverse to propagation [386]. The term involving $\vec{\nabla}\times\vec{A}$ is only dominant in scalar optical fields that have embedded phase singularities and is commonly disregarded when using the TIE for phase retrieval (we will return to this point later in the discussion). After some manipulation a relaxation/iterative method can be applied to approximate solutions Eqn. 4.34 [387]. We observed the solution converging after only a single iteration and chose to use the following reduced form of the approximation

$$\phi \approx \vec{\nabla}_T^{-2}\left(\frac{-k\partial_z I}{I + C}\right), \tag{4.35}$$

where $\vec{\nabla}_T^{-2}$ is the inverse of the transverse Laplacian operator, which can be numerically solved using fast Fourier transforms. Here C is a constant chosen by the user, introduced to deal with intensity nulls (i.e., regions where $I = 0$). It should be noted that C should be chosen to be small in order to not distort the recovered phase, throughout this work we set C to 1 % of the maximum intensity at the plane of interest. It is worth noting that the choice of C does not require any *a priori* knowledge of the phase to be recovered. The wavefront (WF) can then be calculated through constant multiplication WF$= \frac{\lambda}{2\pi}\phi$ for homogeneously polarized fields. It should be noted that there are some limitations on the ϕ distributions which can be recovered by Eqn. 4.35 due to the approximations and assumptions made in its derivation. Notably if ϕ has a (non-flat) structure which results in $\partial_z I = 0$, Eqn. 4.35 will (incorrectly) recover a flat profile due to disregarding $\vec{\nabla}\times\vec{A}$ (we later discuss some methods with potential to overcome this). Additionally the relaxation approximation requires the system to behave linearly between iterations, potential errors due to non-linearity will scale with the distance over which $\partial_z I$ is approximated (we discuss this in the following section).

In order to determine the unknown $\partial_z I(x, y, z)$, images of the intensity at multiple planes along the propagation axis z are required. For our purpose we use three planes (i.e., $z \in [-\delta z, 0, \delta z]$). In order to acquire these images we utilise a $4f$ imaging system with a DMD modulating the far field by a transmission function $P(z) = e^{ik_z(k_x,k_y)z}$, the intensity at the end of the imaging system is described by

$$I_{\text{out}}(x, y) = |\mathcal{F}^{-1}(\mathcal{F}(U(x, y, 0))P(z))|^2 \tag{4.36}$$

where $U(x, y, 0)$ is the field of interest. Coordinate substitutions applied to the Fresnel diffraction integral, combined with an application of the convolution theorem have revealed that the observed intensity is equal to that of the field at the chosen distance z, therefore

$$I_{\text{out}}(x, y) = |U(x, y, z)|^2 = I(x, y, z) \tag{4.37}$$

This holographic implementation of the angular spectrum propagation technique has been reliably used to investigate the propagation dynamics for various purposes [151, 274]. We approximate our intensity gradient along the z axis as

$$\partial_z I(x,y,z) \approx \frac{I_{\text{out}}(x,y,\delta z) - I_{\text{out}}(x,y,-\delta z)}{2\delta z} \tag{4.38}$$

Using Eqn 4.38, $I(x,y,0)$ and Eqn 4.35 we can extract $\phi(x,y,0)$. To facilitate the required modulation of the field by the DMD we employed the complex amplitude modulation scheme discussed in Chapter 2. The associated binary holograms took the following form

$$H(\vec{r}_T) = \frac{1}{2} + \frac{1}{2}\text{sign}\left(\cos(\vec{r}_T \cdot \vec{g}_T + \arg(P(z))) - \cos(\arcsin(|P(z)|))\right) \tag{4.39}$$

where $\vec{r}_T = (x,y)$ are the transverse coordinates and $\vec{g}_T = (g_x, g_y)$ are the Cartesian grating frequencies. A benefit presented by the holographic approach to acquire $\partial_z I$ is that the parameter δz can be adjusted based on the desired application. It has been shown in previous investigations that larger δz leads to higher sensitivity measurements, while smaller values are effective for stronger aberrations and measuring phase objects with high spatial frequencies [24]. It should be noted that while the TIE alone cannot resolve certain structures such as: phase vortices (i.e., wavefronts that helically wrap around the propagation axis corresponding to energy swirling around an intensity null) and flat phase discontinuties (i.e., discontinuous wavefronts lying parallel to the propagation axis), phase flattening techniques can be implemented alongside the TIE allowing these features to be probed [350]. Furthermore these phase flattening procedures have been effectively implemented using DMDs and can be readily integrated into our proposed scheme [388].

4.3.3 Experiment

To validate our technique we utilized the experimental arrangements shown in Fig. 4.14.a. A Gaussian beam produced by a laser (both a HeNe operating at $\lambda = 633$ nm and an Ar-ion operating at either $\lambda = 457(488)$ nm were used) was expanded and collimated using lenses L_E and L_C, respectively. The expanded beam was directed onto the screen of DMD_1 (DLP6500). The DMD was addressed with a binary hologram which facilitated modulating the amplitude and phase of the input field following the approach outlined in Ref. [70]. It should be noted that only the 1^{st} diffraction order holds the desired modulated beam and an additional $4f$ system (omitted from Fig. 4.14.a for clarity) was used to isolate this order at the focal plane with an aperture. We chose to encode a Gaussian amplitude profile as well as two cases of phase distributions: for measuring digitally controlled aberrations an aberrating phase in the form of Zernike aberrations or a numerically generated turbulence phase screen, for measuring physically induced aberrations a flat phase (acting as a probe) was encoded at DMD_1 with an additional $4f$ imaging system allowing phase distributions from a silica turbulence phase plate or NBK7 spherical lens to be measured. The sensor is constructed using lens L_1 which projects the Fourier transform of the aberrated field onto a second DMD_2 (DLP4710 [389]), which was encoded with the transmission function $P(z)$. It should be noted that three holograms corresponding to the different propagation distances can be multiplexed for single shot operation or implemented sequentially if retrieval at the full CCD resolution is desired. Lens L_2 was then used to project the inverse Fourier transform of the field at DMD_2 onto

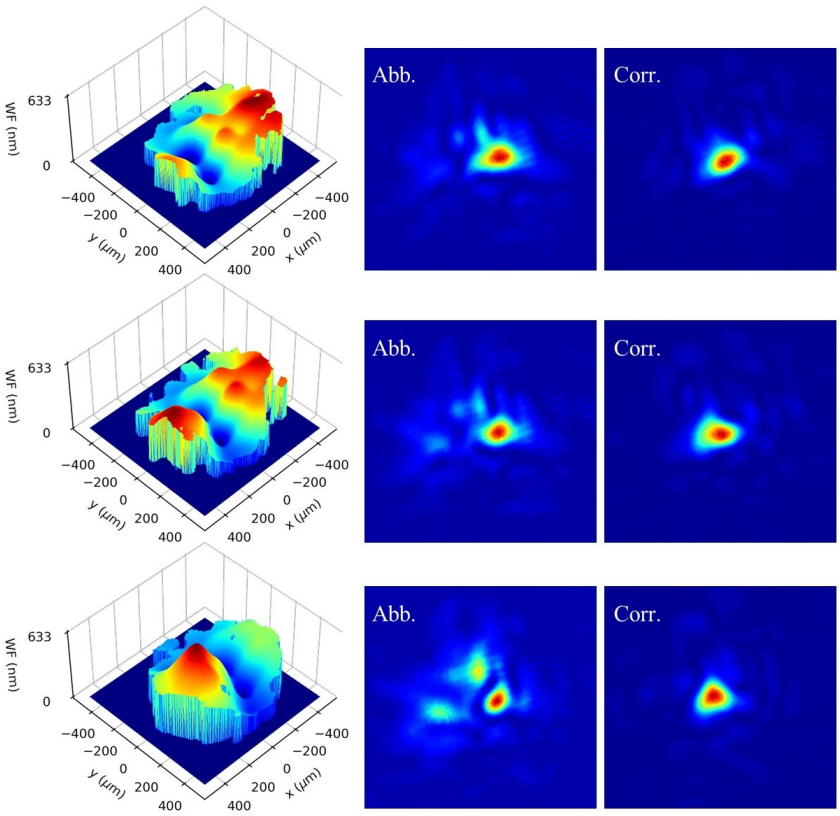


FIGURE 4.16: Recovered wavefront aberrations (left) produced by a turbulence phase plate translated in the x direction, along with the aberrated (middle) and corrected (right) far-field intensities.

a CCD camera (FLIR Grasshopper). It should be noted that multiple diffraction orders will appear in the plane of the CCD, however only the 1^{st} diffraction order(s) are used in the wavefront estimation. For the exemplar measurements presented in this work $\delta z = 10$ mm was chosen, the Gaussian was given a waist radius of $w_0 = 1$ mm and the focal lengths used were: $f_E = 2$ mm, $f_C = 250$ mm, $f_1 = 1$ m and $f_2 = 300$ mm. Since the TIE is only valid in regions with $I > 0$ the recovered phase screens were truncated below the threshold of $I < 0.1 I_{max}$, where I_{max} is the max intensity at the plane of interest. Once the wavefront aberrations were recovered using Eqn. 4.35 the conjugate of the recovered phase was added to DMD_1 in order to adaptively correct the aberration as illustrated in Fig. 4.14.b. The effectiveness of this adaptive correction was determined by measuring the far-field intensities of the aberrated and corrected fields with a second CCD_F (FLIR Chameleon) at the focal plane of L_1 accessed using a 50:50 BS before DMD_2.

4.3.4 Results and Discussion

As a demonstration of effective operation, Fig. 4.15.a shows the performance of the DMD enabled TIE phase recovery scheme on astigmatic (Z_2^2) and trefoil (Z_3^3) Zernike aberrations of various strengths. The general structure and strength of the aberrations are readily recovered as is evident by comparing the recovered and encoded aberrations, the latter shown in the insets. Displaying how recovered phases can be used for adaptive correction in our arrangement Fig. 4.15.b shows encoded and recovered wavefronts from turbulence phase screens (generated using a Fourier-transform technique [390]). It is worth noting that propagating through atmospheric turbulence over long distances requires a split step method using multiple phase screens, our single screen approximation simply serves to verify the effective nature of our wavefront sensing approach at a single plane. The insets display how the conjugate of the recovered phase is able to drastically improve the far-field intensity distribution when used for adaptive correction, evident in the Gaussian like shapes of the corrected intensities. It is expected that any residual aberrations can be removed through a second iteration of the correction procedure. The real-time operation of our adaptive correction procedure is highlighted in Fig. 4.16, where we can see wavefront distortions produced by a turbulence phase plate being translated across a probe Gaussian beam. The wavefronts were captured at ≈ 5 Hz. The translation of features (such as the two prominent valleys) in the recovered wavefront plots is clear and additionally the dynamically captured aberrated and corrected far-field intensities reveal the accuracy of the recovered wavefronts. It should be noted that only the frame rate of the CCD camera restricted the dynamic acquisition rate, while Eqn 4.35 is evaluated in < 2 ms (with an Intel i5-8400 running MatLab) indicating the potential for > 500 Hz acquisition rates if appropriate high-speed CMOS cameras are implemented. In order to highlight the benefit provided by the broadband nature of DMDs, Fig. 4.17 shows the effectiveness of the DMD based sensor at multiple wavelengths. The phase profile of a $f = 50$ mm, BK7, spherical lens was measured using 488 nm and 457 nm wavelength light the results are shown in Fig. 4.17.a. The radially symmetric pattern is clear in both cases with the 488 nm measurement showing some slight aberration in the region highlighted by the dotted block. Radial sections along the dashed lines are shown in Fig. 4.17.b showing a comparison to the theoretical curves predicted by the thin lens approximation $\phi_{Th.} = kr^2/2f$, while there is some deviation from the ideal curves at both wavelengths the general trend and relative relationship between the wavelengths agrees well with expectations. This type of broadband operation is expected to function

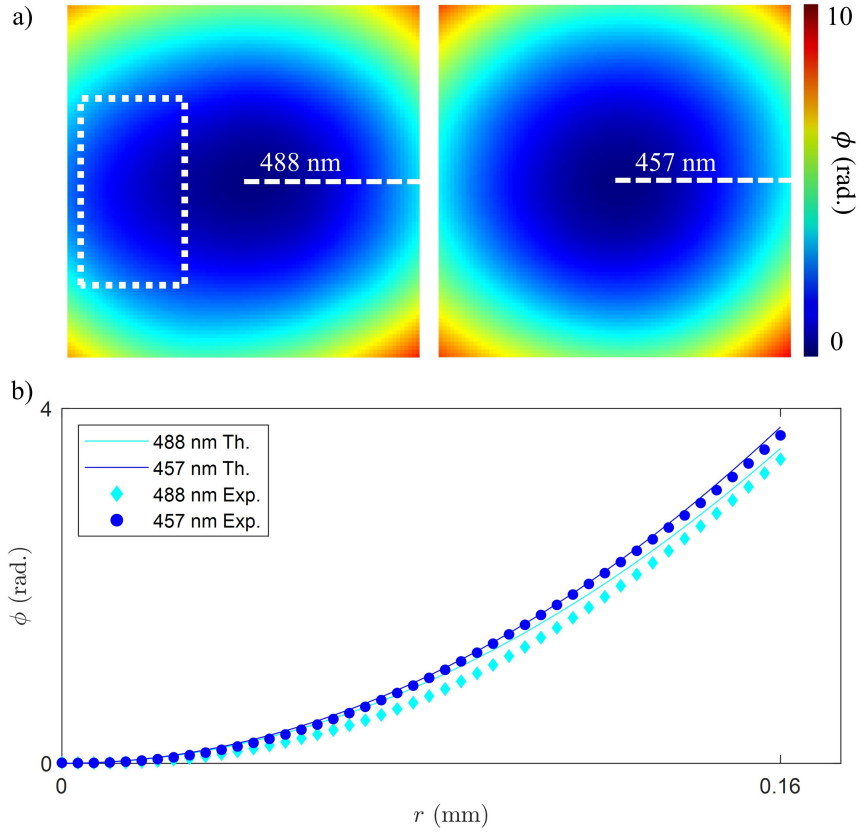


FIGURE 4.17: a) Recovered transverse phase profiles of a $f = 50$ mm focal length, N-BK7 spherical lens using TIE sensing implemented with a DMD at wavelengths of 457 nm and 488 nm. b) Radial cross sections of the phase profiles at 457 nm and 488 nm along the dashed lines. Dotted square indicates a cylindrically assymetric aberration in the 488 nm measurement.

for the 400 nm to 700 nm operating wavelength range of the DMD without the need for re-calibration, revealing a significant advantage over SLM based approaches. In order to demonstrate the polarization invariance of the DMD based sensor turbulence phase plate results were take with vertically and horizontaly polarized light as shown in Fig. 4.18.a, the strong agreement between the two cases is clear with the small deviation likely originating due to the HWP (used to rotate the plane of polarization) increasing the effective propagation distance. A verification of the polarizations captured at the CCD is given in Fig. 4.18.b where each was sent through a vertical and horizontal LP, the non-zero intensities through the orthogonal polarizers are likely due to extinction ratio limitations.

4.3.5 Conclusion

We have demonstrated a proof-of-principle for a simple, micro-mirror enabled, digital wavefront sensor based on the transport of intensity. We have demonstrated the approach using standard Zernike aberrations, static and dynamic turbulence screens as well as broadband optics and at multiple polarizations. Additionally we have shown how the device can be effectively integrated into an adaptive optics arrangement. It can also be noted that the polarization insensitivity of DMDs indicates the potential for the approach to be used with vectorial light, which has been receiving growing interest in recent years [388]. The low cost and dynamic capabilities of

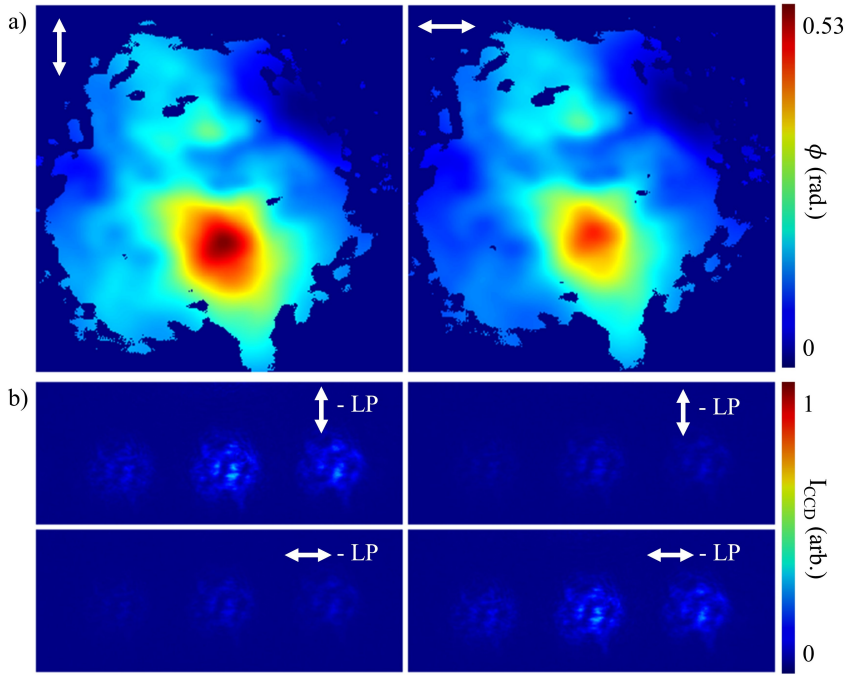


FIGURE 4.18: a) Phase profiles recovered from a turbulence phase plate using Gaussian probe beams with vertical (left) and horizontal (right) polarization. b) CCD images containing the intensity profiles (captured in a single shot at each of the three propagation distances) for each polarized beam through vertical (top) and horizontal (bottom) linear polarizers.

the DMD in conjunction with the broadband operation and versatility of the holographic propagation implementation make this a promising addition to the adaptive optics toolkit.

4.4 Comments on the iterations and variations of vectorial light analysers

The first analyser was constructed using both an SLM and a DMD in order to digitally acquire Stokes intensity measurements. The work revealed that the polarization sensitivity of the SLM made it unsuitable for digitally extracting all the Stokes parameters from a vectorial light field, while the inteferrometric arrangement of the DMD and PG provided a adequate arrangement for digital Stokes polarimetry measurements. The second analyser based on a WP and DMD, which takes a form similar to the optimized generator discussed in Chapter 3, allowed for the complete characterization of vectorial light fields. This included the acquisition of digital Stokes intensity measurements, digital modal projective measurements on individual polarizations allowing for isolation of the correct HOPS on which the vector field lies and combined spatial and polarization projections which allowed for the global relative amplitude and phase of the constituent components to be measured. The stability of this arrangement afforded by the single element separation (WP) and single element recombination (DMD) allowed for the reliable, accurate and automated analysis of arbitrary vector light fields using low cost equipment. The final analyser utilized a DMD in order to perform multiplexed (or sequential) angular spectrum propagation of a scalar light field in order to recover non-singular wavefronts using the TIE. It should be easy to see that this process could be easily integrated into

the vectorial light analyser adding to its range of possible measurements, further bolstering the capabilities of the device. It is notable that the optimal design for the analyser takes a similar form to that of the optimized generator discussed in Chapter 3, further avenues for improvement and optimization of the design in considered in Chapter 6.

Chapter 5

Unitary invariance of vectorial light and how it can be exploited for robust communication

This chapter is based on the papers:

Nape, I., **Singh, K.**, Klug, A., Buono, W., Rosales-Guzman, C., McWilliam, A., ... & Forbes, A. Revealing the invariance of vectorial structured light in complex media. Nature Photonics, 16(7), 538-546. (2022). ***co-first author**

Singh, K., Nape, I., Buono, W. T., Dudley, A., & Forbes, A. A robust basis for multi-bit optical communication with vectorial light. Laser & Photonics Reviews, 2200844. (2023).

Now that we have discussed and demonstrated various vectorial light generators and analysers, we can begin to investigate the transport of vector fields through various optical channels. The generation of arbitrary vector fields in the following investigations was facilitated by the very tools developed in Chapter 3, while the analysis of the fields was performed using the tools discussed in Chapter 4.

5.1 Using our digital tools to investigate the invariance of vectorial light through unitary channels

5.1.1 Introduction

Non-paraxial light is vectorial in 3D and has given rise to exotic states of structured light [11] such as optical skyrmions [261, 391], knotted strands of light [85, 392], flying donuts [393, 394] and Möbius strips [305]. Paraxial light too is vectorial, in 2D, characterised by an inhomogeneous polarization structure across the transverse plane [395]. Vectorial structured light in 2D and 3D has been instrumental in a range of applications (see Refs. [39, 81, 303, 396] and references therein), for example, to drive currents with a direction dictated by the vectorial nature of the optical field [397, 398], imprinting the spatial structure into matter [399], enhanced metrological measurements [400, 401], probing single molecules [402], and to encode more information for larger bandwidths [403–406]. They are easy to create in the laboratory using simple glass cones [407], stressed optics [408] and GRIN lenses [409], as well as from SLMs and DMDs [165, 410], non-linear crystals [411, 412], geometric phase elements [41, 413], metasurfaces [213] and directly from lasers [55].

Given the importance of these structured light fields, much attention has been focused on their propagation through optical systems that are paraxial [414], guided [415] and tight focusing [416, 417], as well as in perturbing media such as turbid [418–421], turbulent [15–18, 422–425] and underwater [426–428]. The conclusions are seemingly contradictory, with compelling evidence that the vectorial structure is stable, and equally compelling evidence that it is not, while the specific nature of each study prohibits making general conclusions on the robustness of vectorial light in arbitrary complex media.

Here we show that the inhomogeneity of a vectorial light field is impervious to complex channels so long as they are unitary (where an inverse process exists), a condition fulfilled for many aberrated optical systems. We illustrate this with two examples featuring strong aberrations: a tilted lens, and atmospheric turbulence simulated on a DMD. We then demonstrate the power of our framework by testing it for transmission through chiral liquids, optical fiber, turbulent air and complex optical aberrations. Our quantum-inspired framework explains the robustness of vectorial light fields by virtue of unitary operations on the vectorial state, manifesting as an intact inhomogeneity even if the vectorial pattern appears spatially distorted due to modal scattering in the component scalar spatial modes. We show that the channel action can be reversed by a reciprocal unitary process applied either pre-channel or post-channel, as well as cross-talk free detection of vectorial fields through complex media. Our study highlights the importance of measurement in the context of vectorial light fields, in doing so resolving a standing paradox on the robustness of vectorial light to perturbations, and provides a general framework for understanding the impact of arbitrary optical aberrations on vectorial structured light fields.

5.1.2 Concept

A vectorial structured light field can be written compactly in a quantum notation as the unnormalised state

$$|\Psi\rangle = |e_1\rangle_A |u_1\rangle_B + |e_2\rangle_A |u_2\rangle_B , \tag{5.1}$$

highlighting the non-separable nature of the two DoFs, A and B, denoting the polarization and the spatial DoF, respectively. In this way, the vectorial field is treated as a quantum-like state (but not quantum and without non-local correlations), by virtue of its non-separable DoFs, akin to a locally entangled state [167, 170, 173, 429, 430]. The polarization DoF is expressed as any pair of orthonormal states, $\{|e_1\rangle$ and $|e_2\rangle\}$ while the spatial mode DoF is given by the orthonormal basis states $\{|u_1\rangle$ and $|u_2\rangle\}$. In a quantum sense, this vectorial structured field would be called a pure state. The vectorial nature can be quantified through a measure of its non-separability [431], the VQF which for succinctness we will call its "vectorness", ranging from 0 (homogeneous polarization structure of scalar light) to 1 (ideally inhomogeneous vectorial polarization structure).

Now imagine that our vectorial light field, $|\Psi_{\text{in}}\rangle$, passes through an arbitrary aberrated optical channel, as illustrated in Fig. 5.1, e.g., static imperfect optics or dynamic turbulent air. If the channel acts on only one DoF then this can be considered a one-sided channel, terminology borrowed from quantum communication theory, describing a situation where only one of the two entangled photons is affected. For our classical light, an example would be when the spatial mode (DoF B) is affected (distorted), while the polarization (DoF A) is not, or vice versa. In our analysis here we will use DoF A as unaffected, but this can be changed by a simple relabeling

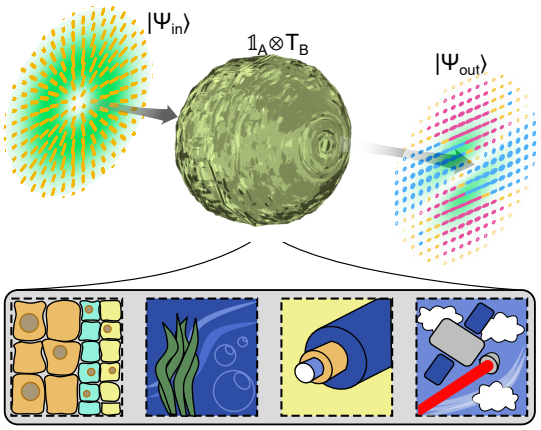


FIGURE 5.1: Complex light in complex channels. A vectorial light field propagates through a perturbing medium. Examples of such perturbing media could be turbid, underwater, optical fiber or turbulent air. Here and elsewhere the beam profiles illustrate intensities (green gradients) overlaid with polarization ellipses indicating right-handed (red), left-handed (blue) and linear (orange) polarizations.

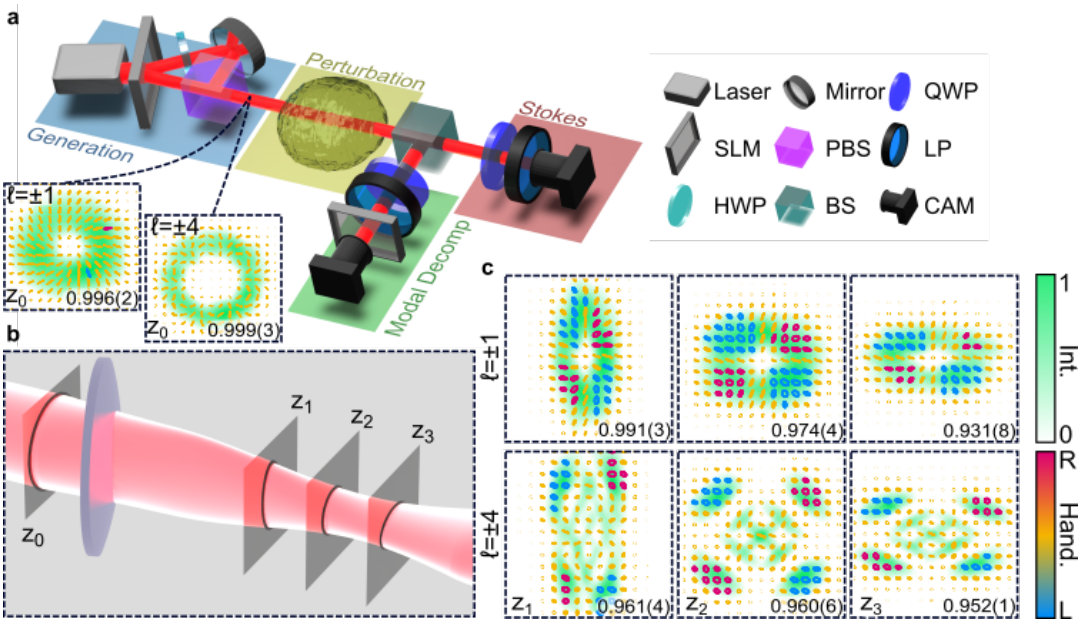


FIGURE 5.2: Vectorial light through a tilted lens. (a) The experiment has four stages: a generation stage to create the vectorial fields, a perturbation stage to pass it through a perturbing medium, and two detection stages to perform Stokes projections and modal decomposition. The insets show the initial $\ell = \pm 1$ (left panel) and $\ell = \pm 4$ (right panel) beams at plane Z_0. (b) Illustration of the propagation through a tilted lens, with exemplary measurement planes indicated as Z_1 through to Z_3. (c) The output $\ell = \pm 1$ and $\ell = \pm 4$ beams at these distances, confirm that the spatial structure alters with distance but that the vectorness (the inset number to each beam frame) does not, remaining above 93%. The optical elements comprise a HWP: half-wave plate, PBS: polarising beam splitter, Pol: polarizer, BS: beam splitter, QWP: quarter-wave plate, and CAM: camera, with the laser at wavelength $\lambda = 633$ nm. All beam profiles are shown as false colour intensity and polarization maps.

exercise. An open question is whether distortions acting only on the spatial DoF would keep the entire structure of the vectorial light field intact? It has been argued that the unaffected DoF acts as an anchor of sorts, keeping the entire field structure

intact, and sometimes phrased as a 'topological protection' of the optical mode when discussing perturbations that affect the spatial but not the polarization DoF.

To answer this question we employ a quantum framework. We show that a unitary one-sided channel, since it may be written as a positive trace-preserving map, transforms a vectorial (pure) input state $|\Psi_{\text{in}}\rangle$ into a vectorial (pure) output state $|\Psi_{\text{out}}\rangle$. Such a transformation may be expressed as

$$|\Psi_{\text{out}}\rangle = (\mathbb{1}_A \otimes T_B)\,|\Psi_{\text{in}}\rangle\,, \tag{5.2}$$

where $|\Psi_{\text{in}}\rangle$ is of the form Eqn. 5.1, the identity operator $\mathbb{1}_A$ acts on the polarization DoF A, while the transmission matrix T_B acts on the spatial DoF B. Without loss of generality, the transmission matrix may be expressed as $T_B = \Sigma_{i,j} t_{ij}\,|u_i\rangle\,\langle u_j|$, and for a unitary channel $t_{ij} = t^*_{ji}$. This allows us to write the output state as

$$|\Psi_{\text{out}}\rangle = |e_1\rangle\,|v_1\rangle + |e_2\rangle\,|v_2\rangle\,, \tag{5.3}$$

where $|v_1\rangle = t_{11}\,|u_1\rangle + t_{12}\,|u_2\rangle$ and $|v_2\rangle = t_{21}\,|u_1\rangle + t_{22}\,|u_2\rangle$. The fact that the channel is unitary moreover preserves the overlap between the spatial basis states, $\langle v_1|v_2\rangle = \langle u_1|\,T_B^\dagger T_B\,|u_2\rangle = \langle u_1|u_2\rangle$, and hence the vectorness of the beams. Orthogonal input modes are transformed into another set of orthogonal output modes, and the vectorness remains invariant. We may interpret the action of the channel as a simple change of basis in the spatial DoF, a rotation of the input basis $|u_i\rangle$ into an adjusted basis set $|v_i\rangle$.

The answer to our question is then as follows: the output remains a non-separable vector beam with the same vectorness as the initial beam. Its spatial structure, however, including its amplitude, phase and polarization profile, will be altered by the distorting medium, and our description of the vectorial structure has changed from Eqn. 5.1 to Eqn. 5.3, expressed in an adjusted basis set $|v_i\rangle$. This is a direct manifestation of the Choi–Jamiolkowski isomorphism in quantum mechanics [432], which establishes a correspondence between a channel operator and a quantum state, so that a measurement on one returns the other [433, 434]. Applied to classical vectorial light, justified because of its non-separability [340], we find that the channel is fully described by its action on the vectorial beam, and to measure the beam fully characterises the channel.

A property of a unitary channel is that the inverse process can be written as

$$|\Psi_{\text{in}}\rangle = (\mathbb{1}_A \otimes T_B)^{-1}\,|\Psi_{\text{out}}\rangle\,, \tag{5.4}$$

because the Hermitian adjoint of the channel operator is simply its inverse, $(\mathbb{1}_A \otimes T_B)^{-1} = (\mathbb{1}_A \otimes T_B)^\dagger$, or in experimental terms: the aberration introduced by transmission through the unitary channel can be undone, when sending the beam back through the channel. Equations 5.2 and 5.4 suggest that: (i) the vectorial nature of the final field shares the same vectorness as the initial field, (ii) the mapping results in a new adjusted basis which can be used for efficient characterisation of the state, and (iii) since the mapping is unitary it can always be unravelled before or after the channel in a lossless manner (under idealized measurement conditions). Note that in this analysis we have not needed to specify details of the DoFs (what the modes or polarization might look like), nor the channel itself (water, air, etc). We now showcase this generality through a series of exemplary test cases covering a wide range of input fields and channel conditions.

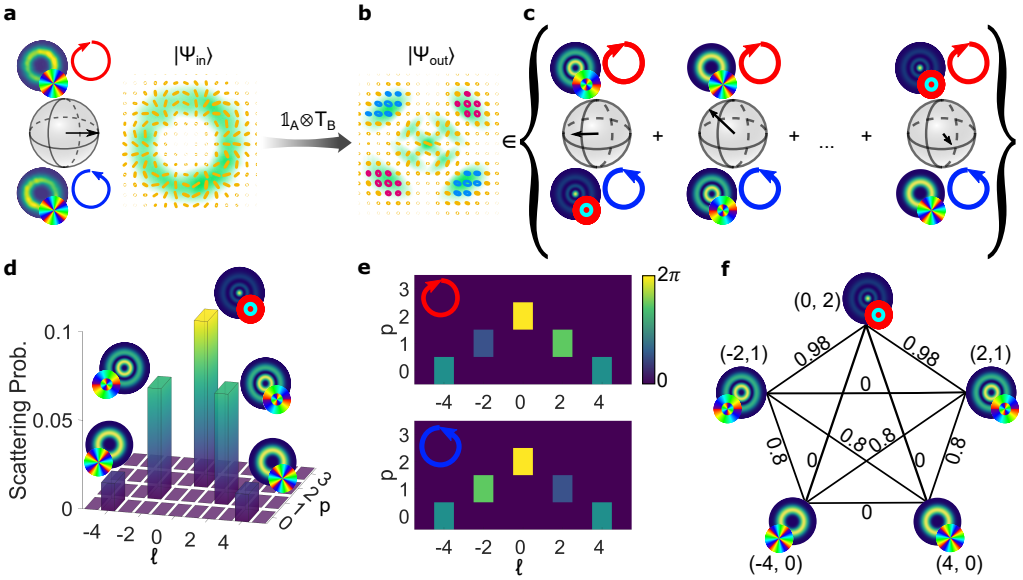


FIGURE 5.3: Impact of scattering across multiple subspaces. (a) The initial vector beam is geometrically represented by an equatorial state vector of unit length on a single $\ell = \pm 4$ HOPS, indicative of a maximally non-separable pure state. The experimental basis states are shown on the poles (as intensities with their respective polarization state on the right) and the vectorial sum (amplitude and polarization structure) is shown on the equator. The tilted lens deforms the initial mode into (b), and this new state can be mapped to multiple HOPSs, each spanned by a different OAM and radial mode (c). Each of these potentially describes a mixed state of some degree of non-separability (non-unit and/or non-equatorial state vectors). The (d) scattering probabilities and (e) phases over the OAM (ℓ) and radial (p) modes for the right (left) ($R(L)$) circular polarization components after the $\ell = \pm 4$ vectorial field traverses the tilted lens channel. The right and left components have equivalent scattering probabilities. There are $N = 5$ states, (ℓ, p), with non-zero probabilities and $N(N-1)/2 = 10$ pairs of multiple subspaces that can be formed. (f) The pairs of states constituting the subspace and corresponding VQF for the vector field in that particular subspace can be represented with a graph having a set of vertices (as the contributing states) connected by weighted edges, respectively. The weights of the edges correspond to the VQF.

5.1.3 Experiment

To generate vector beams we used the setup shown in Fig. 5.2.a. A horizontally polarized Gaussian beam from a HeNe laser (wavelength λ = 633 nm) was expanded and collimated using a $10\times$ objective and a 250 mm focal length lens. The expanded beam was then passed through a HWP before being separated into its horizontally (H) and vertically (V) polarized components using a WP. The plane at the WP was then imaged onto the screen of a DMD (DLP6500) using a $4f$ system. The separation angle of the polarization components from the WP of $\approx 1^\circ$ resulted in the diffracted 0^{th} order components overlapping. To create a desired scalar component mode of the form $U(\mathbf{r}) = |U(\mathbf{r})| \exp(i\Phi)$, where Φ is the phase of the field and U has maximum unit amplitude, the DMD was programmed with a hologram of the form described in Chapter 2 given by

$$H = \frac{1}{2} + \frac{1}{2}\text{sign}\left(\cos\left(2\pi\phi + 2\pi G\right) - \cos(\pi A)\right) , \tag{5.5}$$

with $G(\mathbf{r}) = \mathbf{g} \cdot \mathbf{r}$ a phase ramp function with grating frequencies $\mathbf{g} = (g_x, g_y)$, and $A(\mathbf{r}) = \arcsin(|U(\mathbf{r})|)/\pi$ and $\phi(\mathbf{r}) = \Phi/2\pi$ are the respective, appropriately enveloped, amplitude and phase of the desired complex fields at pixel positions $\mathbf{r} = (x, y)$. Holograms for each polarization component (denoted as H_A and H_B) were multiplexed on the DMD, where the grating frequencies (g_x, g_y) could be chosen to cause the H polarized 1^{st} diffraction order from H_A and the V polarized 1^{st} diffraction order from H_B to spatially overlap. This combined 1^{st} order contained our vector field which was subsequently spatially filtered at the focal plane of a 4f imaging system and imaged onto a second DMD. The second DMD was addressed with a single hologram of the same form as $H_{A/B}$ onto which the turbulence phase screens, along with any correlation filters were encoded (a QWP, was used to convert H and V polarization to R and L respectively). Polarization projections were made using a LP and a QWP before the second DMD. The intensities at the Fourier plane were captured using a CCD (FLIR Grasshopper 3) placed at the focal plane of a $2f$ imaging system.

We measured the non-separability of the vector beams in a basis dependent and independent approach using Stokes parameters and modal decomposition, respectively. Firstly, to measure the Stokes parameters, we used the reduced set of four Stokes intensities, I_H, I_D, I_R and I_L corresponding to the linearly polarized H, D and the circular R and L polarizations. From these measurements we extracted the Stokes parameters,

$$S_0' = I_R + I_L , \tag{5.6}$$
$$S_1' = 2I_H - S_0 , \tag{5.7}$$
$$S_2' = 2I_D - S_0 , \tag{5.8}$$
$$S_3' = I_R - I_L . \tag{5.9}$$

The four intensity projections were acquired through the use of a LP (for I_H and I_D) rotated by 0 and $\pi/4$ radians together with a QWP (for I_R and I_L), oriented at $\pm\pi/4$ radians relative to the fast axis. Subsequently, the basis independent VQF (equivalently non-separability) was determined from $V = \sqrt{1 - (S_1^2 + S_2^2 + S_3^2)/S_0^2}$,

with $S_i = \int S_i'(\mathbf{r})d\mathbf{r}$ being the global Stokes parameters integrated over the transverse plane.

For the basis dependent approach, the overlap between orthogonally polarized projections of the field in question was used as a measure of non-separability, with unity overlap signalling that the field is completely scalar, while a zero overlap indicated a maximally non-separable vector field. This overlap can be characterized by the magnitude of the Bloch vector, s, lying on the surface of a sphere spanned by superpositions of a chosen pair of basis states $|\psi_{1,2}\rangle$. The magnitude can then be seen as a sum-in-quadrature of the Pauli matrix expectation values $\langle\sigma_i\rangle$, as their operation on the basis states gives the unit vectors of the sphere. We can determine these expectation values using projections $\langle P|$ into superpositions of the spatial basis components described by

$$\langle P_j| = \alpha_j\langle\psi_1| + \beta_j\langle\psi_2|\,. \tag{5.10}$$

With $(\alpha,\beta) = \{(1,0),(0,1),\frac{1}{\sqrt{2}}(1,1),\frac{1}{\sqrt{2}}(1,-1),\frac{1}{\sqrt{2}}(1,i),\frac{1}{\sqrt{2}}(1,-i)\}$ for both $|R\rangle$ and $|L\rangle$. These 12 on axis intensity projections are used to calculate the length of the Bloch vector according to

$$\langle\sigma_1\rangle = (I_{13}+I_{23}) - (I_{14}+I_{24})\,, \tag{5.11}$$
$$\langle\sigma_2\rangle = (I_{15}+I_{25}) - (I_{16}+I_{26})\,, \tag{5.12}$$
$$\langle\sigma_3\rangle = (I_{11}+I_{21}) - (I_{11}+I_{22})\,, \tag{5.13}$$

where the i index of I_{ij} corresponds to the $\langle R,L|$ polarization projections and the j index represents the spatial mode projections defined above. The nonseparability is then given by $V = \sqrt{1-s^2}$. In this work the projections into the right- and left-circular polarization components was achieved using a LP and QWP. The subsequent spatial mode projections were performed using a correlation filter encoded into a DMD, and a Fourier lens to produce on-axis intensities I_{ij}.

To determine the adjusted basis, the complex amplitude of an aberrated probe field $|\Psi\rangle_{\text{probe}}$ needs to be measured. This field was approximated using a maximum likelihood estimation procedure, where far field intensities of the right- and left-polarized components of the ideal vector beam through turbulence were captured:

$$I^{R,L}_{\text{probe}} = \langle R,L|\psi(\mathbf{k}=0)\rangle_{\text{probe}}\,. \tag{5.14}$$

Where $|\psi\rangle_{\text{probe}}$ denotes the Fourier transform of $|\Psi\rangle_{\text{probe}}$ and $\mathbf{k} = (k_x,k_y)$. Simulated Fourier intensities, $|\psi\rangle_{\text{Zern}}$, of ideal beams modulated by a phase (modelled by possible weighted combinations of Zernike polynomials Z_j),

$$|\Psi_{\pm1}\rangle_{\text{Zern}} = \exp\left(i\sum_j c_j Z_j\right)\left|\text{LG}_0^{\pm1}\right\rangle\,, \tag{5.15}$$

were generated (spatial dependence has been omitted). The set of coefficients c_j which lead to the lowest square difference in intensity between the experimental and simulated cases,

$$\chi^2 = (I^R_{\text{probe}} - I^R_{\text{Zern}})^2 + (I^L_{\text{probe}} - I^L_{\text{Zern}})^2\,, \tag{5.16}$$

was used to determine the required basis for recovery of the initial beam.

5.1.4 Results

To validate the idea, we built the set-up shown in Fig. 5.2.a, first creating our test vectorial fields before passing them through some perturbing medium. Without any loss of generality, we chose the left- and right-circular basis, $\{|e_1\rangle \equiv |R\rangle$ and $|e_2\rangle \equiv |L\rangle\}$, for the polarization DoF and spatial modes imbued with OAM following $\{|u_1\rangle \equiv |\ell\rangle$ and $|u_2\rangle \equiv |-\ell\rangle\}$, with ℓ the topological charge, forming the topical cylindrical vector vortex beams [310]. The resulting vectorial field was then analysed by both Stokes measurements and modal decomposition. The superimposed intensity and polarization profile of the initial beams (no perturbation) are shown in the inset of Fig. 5.2.a for $\ell = \pm 1$ and $\ell = \pm 4$, both with a radial mode of $p = 0$, with corresponding mode numbers $N = 2p + |\ell| + 1$ of 2 and 5 respectively.

Next, we pass these beams through a highly aberrated system, a tilted lens, illustrated in Fig. 5.2.b. This is known to severely distort OAM modes [435] and is routinely used as an OAM detector by breaking the beam into countable fringes [436]. The results at illustrative distances (Z_1 to Z_3) after the lens are shown in Fig. 5.2.c, for typical tilt angles up to 15° (adjusted to significantly distort the beam). The superimposed intensity and polarization profiles reveal that while the vectorial structure distorts as one moves towards the far-field, the inhomogeneity as measured by the vectorness does not, corroborated by the vectorness of each beam (reported in the insets), all remaining above 93%, i.e., remaining fully vectorial as predicted by the unitary nature of the channel.

In contrast we see that the intensity profiles change morphology, and concomitantly polarization structure. This change can be explained by the coupling of modes outside the original subspace by virtue of the channel operator: the channel scatters the original OAM modes into new mode sets that maintain the same mode number as the input modes. We can visualise this using the HOPS, a geometric representation of vectorial structured light [437, 438], as discussed in Chapter 2. The case for $\ell = \pm 4$ is shown in Fig. 5.3 as an illustrative example. The initial cylindrical vector vortex beam is visualised as an equatorial vector of unit length (a pure state), shown in Fig. 5.3.a. The channel (our tilted lens) maps this initial state to a new field, shown in Fig. 5.3.b, expressed across multiple HOPSs, illustrated in Fig. 5.3.c.

The new HOPSs are made up of all modal pairings that have non-zero modal powers (scattering probabilities). We quantify this by reporting the scattering probabilities and phases for every subspace, shown in Figs. 5.3.d and e, respectively. The initial modes ($\ell_{\text{in}} = \pm 4, p_{\text{in}} = 0$) now only contain ≈12% of the total modal power, with new modal subspaces emerging to carry the rest. The HOPSs are made of *pairings* of these modes, one on each pole, but not all contribute to the vectorness. To determine the contributing pairs, we measure the vectorness for every possible pairing (there are $N(N-1)/2 = 10$ possibilities), with the results shown as a graph in Fig. 5.3.f. In the graph, each vertex corresponds to a non-zero state from (d) and the edges represent possible pairings to form a HOPS. The weight of each edge corresponds to the vectorness of that pairing. The initial subspace $(\pm 4, 0)$ is no longer a non-separable state, with a vectorness of 0, while some of the new subspaces (new HOPSs) can be as high as 98%, i.e., pure vectorial states. The graph can be re-arranged with the zero weighted edges removed to reveal a $K_{3,2}$ bipartite graph structure with two independent vertex sets, $\mathcal{U} = \{(\pm 4, 0), (2, 0)\}$ and $\mathcal{V} = \{(\pm 2, 1)\}$, connected by 6 edges. The notation $K_{3,2}$ indicates that the graph is complete (i.e., all

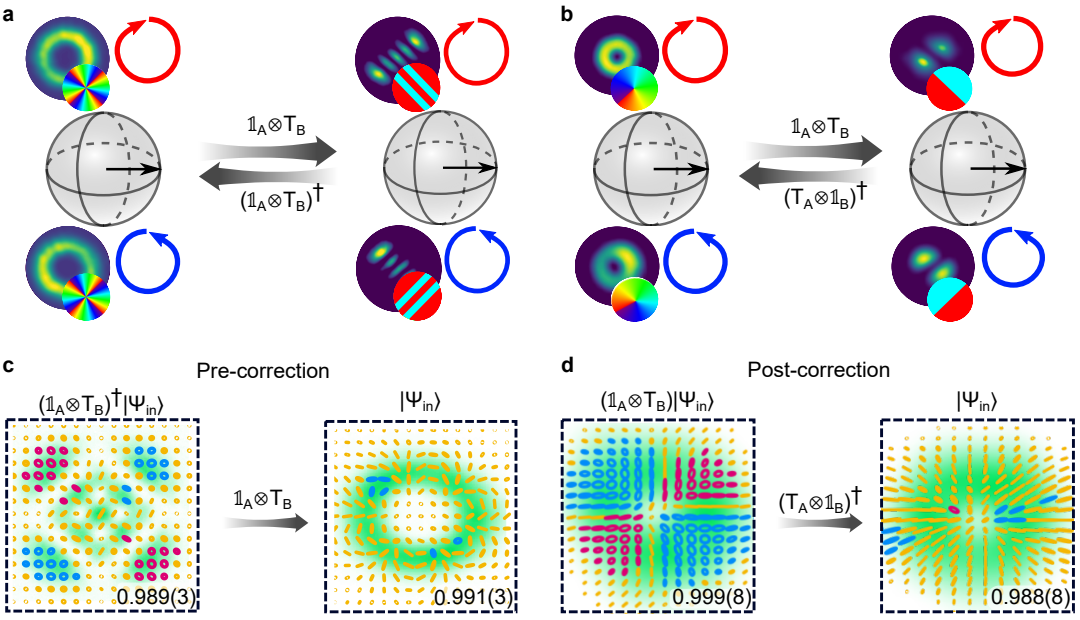


FIGURE 5.4: The unitary channel mapping and its inversion. The unitary channel (tilted lens) $\mathbb{1}_A \otimes T_B$ maps the initial $\ell \pm 4$ vector field from the equator of its corresponding subspace onto a new HOPS spanned by an adjusted basis (shown as experimental images on the poles) where the vectorial structure is also a maximally non-separable pure state. (a) shows the $\ell = \pm 4$ example and (b) the $\ell = \pm 1$ example. Because the unitary channel is a change of basis, the inverse $(\mathbb{1}_A \otimes T_B)^\dagger$ can be applied to map the field back to the original sphere. In (c) the state $(\mathbb{1}_A \otimes T_B)^\dagger |\Psi_{\text{in}}\rangle$ is inserted as a pre-channel correction, resulting in the initial field $|\Psi_{\text{in}}\rangle$ as the output, shown here for $\ell = \pm 4$. In (d) post-channel correction is achieved on the output, shown for $\ell = \pm 1$, where the operation is simply a quarter waveplate, since $\mathbb{1}_A \otimes T_B = T_A \otimes \mathbb{1}_B$ for this subspace.

vertices in each vertex set is connected to all vertices in the other) while the subscripts indicate the number of vertices in each set. Thus of the 10 unique subspaces created from the five scattered modes, only six are non-separable states, occurring for mapping combinations of states between $\mathcal{U}$ and $\mathcal{V}$. One can appreciate that this becomes ever more complicated as the complexity of the medium (and modal scattering) increases.

From this conventional perspective the situation is complicated, but only because the original (OAM) basis modes ($\{|u_1\rangle \equiv |\ell\rangle$ and $|u_2\rangle \equiv |-\ell\rangle\}$) are used to form the HOPSs. We offer a simplification by recognising the unitary nature of the transformation: one can visualise the action of the channel as a mapping (after the channel operation $(\mathbb{1}_A \otimes T_B)$ to a *single* HOPS spanned by the new vectors forming an *adjusted basis*, $|v_1\rangle$ and $|v_2\rangle$, shown in Fig. 5.4.a. This mapping is a result of channel state duality, where the new spatial basis states that the non-separable vectorial field maps onto are isomorphic to the basis states of the unitary channel operation [432]. In this new HOPS the state vector is again maximally non-separable and pure. The new adjusted basis states are complex structured light fields (one may say distorted modes due to the noisy channel), shown as experimental images on the poles. In some special cases the mode may be recognisable: for the $\ell = \pm 1$ state shown in Fig. 5.4.b the mapping returns the Hermite-Gaussian modes as the adjusted basis. This is a special case resulting from the symmetry of the example. Pertinently, the initial state vector in the original HOPS, and the new state vector in the adjusted HOPS are both equatorial and of unit length, representing a maximally non-separable pure state. This means that the vectorness remains intact, even if the polarization structure looks

rather different. Our framework explains why the polarization structure appears to change (a change in HOPS) yet the inhomogeneity does not (the same state vector in each HOPS). This type of invariance to channel noise, also observed in rotationally invariant quantum states, has been exploited to demonstrate robust quantum-key distribution over a 210 m free-space link [439].

Since the mapping is unitary it is possible to invert the action of the channel either as a pre-channel action or post-channel correction, both lossless; conveniently, the experimental steps to determine the channel unitary are straightforward: modal and Stokes projections, and may be implemented in a variety of ways, including sophisticated state-of-the-art adaptive approaches [345, 440, 441]. Using a pre-channel corrective step, we insert the adjusted basis vectorial mode into the tilted lens and allow the aberrations to unravel it back to the original initial state, shown in Fig. 5.4.c. For the $\ell = \pm 1$ example the required inversion operator is just a quarter wave plate, which can be derived analytically from Eqn. (5.4). The counter-intuitive notion that a polarization element can be used to correct a channel that acts only on the spatial mode DoF is explained by the fact that the channel correction, $(\mathbb{1}_A \otimes T_B)^\dagger(\mathbb{1}_A \otimes T_B)$ can be rewritten as $T_A^\dagger T_A \otimes T_B^\dagger T_B = (T_A^\dagger \otimes \mathbb{1}_B)(T_A \otimes \mathbb{1}_B)$, so that the post-channel unitary, $T_B^\dagger = T_A^\dagger$, can be applied to the polarization DoF for $\ell = \pm 1$ (not in general for all modes as this is a special case). The impact of this unitary is shown in Fig. 5.4.d as a post-channel correction, restoring the full vectorial initial state.

Given that the state vector after the channel lives on many HOPSs in the original basis, $\{|u_1\rangle$ and $|u_2\rangle\}$, but only one HOPS in the adjusted basis, $\{|v_1\rangle$ and $|v_2\rangle\}$, it is pertinent to ask in which basis (or HOPS) should one make the vectorial measurement? In the quoted vectorness values thus far, we have circumvented this problem by using a Stokes measurement approach to extract the degree of non-separability [67], with the benefit of sampling in a basis-independent fashion. In contrast, many measurements of structured light are basis dependent, e.g., in classical and quantum communication, where the basis elements form the communication alphabet. In Fig. 5.5.a we show the outcome of a basis-dependent vectorness measurement in the original basis and in the adjusted basis, using the tilted lens as the channel. We see that for some symmetries the choice of basis has no impact on the outcome, as in the case of $\ell = \pm 1$, while for other vectorial fields the impact is significant ($\ell = \pm 4$). It should be noted that the $\ell = \pm 1$ beam through a tilted lens is a special case, because in modal space the state vector has simply been rotated. In general, it is the adjusted basis that always reveals the invariance of the vectorness. The failure of the measurement in the original basis is easily explained by the concatenation of the measurement subspace to just one of the many HOPSs in which the state resides, and the consequent reduction of the state vector to a mixed and separable state because information is lost to other OAM subspaces.

To make clear that the tilted lens is not a special case, we alter the channel to atmospheric turbulence simulated on a SLM, and this time measure the vectorness as a function of the turbulence strength in the original basis and in a basis independent fashion, with the result shown in Fig. 5.5.b. We find that a measurement in the original basis shows a decay in the vectorial nature of the light as the turbulence strength increases, whereas the basis-independent approach reveals the unitary nature of turbulence: while the spatial structure is complex and altered, its vectorness remains intact and invariant to the turbulence strength. Here, all the measurements were performed in the far-field, so that the phase-only perturbations manifest as phase and amplitude effects. We clearly see the paradox: the vectorial structure can

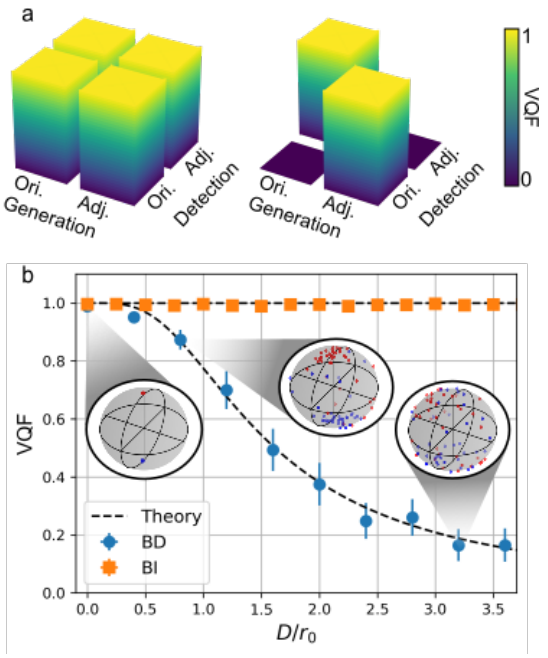


FIGURE 5.5: The choice of measurement basis. (a) Measurement of the vectorness in the original (Ori.) and adjusted (Adj.) basis $\ell = \pm 1$ (left) and $\ell = \pm 4$ (right) in the far-field of the tilted lens. (b) Measurement of the vectorness of an initial $\ell = \pm 1$ mode through experimentally simulated atmospheric turbulence as a function of the turbulence strength (D/r_0). A basis-dependent (BD) measurement in the original basis ($\ell = \pm 1$) shows a decay in vectorness, while the basis-independent (BI) approach reveals an invariance. Experimental data (points) show excellent agreement with theory (dashed curves). The insets show the left (red) and right (blue) polarization projections on the $\ell = \pm 1$ modal sphere for three example turbulence strengths (low, medium and strong). Each point on the spheres represents one instance from the experimental turbulence ensemble. Error bars are plotted as standard deviations from 50 instances of simulated turbulence.

appear robust or not depending on how the measurement was done. This result highlights the important role of measurement in determining the salient properties of vectorial light fields.

The inset spheres in Fig. 5.5.b show the left (red) and right (blue) state vector projections on the $\ell = \pm 1$ modal sphere [442] for low, medium and strong turbulence. Each instance of a turbulence strength is a red (blue) point, the scatter of which and deviation from the poles is indicative of modal cross-talk. This is a visual representation of why the vectorness decays when one considers only one sphere in the original basis: the original states are orthogonal (points on opposite poles with little scatter) but as turbulence increases they disperse across the sphere, resulting in superpositions of OAM, which become maximally mixed. For example, looking only at the $\ell = \pm 1$ subspace, the state may evolve following (ignoring normalisation): $|R\rangle|1\rangle \rightarrow |R\rangle|1\rangle + i|R\rangle|-1\rangle$ and likewise $|L\rangle|-1\rangle \rightarrow |L\rangle|-1\rangle - i|L\rangle|1\rangle$. The original vectorial state becomes $|R\rangle|1\rangle + |L\rangle|-1\rangle \rightarrow |L\rangle|-1\rangle + i|L\rangle|1\rangle + |R\rangle|1\rangle + |R\rangle|-1\rangle = (|R\rangle + i|L\rangle)(|1\rangle + |-1\rangle)$, which is a scalar, diagonally polarized, Hermite-Gaussian beam with a vectorness of 0. One can deduce from this simple example that if only some modal spaces are considered in the beam analysis, then vectorial modes can reduce to scalar modes, but not vice versa.

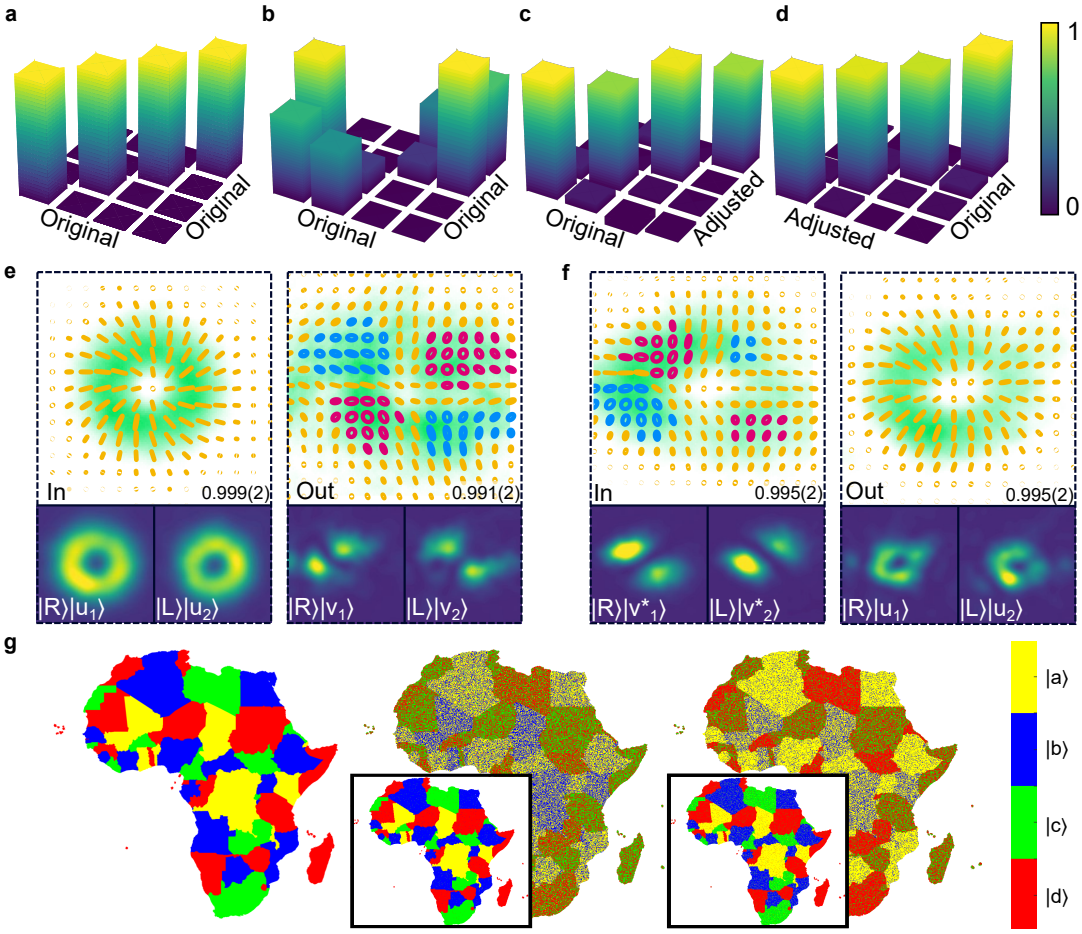


FIGURE 5.6: Unravelling turbulence. Cross-talk matrices for preparation and measurement in the original basis for (a) no turbulence and (b) medium turbulence ($D/r_0 = 1.6$). (c) Measuring or (d) preparing in the adjusted basis removes the cross-talk. (e) The unitary action of the channel distorts the polarization structure of the initial beam but not its vectorial homogeneity, with the vectorness given in the insets. Below the polarization structure are the spatial modes composing the original basis ($u_{1,2}$) and perturbed basis ($v_{1,2}$) along with their polarization states $|R\rangle$ and $|L\rangle$. (f) The unravelling of the turbulence by a lossless unitary applied pre-channel, restoring the initial beam after the turbulence. The adjusted basis modes ($v^*_{1,2}$) and the corrected basis modes ($u_{1,2}$) are shown below the polarization structures with their respective polarization states. In (g), an image (left) encoded in the original basis is distorted after transmission through moderately weak (middle) and medium (right) turbulence characterized by $D/r_0 = 1$ and $D/r_0 = 1.6$, respectively. The same image is transmitted through the channel but decoded in the adjusted basis, for distortion-free communication, shown in the insets.

In Figs. 5.6.a and b we show typical cross-talk matrices with and without turbulence, respectively, where the input and output modes are both expressed in the original basis, $\{|R\rangle|u_1\rangle, |R\rangle|u_2\rangle, |L\rangle|u_1\rangle, |L\rangle|u_2\rangle\}$. The cross-talk in (b) is deleterious for both classical and quantum communication. However, the unitary nature of the channel means that there is an adjusted basis, $\{|R\rangle|v_1\rangle, |R\rangle|v_2\rangle, |L\rangle|v_1\rangle, |L\rangle|v_2\rangle\}$, where the state vector is pure. Consequently, a post- or pre-channel unitary can undo the action of the channel, removing the cross-talk, as shown in Figs. 5.6.c and d. The post-channel unitary is simply a measurement in the new adjusted basis, requiring nothing more than a change to the detection optics (holograms in our example) based on the channel under study. In Fig. 5.6.d, the preparation optics are programmed to prepare the state in the adjusted basis, but measure it in the original

basis, once again returning a cross-talk free result. While the action of the channel is to distort the initial beam, as shown in Fig. 5.6.e, the channel action can be reversed as shown in Fig. 5.6.f, restoring the initial beam. This is a visualisation of the low cross-talk matrix in Fig. 5.6.d: sending in the adjusted basis but measuring in the original basis. The scalar version of the basis modes are shown in Figs. 5.6.e and f as insets below each polarization profile, starting with the original modes, which become perturbed due to turbulence. The adjusted basis, with scalar versions shown in the insets of Fig. 5.6.f, maintains the orthogonality of the modes, and shows the key to the restoration of the initial field. When the adjusted basis is the input, the output is the corrected mode in the original basis. These results suggest that cross-talk free communication is possible with a judiciously selected basis set for the preparation or measurement, exploiting the fact that the vectorial state is intact in the adjusted basis. We use this fact in Fig. 5.6.g to encode graphical information using our modal set, send it across the channel, and decode it on the other side. Turbulence causes cross-talk, distorting the image, but this can easily be overcome by simply decoding (measuring) in the adjusted basis, with results shown for medium and strong turbulence. A measurement in the adjusted basis reveals minimal modal decay, minimal cross-talk and high-fidelity information transfer across this noisy channel, with the small deviations due to experimental imperfections. It is worth noting that if the channel conditions change dynamically, probes will need to be sent at a rate comparable to the channel.

Finally, in Fig. 5.7, we show results that highlight the power and versatility of this framework, and the importance of its implications. The central message is the invariance of the polarization inhomogeneity of vectorial light in a wide range of complex media. In Fig. 5.7.a we report results on a 200 mm physical path through a heated channel where the induced temperature gradients in the air path results in optical distortions (measured in the far field). Although the medium is dynamically changing, in principle in some unknown manner, the vectorness remains intact, a fact tested across multiple input vectorial states and shown in the middle panel for $\ell = \pm 10$. Data was collected at $\approx$ 38 Hz, with the inset showing a zoomed time window. Controlling the source temperature to alter the aberration strength does not alter the vectorness, shown for $\ell = \pm 1$ and $\ell = \pm 5$ examples in the right panel. We also show results measured in the original modal basis: in this case the invariance is lost, again confirming the important role of measurement in the context of vectorial light.

In Fig. 5.7.b we deliver a radially polarized vectorial beam through a setup for optical trapping and tweezing, and introduce aberrations into the path. We show that without any correction the trap stiffness (a measure of how good the trap is) decreases by 10$\times$; after applying a pre-channel unitary transformation we can recover most (6$\times$) of the original trap performance, as illustrated by the restricted motion of the particle in the trap. In our case the adaptive optical routines were rudimentary whereas the state-of-the-art vectorial adaptive solutions [345, 440, 441] promise a much enhanced performance and potentially full recovery.

So far all the channels have acted on the spatial mode and left the polarization as the unaffected DoF. In Fig. 5.7.c we show results after passing $\ell = \pm 1$ vectorial beams through a 1 m length of few-mode optical fiber, stressed and bent to induce polarization coupling. The output beams were measured in both the original basis and adjusted basis, with the cross-talk matrices shown for both in the bottom panels. The results show high cross-talk when measured in the original basis (Fidelity of 39%) and minimum cross-talk when measured in the adjusted basis (Fidelity of

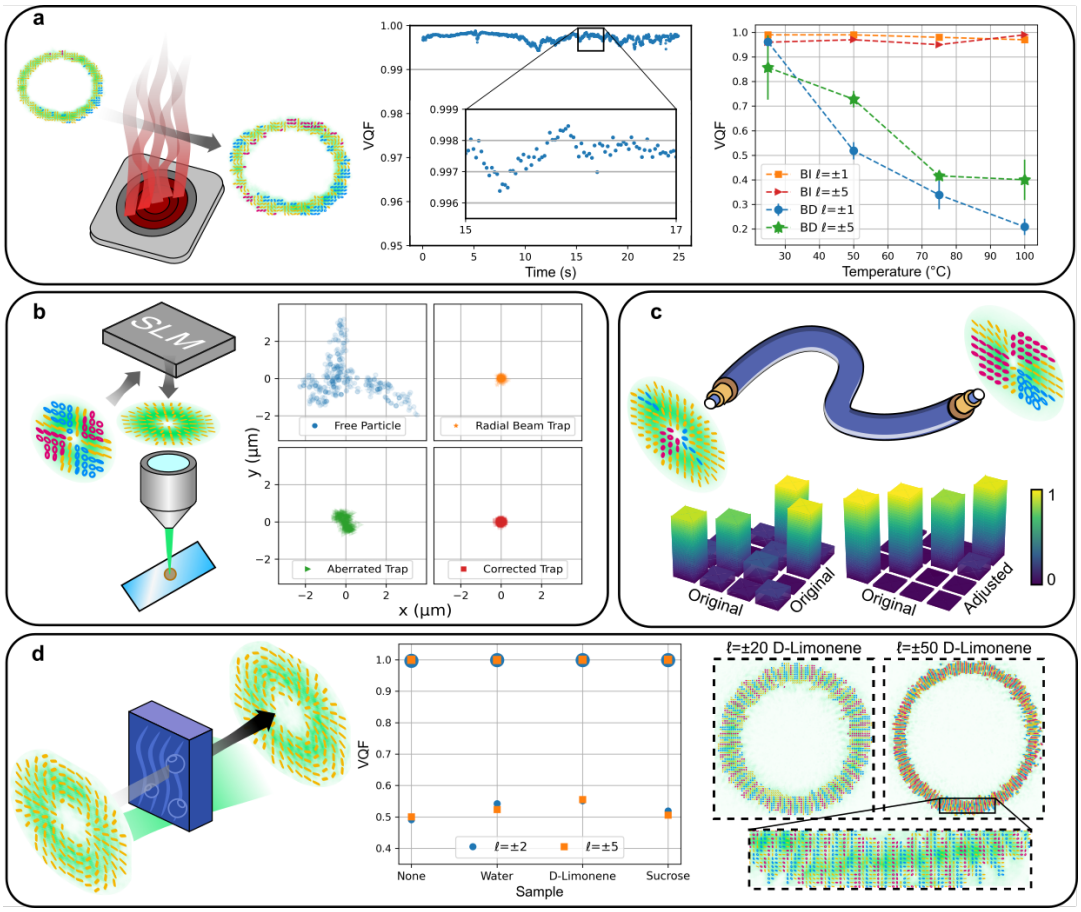


FIGURE 5.7: Real-world channels. (a) Measured VQF as a function of time for an $\ell = \pm 10$ beam over a temperature controlled hot plate ($\approx$ 200 mm path), with the inset showing a zoomed time window. The right panel shows the averaged VQF for particular temperature settings for $\ell = \pm 1$ and $\ell = \pm 5$ beams, showing the invariance of the vectorness for a basis independent (BI) measurement, and a decay when measured in a basis dependent (BD) fashion. (b) Particle movement (measured in x and y co-ordinates) in an optical trapping and tweezing system shows a trap stiffness decrease by $10\times$ when aberrated, recovering by $6\times$ when a pre-channel unitary is applied. (c) Delivery of vectorial light through a 1 m length of few-mode optical fiber shows a low Fidelity of 39% due to cross-talk when measured in the original basis, but increasing to 90% when measured in the adjusted basis. (d) After a 50 mm passage through a liquid medium, the vectorness remains intact (for input VQF of 0.5 and 1) even for chiral media such as D-Limonene. The graph shows VQF measurements for $\ell = \pm 2$ and $\ell = \pm 5$ through various liquids. The insets in the right panel show $\ell = \pm 20$ and $\ell = \pm 50$ output beams after the D-Limonene sample, both with a VQF above 0.99 (measured in a basis independent manner).

90%), confirming that there is a new HOPS where no correction is needed in order to recover the information carried by the state, important for optical communications.

Finally, in Fig. 5.7.d we show results after passing vectorial beams through liquid media of 50 mm length, from water to the chiral media of D-Limonene and Sucrose. In the chiral media, the polarization is the affected DoF, with a local polarization rotation of about 40°, as can be seen in the example data included in the left panel. Regardless of the medium and input beam type, the vectorness remains invariant. The graph (middle panel) shows results for $\ell = \pm 2$ and $\ell = \pm 5$, with input VQFs of 0.5 and 1. The insets on the right show $\ell = \pm 20$ and $\ell = \pm 50$ output beam profiles from the D-Limonene medium, both with a VQF above 0.99.

5.1.5 Discussion and Conclusion

Our results show that vectorial structured light in complex media will evolve from the near-field to the far-field, generally appearing spatially distorted in amplitude, phase and polarization structure, although unaltered in vectorial inhomogeneity. This is explained by the unitary nature of such channels, mapping the state from a HOPS spanned by the original basis to a new HOPS spanned by an adjusted basis, as if only our perspective has altered. Any measurement in the original basis will show an apparent decay of the vectorness in strongly perturbing media even though the degree of polarization remains intact - a hidden invariance that can be observed through a judicious measurement. The role of measurement in quantum studies is well appreciated, and here too the vectorness of a classical beam can be found to be high *and* low, seemingly contradictory outcomes, yet both equally valid based on the choice of measurement. This is not only of fundamental importance but also of practical relevance: we have shown how to make a basis choice for preparation and/or measurement to negate modal cross-talk, with obvious benefits in classical and quantum communication across noisy channels, as well as in imaging through complex media. Recent studies on characterizing multimode fibers for imaging applications offer powerful methods to characterize channels to ensure measurements are done in a manner which preserves information fidelity [443, 444].

The argument for robustness of vectorial light in channels where the polarization is not directly affected is egregious: our quantum notation makes clear that the entire state is altered since its two DoFs are non-separable, in the same way that a true bi-photon quantum state is altered if just one of the two photons is perturbed - both examples of one-sided channels. Our statement is corroborated here by theoretical examples and experimental proof, particularly illustrated by the example of operating on the "unaffected" polarization DoF to correct the entire vectorial state.

Our analysis has considered unitary complex channels where one of the two DoFs is unaffected, covering a myriad of practical cases. These include channels with absolute losses (the same for each mode), which can be accounted for by a renormalisation, while reduced amplitudes and adjusted phases due to modal or polarization cross-talk are fully accounted for in the theory. We remark that not all channels are one-sided and unitary, for example in strongly scattering biological systems [445]. Although scattering can in many cases be reversible and thus handled by our theory, there are cases when this will not be true. Here it is the *relative* modal losses of the initial states, say $|L\rangle\,|\ell\rangle$ and $|R\rangle\,|-\ell\rangle$, that breaks the reversibility, often due to detection that is either time averaged or inefficient: not all the light is collected, and the deficiency is mode dependent. Such cases may be handled by extending the applied quantum toolbox to cover a two-sided channel, and to introduce tools for mixed quantum states, e.g., quantum state tomographies and purity measures, to cover the non-unitary channels. We also point out that the decay dynamics of the channel can be determined from a non-separable state irrespective of whether the channel is unitary [433]. Thus while the invariance of the vectorness requires that the channel is unitary, the pre- and post-channel correction does not, although it may no longer be lossless. Our work has already revealed the benefit of a quantum framework applied to classical vectorial light, and thus one can anticipate further benefits and insights as the scope is extended.

In conclusion, we have provided a general framework for understanding the impact of aberrations on vectorial light fields, in doing so revealing the unitary nature of many complex media. Our work resolves a standing debate on the robustness of vectorial light in complex media, and will be invaluable to the exploding community

working with vectorial structured light and its applications.

5.2 Using our digital tools to achieve robust communication through turbulent free-space

5.2.1 Introduction

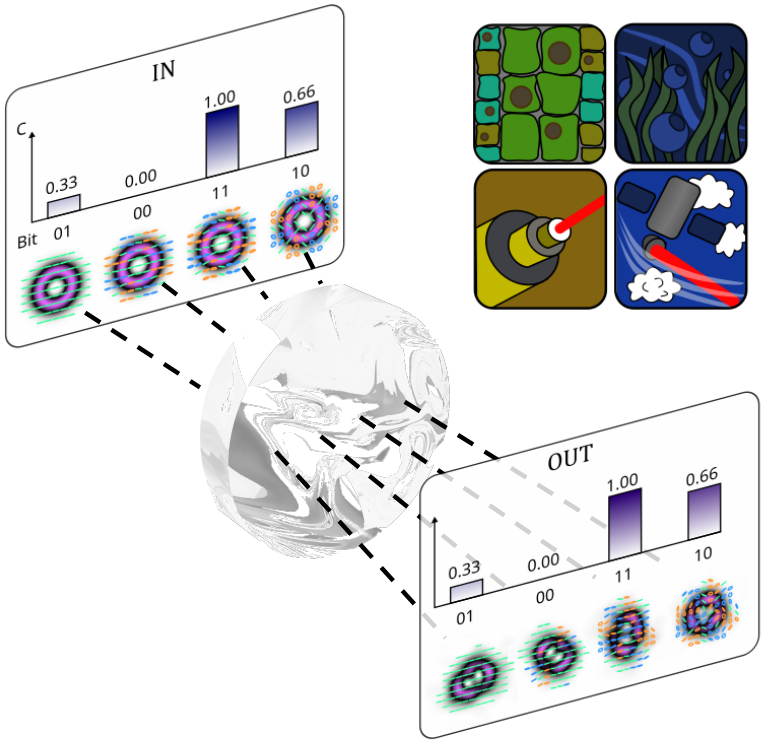


FIGURE 5.8: Modal vectorness for multi-bit encoding. Conceptual visualization of a sequence of vector beams with tuneable vectorness (denoted as C). Each C value is binned into the user-defined basis allowing for the received C to map to a bit-string of length determined by the basis choice. After propagating through an aberrating channel (e.g. atmospheric turbulence, underwater, single-mode fiber or even transparent cellular material) the intensity and polarization profiles of the beams are distorted, however the C is left unaffected.

Optical communication has been an integral part of human society since recorded time, initially visual and thus free-space based, with wire-based solutions only emerging 200 years ago, from copper wire to modern day fiber optics. Today, our optical communication solutions are rapidly reaching their capacity limit [446, 447], requiring new DoFs for packing information into light. Here so-called structured light comes to the fore [11], where light's spatial DoF is used in space division multiplexing (SDM) [448] and MDM (as discussed in Chapter 1) [449], for more channels and more capacity per channel, with significant advances over recent years [450, 451]. Topical among the multiplexing techniques is the use of OAM modes, with excellent reviews available on the topic [452–454]. For instance, in free-space reaching petabits-per-second data rates in the laboratory [455] and 80 gigabits per second over 260 metres [456] while advances in optical fiber have shown 1.6 Tbit/s OAM communication over kilometer lengths with a custom ring core fiber [457]. In both these channels, modal cross-talk is a limiting factor.

Atmospheric turbulence induced modal scattering in free-space links is a particularly severe example [15, 458–465], impeding classical and quantum communication links with structured light to only hundreds of meters [456]. To mitigate this, there has been active research in searching for robust states of structured light in turbulence, including Bessel-Gaussian [122, 466–476], Hermite-Gaussian [477–480], Laguerre-Gaussian [481–485] and Ince-Gaussian [486] beams, but none have shown to be robust in laboratory and real-world experiments. This can be explained best from the perspective of OAM: the atmosphere itself can transfer OAM to and from the beam, so that all beams will be affected equivalently regardless of their initial structure [487]. The utilization of other DOFs such as time binning with appropriate unbalanced interferometric detectors has shown some resilience in turbulence and fiber quantum key distribution experiments [488, 489]. A recent development has been the creation of vectorial combinations of OAM, for vector vortex light [39, 310] with inhomogeneous polarization patterns, and these too have found applications in optical communication, both classical [405, 490] and quantum [131, 341, 491, 492]. Unfortunately they have been found not to be resilient in turbulence [18, 340, 423–425], a fact that has been generalised to many different channels, revealing that the vectorial nature of such light remains invariant even as the spatial pattern itself alters [365]. It is this "altering" or distorting of the pattern that impedes MDM, since its very premise is to "recognise" the original pattern in its undistorted form.

Here we present a novel approach to exploiting MDM in optical communication, foregoing the discrete modal basis of MDM and instead exploiting the polarization inhomogeneity (vectorness) of vectorial light as an encoding basis in a manner that does not require the mode itself to be recognised: a modal basis without the penalty of a modal detection. Similar to amplitude, it spans 0 (scalar light) to 1 (fully vectorial) but with the pertinent benefit that the full range can be used as a high-dimensional alphabet, rather than the two dimensional (on/off) amplitude alphabet. Because the vectorness is an invariant quantity, it remains intact even in the presence of aberrations, where all parties will receive the same information regardless of their particular channel conditions. This implies the potential for optical communication free of channel noise without the need for adaptive optics or digital corrective procedures. We demonstrate our encoding scheme on a highly-aberrated channel of dynamically changing atmospheric turbulence, chosen as an extreme example of a noisy channel, showing correction-free data transmission under a wide range of conditions, with the dimensionality of the encoding primarily limited by detector noise. Our approach replaces conventional amplitude modulation with a modal alternative for potentially orders of magnitude channel information enhancement, offering a new approach to exploiting structured light for optical communication.

5.2.2 Concept

Our technique involves exploiting the spatial mode basis using vector fields of the form

$$|\Psi\rangle = \sqrt{a}|\psi_+\rangle|H\rangle + \sqrt{1-a}|\psi_-\rangle|V\rangle\,, \tag{5.17}$$

where $|\psi_\pm\rangle$ represents any pair of orthogonal spatial modes, $|H(V)\rangle$ are the horizontal(vertical) linear polarization Jones vectors and the real amplitude determined by a ensures that the total power in the field remains constant for $a \in [0,1]$. Such

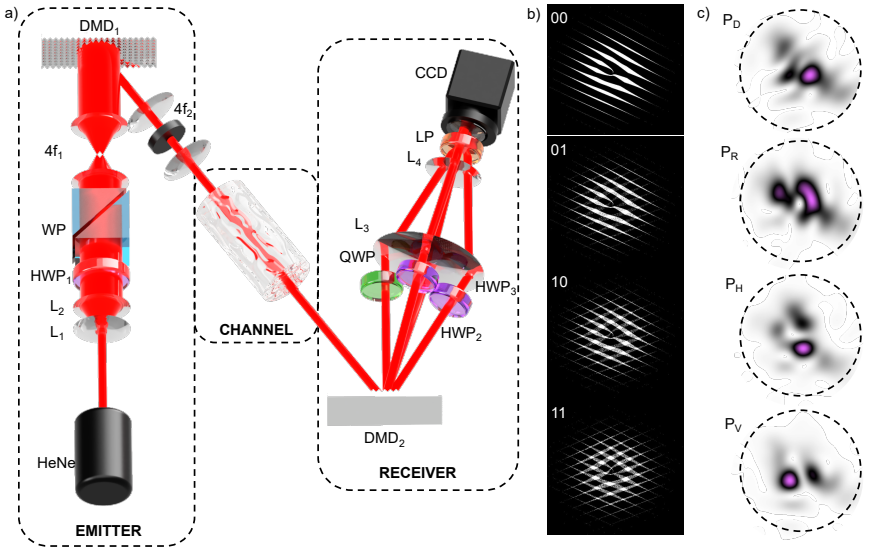


FIGURE 5.9: Experimental demonstration. a) Diagram showing the setup used to generate vector fields with tune-able concurrence (EMITTER) and measure the concurrence (RECEIVER) after propagating through heated air (CHANNEL) - [L_i - lens, HWP_i - half-wave plate, WP - Wollaston prism, DMD_i - digital micro-mirror device, LP - linear polarizer, CCD - charge-coupled device]. b) Exemplar multiplexed binary amplitude holograms used to holographically control the concurrence of generated beams via weighting parameter a - associated bit strings are displayed. c) Exemplar Stokes intensities which are integrated over the dashed circles in order to calculate the concurrence [P_H - horizontal, P_V - horizontal, P_D - diagonal and P_R - right-circular polarization integrated powers].

beams are ubiquitous, and in particular are the natural modes of both optical fiber and free space when $|\psi_\pm\rangle$ are chosen appropriately [39]. It has been shown that fields of this type have a degree of non-separability in their spatial and polarization DoFs which can be quantified using a quantum inspired metric (the concurrence), termed the VQF [66, 493], and which we will refer to as the *vectorness* for short. The concurrence, C, for the field in Eqn 5.17 is given by [494]

$$C = 2\sqrt{\langle\psi_+|\psi_+\rangle\langle\psi_-|\psi_-\rangle - |\langle\psi_+|\psi_-\rangle|^2}\,, \tag{5.18}$$

which reduces to $C = 2|\sqrt{a(1-a)}|$. We see that the weighting parameter a allows C to be varied monotonically from a minimum value of $C = 0$, which represents completely scalar fields (homogeneously polarized), to a maximum of $C = 1$ which represents fields with maximally non-separable spatial and polarization DoFs (inhomogeneously polarized), with the required amplitude modulation trivially found from

$$a = \frac{1}{2}(1 \pm \sqrt{1 - C^2})\,. \tag{5.19}$$

Note that both C and a span from 0 to 1, but the invariance of C allows us to use it as a multi-bit encoding basis. This is because all measures of C will agree on the value regardless of the detector type (and we will show, regardless of the channel conditions), a property inherited from its quantum-inspired description. This is in stark contrast to a measurement of the amplitude, a, directly, where disparate detector efficiencies and channel noise/loss mean no universal agreement on a, thus reducing the full multi-bit bandwidth spanning 0 through to 1, to just 0 or 1 (one

bit) for light or no light. To use the vectorness as measured by C as an encoding basis we can assign unique information to values separated by ΔC, for $N \approx 1/\Delta C$ as the number of elements in the basis (we will return later to how small ΔC can be). This allows us to transmit $d = \log_2 N$ bits per on/off pulse, rather than the one bit with the traditional non-modal amplitude approach. We illustrate this concept in Fig. 5.8, where initial modes (IN) are passed through an aberrating channel and emerge distorted (OUT). Although the spatial mode structure appears scrambled and would have high modal cross-talk, the vectorness remains intact with no cross-talk, and can therefore be used as a multi-bit encoding basis. Here concurrence values of $C = \{0, 0.33, 0.66, 1\}$ are used with $N = 4$ as an example. Although in the remainder of this paper we will use turbulence as our example channel, it could be optical fiber, underwater or cellular media too, as illustrated in Fig. 5.8. It is worth noting that an infinite set of modes can have a given C value, and that modes with different values of C are not orthogonal to each other. Our choice to refer to our encoding alphabet as a basis is made to allow for an easy comparison to alternatives such as MDM.

Now that we have defined how we construct a communication basis from the concurrence of classical vector beams, we can investigate how this basis responds to propagation through the atmosphere where spatially varying air densities due to both pressure and temperature variations induce a spatially varying refractive index according to the Gladstone-Dale law. We select turbulence as an example only, chosen because it represents a particularly dynamic and extreme distorting medium. We can express the total phase change, $\Phi(\vec{r}_T)$, through a width of turbulent medium using the thin screen approximation [495]. This phase acts only on the spatial DoF via the operator in the position basis $\hat{P}_\Phi = \int e^{i\Phi(\vec{r}_T)} |\vec{r}_T\rangle\langle\vec{r}_T| d\vec{r}_T$. We also choose to allow propagation to the far-field for phase-only distortions to become phase and intensity fluctuations, modelled by using a Fourier transform operator $\mathcal{F}$. We thus express our field after propagating into the far-field through turbulence as

$$|\phi_\pm\rangle = \mathcal{F}\hat{P}_\Phi |\psi_\pm\rangle \,. \tag{5.20}$$

We can now take note of an important property of this transformation, namely, that it is unitary and therefore preserves inner products such that $\langle\phi_\pm|\phi_\pm\rangle = \langle\psi_\pm|\psi_\pm\rangle$ and $\langle\phi_\mp|\phi_\pm\rangle = \langle\psi_\mp|\psi_\pm\rangle$. From Eqn 5.18 we see immediately that this implies the invariance of the vectorness (concurrence) to this channel, and obviously extended to other similar transformations. The result of this is illustrated in Fig. 5.8, where the vectorness and the bit-strings they are mapped to are unchanged through the channel, even though the intensity and polarization profiles are severely distorted. This theoretical concept reveals the potential of vectorness as a robust multi-bit information carrier.

5.2.3 Experiment

In order to demonstrate the effective high dimensional information transfer using concurrence as the communication basis, we utilized the setup shown in Fig. 5.9.a. A Gaussian beam produced by a HeNe laser (wavelength 633 nm) was expanded and collimated using lenses L_1 and L_2 respectively. The plane of polarization was converted to 45° using a HWP_1 before passing through a WP which separated the horizontally and vertically polarized components of the expanded beam at an angle of $\approx 1°$. The plane at the WP was imaged onto the screen of a DMD_1 using a $4f_1$

imaging system. DMD_1 was addressed using two multiplexed binary amplitude holograms of the form discussed in Chapter 2

$$H_{A/B}(\vec{r}) = \frac{1}{2} + \frac{1}{2}\text{sign}[\cos\Big(\varphi_{A/B}(\vec{r}_T) + 2\pi(\vec{g}_T^{A/B} \cdot \vec{r}_T)\Big) - \cos(\arcsin(A_{A/B}(\vec{r}_T)))], \tag{5.21}$$

facilitating the modulation of the complex field $U_{A/B} = A_{A/B}e^{i\varphi_{A/B}}$, where $\vec{g}_T^{A/B} = (g_x^{A/B}, g_y^{A/B})$ are grating frequencies [51]. In order to control the relative amplitudes of the resulting beams, complimentary weighted random matrices were multiplied to $H_{A/B}$ according to the method outlined in Ref. [496]. Examples of the multiplexed gratings corresponding the different concurrence values are shown in Fig. 5.9.b. By selecting $\vec{g}^{A/B}$ appropriately, the $+1$ diffraction orders of independently modulated, orthogonally polarized components were spatially overlapped - creating our vector beam $|\Psi\rangle$ [165]. For our case $|\psi_\pm\rangle \equiv LG_0^{\pm 1}$ were chosen. The combined diffraction order was isolated using an aperture placed at the focal plane of a $4f_2$ imaging system - which imaged $|\Psi\rangle$ onto a second DMD_2. DMD_2 was addressed by simple binary diffraction gratings which were multiplexed in order to produce four copies of $|\Psi\rangle$, these copies were allowed to propagate into the far field through a 200 mm length of air - heated by a plate at 185°C. Additionally 3 of the 4 paths were each passed through a $HWP_{2,3}$ (fast axes at 45 and 22.5°, respectively) or a QWP (fast axis at 45°). Lenses L_3 and L_4 were used to demagnify the four beams onto a CCD camera, while filtering using a LP (transmission axis at 0°). The intensities projected onto the CCD correspond to the horizontal, vertical, diagonal and right-circular polarized components - which allowed for the determination of C [106]. Simulated examples of the far field Stokes intensities showing the region of integration (dashed circles) are given in Fig. 5.9.c.

The Stokes measurements were used to calculate C according to [67]

$$C = \sqrt{1 - \frac{(P_H - P_V)^2 + (2P_D - P_H - P_V)^2 + (2P_R - P_H - P_V)^2}{(P_H + P_V)^2}}, \tag{5.22}$$

where $P_i = \int\int I_i dr_T$ represent the powers obtained from the transversely integrated Stokes intensities, the dashed circle in Fig. 5.9.c indicate the necessary region of integration.

In order to probe the performance of our encoding scheme along with alternatives under controllable conditions we implemented a static turbulence phase screen, $\Phi(\vec{r}_T)$ which was used to modulate the phase of our beams during their generation (i.e., on DMD_1). The screen was generated using a fast-Fourier transform technique according to the following expression

$$\Phi(\vec{r}_T) = \text{Re}\left(\mathcal{F}^{-1}(M_{rand}\sqrt{\theta})\right), \tag{5.23}$$

where Re is the real-part, M_{rand} is a complex Gaussian random matrix centered at 0 with unit deviation and θ is the Kolmogorov-Weiner spectrum - conventionally determined (in pixel coordinates (i, j)) by the following expression

$$\theta(i,j) = 0.023 \left(\frac{2D}{r_0}\right)^{\frac{5}{3}} (i^2 + j^2)^{-\frac{11}{3}}, \tag{5.24}$$

where D is the hard aperture of the screen and r_0 is the Fried parameter (diameter over which the root-mean-squared wavefront aberration is 1 radian) [497]. It has been found that Eqn. 5.24 does not accurately model the statistics in the low spatial frequency region (which is notably dominant in the Kolmogorov regime). In order to accurately model this region of the spectrum we employed additional subharmonic sampling according to the method outlined in Ref. [390] - when calculating our spectrum. In our experiment we set $r_0 = 1.5$ mm.

To facilitate a comparison to OAM based encoding we generated scalar $U_{emitted} = LG_p^l$ modes by setting $a = 0$ on DMD_1. For simplicity only the OAM associated azimuthal index l was varied on the interval $[-5, 5]$ to form the communication basis - while setting $p = 0$. To determine crosstalk between basis elements we utilized correlation filters encoded on the second DMD_2 along with the far-field propagation to perform inner product measurements with each of the basis elements. The correlation filters were implemented according to Eqn 5.21 with $U_A = (LG_0^l)^*$ - resulting in the following intensity profile, to be captured in the far-field by the CCD,

$$I_{FF} = \left| \int U_{emitted} (LG_0^l)^* e^{i2\pi \vec{k}_T \cdot \vec{r}_T} d\vec{r}_T \right|^2, \tag{5.25}$$

where it is clear that measuring the on axis intensity in the far-field (i.e., where $\vec{k}_T = 0$) results in the absolute-squared inner product between the emitted field and the given basis element. This procedure is referred to as modal decomposition and a thorough tutorial is available in Ref. [498].

5.2.4 Results

In order to verify the effectiveness of the suggested encoding scheme, we utilized the experimental setup seen in Fig. 5.9.a. The vector beams were generated using an interferometer consisting of a WP, an imaging system and a DMD_1, where the independent complex modulation of horizontally and vertically polarized components of a diagonally polarized (approximate) plane wave was facilitated by two multiplexed binary amplitude holograms [165]. In order to control C the relative efficiencies of the holograms were tuned according to Eqn. 5.19 by varying the amplitude, a, with exemplar multiplexed holograms for a $N = 4$ vectorness basis shown in Fig. 5.9.b. The vectorial beam was passed through a dynamically aberrated channel created by a heater set to a steady state temperature of $T \approx 185°$C to induce turbulence in the air along ≈ 200 mm of beam path. The resulting beam was then passed to the detection system, a custom built single shot Stokes polarimetry arrangement, composed of a second DMD_2 encoded with multiplexed binary gratings which diffracted 4 copies of the vector field into the ± 1 diffraction orders. The beams were allowed to propagate to the far field for the phase distortion to manifest as both amplitude and phase distortion. The four copies were then imaged onto the sensor of a CCD camera - initially a low-cost FLIR Chameleon was used and later replaced by a higher quality FLIR Grasshopper to highlight the role of detector sensitivity. Prior to the CCD, each of the four copies were passed through different combinations of QWP and HWPs and a common LP in order to capture horizontally (I_H), vertically (I_V), diagonally (I_D) and right-circularly (I_R) polarized Stokes intensity measurements from which

the concurrence was calculated. Furthermore, the Stokes measurements form an over-complete set of polarization projections, making our decoding step independent of the polarization basis that the modes were prepared in, i.e., the sender or the channel can alter the polarization basis without any effect on the outcome. Figure 5.9.c shows exemplar Stokes intensities integrated over the dashed region to obtain associated powers $P_{H,V,D,R}$, from which the concurrence could be determined.

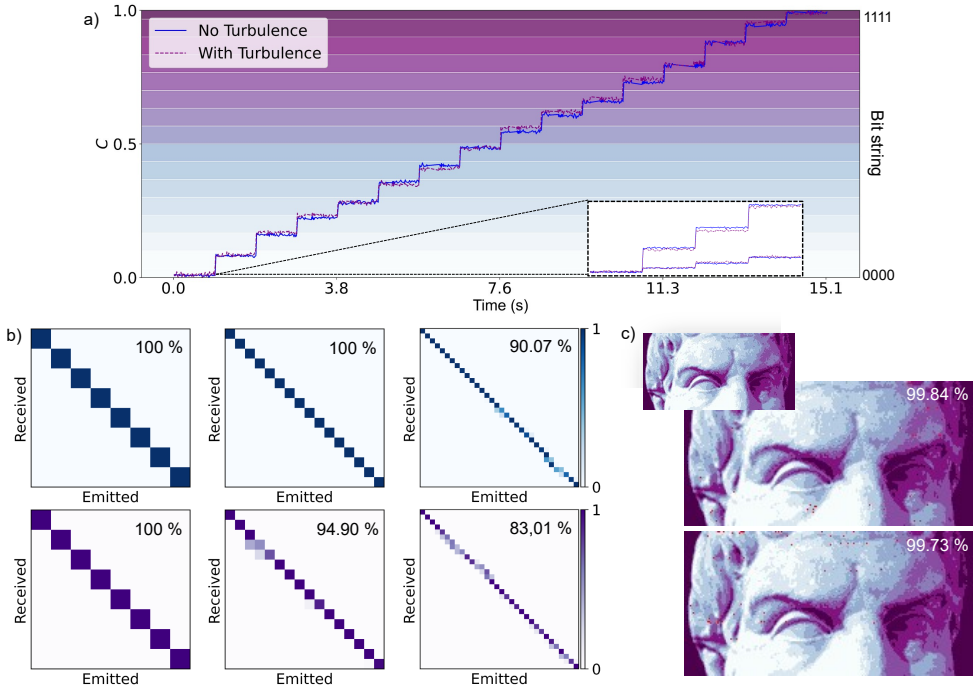


FIGURE 5.10: Discretized bases, crosstalk and multi-bit information transfer. a) Received concurrence of an input value varied in 16 discreet steps (insets show partial results for 8 and 32 steps) through still (solid line) and turbulent (dashed line) air. b) Crosstalk matrices (with associated fidelity) for the emitted and received concurrence through still (top) and turbulent (bottom) air for bases with $N = 8, 16$ and 32 (left to right). c) 3 Bit (8 level) image transmitted through still (top) and turbulent (bottom) air - red pixels highlight errors (inset shows the ground truth image) while the values report the image fidelity.

The key to our proposed technique is that C does not change due to beam distortions, so that the full range from 0 to 1 can be used in a user-defined number of steps (N) independent of how perturbing the channel is. This sub-division of the available encoding space is shown in Fig. 5.10.a for $N = 16$ (with $N = \{8, 32\}$ included as an inset). To indicate the low cross-talk, the transmitted vector beam was allowed to "idle" at each basis element (delineated into bins shown as shaded bars) while repeated measurements were taken, confirming only small dynamic changes in still and turbulent air alike. The robust nature of the encoding is quantified by the cross-talk matrices in Fig. 5.10.b for up to $N = 32$, corresponding to 32 vectorial modes, yet with low levels of cross-talk. Finally, we use the system to transmit information over this dynamically changing turbulent channel with no adjustment to the received data signal, resulting in the high fidelity images shown in Fig. 5.10.c for still (top) and turbulent (bottom) air using $N = 8$. The consistency of the results under different channel conditions validates the concept. The notable feature of this approach is that the number of modes used can be tailored up to a maximum

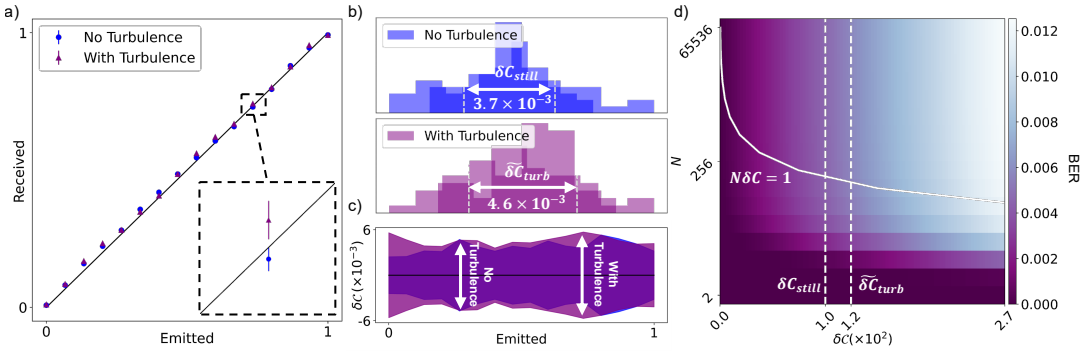


FIGURE 5.11: Noise, statistical variation and bit-errors. a) Mean received concurrence (over 50 points) per element in the $N = 16$ basis in both still (circles) and turbulent (triangles) air, error bars are visible in the inset. b) Distribution of received C values about their target for two example basis elements both without (top) and with (bottom) turbulence - values report the mean deviations across the $N = 16$ basis. c) Measured standard deviation for each element in the $N = 16$ basis through still and turbulent air, where the large overlap illustrates the turbulence invariance. d) Theoretically predicted BER as a function of the statistical spread δC and basis choice N, the white solid line represents the points where $N\delta C = 1$ and white dashed lines represent the deviations of our receiver under different channel conditions - δC_{still} and $\widetilde{\delta C}_{\text{turb}}$.

$N_{\max} = 1/\delta C$, where δC is the inherent noise in the system - calculated as the standard deviation of repeated measurements at a given C. Next, we take a closer look at this to estimate the potential of the approach and show that, as expected, δC is limited primarily by detector noise and not the condition of the channel itself.

We see from the "idling" results of Fig. 5.10.a that the noise of the still and turbulent air are comparable, suggesting that detector noise is the primary cause of the statistical variation of a given vectorness about the target, as anticipated by theory. This results in only very small errors between what was emitted and what was received, as illustrated in Fig. 5.11.a, for $N = 16$ as an example, with the small scale of the deviation shown in the enlarged inset. A statistical analysis of the experimental noise, shown graphically in Fig. 5.11.b, reveals that $\delta C_{\text{still}} \approx 3.7 \times 10^{-3}$ in still air (no turbulence), which we take to represent the inherent noise of the detection system. When instantaneous turbulent channel conditions are introduced we observe only a slight increase in noise to $\widetilde{\delta C}_{\text{turb}} \approx 4.6 \times 10^{-3}$, which we attribute to the signal-to-noise limit of our detector, i.e., defocusing aberrations in turbulence leading to a signal below the noise threshold of the detector. It is notable that a spread in the received C due to detector noise is akin to the spectral spread observed in OAM due to channel aberrations. We confirm too that the noise is not mode specific, as shown by the small difference in variance with and without turbulence in Fig. 5.11.c. This validates the claim that the minimum subdivision of the encoding space, or maximum number of modes (or bits), is limited primarily by detector noise and not channel conditions, contrary to traditional MDM schemes.

To probe the potential of this approach we consider how a given detector noise limit (δC) and subdivision choice (N) affect the resulting bit-error-rate (BER), using our turbulence channel as an example. The BER is the ratio of incorrectly received bits to total transmitted bits and represents how crosstalk in the scheme affects the information transfer. The results of this are illustrated graphically in Fig. 5.11.d. In order to quantify the relationship between the cross-talk inducing δC and the system fidelity we can analytically inspect the overlap of neighbouring basis elements to

reveal the BER for a given choice of basis (i.e., N) and δC

$$\mathrm{BER}(N, \delta C) = \bar{E}(N)\frac{\delta C}{2}\sqrt{\frac{\pi}{2}}e^{-\frac{N-2}{2\delta C}}\,\mathrm{erf}\left(\sqrt{\frac{2}{\delta C}}\right), \tag{5.26}$$

where erf() represents the error function and $\bar{E}(N)$ is the mean bit-error per erroneously binned measurement for a given basis choice. If we inspect the BER for different channel conditions and basis choices, as shown in Fig. 5.11.d, we notice how reducing δC allows for the use of denser choice of basis while maintaining a low BER. The white curve in Fig. 5.11.d indicates the special cases of $N\delta C = 1$, with the associated line acting as a limit for the basis size under a given channel condition. It is however notable that this overlap is significantly lower than the modal overlap experienced by MDM systems, and that with a suitable detector acceptable BERs on the order of 10^{-9} are plausible. These results indicate that the effectiveness of the technique for high dimensional information transfer places the burden only on the signal-to-noise ratio of the detector system. The notably poor diffraction efficiency offered by DMDs [50] and the limited dynamic range of CCDs means that our particular system suffers from a lower signal-to-noise ratio (SNR) than alternatives, such as the sensitive photodiodes used in free-space communication links. The white dashed lines in Fig. 5.11.d indicate the mean measured δC for our system with and without turbulence. The associated $\mathrm{BER}(N = 8) \approx 2 \times 10^{-3}$ also agrees well with the fidelities reported in Fig. 5.10.c.

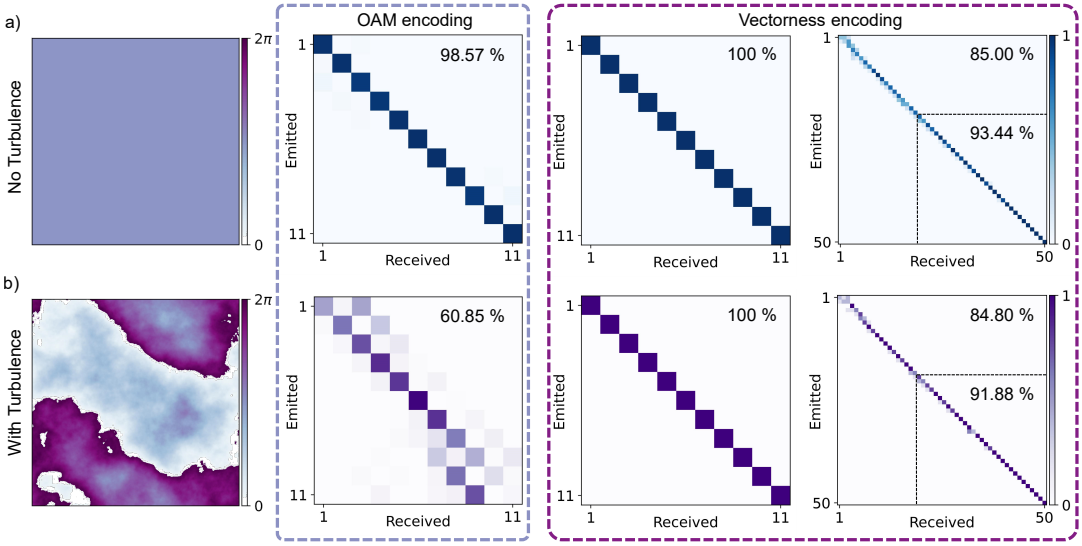


FIGURE 5.12: Channel invariance comparison to OAM encoding. Crosstalk matrices through a) ideal and b) aberrated channels using both OAM (with $N = 11$) and vectorness (with $N = 11$ and $N = 50$) encoding schemes. The turbulence phase screen used to aberrate the beams is shown in the left panel of b). A truncated 32 mode subset of the $N = 50$ basis is highlighted showing improved fidelity.

The highlight of the proposed vectorness based encoding scheme is that its invariance to the channel conditions makes it a more robust choice in comparison to direct modal encoding schemes. To illustrate this point we will use the OAM basis as a comparative example. Additionally we changed the CCD detector from a 58.81 dB to a 60.62 dB dynamic range model to further highlight the role of detector choice and to allow a larger basis to be explored (more subdivisions). The setup

of Fig. 5.9 (using DMD_2) allowed us to generate and perform spatial mode projections on scalar LG_p^l modes of azimuthal order l and radial order p. The results in Fig. 5.12.a show the baseline case with no turbulence for direct OAM encoding and indirect OAM encoding using the vectorness. In the direct OAM case, we utilized an 11 mode basis spanning the range of $l \in [-5, 5]$ with $p = 0$. Here the size of the OAM basis was constrained by the system aperture, as increasing mode order results in ever larger beams. Our modal vectorness scheme can be executed with low order modes for the same size across all bit-levels, and so does not suffer from this limitation. The detector noise limit in the vectorness scheme allowed us to probe a $N = 50$ basis, far larger than OAM encoding approaches which typically range from $N = 4$ to $N = 34$ [244, 405]. To the best of our knowledge $N = 50$ is the largest number of vectorial modes used in a communication link experiment. The fidelities in Fig. 5.12.a are indicative of experimental limitations (detector noise) and can be taken as the baseline values.

Since we are interested in the effect of the channel, we replaced our dynamic channel aberrations with a static turbulence phase screen with a fixed Fried parameter of $r_0 = 1.5$ mm as displayed in the left panel of Fig. 5.12.b. The static screen allowed for a controlled comparison of how the crosstalk in each of the schemes changes when the channel perturbations are introduced. The 37.72 % decrease in fidelity using OAM encoding is in stark contrast to the 0 % change observed using vectorness encoding at the same basis size ($N = 11$). When pushing the dimensionality of the new encoding scheme further, the channel induced crosstalk only increases marginally, in the order of 1 %.

There are two important observations one can make from the vectorness data in Fig 5.12. Firstly, the baseline (no turbulence) indicates how the detector choice limits the maximum subdivision number by its noise, setting a limit on how small δC can be. For our detector at $N = 50$ the baseline fidelity is 85 %, but can be improved to 93 % by using a smaller number of modes ($N < N_{\max}$) in the available space - while also maintaining the modal density. With better detector technology the maximum number of modes can be significant, or the impact of noise made small by using a smaller encoding alphabet. Secondly, a comparison of the baseline (no turbulence) to the baseline with channel noise (with turbulence) makes crystal clear that the channel noise is negligible in the new scheme, validating our central claim. In no other modal approach is the channel noise so inconsequential, here contributing in the ≈ 1 % range.

5.2.5 Discussion and conclusion

The proposed scheme and the results of our demonstration reveal its potential for multi-bit encoding using a new modal version of amplitude modulation, enabling a d-fold increase in information density using existing amplitude modulation technology for superior data transmission rates. Unlike MDM systems, our source of noise is primarily detector based, while being almost completely invariant to channel noise, negating the need for adaptive error-correction, which we showed using atmospheric turbulence as an extreme example. This is illustrated by using 50 spatial modes in a turbulent channel with a cross-talk that is comparable to the no-turbulence case, differing by less then 2 %. For comparison, our crosstalk observed between 11 OAM modes was 37.72 % but zero for the vectorness approach, while other studies with 4 orthogonal vector OAM modes have reported $\approx 20\%$ crosstalk even in weak turbulence conditions [18], while crosstalk between 7 neighbouring

scalar OAM modes reached 13.2% even with corrective measures [499]. Our observed BER using 8 modes, on the order of 2×10^{-3}, is comparable to that achieved in error-corrected MDM systems [244], even though we have deployed only a proof-of-principle version of the experiment with rudimentary detectors. Our direct comparison to OAM encoding revealed the superior channel invariance while also demonstrating how a larger basis (e.g., up to 50) can be achieved with the same system aperture which constrained the OAM basis to 11 modes - this is since the increase of basis size in OAM encoding requires larger mode orders which require larger apertures, while our approach can scale the number of modes up to the noise floor of the detector.

We point out that while the particular vector beams we used were composed of OAM endowed LG_p^l modes, the core feature of our scheme is the utilization of vector beams (our modal basis) in a manner that does not require the spatial modes nor orthogonal polarization components to be detected or recognised. Instead, only their vectorness is detected, an invariant quantity that is found by an *integrated* modal signal. It is a modal approach without the penalty of detecting modes. In this regard, while our proof-of-principle experiment used a CCD camera for detection, fast and sensitive photo-detectors are all that is required for a real-world implementation. Because our channel-invariant basis is derived from spatial modes without actually detecting them and is independent of the polarization basis that they were prepared in, it brings with it some significant benefits over traditional MDM schemes that use the modes themselves as the basis. For instance, (i) system misalignment is mitigated since the integrated detection (a power) is spatially invariant, (ii) the modes can be selected with low order to reduce divergence [14] (since more information does not require higher mode numbers), (iii) like amplitude modulation, our scheme does not prohibit other enhancement schemes such as wavelength division multiplexing (WDM) to further improve information density, including even MDM if modal correction is applied, and further, (iv) unlike alternative vectorial techniques [405, 490], the nature of our detection scheme is over-complete even in the polarization basis, and therefore means that the sender and receiver do not have to agree on the measurement basis, allowing the scheme to work even in polarization scrambling media such as stressed optical fiber. These benefits are provided by the vectorness, a physical quantity which displays resilience to transformations which generally hinder modal communication systems. The trade-off lies in the scaling of our scheme, in order to increase d by 1, N has to double (for comparison MDM requires a $N = d$ increase in the number of modes for an equivalent increase in capacity). This places the burden of performance on the power and amplitude modulation resolution of the emitter and the SNR of the receiver - all factors which already receive considerable attention in free space optical communication systems.

To conclude, we have presented how the vectorness of vectorial light can be used as a new modal version of amplitude modulation, exploiting spatial modes in a manner that makes them effectively immune to channel noise, with the number of modes used limited primarily by the sensitivity of the detectors used. We have demonstrated high fidelity, correction-free, multi-bit information transfer to verify our technique, even through dynamic turbulence, an extreme example of a communications channel. Our approach can be extended to other channels too, such as optical fiber and under-water, since the invariance property will hold in all such channels. We believe this approach will open up a new avenue for high-bandwidth optical communication, with the immediate benefits of MDM but without the modal cross-talk challenges. The vectorness presents a new scheme for information encoding, which if coupled with other communication techniques such as WDM and SDM,

can be used to push the boundaries of optical communication.

Chapter 6

Conclusion and prospectives

We can now summarize the contents of this thesis which has followed the development, demonstration and optimization of vectorial light generation and detection tools in a variety of contexts.

We first looked at a vectorial light generation device based on an SLM where multiplexed gratings were used to generate independently modulated BG_l superpositions, where we subsequently combined the beams using a Mach-Zehnder inteferometer with a HWP used to convert the polarization of one of the beams into its orthogonal state. The fields we produced using this arrangement exhibited the theoretically predicted acceleration and detection of local Stokes vectors and the associated non-linear change in the global structure. The evolution of individual Stokes intensity projections revealed interesting propagation dynamics related to the flow of energy into and out of the central region of the beams and concurrent work indicate that these structures may prove useful for high precision distance measurements [500]. While the SLM based device was capable of producing adequate vectorial fields, some significant systematic problems were revealed during its implementation. Foremost, the independent paths taken by the orthogonally polarized beams prior to combination in the BS resulted in fluctuations between the relative phase between them. These fluctuations were highly sensitive to environmental vibrations, indicating that the arrangement would not be suitable in industrial environments where such factors may be unavoidable. Changes in these relative phases are particularly detrimental when polarization structure is sensitive to local polarization rotations, such as in our work where we had to insure a stable laboratory environment in order to acquire the necessary measurements.

We then proceeded to generate novel vectorial fields by using a DMD and PBS. This arrangement involved separating horizontal and vertical plane waves with the PBS and then directing them onto a DMD screen at a small 1.5° separation angle. We then exploited the polarization insensitivity of the DMD by encoding multiplexed holograms in order to independently shape the amplitude and phase of each beam. We also tuned the grating frequencies of each of the holograms in order to make the two, independently modulated, orthogonally polarized beams colinear thus creating our vector beam. The polarization dependent phase and amplitude control allowed us to emulate an axicon lens, in which one half of the lens transmitted left circular polarization and the other half transmitted right circular polarization. By analysing the resulting fields using Stokes polarimetry we observed the (theoretically predicted) formation of a 1-dimensional BG_l beam along the splitting axis (line between the two orthogonally transmitting halves). In the direction orthogonal to the splitting axis we observed a pattern with dependence on the Struve functions,

which are solutions to the inhomogeneous Bessel equation highlighting the polarization inhomogeneity of our vectorial axicon. Furthermore, the diagonal polarization projections produced regular BG_l beams. These three observations can each be explained by three of the Arago-Fresnel laws, revealing the rich polarization interference dynamics of the vectorial axicon enabled by this device. The implementation of the DMD as both a shaping and interfering component drastically improved the relative phase stability in comparison to the SLM based device. A limitation of the device lay in the requirement of the 1.5° separation angle between the plane waves incident on the DMD, which neccesitated a very large distance ($\approx$ 1 m) between the PBS and the DMD. This large distance makes this device impractical for many applications and resulted in significant beam wander. The use of a DMD, however, presented a variety of advantages since the polarization independence of the DMD afforded superior interferometric stability.

We then continued exploring the capabilities of the aforementioned DMD and PBS based device. We did this by exploiting the dynamic polarization dependent modulation of the device in order to produce a probe beam, which could be used to characterize spatially resolved birefringence and chirality. The probe was formed by a scalar Gaussian beam, the polarization of which was made to dynamically trace out a great circle on the Poincaré sphere. For measuring linear birefringence this circle was on the meridian, while for measuring chirality (or circular birefringence) it was on the equator. This probe beam was passed through the desired sample and imaged using a CCD camera after being filtered by a diagonally transmitting linear polarizer. The imaged intensity would vary sinusoidally with the changing probe polarization, the sample would cause local shifts to this curve from which the birefringence/chirality could be extracted. We verified the device's performance on simple wave-plates, chiral sugar solutions and SLMs as well complex liquid crystal optics and even nanostructured metasurfaces. This investigation showed that in addition to generating effectively arbitrary vectorial fields, the device could also function as a metrology device enabling superior SLM calibration, pharmaceutical concentration measurements and optical efficiency calculations.

The next iteration of the device retained the DMD as a shaping and interfering component, but replaced the PBS with a WP. The WP naturally separates the horizontal and vertical polarization components at a 1° angle, which allows for a simple (and short) $4f$ imaging system to be used to image the two beams onto the DMD screen. This compact arrangement allowed for very stable interference along with a beam that remained stable. We utilized this compact device to generate optical skyrmions in the Stokes vector field with BG_l modes. Along with generating the structures we also engineered them in a way that the local Stokes vectors precessed along propagation, which is analogous to the time dynamic behaviour of light-matter and magnetic systems. The device was able to accurately generate and digitally propagate these interesting structures in an incredibly stable manner.

Having developed a capable generation device, we then looked at detecting vectorial light using a self-contained digital device. The first aspect we looked at was extracting the spatially varying Stokes parameters of vectorial light fields. We did this by separating the right- and left-circularly polarized components of the field using a PG. Each of the two components were then imaged onto separate halves of a DMD screen, after which they were interfered using a Mach-Zehnder interferometer while using a half-wave plate to ensure both beams have the same polarization. The DMD

was used to adjust the relative phase between the two components allowing for the projection of the horizontally and diagonally polarized intensities which were captured by a CCD. Furthermore the intensities of right- and left-circular components could be measured by blocking one of the interferometer arms using the DMD. The results we obtained showed that with these four intensity projections all the Stokes parameters could be reliably recovered in a spatially varying manner. During the processed we also attempted to use a similar PG based device in conjunction with an SLM, which revealed itself to be incapable of extracting all the Stokes parameters due to the inherent polarization dependence of the SLM. Similar to the issues encountered using a Mach-Zehnder interferrometer to generate vectorial light, the relative phase (between the right- and left-circularly polarized components) fluctuated under the influence of vibration. Since two of the four the Stokes intensity projection are reliant on the relative phase, this is a significant issue which necessitates a stable laboratory environment for accurate sensing.

We then optimized the design of the detection device by replacing the PG with a WP, such that the device took an almost identical form to the vectorial light generator. Consequently, this analyzer inherited the superior stability of the generation device. We demonstrated the effectiveness of the analyzer by using it to perform a complete characterization of a variety of vectorial fields. This comprised of Stokes polarimetry, modal projection and combined polarization and modal measurements, which gave us the complete polarization profiles along with the constituent modes as well as their relative amplitudes and phases. The fields analyzed comprised of simple vector beams as well as those with large OAM and fractional OAM which have intricate modal distributions. This device is a powerful tool for general polarization sensing of relevance to certain types of microscopy and metrology (e.g., stress imaging), while the modal projections could effectively automate communication schemes based on spatial modes.

We moved on from polarization and modal based measurements using our DMD based devices and investigated the ability of a DMD to perform as a broadband wavefront sensor. This involved placing the DMD in the far field of a $4f$ imaging system which allowed for the, single shot, propagation of a field to different positions on the same CCD sensor. From these intensity profiles the wavefront of field could be recovered using the TIE, solved using Fourier based techniques. The results obtained using the device indicate the reliable recovery of a variety wavefront aberrations at multiple wavelengths and at with multiple polarizations. The simplicity of the arrangement means it can also be integrated into the aforementioned vectorial light analyzer, where a user would simply need to image the far-field of their beam into the device. The polarization insensitivity also indicates that the analysis can be readily extended to vectorial fields, however consideration needs to be taken to avoid singularities in the wavefronts.

Once we had refined versions of our vectorial light generator and analyzer we used them in order to to understand the physics of fields propagating through distorting media. We used the generator to create various vectorial fields, passed these fields through various perturbing channels and then used the analyzer to project the constituent modes into various bases. We revealed that the vectorial state itself remained invariant, as the channels produced simple unitary rotations within the vector space containing the constituent spatial modes. By correctly characterizing the channel the projection basis could be appropriately rotated to recover the state

correctly. The generator and analyzer were capable of automating this process, from the generation to the characterization and adjusted measurement in an incredibly convenient manner. Revealing how these devices can allow us to probe the fundamental physics of vector fields at will.

Once we utilized our vectorial light tools to verify the invariance of vector states of light to aberrating channels, we exploited this property in order to develop a powerful information encoding scheme which allowed us to communicate through atmospheric turbulence with almost no errors. We achieved this by encoding information into the VQF of vector beams, since the unitary nature of the channels leave this property of the beams completely unperturbed even though the spatial structure undergoes distortion. We demonstrated this by generating various vector beams with different VQFs and transmitting them through turbulent air, after which we measured the VQF using a single shot Stokes polarimetry measurements. The results showed a significant improvement over conventional modal encoding schemes which rely on spatial mode projections and overcomes a problem which has hindered high capacity information transfer in free-space optical communication for decades.

Now that that effective designs for a vectorial light generator and analyzer have been identified, further development to reduce the size and enable the portability of the devices is necessary to demonstrate commercial viability. An even more compact arrangement of the generation device is shown in Fig. 6.1, where the expansion and collimation of an input laser beam is integrated into the imaging system between the WP and DMD reducing the footprint for the optical components to <15 cm, this serves as the bedrock for a self contained vectorial light generator prototype which is currently under development for deployment to laboratories for field testing. Alternative versions of the analyzer could replace the expansion and collimation system with a $4f$ imaging system, enabling the direct characterization of beams from laser sources.

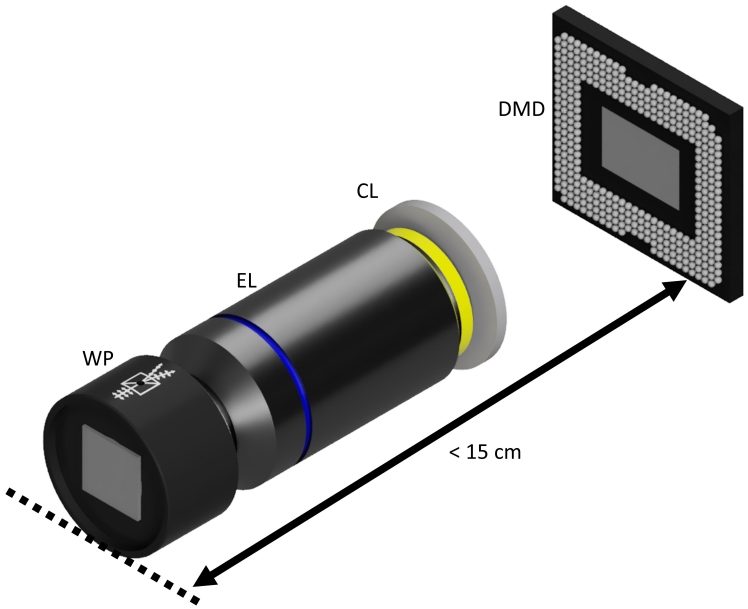


FIGURE 6.1: Elements for a versatile, compact and stable vectorial light generator.

Throughout the development and demonstrations presented throughout this thesis, additional implementations of the devices for birefringence measurements were conducted in collaboration with industry partners. The measurements were taken on artificially stressed, and pumped laser rods to obtain quantitative information for laser engineers to use in their design process. Modal projective measurements using the analyzer were also conducted on a new class of nanostructured silica modal plates [56]. The coinciding of these deployments with the development process highlights the growing need for widespread access to cheap, versatile, self-contained vectorial light generators and analyzers throughout academia and industry. It is my hope that this thesis serves as the first thorough documentation for tools that will become ubiquitous in a range of future applications which make use of light to advance our species as has been the case for past millennia.

Bibliography

1. Sines, G. & Sakellarakis, Y. A. Lenses in antiquity. *American Journal of Archaeology* **91,** 191–196 (1987).
2. Darrigol, O. *A history of optics from Greek antiquity to the nineteenth century* (OUP Oxford, 2012).
3. Maiman, T. H. *et al.* Stimulated optical radiation in ruby (1960).
4. Seideman, T. Barcodes sweep the world. *Wonders of modern technology* (1993).
5. Starkweather, G. *Laser printer design* in *OSA Annual Meeting* (1990), TuBB2.
6. Everest, C. & Everest, M. *Thermal measurements using infrared thermometry-A new generation of infrared thermometers* in *31st International Instrumentation Symposium* (1985), 1–6.
7. Easton, R. L. *TAT-8: The First Transatlantic Optical System* in *Fiber Optics Reliability: Benign and Adverse Environments III* **1174** (1990), 114–122.
8. PASKI, R. M. *The TAT-8 undersea cable system* in *Optical Fiber Communication Conference* (1989), THL1.
9. Hilton, P. A. *Early days of laser cutting* in *Lasers in Material Processing* **3097** (1997), 10–16.
10. McDonald, M. B. *et al.* Central photorefractive keratectomy for myopia: the blind eye study. *Archives of Ophthalmology* **108,** 799–808 (1990).
11. Forbes, A., de Oliveira, M. & Dennis, M. R. Structured light. *Nature Photonics* **15,** 253–262 (2021).
12. Keller, U. & Paschotta, R. *Ultrafast Lasers* 2002.
13. Agrawal, G. P. *Fiber-optic communication systems* (John Wiley & Sons, 2012).
14. Willner, A. E. & Liu, C. Perspective on using multiple orbital-angular-momentum beams for enhanced capacity in free-space optical communication links. *Nanophotonics* **10,** 225–233 (2021).
15. Cox, M. A. *et al.* Structured light in turbulence. *IEEE Journal of Selected Topics in Quantum Electronics* **27,** 1–21 (2020).
16. Lochab, P., Senthilkumaran, P. & Khare, K. Designer vector beams maintaining a robust intensity profile on propagation through turbulence. *Physical Review A* **98,** 023831 (2018).
17. Cheng, W., Haus, J. W. & Zhan, Q. Propagation of vector vortex beams through a turbulent atmosphere. *Optics express* **17,** 17829–17836 (2009).
18. Cox, M. A., Rosales-Guzmán, C., Lavery, M. P., Versfeld, D. J. & Forbes, A. On the resilience of scalar and vector vortex modes in turbulence. *Optics Express* **24,** 18105–18113 (2016).
19. Chason, E. & Mayer, T. Thin film and surface characterization by specular X-ray reflectivity. *Critical Reviews in Solid State and Material Sciences* **22,** 1–67 (1997).

20. Rodríguez-Fajardo, V. *et al.* All-digital 3-dimensional profilometry of nano-scaled surfaces with spatial light modulators. *Applied Physics B* **127,** 1–7 (2021).
21. Welsh, B. M., Ellerbroek, B. L., Roggemann, M. C. & Pennington, T. L. Fundamental performance comparison of a Hartmann and a shearing interferometer wave-front sensor. *Applied optics* **34,** 4186–4195 (1995).
22. Dudley, A., Milione, G., Alfano, R. R. & Forbes, A. All-digital wavefront sensing for structured light beams. *Optics express* **22,** 14031–14040 (2014).
23. Sroor, H., Moodley, C., Rodríguez-Fajardo, V., Zhan, Q. & Forbes, A. Modal description of paraxial structured light propagation: tutorial. *JOSA A* **38,** 1443–1449 (2021).
24. Zuo, C. *et al.* Transport of intensity equation: a tutorial. *Optics and Lasers in Engineering* **135,** 106187 (2020).
25. Ohmi, M. *et al.* High-sensitivity two-dimensional thermal-and mechanical-stress-induced birefringence measurements in a Nd: YAG rod. *Applied optics* **33,** 6368–6372 (1994).
26. Stoffel, D. *et al.* Study of stress-induced birefringence in an inhomogeneously pumped laser rod with spatial and temporal resolution. *JOSA B* **36,** 1044–1053 (2019).
27. Abbe, E. VII.—On the Estimation of Aperture in the Microscope. *Journal of the Royal Microscopical Society* **1,** 388–423 (1881).
28. Hell, S. W. & Wichmann, J. Breaking the diffraction resolution limit by stimulated emission: stimulated-emission-depletion fluorescence microscopy. *Optics letters* **19,** 780–782 (1994).
29. Török, P. & Munro, P. The use of Gauss-Laguerre vector beams in STED microscopy. *Optics express* **12,** 3605–3617 (2004).
30. Quabis, S., Dorn, R., Eberler, M., Glöckl, O. & Leuchs, G. Focusing light to a tighter spot. *Optics communications* **179,** 1–7 (2000).
31. Dorn, R., Quabis, S. & Leuchs, G. Sharper focus for a radially polarized light beam. *Physical review letters* **91,** 233901 (2003).
32. Olarte, O. E., Andilla, J., Gualda, E. J. & Loza-Alvarez, P. Light-sheet microscopy: a tutorial. *Advances in Optics and Photonics* **10,** 111–179 (2018).
33. Duocastella, M. & Arnold, C. B. Bessel and annular beams for materials processing. *Laser & Photonics Reviews* **6,** 607–621 (2012).
34. Niziev, V. & Nesterov, A. Influence of beam polarization on laser cutting efficiency. *Journal of Physics D: Applied Physics* **32,** 1455 (1999).
35. Sroor, H., Litvin, I., Naidoo, D. & Forbes, A. Amplification of higher order Poincare sphere beams through Nd: YLF and Nd: YAG crystals. *Applied Physics B* **125,** 1–9 (2019).
36. Grier, D. G. A revolution in optical manipulation. *nature* **424,** 810–816 (2003).
37. Simpson, N., Allen, L. & Padgett, M. Optical tweezers and optical spanners with Laguerre–Gaussian modes. *Journal of modern optics* **43,** 2485–2491 (1996).
38. Kritzinger, A., Forbes, A. & Forbes, P. B. Optical trapping and fluorescence control with vectorial structured light. *Scientific reports* **12,** 1–12 (2022).
39. Rosales-Guzmán, C., Ndagano, B. & Forbes, A. A review of complex vector light fields and their applications. *Journal of Optics* **20,** 123001 (Nov. 2018).

40. Rubinsztein-Dunlop, H. *et al.* Roadmap on structured light. *Journal of Optics* **19,** 013001. http://stacks.iop.org/2040-8986/19/i=1/a=013001 (2017).
41. Marrucci, L., Manzo, C. & Paparo, D. Optical Spin-to-Orbital Angular Momentum Conversion in Inhomogeneous Anisotropic Media. *Physical Review Letters* **96,** 163905 (2006).
42. Rubano, A., Cardano, F., Piccirillo, B. & Marrucci, L. Q-plate technology: a progress review. *JOSA B* **36,** D70–D87 (2019).
43. Gutiérrez-Vega, J. C. Pancharatnam–Berry phase of optical systems. *Optics letters* **36,** 1143–1145 (2011).
44. Sephton, B., Dudley, A. & Forbes, A. Revealing the radial modes in vortex beams. *Applied optics* **55,** 7830–7835 (2016).
45. Piccardo, M. & Ambrosio, A. Recent twists in twisted light: A Perspective on optical vortices from dielectric metasurfaces. *Applied Physics Letters* **117,** 140501 (2020).
46. Yu, N. & Capasso, F. Flat optics with designer metasurfaces. *Nature materials* **13,** 139–150 (2014).
47. Arbabi, E., Kamali, S. M., Arbabi, A. & Faraon, A. Full-Stokes imaging polarimetry using dielectric metasurfaces. *Acs Photonics* **5,** 3132–3140 (2018).
48. Rosales-Guzmán, C. & Forbes, A. *How to shape light with spatial light modulators* (SPIE Press, 2017).
49. Arrizón, V., Ruiz, U., Carrada, R. & González, L. A. Pixelated phase computer holograms for the accurate encoding of scalar complex fields. *JOSA A* **24,** 3500–3507 (2007).
50. Scholes, S., Kara, R., Pinnell, J., Rodríguez-Fajardo, V. & Forbes, A. Structured light with digital micromirror devices: a guide to best practice. *Optical Engineering* **59,** 041202 (2019).
51. Lee, W.-H. Binary computer-generated holograms. *Applied Optics* **18,** 3661–3669 (1979).
52. Instruments, T. *DLPLCR65EVM* https://www.ti.com/tool/DLPLCR65EVM (2023).
53. AG, H. P. *Spatial Light Modulators* https://holoeye.com/spatial-light-modulators/ (2023).
54. Cox, M. A., Toninelli, E., Cheng, L., Padgett, M. J. & Forbes, A. A high-speed, wavelength invariant, single-pixel wavefront sensor with a digital micromirror device. *IEEE Access* **7,** 85860–85866 (2019).
55. Forbes, A. Structured Light from Lasers. *Laser & Photonics Reviews* **13,** 1900140 (2019).
56. Coursault, D. & Brasselet, E. Nanostructured silica spin–orbit optics for modal vortex beam shaping. *Nanophotonics* **11,** 805–812 (2021).
57. Piccardo, M. *et al.* Roadmap on multimode light shaping. *Journal of Optics* **24,** 013001 (2021).
58. Born, M. & Wolf, E. *Principles of optics: electromagnetic theory of propagation, interference and diffraction of light* (Elsevier, 2013).
59. Vallone, G. On the properties of circular beams: normalization, Laguerre–Gauss expansion, and free-space divergence. *Optics letters* **40,** 1717–1720 (2015).

60. Allen, L., Beijersbergen, M. W., Spreeuw, R. & Woerdman, J. Orbital angular momentum of light and the transformation of Laguerre-Gaussian laser modes. *Physical review A* **45,** 8185 (1992).
61. Feng, S. & Winful, H. G. Physical origin of the Gouy phase shift. *Optics letters* **26,** 485–487 (2001).
62. Siegman, A. E. *Lasers* 645 (University science books, 1986).
63. Durnin, J., Miceli Jr, J. & Eberly, J. Diffraction-free beams. *Physical review letters* **58,** 1499 (1987).
64. Goldstein, D. H. *Polarized light* (CRC press, 2017).
65. Lyons, D. W. An Elementary Introduction to the Hopf Fibration. *Mathematics Magazine* **76,** 87–98 (2003).
66. Ndagano, B., Sroor, H., McLaren, M., Rosales-Guzmán, C. & Forbes, A. Beam quality measure for vector beams. *Optics letters* **41,** 3407–3410 (2016).
67. Selyem, A., Rosales-Guzmán, C., Croke, S., Forbes, A. & Franke-Arnold, S. Basis-independent tomography and nonseparability witnesses of pure complex vectorial light fields by Stokes projections. *Physical Review A* **100,** 063842 (2019).
68. Wootters, W. K. Entanglement of formation and concurrence. *Quantum Information & Computation* **1,** 27–44 (2001).
69. Yi, X. *et al.* Hybrid-order Poincaré sphere. *Physical Review A* **91,** 023801 (2015).
70. Mirhosseini, M. *et al.* Rapid generation of light beams carrying orbital angular momentum. *Optics express* **21,** 30196–30203 (2013).
71. Siviloglou, G., Broky, J., Dogariu, A. & Christodoulides, D. Observation of accelerating Airy beams. *Physical Review Letters* **99,** 213901 (2007).
72. Vetter, C., Eichelkraut, T., Ornigotti, M. & Szameit, A. Generalized radially self-accelerating helicon beams. *Physical review letters* **113,** 183901 (2014).
73. Schulze, C. *et al.* Accelerated rotation with orbital angular momentum modes. *Physical Review A* **91,** 043821 (Apr. 2015).
74. Webster, J., Rosales-Guzmán, C. & Forbes, A. Radially dependent angular acceleration of twisted light. *Optics Letters* **42,** 675 (Feb. 2017).
75. Patsyk, A., Bandres, M. A., Bekenstein, R. & Segev, M. Observation of accelerating wave packets in curved space. *Physical Review X* **8,** 011001 (2018).
76. Voloch-Bloch, N., Lereah, Y., Lilach, Y., Gover, A. & Arie, A. Generation of electron Airy beams. *Nature* **494,** 331–335 (2013).
77. Pierce, J. *et al.* Coiling free electron matter waves. *New Journal of Physics* **21,** 043018 (2019).
78. Efremidis, N. K., Chen, Z., Segev, M. & Christodoulides, D. N. Airy beams and accelerating waves: an overview of recent advances. *Optica* **6,** 686–701 (2019).
79. Bandres, M. A. *et al.* Accelerating optical beams. *Optics and Photonics News* **24,** 30–37 (2013).
80. Chen, J., Wan, C. & Zhan, Q. Vectorial optical fields: recent advances and future prospects. *Science Bulletin* **63,** 54–74 (Jan. 2018).
81. Otte, E., Alpmann, C. & Denz, C. Polarization Singularity Explosions in Tailored Light Fields. *Laser & Photonics Reviews* **12,** 1700200 (2018).

82. Aiello, A., Banzer, P., Neugebauer, M. & Leuchs, G. From transverse angular momentum to photonic wheels. *Nature Photonics* **9,** 789 (2015).
83. Zhang, G.-L., Tu, C., Li, Y. & Wang, H.-T. Observation of polarization topological singular lines. *Photonics Research* **7,** 705 (May 2019).
84. Bauer, T. *et al.* Observation of optical polarization Möbius strips. *Science* **347,** 964–966 (Jan. 2015).
85. Larocque, H. *et al.* Reconstructing the topology of optical polarization knots. *Nature Physics* **14,** 1079–1082 (July 2018).
86. Khajavi, B. & Galvez, E. J. High-order disclinations in space-variant polarization. *Journal of Optics* **18,** 084003 (July 2016).
87. Holmes, B. M. & Galvez, E. J. Poincaré Bessel beams: structure and propagation. *Journal of Optics* **21,** 104001 (Sept. 2019).
88. Otte, E., Rosales-Guzmán, C., Ndagano, B., Denz, C. & Forbes, A. Entanglement beating in free space through spin–orbit coupling. *Light: Science & Applications* **7,** 18009 (2018).
89. Vyas, S., Kozawa, Y. & Miyamoto, Y. Creation of polarization gradients from superposition of counter propagating vector LG beams. *Opt. Express* **23,** 33970–33979 (2015).
90. Li, P. *et al.* Self-accelerated optical activity in free space induced by the Gouy phase. *Photonics Research* **8,** 475 (Mar. 2020).
91. Li, P. *et al.* Polarization oscillating beams constructed by copropagating optical frozen waves. *Photonics Research* **6,** 756 (June 2018).
92. Fu, S., Zhang, S. & Gao, C. Bessel beams with spatial oscillating polarization. *Scientific Reports* **6** (Aug. 2016).
93. Li, P. *et al.* Quasi-Bessel beams with longitudinally varying polarization state generated by employing spectrum engineering. *Optics Letters* **41,** 4811 (Oct. 2016).
94. Gibson, C. J., Bevington, P., Oppo, G.-L. & Yao, A. M. Control of polarization rotation in nonlinear propagation of fully structured light. *Physical Review A* **97,** 033832 (2018).
95. Yao, A. M., Gibson, C. J. & Oppo, G.-L. Control of spatially rotating structures in diffractive Kerr cavities. *Optics express* **27,** 31273–31289 (2019).
96. Wen, B., Rui, G., Jun, H., Cui, Y. & Gu, B. Polarization rotation and singularity evolution of fundamental Poincaré beams through anisotropic Kerr nonlinearities. *Journal of Optics* (2020).
97. Freund, I. Second-harmonic generation of polarization singularities. *Optics Letters* **27,** 1640 (Sept. 2002).
98. Buono, W. T. *et al.* Polarization-controlled orbital angular momentum switching in nonlinear wave mixing. *Optics Letters* **43,** 1439 (Mar. 2018).
99. Radwell, N., Clark, T., Piccirillo, B., Barnett, S. & Franke-Arnold, S. Spatially Dependent Electromagnetically Induced Transparency. *Physical Review Letters* **114** (Mar. 2015).
100. Wang, J., Castellucci, F. & Franke-Arnold, S. Vectorial light-matter interaction - exploring spatially structured complex light fields. *arXiv*. arXiv: 2007.11316v1 [physics.optics] (July 22, 2020).

101. Kanda, N. *et al.* The vectorial control of magnetization by light. *Nature Communications* **2** (June 2011).

102. Berry, M. V. Optical currents. *Journal of Optics A: Pure and Applied Optics* **11,** 094001 (2009).

103. Zenkova, C. Y., Gorsky, M. P., Maksimyak, P. P. & Maksimyak, A. P. Optical currents in vector fields. *Applied Optics* **50,** 1105 (Mar. 2011).

104. Otte, E., Asché, E. & Denz, C. Shaping optical spin flow topologies by the translation of tailored orbital phase flow. *Journal of Optics* **21,** 064001 (Apr. 2019).

105. Ruchi & Senthilkumaran, P. Optical currents in Poincaré beams. *Physical Review A* **102** (July 2020).

106. Singh, K., Tabebordbar, N., Forbes, A. & Dudley, A. Digital Stokes polarimetry and its application to structured light: tutorial. *JOSA A* **37,** C33–C44 (2020).

107. Barron, L. D. *Molecular light scattering and optical activity* ISBN: 9780511231216 (Cambridge University Press, Cambridge, UK New York, 2004).

108. Schadt, M. & Helfrich, W. Voltage-dependent optical activity of a twisted nematic liquid crystal. *Applied Physics Letters* **18,** 127–128 (Feb. 1971).

109. Nafie, L. A. Infrared and Raman vibrational optical activity: theoretical and experimental aspects. *Annual Review of Physical Chemistry* **48,** 357–386 (Oct. 1997).

110. Barron, L. D., Hecht, L., McColl, I. H. & Blanch, E. W. Raman optical activity comes of age. *Molecular Physics* **102,** 731–744 (Apr. 2004).

111. Plum, E. *et al.* Metamaterials: Optical Activity without Chirality. *Physical Review Letters* **102** (Mar. 2009).

112. Park, H. S., Kim, T.-T., Kim, H.-D., Kim, K. & Min, B. Nondispersive optical activity of meshed helical metamaterials. *Nature Communications* **5** (Nov. 2014).

113. Durnin, J. Exact solutions for nondiffracting beams. I. The scalar theory. *JOSA A* **4,** 651–654 (1987).

114. Bouchal, Z., Wagner, J. & Chlup, M. Self-reconstruction of a distorted nondiffracting beam. *Optics Communications* **151,** 207–211 (1998).

115. Milione, G. *et al.* Measuring the self-healing of the spatially inhomogeneous states of polarization of vector Bessel beams. *Journal of Optics* **17,** 035617 (2015).

116. Li, P. *et al.* Generation and self-healing of vector Bessel-Gauss beams with variant state of polarizations upon propagation. *Optics express* **25,** 5821–5831 (2017).

117. Litvin, I. A., McLaren, M. G. & Forbes, A. A conical wave approach to calculating Bessel–Gauss beam reconstruction after complex obstacles. *Optics Communications* **282,** 1078–1082 (2009).

118. Arlt, J., Garces-Chavez, V., Sibbett, W. & Dholakia, K. Optical micromanipulation using a Bessel light beam. *Optics Communications* **197,** 239–245 (2001).

119. Garces-Chavez, V., McGloin, D., Melville, H., Sibbett, W. & Dholakia, K. Simultaneous micromanipulation in multiple planes using a self-reconstructing light beam. *Nature* **419,** 145–147 (2002).

120. Kollarova, V. *et al. Application of nondiffracting beams to wireless optical communications* in *Proc. SPIE* **6736** (2007), 67361C.

121. Li, S. & Wang, J. Adaptive free-space optical communications through turbulence using self-healing Bessel beams. *Scientific Reports* **7,** 43233 (2017).

122. Ahmed, N. *et al.* Mode-division-multiplexing of multiple Bessel-Gaussian beams carrying orbital-angular-momentum for obstruction-tolerant free-space optical and millimetre-wave communication links. *Scientific reports* **6,** 22082 (2016).

123. Chen, S. *et al.* Demonstration of 20-Gbit/s high-speed Bessel beam encoding/decoding link with adaptive turbulence compensation. *Optics letters* **41,** 4680–4683 (2016).

124. Trichili, A. *et al.* Detection of Bessel beams with digital axicons. *Optics express* **22,** 17553–17560 (2014).

125. Fahrbach, F. O., Simon, P. & Rohrbach, A. Microscopy with self-reconstructing beams. *Nature Photonics* **4,** 780–785. https://www.nature.com/articles/nphoton.2010.204 (Nov. 2010).

126. Jáuregui, R. & Hacyan, S. Quantum-mechanical properties of Bessel beams. *Physical Review A* **71,** 033411 (2005).

127. McLaren, M., Mhlanga, T., Padgett, M. J., Roux, F. S. & Forbes, A. Self-healing of quantum entanglement after an obstruction. *Nature communications* **5,** ncomms4248 (2014).

128. McLaren, M. *et al.* Entangled Bessel-Gaussian beams. *Opt. Express* **20,** 23589–23597 (2012).

129. Pyragaite, V. *et al.* Parametric down-conversion of higher-order Bessel optical beams in quadratic nonlinear medium. *Opt. Commun.* **240,** 191–200 (2004).

130. McLaren, M., Romero, J., Padgett, M. J., Roux, F. S. & Forbes, A. Two-photon optics of Bessel-Gaussian modes. *Phys. Rev. A* **88,** 033818 (2013).

131. Nape, I. *et al.* Self-healing high-dimensional quantum key distribution using hybrid spin-orbit Bessel states. *Optics express* **26,** 26946–26960 (2018).

132. Gutiérrez-López, D. *et al.* Spatial control of spontaneous parametric down-conversion photon pairs through the use of apertured Bessel-Gauss pump beams. *Physical Review A* **100,** 013802 (2019).

133. Ryu, C., Henderson, K. & Boshier, M. Creation of matter wave Bessel beams and observation of quantized circulation in a Bose–Einstein condensate. *New Journal of Physics* **16,** 013046 (2014).

134. Grillo, V. *et al.* Generation of Nondiffracting Electron Bessel Beams. *Phys. Rev. X* **4,** 011013 (2014).

135. Chávez-Cerda, S. A new approach to bessel beams. *Journal of Modern Optics* **46,** 923–930 (1999).

136. Vicente, O. C. & Caloz, C. Bessel beams: a unified and extended perspective. *Optica* **8,** 451–457 (2021).

137. Vasilyeu, R., Dudley, A., Khilo, N. & Forbes, A. Generating superpositions of higher–order Bessel beams. *Opt. Express* **17,** 23389–23395 (2009).

138. McLeod, J. H. The axicon: a new type of optical element. *JOSA* **44,** 592–597 (1954).

139. Vasara, A., Turunen, J. & Friberg, A. T. Realization of general nondiffracting beams with computer-generated holograms. *JOSA A* **6,** 1748–1754 (1989).

140. Indebetouw, G. Nondiffracting optical fields: some remarks on their analysis and synthesis. *JOSA A* **6,** 150–152 (1989).

141. Durnin, J. E. & Eberly, J. H. *Diffraction free arrangement* US Patent 4,887,885. Dec. 1989.

142. Uehara, K. & Kikuchi, H. Generation of nearly diffraction-free laser beams. *Applied Physics B: Lasers and Optics* **48,** 125–129 (1989).

143. Pääkkönen, P. & Turunen, J. Resonators with Bessel–Gauss modes. *Optics communications* **156,** 359–366 (1998).

144. Khilo, A. N., Katranji, E. G. & Ryzhevich, A. A. Axicon-based Bessel resonator: analytical description and experiment. *JOSA A* **18,** 1986–1992 (2001).

145. Rogel-Salazar, J., New, G. & Chávez-Cerda, S. Bessel–Gauss beam optical resonator. *Optics communications* **190,** 117–122 (2001).

146. Litvin, I. A., Khilo, N. A., Forbes, A. & Belyi, V. N. Intra–cavity generation of Bessel–like beams with longitudinally dependent cone angles. *Optics express* **18,** 4701–4708 (2010).

147. Lohmann, A. W., Ojeda-Castañeda, J. & Serrano-Heredia, A. Bessel functions: parallel display and processing. *Opt. Lett.* **19,** 55–57 (Jan. 1994).

148. Chavez-Cerda, S., Romero-Antequera, D. L. & Moya-Cessa, H. M. *Pseudo Discrete Diffraction: Modes of Virtual Waveguide Arrays* in *Proceedings of EOS Topical Meeting on Diffractive Optics 2010* ISBN:9781617389597 (European Optical Society, 2010), 98–99.

149. Perez-Leija, A. *et al.* Discrete-like diffraction dynamics in free space. *Opt. Express* **21,** 17951–17960. http://www.opticsexpress.org/abstract.cfm?URI=oe-21-15-17951 (July 2013).

150. Dudley, A., Li, Y., Mhlanga, T., Escuti, M. & Forbes, A. Generating and measuring nondiffracting vector Bessel beams. *Optics letters* **38,** 3429–3432 (2013).

151. Singh, K., Buono, W. T., Forbes, A. & Dudley, A. Accelerating polarization structures in vectorial fields. *Optics Express* **29,** 2727–2737 (2021).

152. Aleksanyan, A. & Brasselet, E. Spin–orbit photonic interaction engineering of Bessel beams. *Optica* **3,** 167–174 (2016).

153. Pfeiffer, C. & Grbic, A. Controlling vector Bessel beams with metasurfaces. *Physical Review Applied* **2,** 044012 (2014).

154. Kondakci, H. E. & Abouraddy, A. F. Diffraction-free pulsed optical beams via space-time correlations. *Optics express* **24,** 28659–28668 (2016).

155. Kondakci, H. E. & Abouraddy, A. F. Diffraction-free space–time light sheets. *Nature Photonics* **11,** 733–740 (2017).

156. Gori, F., Guattari, G. & Padovani, C. Bessel-gauss beams. *Optics communications* **64,** 491–495 (1987).

157. Barakat, R. Analytic proofs of the Arago–Fresnel laws for the interference of polarized light. *J. Opt. Soc. Am. A* **10,** 180–185. http://josaa.osa.org/abstract.cfm?URI=josaa-10-1-180 (Jan. 1993).

158. Young, T. I. The Bakerian Lecture. Experiments and calculations relative to physical optics. *Philosophical transactions of the Royal Society of London,* 1–16 (1804).

159. Gossman, D., Perez-Garcia, B., Hernandez-Aranda, R. I. & Forbes, A. Optical interference with digital holograms. *American Journal of Physics* **84,** 508–516 (2016).

160. Yao, E., Franke-Arnold, S., Courtial, J., Barnett, S. & Padgett, M. Fourier relationship between angular position and optical orbital angular momentum. *Optics Express* **14,** 9071–9076 (2006).

161. Wood, R. Some New Cases of Interference and Diffraction. *Proceedings of the Physical Society of London (1874-1925)* **19,** 86 (1903).

162. Semel, M. Spectropolarimetry and polarization-dependent fringes. *Astronomy & Astrophysics* **401,** 1–14 (2003).

163. Collett, E. Mathematical formulation of the interference laws of Fresnel and Arago. *American Journal of Physics* **39,** 1483–1495 (1971).

164. Bandres, M. A., Gutiérrez-Vega, J. C. & Chávez-Cerda, S. Parabolic nondiffracting optical wave fields. *Optics letters* **29,** 44–46 (2004).

165. Rosales-Guzmán, C. *et al.* Polarisation-insensitive generation of complex vector modes from a digital micromirror device. *Scientific Reports* **10,** 1–9 (2020).

166. Voelz, D. *Computational fourier optics: a MATLAB tutorial* in (2011).

167. Spreeuw, R. J. A classical analogy of entanglement. *Foundations of physics* **28,** 361–374 (1998).

168. Qian, X.-F., Little, B., Howell, J. C. & Eberly, J. Shifting the quantum-classical boundary: theory and experiment for statistically classical optical fields. *Optica* **2,** 611–615 (2015).

169. Eberly, J. H. *et al.* Quantum and classical optics–emerging links. *Physica Scripta* **91,** 063003. http://stacks.iop.org/1402-4896/91/i=6/a=063003 (2016).

170. Qian, X.-F. & Eberly, J. Entanglement and classical polarization states. *Optics Letters* **36,** 4110–4112 (2011).

171. Qian, X.-F., Vamivakas, A. N. & Eberly, J. H. Emerging Connections: Classical and Quantum Optics. *Optics and Photonics News* **28,** 34–41 (2017).

172. Konrad, T. & Forbes, A. Quantum mechanics and classical light. *Contemporary Physics* **60,** 1–22 (2019).

173. Forbes, A., Aiello, A. & Ndagano, B. Classically Entangled Light. *Progress in Optics* **64,** 99 (2019).

174. Töppel, F., Aiello, A., Marquardt, C., Giacobino, E. & Leuchs, G. Classical entanglement in polarization metrology. *New Journal of Physics* **16,** 073019 (2014).

175. Hu, X.-B. *et al.* Free-space local nonseparability dynamics of vector modes. *Photonics Research* **9,** 439–445 (2021).

176. Qian, X.-F., Vamivakas, A. & Eberly, J. Entanglement limits duality and vice versa. *Optica* **5,** 942–947 (2018).

177. Cheshire, P. F. J. The President's address: The early history of the polariscope, and the polarizing microscope. *Journal of the Royal Microscopical Society* **43,** 1–18 (1923).

178. Biot, J.-B. *Traité de physique expérimentale et mathématique* (Deterville, 1816).

179. Wong, D., Poole, S. B. & Sceats, M. G. Stress-birefringence reduction in elliptical-core fibers under ultraviolet irradiation. *Optics Letters* **17,** 1773 (Dec. 1992).

180. Clarkson, W. A., Felgate, N. S. & Hanna, D. C. Simple method for reducing the depolarization loss resulting from thermally induced birefringence in solid-state lasers. *Optics Letters* **24,** 820 (June 1999).

181. Stolen, R. & Ashkin, A. Optical Kerr effect in glass waveguide. *Applied Physics Letters* **22,** 294–296 (Mar. 1973).

182. Oh, E., Bartholomew, D. U., Ramdas, A. K., Furdyna, J. K. & Debska, U. Birefringence and Faraday effect inCd1-xMnxSe. *Physical Review B* **42,** 5201–5211 (Sept. 1990).

183. Duggan, R., del Pino, J., Verhagen, E. & Alù, A. Optomechanically Induced Birefringence and Optomechanically Induced Faraday Effect. *Physical Review Letters* **123,** 023602 (July 2019).

184. Kaminsky, W. Experimental and phenomenological aspects of circular birefringence and related properties in transparent crystals. *Reports on Progress in Physics* **63,** 1575–1640 (Sept. 2000).

185. Tanemura, T. & Kikuchi, K. Circular-Birefringence Fiber for Nonlinear Optical Signal Processing. *Journal of Lightwave Technology* **24,** 4108–4119 (Nov. 2006).

186. Sorge, J. B., van Popta, A. C., Sit, J. C. & Brett, M. J. Circular birefringence dependence on chiral film porosity. *Optics Express* **14,** 10550 (2006).

187. Bell, L. Note on Some Meteorological Uses of the Polariscope. *Proceedings of the American Academy of Arts and Sciences* **43,** 407 (1908).

188. Richartz, M. An Improvement of Savart's Polariscope. *Journal of the Optical Society of America* **38,** 623 (July 1948).

189. Petersen, C. *et al.* Relationship between DNA damage and sperm head birefringence. *Reproductive BioMedicine Online* **22,** 583–589 (June 2011).

190. Bueno, J. M. & Vargas-Martin, F. Measurements of the corneal birefringence with a liquid-crystal imaging polariscope. *Applied Optics* **41,** 116 (Jan. 2002).

191. Ferre, J. & Gehring, G. A. Linear optical birefringence of magnetic crystals. *Reports on Progress in Physics* **47,** 513–611. https://doi.org/10.1088%5C%2F0034-4885%5C%2F47%5C%2F5%5C%2F002 (May 1984).

192. Horn, G., Lesniak, J., Mackin, T. & Boyce, B. Infrared grey-field polariscope: A tool for rapid stress analysis in microelectronic materials and devices. *Review of Scientific Instruments* **76,** 045108 (Apr. 2005).

193. Pin, W. & Asundi, A. Full-field retardation measurement of a liquid crystal cell with a phase shift polariscope. *Applied Optics* **47,** 4391 (Aug. 2008).

194. Mukhopadhyay, S., Sarkar, S., Bhattacharya, K. & Hazra, L. Polarization phase shifting interferometric technique for phase calibration of a reflective phase spatial light modulator. *Optical Engineering* **52,** 035602 (Mar. 2013).

195. Wu, S.-T., Efron, U. & Hess, L. D. Birefringence measurements of liquid crystals. *Applied Optics* **23,** 3911 (Nov. 1984).

196. Nomura, T. & Javidi, B. Object recognition by use of polarimetric phase-shifting digital holography. *Optics Letters* **32,** 2146 (July 2007).

197. Otani, Y., Shimada, T. & Yoshizawa, T. The Local-Sampling Phase Shifting Technique for Precise Two-Dimensional Birefringence Measurement. *Optical Review* **1,** 103–106 (Nov. 1994).

198. Ghosh, N. & Bhattacharya, K. Polarization phase-shifting interferometric technique for complete evaluation of birefringence. *Applied Optics* **50,** 2179 (May 2011).

199. Lo, Y.-L., Lin, J.-F. & Lee, S.-Y. Polariscope for simultaneous measurement of the principal axis and the phase retardation by use of two phase-locked extractions. *Applied Optics* **43,** 6248 (Dec. 2004).

200. Yoshizawa, T. *Handbook of optical metrology Principles and Applications* 919 pp. ISBN: 1466573619. https://www.ebook.de/de/product/24222745/handbook_of_optical_metrology.html (CRC, 2017).

201. Shribak, M. & Oldenbourg, R. Techniques for fast and sensitive measurements of two-dimensional birefringence distributions. *Applied Optics* **42,** 3009–3017 (2003).

202. Magalhães, P. A. A., Magalhães, C. A. & Magalhães, A. L. M. A. Computational methods of phase shifting to stress measurement with photoelasticity using plane polariscope. *Optik* **130,** 213–226 (Feb. 2017).

203. Hipps, K. & Crosby, G. Applications of the photoelastic modulator to polarization spectroscopy. *Journal of Physical Chemistry* **83,** 555–562 (1979).

204. Shribak, M. Complete polarization state generator with one variable retarder and its application for fast and sensitive measuring of two-dimensional birefringence distribution. *Journal of the Optical Society of America A* **28,** 410 (Feb. 2011).

205. Alali, S., Gribble, A. & Vitkin, I. A. Rapid wide-field Mueller matrix polarimetry imaging based on four photoelastic modulators with no moving parts. *Optics Letters* **41,** 1038 (Feb. 2016).

206. Alali, S., Yang, T. & Vitkin, I. A. Rapid time-gated polarimetric Stokes imaging using photoelastic modulators. *Optics Letters* **38,** 2997 (Aug. 2013).

207. Diner, D. J. *et al.* First results from a dual photoelastic-modulator-based polarimetric camera. *Applied Optics* **49,** 2929 (May 2010).

208. Gribble, A., Layden, D. & Vitkin, I. A. Experimental validation of optimum input polarization states for Mueller matrix determination with a dual photoelastic modulator polarimeter. *Optics Letters* **38,** 5272 (Dec. 2013).

209. Layden, D., Wood, M. F. G. & Vitkin, I. A. Optimum selection of input polarization states in determining the sample Mueller matrix: a dual photoelastic polarimeter approach. *Optics Express* **20,** 20466 (Aug. 2012).

210. Arteaga, O., Freudenthal, J., Wang, B. & Kahr, B. Mueller matrix polarimetry with four photoelastic modulators: theory and calibration. *Applied Optics* **51,** 6805 (Sept. 2012).

211. Bueno, J. M. Polarimetry using liquid-crystal variable retarders: theory and calibration. *Journal of Optics A: Pure and Applied Optics* **2,** 216–222 (May 2000).

212. Lin, J.-F. Simultaneous measurement of optical rotation angle and retardance. *Optics communications* **281,** 940–947 (2008).

213. Devlin, R. C., Ambrosio, A., Rubin, N. A., Mueller, J. B. & Capasso, F. Arbitrary spin-to–orbital angular momentum conversion of light. *Science* **358,** 896–901 (2017).

214. Cheeseman, J. R., Frisch, M. J., Devlin, F. J. & Stephens, P. J. Hartree- Fock and density functional theory ab initio calculation of optical rotation using GIAOs: basis set dependence. *The Journal of Physical Chemistry A* **104,** 1039–1046 (2000).

215. Pecul, M., Ruud, K., Rizzo, A. & Helgaker, T. Conformational effects on the optical rotation of alanine and proline. *The Journal of Physical Chemistry A* **108,** 4269–4276 (2004).

216. Sephton, B. *et al.* Purity and efficiency of hybrid orbital angular momentum-generating metasurfaces. *Journal of Nanophotonics* **14,** 016005 (2020).

217. Kumagai, T., Tottori, Y., Miyata, R. & Kajioka, H. Glucose sensor with a Sagnac interference optical system. *Applied optics* **53,** 720–726 (2014).

218. Turtaev, S. *et al.* Comparison of nematic liquid-crystal and DMD based spatial light modulation in complex photonics. *Optics express* **25,** 29874–29884 (2017).

219. Heist, S., Mann, A., Kühmstedt, P., Schreiber, P. & Notni, G. Array projection of aperiodic sinusoidal fringes for high-speed three-dimensional shape measurement. *Optical Engineering* **53,** 112208 (2014).

220. Zhao, H., Diao, X., Jiang, H. & Li, X. High-speed triangular pattern phase-shifting 3D measurement based on the motion blur method. *Optics express* **25,** 9171–9185 (2017).

221. González, H. *et al.* High sampling rate single-pixel digital holography system employing a DMD and phase-encoded patterns. *Optics express* **26,** 20342–20350 (2018).

222. Zhang, Y., Liu, Y. & Wang, S. Digital mirror device application in reduction of wave-front phase errors. *Sensors* **9,** 2345–2351 (2009).

223. An, H. *et al.* Spatial-temporal phase unwrapping algorithm for fringe projection profilometry. *Optics Express* **29,** 20657–20672 (2021).

224. Maznev, A. & Wright, O. Upholding the diffraction limit in the focusing of light and sound. *Wave Motion* **68,** 182–189 (2017).

225. Wang, Y., Kang, Q., Zhang, Y. & Liu, X. Optically computed optical coherence tomography for volumetric imaging. *Optics Letters* **45,** 1675 (Mar. 2020).

226. Yoon, S.-J., Lee, J.-S., Rockstuhl, C., Lee, C. & Lee, K.-G. Experimental quantum polarimetry using heralded single photons. *Metrologia* **57,** 045008 (June 2020).

227. Ding, F., Tang, S. & Bozhevolnyi, S. I. Recent Advances in Polarization-Encoded Optical Metasurfaces. *Advanced Photonics Research,* 2000173 (Mar. 2021).

228. Arellano, N. I. T. Radial polarizing phase-shifting interferometry with applications to single-shot n interferogram measurements and potential usage for white light interferogram analysis. *Applied Optics* **59,** 3246 (Mar. 2020).

229. Skyrme, T. H. R. A unified field theory of mesons and baryons. *Nuclear Physics* **31,** 556–569 (1962).

230. Zahed, I. & Brown, G. The Skyrme model. *Physics Reports* **142,** 1–102 (1986).

231. Naya, C. & Sutcliffe, P. Skyrmions and Clustering in Light Nuclei. *Physical Review Letters* **121** (2018).

232. Eisenberg, J. & Kälbermann, G. The use of skyrmions for two-nucleon systems. *Progress in Particle and Nuclear Physics* **22,** 1–42 (1989).

233. Yu, X. *et al.* Real-space observation of a two-dimensional skyrmion crystal. *Nature* **465,** 901–904 (2010).

234. Fert, A., Cros, V. & Sampaio, J. Skyrmions on the track. *Nature nanotechnology* **8,** 152–156 (2013).

235. Fert, A., Reyren, N. & Cros, V. Magnetic skyrmions: advances in physics and potential applications. *Nature Reviews Materials* **2,** 1–15 (2017).

236. Nagaosa, N. & Tokura, Y. Topological properties and dynamics of magnetic skyrmions. *Nature Nanotechnology* **8,** 899–911 (2013).

237. Zhang, X. *et al.* Skyrmion-electronics: writing, deleting, reading and processing magnetic skyrmions toward spintronic applications. *Journal of Physics: Condensed Matter* **32,** 143001 (2020).

238. Lima Fernandes, I., Blügel, S. & Lounis, S. Spin-orbit enabled all-electrical readout of chiral spin-textures. *Nature Communications* **13,** 1–10 (2022).

239. Soskin, M., Boriskina, S. V., Chong, Y., Dennis, M. R. & Desyatnikov, A. Singular optics and topological photonics. *Journal of Optics* **19,** 010401 (Dec. 2016).

240. Dennis, M. R., Kivshar, Y. S., Soskin, M. S. & Jr, G. A. S. Singular Optics: more ado about nothing. *Journal of Optics A: Pure and Applied Optics* **11,** 090201 (Aug. 2009).

241. Rivera, N. & Kaminer, I. Light–matter interactions with photonic quasiparticles. *Nature Reviews Physics* **2,** 538–561 (2020).

242. Gutiérrez-Cuevas, R. & Pisanty, E. Optical polarization skyrmionic fields in free space. *Journal of Optics* **23,** 024004 (2021).

243. Ornelas, P., Nape, I., Koch, R. d. M. & Forbes, A. Non-local Skyrmions as topologically resilient quantum entangled states of light. *arXiv preprint arXiv:2210.04690* (2022).

244. Wang, J. *et al.* Terabit free-space data transmission employing orbital angular momentum multiplexing. *Nature photonics* **6,** 488–496 (2012).

245. Karnieli, A., Tsesses, S., Bartal, G. & Arie, A. Emulating spin transport with nonlinear optics, from high-order skyrmions to the topological Hall effect. *Nature Communications* **12,** 1–9 (2021).

246. Gahagan, K. T. & Swartzlander, G. A. Optical vortex trapping of particles. *Summaries of papers presented at the Conference on Lasers and Electro-Optics,* 155–156 (1996).

247. Padgett, M. & Bowman, R. Tweezers with a twist. *Nature Photonics* **5,** 343–348 (2011).

248. Shen, Y., Martinez, E. C. & Rosales-Guzman, C. Generation of Optical Skyrmions with Tunable Topological Textures. *ACS Photonics* (2022).

249. Zhang, Q., Xie, Z., Du, L., Shi, P. & Yuan, X. Bloch-type photonic skyrmions in optical chiral multilayers. *Phys. Rev. Research* **3,** 023109 (2 2021).

250. Zhang, Q. *et al.* Optical topological lattices of Bloch-type skyrmion and meron topologies. *Photon. Res.* **10,** 947–957 (2022).

251. Sohn, H. R. O., Liu, C. D., Wang, Y. & Smalyukh, I. I. Light-controlled skyrmions and torons as reconfigurable particles. *Opt. Express* **27,** 29055–29068 (2019).

252. Tsesses, S. *et al.* Optical skyrmion lattice in evanescent electromagnetic fields. *Proceedings of the Royal Society of London. Series A: Mathematical, Physical and Engineering Sciences* **361,** 993–996 (2018).

253. Du, L., Yang, A., Zayats, A. V. & Yuan, X. Deep-subwavelength features of photonic skyrmions in a confined electromagnetic field with orbital angular momentum. *Nature Physics* **15,** 650–654 (2019).

254. Ghosh, A., Yang, S., Dai, Y. & Petek, H. The Spin Texture Topology of Polygonal Plasmon Fields. *ACS Photonics* (2023).

255. Byrnes, T., Kim, N. Y. & Yamamoto, Y. Exciton–polariton condensates. *Nature Physics* **10,** 803–813 (2014).

256. Beckley, A. M., Brown, T. G. & Alonso, M. A. Full Poincaré beams. *Opt. Express* **18,** 10777–10785 (2010).

257. Lin, W., Ota, Y., Arakawa, Y. & Iwamoto, S. Microcavity-based generation of full Poincaré beams with arbitrary skyrmion numbers. *Phys. Rev. Research* **3,** 023055 (2 2021).

258. Faddeev, L. D. & Korepin, V. E. Quantization of Solitons. *Theoretical and Mathematical Physics* **25,** 1039–1049 (1975).

259. Battye, R. & Sutcliffe, P. M. Solitons, links and knots. *Proceedings of the Royal Society of London. Series A: Mathematical, Physical and Engineering Sciences* **455,** 4305–4331 (1999).

260. Manton, N. & Sutcliffe, P. *Topological Solitons* ISBN: 9781139454698. https://books.google.co.za/books?id=e2tPhFdSUf8C (Cambridge University Press, 2004).

261. Gao, S. *et al.* Paraxial skyrmionic beams. *Physical Review A* **102,** 053513 (2020).

262. Kuratsuji, H. & Tsuchida, S. Evolution of the Stokes parameters, polarization singularities, and optical skyrmion. *Physical Review A* **103,** 023514 (2021).

263. Sugic, D. *et al.* Particle-like topologies in light. *Nature communications* **12,** 1–10 (2021).

264. Urbantke, H. The Hopf fibration—seven times in physics. *Journal of Geometry and Physics* **46,** 125–150. ISSN: 0393-0440 (2003).

265. Donati, S. *et al.* Twist of generalized skyrmions and spin vortices in a polariton superfluid. *Proceedings of the National Academy of Sciences* **113,** 14926–14931 (2016).

266. Dominici, L. *et al.* Full-Bloch beams and ultrafast Rabi-rotating vortices. *Physical Review Research* **3,** 013007 (2021).

267. Gao, S. *Skyrmionic beams and quantum matched filtering* PhD thesis (University of Glasgow, 2022).

268. Watson, G. N. *A treatise on the theory of Bessel Functions* ISBN: 9780521483919 (Cambridge University Press, 1922).

269. Kuratsuji, H. & Kakigi, S. Maxwell-Schrödinger equation for polarized light and evolution of the Stokes parameters. *Physical review letters* **80,** 1888 (1998).

270. Zamboni-Rached, M. Stationary optical wave fields with arbitrary longitudinal shape by superposing equal frequency Bessel beams: Frozen Waves. *Optics Express* **12,** 4001–4006 (2004).

271. Zamboni-Rached, M., Recami, E. & Hernández-Figueroa, H. E. Theory of "frozen waves": modeling the shape of stationary wave fields. *JOSA A* **22,** 2465–2475 (2005).

272. Dorrah, A. H., Zamboni-Rached, M. & Mojahedi, M. Controlling the topological charge of twisted light beams with propagation. *Physical Review A* **93,** 063864 (2016).

273. Dorrah, A. H., Rosales-Guzmán, C., Forbes, A. & Mojahedi, M. Evolution of orbital angular momentum in three-dimensional structured light. *Physical Review A* **98,** 043846 (2018).

274. Schulze, C., Flamm, D., Duparré, M. & Forbes, A. Beam-quality measurements using a spatial light modulator. *Optics letters* **37,** 4687–4689 (2012).

275. Pye, J. D. *Polarised light in science and nature* (CRC Press, 2015).

276. Cloude, S. *Polarisation: applications in remote sensing* (Oxford university press, 2010).

277. Collett, E. The description of polarization in classical physics. *American Journal of Physics* **36,** 713–725 (1968).

278. Collett, E. Polarized Light: Fundamentals and Applications, Marcel Dekkar. *Inc. NY* (1993).

279. Wolf, E. Optics in terms of observable quantities. *Il Nuovo Cimento (1943-1954)* **12,** 884–888 (1954).

280. Stokes, G. G. On the composition and resolution of streams of polarized light from different sources. *Transactions of the Cambridge Philosophical Society* **9,** 399 (1851).

281. Shurcliff, W. A. *Polarized light; production and use* (Harvard University Press, 1962).

282. Clarke, D. & Grainger, J. Polarized light and optical measurement. *American Journal of Physics* **40,** 1055–1056 (1971).

283. Born, M. & Wolf, E. *Principles of Optics. Sixth (corrected) Edition* 1997.

284. McMaster, W. H. Polarization and the Stokes parameters. *American Journal of Physics* **22,** 351–362 (1954).

285. Berry, H., Curtis, L., Ellis, D. & Schectman, R. Anisotropy in the beam-foil light source. *Physical Review Letters* **32,** 751 (1974).

286. Schaefer, B., Collett, E., Smyth, R., Barrett, D. & Fraher, B. Measuring the Stokes polarization parameters. *American Journal of Physics* **75,** 163–168 (2007).

287. Collett, E. Determination of the ellipsometric characteristics of optical surfaces using nanosecond laser pulses. *Surface Science* **96,** 156–167 (1980).

288. Azzam, R. Division-of-amplitude photopolarimeter (DOAP) for the simultaneous measurement of all four Stokes parameters of light. *Optica Acta: International Journal of Optics* **29,** 685–689 (1982).

289. Fridman, M., Nixon, M., Grinvald, E., Davidson, N. & Friesem, A. A. Real-time measurement of space-variant polarizations. *Optics express* **18,** 10805–10812 (2010).

290. Hauge, P. Recent developments in instrumentation in ellipsometry. *Surface Science* **96,** 108–140 (1980).

291. Azzam, R. Arrangement of four photodetectors for measuring the state of polarization of light. *Optics letters* **10,** 309–311 (1985).

292. Berry, H. G., Gabrielse, G. & Livingston, A. Measurement of the Stokes parameters of light. *Applied optics* **16,** 3200–3205 (1977).

293. Garcia-Caurel, E., De Martino, A. & Drevillon, B. Spectroscopic Mueller polarimeter based on liquid crystal devices. *Thin Solid Films* **455,** 120–123 (2004).

294. Myhre, G. *et al.* Liquid crystal polymer full-stokes division of focal plane polarimeter. *Optics express* **20,** 27393–27409 (2012).

295. Mueller, J. B., Leosson, K. & Capasso, F. Ultracompact metasurface in-line polarimeter. *Optica* **3,** 42–47 (2016).

296. Shibata, S., Hagen, N., Kawabata, S. & Otani, Y. Compact and high-speed Stokes polarimeter using three-way polarization-preserving beam splitters. *Applied optics* **58,** 5644–5649 (2019).

297. Forbes, A., Dudley, A. & McLaren, M. Creation and detection of optical modes with spatial light modulators. *Advances in Optics and Photonics* **8,** 200–227 (2016).

298. Lazarev, G., Chen, P.-J., Strauss, J., Fontaine, N. & Forbes, A. Beyond the display: Phase-only liquid crystal on Silicon devices and their applications in photonics. *Optics express* **27,** 16206–16249 (2019).

299. Hornbeck, L. J. *Digital light processing and MEMS: An overview* in *Digest IEEE/Leos 1996 Summer Topical Meeting. Advanced Applications of Lasers in Materials and Processing* (1996), 7–8.

300. Ren, Y.-X., Lu, R.-D. & Gong, L. Tailoring light with a digital micromirror device. *Annalen der physik* **527,** 447–470 (2015).

301. Peña, A. & Andersen, M. F. Complete polarization and phase control with a single spatial light modulator for the generation of complex light fields. *Laser Physics* **28,** 076201 (2018).

302. Shen, Y. *et al.* Optical vortices 30 years on: OAM manipulation from topological charge to multiple singularities. *Light: Science & Applications* **8,** 1–29 (2019).

303. Forbes, A. & Nape, I. Quantum mechanics with patterns of light: Progress in high dimensional and multidimensional entanglement with structured light. *AVS Quantum Science* **1,** 011701 (2019).

304. Hu, Q., Dai, Y., He, C. & Booth, M. J. Arbitrary vectorial state conversion using liquid crystal spatial light modulators. *Optics Communications* **459,** 125028 (2020).

305. Bauer, T. *et al.* Observation of optical polarization Möbius strips. *Science* **347,** 964–966 (2015).

306. Galvez, E. J. *et al.* Multitwist Möbius strips and twisted ribbons in the polarization of paraxial light beams. *Scientific reports* **7,** 1–9 (2017).

307. Galvez, E. J., Khadka, S., Schubert, W. H. & Nomoto, S. Poincaré-beam patterns produced by nonseparable superpositions of Laguerre–Gauss and polarization modes of light. *Applied optics* **51,** 2925–2934 (2012).

308. Otte, E. & Denz, C. Sculpting complex polarization singularity networks. *Optics letters* **43,** 5821–5824 (2018).

309. Otte, E., Alpmann, C. & Denz, C. Higher-order polarization singularitites in tailored vector beams. *Journal of Optics* **18,** 074012 (2016).

310. Zhan, Q. Cylindrical vector beams: from mathematical concepts to applications. *Advances in Optics and Photonics* **1,** 1–57 (2009).

311. Liu, S. *et al.* Highly efficient generation of arbitrary vector beams with tunable polarization, phase, and amplitude. *Photonics Research* **6,** 228–233 (2018).

312. Perez-Garcia, B., López-Mariscal, C., Hernandez-Aranda, R. I. & Gutiérrez-Vega, J. C. On-demand tailored vector beams. *Applied Optics* **56,** 6967–6972 (Aug. 2017).

313. Han, W., Yang, Y., Cheng, W. & Zhan, Q. Vectorial optical field generator for the creation of arbitrarily complex fields. *Optics express* **21,** 20692–20706 (2013).

314. McLaren, M., Konrad, T. & Forbes, A. Measuring the nonseparability of vector vortex beams. *Physical Review A* **92,** 023833 (2015).

315. D'Ambrosio, V. *et al.* Entangled vector vortex beams. *Physical Review A* **94,** 030304 (2016).

316. Toninelli, E. *et al.* Concepts in quantum state tomography and classical implementation with intense light: a tutorial. *Advances in Optics and Photonics* **11,** 67–134 (2019).

317. Hu, X.-B., Zhao, B., Zhu, Z.-H., Gao, W. & Rosales-Guzmán, C. In situ detection of a cooperative target's longitudinal and angular speed using structured light. *Optics letters* **44,** 3070–3073 (2019).

318. Zhao, B. *et al.* Real-time Stokes polarimetry using a digital micromirror device. *Optics express* **27,** 31087–31093 (2019).

319. Manthalkar, A. *et al.* All-digital Stokes polarimetry with a digital micromirror device. *Optics Letters* **45,** 2319–2322 (2020).

320. Zhao, B. *et al.* Determining the non-separability of vector modes with digital micromirror devices. *Applied Physics Letters* **116,** 091101 (2020).

321. Mitchell, K. J., Turtaev, S., Padgett, M. J., Čižmár, T. & Phillips, D. B. High-speed spatial control of the intensity, phase and polarisation of vector beams using a digital micro-mirror device. *Optics Express* **24,** 29269–29282 (2016).

322. Shin, S., Lee, K., Yaqoob, Z., So, P. T. & Park, Y. Reference-free polarization-sensitive quantitative phase imaging using single-point optical phase conjugation. *Optics express* **26,** 26858–26865 (2018).

323. Hornbeck, L. J. *Deformable mirror light modulator* US Patent 4,441,791. Apr. 1984.

324. Hornbeck, L. J. *Current status of the digital micromirror device (DMD) for projection television applications* in *Proceedings of IEEE International Electron Devices Meeting* (1993), 381–384.

325. Sampsell, J. B. Digital micromirror device and its application to projection displays. *Journal of Vacuum Science & Technology B: Microelectronics and Nanometer Structures Processing, Measurement, and Phenomena* **12,** 3242–3246 (1994).

326. Kreis, T. M., Aswendt, P. & Höfling, R. Hologram reconstruction using a digital micromirror device. *Optical Engineering* **40** (2001).

327. Li, Y., Kim, J. & Escuti, M. J. Orbital angular momentum generation and mode transformation with high efficiency using forked polarization gratings. *Applied optics* **51,** 8236–8245 (2012).

328. Komanduri, R. & Escuti, M. High efficiency reflective liquid crystal polarization gratings. *Applied Physics Letters* **95,** 091106 (2009).

329. Nicolescu, E. & Escuti, M. J. Polarization-independent tunable optical filters using bilayer polarization gratings. *Applied optics* **49,** 3900–3904 (2010).

330. Lee, W.-H. Binary synthetic holograms. *Applied optics* **13,** 1677–1682 (1974).

331. Senthilkumaran, P. *et al.* Optical currents in Poincaré beams. *Physical Review A* **102,** 013509 (2020).

332. Milione, G., Nguyen, T. A., Leach, J., Nolan, D. A. & Alfano, R. R. Using the nonseparability of vector beams to encode information for optical communication. *Optics letters* **40,** 4887–4890 (2015).

333. Berg-Johansen, S. *et al.* Classically entangled optical beams for high-speed kinematic sensing. *Optica* **2,** 864–868 (2015).

334. Bautista, G. & Kauranen, M. Vector-field nonlinear microscopy of nanostructures. *ACS Photonics* **3,** 1351–1370 (2016).

335. Matsusaka, S., Kozawa, Y. & Sato, S. Micro-hole drilling by tightly focused vector beams. *Optics letters* **43,** 1542–1545 (2018).

336. Hall, D. G. Vector-beam solutions of Maxwell's wave equation. *Optics letters* **21,** 9–11 (1996).

337. Sroor, H. *et al.* High-purity orbital angular momentum states from a visible metasurface laser. *Nature Photonics*, 1–6 (2020).

338. Dorrah, A. H., Rubin, N. A., Zaidi, A., Tamagnone, M. & Capasso, F. Metasurface optics for on-demand polarization transformations along the optical path. *Nature Photonics* **15,** 287–296 (2021).

339. Rosales-Guzmán, C., Bhebhe, N. & Forbes, A. Simultaneous generation of multiple vector beams on a single SLM. *Optics express* **25,** 25697–25706 (2017).

340. Ndagano, B. *et al.* Characterizing quantum channels with non-separable states of classical light. *Nature Physics* **13,** 397 (2017).

341. Ndagano, B. *et al.* A deterministic detector for vector vortex states. *Scientific reports* **7,** 1–8 (2017).

342. Moreno, I. *et al.* Vector beam polarization state spectrum analyzer. *Scientific reports* **7,** 1–10 (2017).

343. He, C. *et al.* Full Poincar\'e mapping for ultra-sensitive polarimetry. *arXiv preprint arXiv:2101.09372* (2021).

344. He, C. & Booth, M. J. *Full Poincaré polarimetry for enhanced microscopic sensing* in *Novel Techniques in Microscopy* (2021), NM1C–2.

345. Hu, Q., He, C. & Booth, M. J. Arbitrary complex retarders using a sequence of spatial light modulators as the basis for adaptive polarisation compensation. *Journal of Optics* **23,** 065602 (2021).

346. He, C., Hu, Q., Dai, Y. & Booth, M. J. *Vectorial adaptive optics-correction of polarization and phase* in *Adaptive Optics: Analysis, Methods & Systems* (2020), OF2B–5.

347. Liu, S. *et al.* A method for simultaneously measuring polarization and phase of arbitrarily polarized beams based on Pancharatnam-Berry phase. *Applied Physics Letters* **110,** 171112 (2017).

348. Qi, S. *et al.* Dynamically measuring the holo-information of light fields in three-dimensional space using a periodic polarization-structured light. *Science China Physics, Mechanics & Astronomy* **64,** 1–8 (2021).

349. Ge, B., Zhou, R., Takiguchi, Y., Yaqoob, Z. & So, P. T. Single-Shot Optical Anisotropy Imaging with Quantitative Polarization Interference Microscopy. *Laser & photonics reviews* **12,** 1800070 (2018).

350. Schulze, C. *et al.* Wavefront reconstruction by modal decomposition. *Optics express* **20,** 19714–19725 (2012).

351. Barakat, R. Analytic proofs of the Arago–Fresnel laws for the interference of polarized light. *JOSA A* **10,** 180–185 (1993).

352. Götte, J. B., Franke-Arnold, S., Zambrini, R. & Barnett, S. M. Quantum formulation of fractional orbital angular momentum. *Journal of Modern Optics* **54,** 1723–1738 (2007).

353. Götte, J. B. *et al.* Light beams with fractional orbital angular momentum and their vortex structure. *Optics express* **16,** 993–1006 (2008).

354. ISO. **ISO** 15367-1:2003 lasers and laser-related equipment – test methods for determination of the shape of a laser beam wavefront – Part 1: Terminology and fundamental aspects. *ISO* (2003).

355. Beverage, J., Shack, R. & Descour, M. Measurement of the three-dimensional microscope point spread function using a Shack–Hartmann wavefront sensor. *Journal of microscopy* **205,** 61–75 (2002).

356. Shechtman, Y., Sahl, S. J., Backer, A. S. & Moerner, W. E. Optimal point spread function design for 3D imaging. *Physical review letters* **113,** 133902 (2014).

357. Shechtman, Y. Recent advances in point spread function engineering and related computational microscopy approaches: from one viewpoint. *Biophysical reviews* **12,** 1303–1309 (2020).

358. Véran, J.-P., Rigaut, F., Maıtre, H. & Rouan, D. Estimation of the adaptive optics long-exposure point-spread function using control loop data. *JOSA A* **14,** 3057–3069 (1997).

359. Siemons, M., Hulleman, C., Thorsen, R., Smith, C. & Stallinga, S. High precision wavefront control in point spread function engineering for single emitter localization. *Optics express* **26,** 8397–8416 (2018).

360. Chalita, M. R., Chavala, S., Xu, M. & Krueger, R. R. Wavefront analysis in post-LASIK eyes and its correlation with visual symptoms, refraction, and topography. *Ophthalmology* **111,** 447–453 (2004).

361. Schallhorn, S. C. *et al.* Wavefront-guided LASIK for the correction of primary myopia and astigmatism: a report by the American Academy of Ophthalmology. *Ophthalmology* **115,** 1249–1261 (2008).

362. Li, M., Cvijetic, M., Takashima, Y. & Yu, Z. Evaluation of channel capacities of OAM-based FSO link with real-time wavefront correction by adaptive optics. *Optics express* **22,** 31337–31346 (2014).

363. Li, M. & Cvijetic, M. Coherent free space optics communications over the maritime atmosphere with use of adaptive optics for beam wavefront correction. *Applied optics* **54,** 1453–1462 (2015).

364. Li, M., Gao, W. & Cvijetic, M. Slant-path coherent free space optical communications over the maritime and terrestrial atmospheres with the use of adaptive optics for beam wavefront correction. *Applied Optics* **56,** 284–297 (2017).

365. Nape, I. *et al.* Revealing the invariance of vectorial structured light in complex media. *Nature Photonics* **16,** 538–546 (2022).

366. Monjardin, J., Nowak, K., Baker, H. & Hall, D. Correction of beam errors in high power laser diode bars and stacks. *Optics Express* **14,** 8178–8183 (2006).

367. Sanner, N. *et al.* 100-kHz diffraction-limited femtosecond laser micromachining. *Applied Physics B* **80,** 27–30 (2005).

368. Fourmaux, S. *et al.* Laser beam wavefront correction for ultra high intensities with the 200 TW laser system at the advanced laser light source. *Optics express* **16,** 11987–11994 (2008).

369. Bates, W. A wavefront shearing interferometer. *Proceedings of the Physical Society (1926-1948)* **59,** 940 (1947).

370. Love, G. D., Oag, T. J. & Kirby, A. K. Common path interferometric wavefront sensor for extreme adaptive optics. *Optics express* **13,** 3491–3499 (2005).

371. Ralph, D. T., Altin, P. A., Rabeling, D. S., McClelland, D. E. & Shaddock, D. A. Interferometric wavefront sensing with a single diode using spatial light modulation. *Applied Optics* **56,** 2353–2358 (2017).

372. Platt, B. C. & Shack, R. *History and principles of Shack-Hartmann wavefront sensing* 2001.

373. Granata, M., Buy, C., Ward, R. & Barsuglia, M. Higher-order Laguerre-Gauss mode generation and interferometry for gravitational wave detectors. *Physical review letters* **105,** 231102 (2010).

374. Tao, L., Green, A. & Fulda, P. Higher-order Hermite-Gauss modes as a robust flat beam in interferometric gravitational wave detectors. *Physical Review D* **102,** 122002 (2020).

375. Roddier, F. Curvature sensing and compensation: a new concept in adaptive optics. *Applied Optics* **27,** 1223–1225 (1988).

376. Roddier, F. Wavefront sensing and the irradiance transport equation. *Applied optics* **29,** 1402–1403 (1990).

377. Gureyev, T. E. & Nugent, K. A. Rapid quantitative phase imaging using the transport of intensity equation. *Optics communications* **133,** 339–346 (1997).

378. Zuo, C. *et al.* High-resolution transport-of-intensity quantitative phase microscopy with annular illumination. *Scientific reports* **7,** 1–22 (2017).

379. Li, Y. *et al.* Quantitative phase microscopy for cellular dynamics based on transport of intensity equation. *Optics Express* **26,** 586–593 (2018).

380. Gritsenko, I., Kovalev, M., Krasin, G., Konoplyov, M. & Stsepuro, N. *Computational method for wavefront sensing based on transport-of-intensity equation* in *Photonics* **8** (2021), 177.

381. Ribak, E. N. *Experimental limits on curvature sensing* in *Optics in Atmospheric Propagation and Adaptive Systems III* **3866** (1999), 217–220.

382. Gupta, A. K., Mahendra, R. & Nishchal, N. K. Single-shot phase imaging based on transport of intensity equation. *Optics Communications* **477,** 126347 (2020).

383. Nguyen, T. & Nehmetallah, G. Non-interferometric tomography of phase objects using spatial light modulators. *Journal of Imaging* **2,** 30 (2016).

384. Lingel, C., Haist, T. & Osten, W. Spatial-light-modulator-based adaptive optical system for the use of multiple phase retrieval methods. *Applied Optics* **55,** 10329–10334 (2016).

385. Hornbeck, L. J. *Deformable-mirror spatial light modulators* in *Spatial Light Modulators and Applications III* **1150** (1990), 86–103.

386. Paganin, D. & Nugent, K. A. Noninterferometric phase imaging with partially coherent light. *Physical review letters* **80,** 2586 (1998).

387. Mehrabkhani, S., Wefelnberg, L. & Schneider, T. Fourier-based solving approach for the transport-of-intensity equation with reduced restrictions. *Optics Express* **26,** 11458–11470 (2018).

388. Singh, K. & Dudley, A. Digital toolbox for vector field characterization. *Nanophotonics* **11,** 753–761 (2022).

389. Cox, M. A. & Drozdov, A. V. Converting a Texas Instruments DLP4710 DLP evaluation module into a spatial light modulator. *Applied Optics* **60,** 465–469 (2021).

390. Lane, R., Glindemann, A. & Dainty, J. Simulation of a Kolmogorov phase screen. *Waves in random media* **2,** 209 (1992).

391. Shen, Y., Hou, Y., Papasimakis, N. & Zheludev, N. I. Supertoroidal light pulses as electromagnetic skyrmions propagating in free space. *Nature communications* **12,** 5891 (2021).

392. Galvez, E. J., Rojec, B. L., Kumar, V. & Viswanathan, N. K. Generation of isolated asymmetric umbilics in light's polarization. *Physical Review A* **89,** 031801 (2014).

393. Zdagkas, A. *et al.* Observation of toroidal pulses of light. *arXiv preprint arXiv:2102.03636* (2021).

394. Keren-Zur, S., Tal, M., Fleischer, S., Mittleman, D. M. & Ellenbogen, T. Generation of spatiotemporally tailored terahertz wavepackets by nonlinear metasurfaces. *Nature communications* **10,** 1–6 (2019).

395. Brown, T. G. Unconventional polarization states: beam propagation, focusing, and imaging. *Progress in Optics* **56,** 81–129 (2011).

396. Wang, J., Castellucci, F. & Franke-Arnold, S. Vectorial light–matter interaction: Exploring spatially structured complex light fields. *AVS Quantum Science* **2,** 031702 (2020).

397. Sederberg, S. *et al.* Vectorized optoelectronic control and metrology in a semiconductor. *Nature Photonics* **14,** 680–685 (2020).

398. Fang, Y. *et al.* Photoelectronic mapping of the spin–orbit interaction of intense light fields. *Nature Photonics* **15,** 115–120 (2021).

399. El Ketara, M., Kobayashi, H. & Brasselet, E. Sensitive vectorial optomechanical footprint of light in soft condensed matter. *Nature Photonics* **15,** 121–124 (2021).

400. Hawley, R. D., Cork, J., Radwell, N. & Franke-Arnold, S. Passive broadband full Stokes polarimeter using a Fresnel cone. *Scientific Reports* **9.** https://doi.org/10.1038/s41598-019-39118-0 (Feb. 2019).

401. Fang, L., Wan, Z., Forbes, A. & Wang, J. Vectorial Doppler metrology. *Nature Communications* **12,** 1–10 (2021).

402. Curcio, V., Alemán-Castañeda, L. A., Brown, T. G., Brasselet, S. & Alonso, M. A. Birefringent Fourier filtering for single molecule coordinate and height super-resolution imaging with dithering and orientation. *Nature communications* **11,** 1–13 (2020).

403. Milione, G. *et al.* 4× 20 Gbit/s mode division multiplexing over free space using vector modes and a q-plate mode (de) multiplexer. *Optics Letters* **40,** 1980–1983 (2015).

404. Zhang, J. *et al.* Fiber Vector Eigenmode Multiplexing based High Capacity Transmission over 5-km FMF with Kramers-Kronig Receiver. *Journal of Lightwave Technology* (2021).

405. Zhu, Z. *et al.* Compensation-free high-dimensional free-space optical communication using turbulence-resilient vector beams. *Nature communications* **12,** 1–8 (2021).

406. Zhao, Y. & Wang, J. High-base vector beam encoding/decoding for visible-light communications. *Optics Letters* **40,** 4843–4846 (2015).

407. Radwell, N., Hawley, R., Götte, J. & Franke-Arnold, S. Achromatic vector vortex beams from a glass cone. *Nature communications* **7,** 1–6 (2016).

408. Beckley, A. M., Brown, T. G. & Alonso, M. A. Full poincaré beams. *Optics express* **18,** 10777–10785 (2010).

409. He, C. *et al.* Complex vectorial optics through gradient index lens cascades. *Nature Communications* **10** (Sept. 2019).

410. Chen, J. *et al.* Compact vectorial optical field generator based on a 10-megapixel resolution liquid crystal spatial light modulator. *Optics Communications,* 127112 (2021).

411. Wu, H.-J. *et al.* Vectorial nonlinear optics: Type-II second-harmonic generation driven by spin-orbit-coupled fields. *Physical Review A* **100,** 053840 (2019).

412. Tang, Y. *et al.* Harmonic spin–orbit angular momentum cascade in nonlinear optical crystals. *Nature Photonics* **14,** 658–662 (2020).

413. Nassiri, M. G. & Brasselet, E. Multispectral Management of the Photon Orbital Angular Momentum. *Physical Review Letters* **121,** 213901 (2018).

414. Beckley, A. M., Brown, T. G. & Alonso, M. A. Full Poincaré beams II: partial polarization. *Optics express* **20,** 9357–9362 (2012).

415. Ma, Z. & Ramachandran, S. Propagation stability in optical fibers: role of path memory and angular momentum. *Nanophotonics* **1** (2020).

416. Biss, D. P. & Brown, T. Primary aberrations in focused radially polarized vortex beams. *Optics express* **12,** 384–393 (2004).

417. Youngworth, K. S. & Brown, T. G. Focusing of high numerical aperture cylindrical-vector beams. *Optics Express* **7,** 77–87 (2000).

418. Mamani, S. *et al.* Transmission of classically entangled beams through mouse brain tissue. *Journal of biophotonics,* e201800096 (2018).

419. Gianani, I. *et al.* Transmission of vector vortex beams in dispersive media. *Advanced Photonics* **2,** 036003 (2020).

420. Biton, N., Kupferman, J. & Arnon, S. OAM light propagation through tissue. *Scientific Reports* **11,** 1–9 (2021).

421. Suprano, A. *et al.* Propagation of structured light through tissue-mimicking phantoms. *Optics Express* **28,** 35427–35437 (2020).

422. Gu, Y., Korotkova, O. & Gbur, G. Scintillation of nonuniformly polarized beams in atmospheric turbulence. *Optics letters* **34,** 2261–2263 (2009).

423. Cai, Y., Lin, Q., Eyyuboğlu, H. T. & Baykal, Y. Average irradiance and polarization properties of a radially or azimuthally polarized beam in a turbulent atmosphere. *Optics express* **16,** 7665–7673 (2008).

424. Ji-Xiong, P., Tao, W., Hui-Chuan, L. & Cheng-Liang, L. Propagation of cylindrical vector beams in a turbulent atmosphere. *Chinese Physics B* **19,** 089201 (2010).

425. Wang, T. & Pu, J. Propagation of non-uniformly polarized beams in a turbulent atmosphere. *Optics communications* **281,** 3617–3622 (2008).

426. Hufnagel, F. *et al.* Investigation of underwater quantum channels in a 30 meter flume tank using structured photons. *New Journal of Physics* **22,** 093074 (2020).

427. Bouchard, F. *et al.* Quantum cryptography with twisted photons through an outdoor underwater channel. *Optics express* **26,** 22563–22573 (2018).

428. Ren, Y. *et al.* Orbital angular momentum-based space division multiplexing for high-capacity underwater optical communications. *Scientific reports* **6,** 1–10 (2016).

429. Kagalwala, K. H., Di Giuseppe, G., Abouraddy, A. F. & Saleh, B. E. Bell's measure in classical optical coherence. *Nature Photonics* **7,** 72–78 (2013).

430. Reyes, S. M., Nolan, D. A., Shi, L. & Alfano, R. R. Special classes of optical vector vortex beams are Majorana-like photons. *Optics Communications* **464,** 125425 (2020).

431. McLaren, M., Konrad, T. & Forbes, A. Measuring the nonseparability of vector vortex beams. *Physical Review A* **92,** 023833 (2015).

432. Jiang, M., Luo, S. & Fu, S. Channel-state duality. *Physical Review A* **87,** 022310 (2013).

433. Konrad, T. *et al.* Evolution equation for quantum entanglement. *Nature physics* **4,** 99–102 (2008).

434. Valencia, N. H., Goel, S., McCutcheon, W., Defienne, H. & Malik, M. Unscrambling entanglement through a complex medium. *Nature Physics* **16,** 1112–1116 (2020).

435. Mamani, S. *et al.* Hybrid generation and analysis of vector vortex beams. *Applied Optics* **56,** 2171–2175 (2017).

436. Vaity, P., Banerji, J. & Singh, R. Measuring the topological charge of an optical vortex by using a tilted convex lens. *Physics Letters A* **377,** 1154–1156 (June 2013).

437. Milione, G., Sztul, H., Nolan, D. & Alfano, R. Higher-order Poincaré sphere, Stokes parameters, and the angular momentum of light. *Physical review letters* **107,** 053601 (2011).

438. Holleczek, A., Aiello, A., Gabriel, C., Marquardt, C. & Leuchs, G. Classical and quantum properties of cylindrically polarized states of light. *Optics express* **19,** 9714–9736 (2011).

439. Vallone, G. *et al.* Free-Space Quantum Key Distribution by Rotation-Invariant Twisted Photons. *Physical Review Letters* **113,** 060503 (2014).

440. He, C., Antonello, J. & Booth, M. J. Vectorial adaptive optics. *arXiv preprint arXiv:2110.02606* (2021).

441. De Oliveira, A., da Silva, N. R., de Araújo, R. M., Ribeiro, P. S. & Walborn, S. Quantum Optical Description of Phase Conjugation of Vector Vortex Beams in Stimulated Parametric Down-Conversion. *Physical Review Applied* **14,** 024048 (2020).

442. Padgett, M. J. & Courtial, J. Poincaré-sphere equivalent for light beams containing orbital angular momentum. *Optics letters* **24,** 430–432 (1999).

443. Plöschner, M., Tyc, T. & Čižmár, T. Seeing through chaos in multimode fibres. *Nature Photonics* **9,** 529–535 (2015).

444. Carpenter, J., Eggleton, B. J. & Schröder, J. Complete spatiotemporal characterization and optical transfer matrix inversion of a 420 mode fiber. *Optics letters* **41,** 5580–5583 (2016).

445. He, C. *et al.* Polarisation optics for biomedical and clinical applications: a review. *Light: Science & Applications* **10,** 1–20 (2021).

446. Richardson, D. J. Filling the light pipe. *Science* **30,** 327–328 (2010).

447. Richardson, D., Fini, J. & Nelson, L. Space-division multiplexing in optical fibres. *Nature Photonics* **7,** 354 (2013).

448. Li, G., Bai, N., Zhao, N. & Xia, C. Space-division multiplexing: the next frontier in optical communication. *Advances in Optics and Photonics* **6,** 413–487 (2014).

449. Berdagué, S. & Facq, P. Mode division multiplexing in optical fibers. *Appl. Opt.* **21,** 1950–1955 (1982).

450. Trichili, A., Park, K.-H., Zghal, M., Ooi, B. S. & Alouini, M.-S. Communicating Using Spatial Mode Multiplexing: Potentials, Challenges, and Perspectives. *IEEE Communications Surveys & Tutorials* **21,** 3175–3203 (2019).

451. Trichili, A., Cox, M. A., Ooi, B. S. & Alouini, M.-S. Roadmap to free space optics. *JOSA B* **37,** A184–A201 (2020).

452. Padgett, M. J. Orbital angular momentum 25 years on. *Optics Express* **25,** 11265–11274 (2017).

453. Willner, A. E. *et al.* Optical communications using orbital angular momentum beams. *Advances in Optics and Photonics* **7,** 66–106 (Mar. 2015).

454. Willner, A. E., Pang, K., Song, H., Zou, K. & Zhou, H. Orbital angular momentum of light for communications. *Applied Physics Reviews* **8,** 041312 (2021).

455. Wang, J. *et al. N-dimentional multiplexing link with 1.036-Pbit/s transmission capacity and 112.6-bit/s/Hz spectral efficiency using OFDM-8QAM signals over 368 WDM pol-muxed 26 OAM modes* in *2014 The European Conference on Optical Communication* (2014), 1–3.

456. Zhao, Y. *et al. Experimental demonstration of 260-meter security free-space optical data transmission using 16-QAM carrying orbital angular momentum (OAM) beams multiplexing* in *Optical fiber communication conference* (2016), Th1H–3.

457. Bozinivic, N. *et al.* Terabit- scale orbital angular momentum mode division multiplexing in fibers. *Science* **340** (2013).

458. Anguita, J. A., Neifeld, M. A. & Vasic, B. V. Turbulence-induced channel crosstalk in an orbital angular momentum-multiplexed free-space optical link. *Appl. Opt.* **47,** 2414–2429 (2008).

459. Ren, Y. *et al.* Experimental characterization of a 400 Gbit/s orbital angular momentum multiplexed free-space optical link over 120 m. *Optics Letters* **41,** 622–625 (2016).

460. Krenn, M. *et al.* Communication with spatially modulated light through turbulent air across Vienna. *New Journal of Physics* **16,** 113028 (2014).

461. Rodenburg, B. *et al.* Influence of atmospheric turbulence on states of light carrying orbital angular momentum. *Optics Letters* **37,** 3735 (2012).

462. Zhang, L., Shen, F., Lan, B. & Tang, A. Mode-dependent crosstalk and detection probability of orbital angular momentum of optical vortex beam through atmospheric turbulence. *Journal of Optics* **22,** 075607 (2020).

463. Malik, M. *et al.* Influence of atmospheric turbulence on optical communications using orbital angular momentum for encoding. *Optics express* **20,** 13195–13200 (2012).

464. Chen, C., Yang, H., Tong, S. & Lou, Y. Changes in orbital-angular-momentum modes of a propagated vortex Gaussian beam through weak-to-strong atmospheric turbulence. *Optics express* **24,** 6959–6975 (2016).

465. Tyler, G. A. & Boyd, R. W. Influence of atmospheric turbulence on the propagation of quantum states of light carrying orbital angular momentum. *Optics Letters* **34,** 142–144 (2009).

466. Mphuthi, N., Botha, R. & Forbes, A. Are Bessel beams resilient to aberrations and turbulence? *JOSA A* **35,** 1021–1027 (2018).

467. Watkins, R. J. *et al.* Experimental probing of turbulence using a continuous spectrum of asymmetric OAM beams. *Optics express* **28,** 924–935 (2020).

468. Vetter, C. *et al.* Realization of Free-Space Long-Distance Self-Healing Bessel Beams. *Laser & Photonics Reviews* **13,** 1900103 (2019).

469. Yuan, Y. *et al.* Beam wander relieved orbital angular momentum communication in turbulent atmosphere using Bessel beams. *Scientific reports* **7,** 1–7 (2017).

470. Mphuthi, N. *et al.* Free-space optical communication link with shape-invariant orbital angular momentum Bessel beams. *Applied Optics* **58,** 4258–4264 (2019).

471. Lukin, I. P. Mean intensity of a fundamental Bessel beam in turbulent atmosphere. *Optical Engineering* **53,** 096104 (2014).

472. Bao-Suan, C. & Ji-Xiong, P. Propagation of Gauss–Bessel beams in turbulent atmosphere. *Chinese Physics B* **18,** 1033 (2009).

473. Zhu, K., Zhou, G., Li, X., Zheng, X. & Tang, H. Propagation of Bessel-Gaussian beams with optical vortices in turbulent atmosphere. *Optics Express* **16,** 21315–21320 (2008).

474. Nelson, W., Palastro, J., Davis, C. & Sprangle, P. Propagation of Bessel and Airy beams through atmospheric turbulence. *JOSA A* **31,** 603–609 (2014).

475. Cheng, M., Guo, L., Li, J. & Zhang, Y. Channel capacity of the OAM-based free-space optical communication links with Bessel–Gauss beams in turbulent ocean. *IEEE Photonics Journal* **8,** 1–11 (2016).

476. Doster, T. & Watnik, A. T. Laguerre–Gauss and Bessel–Gauss beams propagation through turbulence: analysis of channel efficiency. *Applied optics* **55,** 10239–10246 (2016).

477. Cox, M. A. *et al.* The Resilience of Hermite- and Laguerre-Gaussian Modes in Turbulence. *Journal of Lightwave Technology* **37,** 3911–3917. ISSN: 0733-8724. eprint: 1901.07203. https://ieeexplore.ieee.org/document/8668467/ (Aug. 2019).

478. Ndagano, B., Mphuthi, N., Milione, G. & Forbes, A. Comparing mode-crosstalk and mode-dependent loss of laterally displaced orbital angular momentum and Hermite–Gaussian modes for free-space optical communication. *Optics Letters* **42,** 4175. ISSN: 0146-9592. https://www.osapublishing.org/abstract.cfm?URI=ol-42-20-4175 (Oct. 2017).

479. Restuccia, S., Giovannini, D., Gibson, G. & Padgett, M. Comparing the information capacity of Laguerre–Gaussian and Hermite–Gaussian modal sets in a finite-aperture system. *Optics Express* **24,** 27127. ISSN: 1094-4087. https://www.osapublishing.org/abstract.cfm?URI=oe-24-24-27127 (Nov. 2016).

480. Ndagano, B., Mphuthi, N., Milione, G. & Forbes, A. Comparing mode-crosstalk and mode-dependent loss of laterally displaced orbital angular momentum and Hermite–Gaussian modes for free-space optical communication. *Optics letters* **42,** 4175–4178 (2017).

481. Trichili, A. *et al.* Optical communication beyond orbital angular momentum. *Scientific Reports* **6,** 27674 (June 2016).

482. Zhao, N., Li, X., Li, G. & Kahn, J. M. Capacity limits of spatially multiplexed free-space communication. *Nature photonics* **9,** 822 (2015).

483. Zhou, Y. *et al.* Using all transverse degrees of freedom in quantum communications based on a generic mode sorter. *Optics express* **27,** 10383–10394 (2019).

484. Xie, G. *et al.* Experimental demonstration of a 200-Gbit/s free-space optical link by multiplexing Laguerre–Gaussian beams with different radial indices. *Optics Letters* **41,** 3447–3450 (Aug. 2016).

485. Li, L. *et al.* Power loss mitigation of orbital-angular-momentum-multiplexed free-space optical links using nonzero radial index Laguerre–Gaussian beams. *JOSA B* **34,** 1–6 (2017).

486. Gu, X., Chen, L. & Krenn, M. Phenomenology of complex structured light in turbulent air. *ArXiv,* 1906.03581v1 (2019).

487. Klug, A., Nape, I. & Forbes, A. The orbital angular momentum of a turbulent atmosphere and its impact on propagating structured light fields. *New Journal of Physics* **23,** 093012 (2021).

488. Jin, J. *et al.* Genuine time-bin-encoded quantum key distribution over a turbulent depolarizing free-space channel. *Optics express* **27,** 37214–37223 (2019).

489. Vagniluca, I. *et al.* Efficient time-bin encoding for practical high-dimensional quantum key distribution. *Physical Review Applied* **14,** 014051 (2020).

490. Milione, G. *et al.* Gbit/s mode division multiplexing over free space using vector modes and a q-plate mode (de)multiplexer. *Optics Letters* **40,** 1980–1983. http://ol.osa.org/abstract.cfm?URI=ol-40-9-1980 (May 2015).

491. Sit, A. *et al.* High-dimensional intracity quantum cryptography with structured photons. *Optica* **4,** 1006 (2017).

492. Ndagano, B., Nape, I., Cox, M. A., Rosales-Guzman, C. & Forbes, A. Creation and detection of vector vortex modes for classical and quantum communication. *Journal of Lightwave Technology* **36,** 292–301 (2018).

493. McLaren, M., Konrad, T. & Forbes Andrew. Measuring the non-separability of vector vortex beams. *Physical Review A* **92,** 23833 (2015).

494. Wootters, W. K. Entanglement of formation of an arbitrary state of two qubits. *Physical Review Letters* **80,** 2245 (1998).

495. Herman, B. J. & Strugala, L. A. *Propagation of High-Energy Laser Beams through the Earth's Atmosphere* in. **1221** (1990), 183–192.

496. Hu, X.-B., Ma, S.-Y. & Rosales-Guzmán, C. High-speed generation of singular beams through random spatial multiplexing. *Journal of Optics* **23,** 044002 (2021).

497. Fried, D. L. Optical resolution through a randomly inhomogeneous medium for very long and very short exposures. *JOSA* **56,** 1372–1379 (1966).

498. Pinnell, J. *et al.* Modal analysis of structured light with spatial light modulators: a practical tutorial. *JOSA A* **37,** C146–C160 (2020).

499. Zhou, Y. *et al.* Multiprobe time reversal for high-fidelity vortex-mode-division multiplexing over a turbulent free-space link. *Physical Review Applied* **15,** 034011 (2021).

500. Prabhakar, S., Plachta, S. Z., Ornigotti, M. & Fickler, R. High-accuracy longitudinal position measurement using self-accelerating light. *Applied Optics* **60,** 3203–3210 (2021).